

学位論文

Millimeter and Submillimeter Studies
on the Active Trinity of Gas, Stars, and Black Holes
in the Central Regions of Seyfert Galaxies

(セイファート銀河中心部における活動的なガス、星、
ブラックホールの三相のミリ波サブミリ波帯における研究)

平成 28 年 6 月 博士 (理学) 申請

東京大学大学院 理学系研究科
天文学専攻

泉 拓磨

To My Parents,

Millimeter and Submillimeter
Studies on the Active Trinity of Gas,
Stars, and Black Holes in the
Central Regions of Seyfert Galaxies

Takuma Izumi



東京大学
THE UNIVERSITY OF TOKYO

Department of Astronomy, School of Science
The University of Tokyo

A Thesis for the Degree of
Doctor of Philosophy

June 2016

Abstract

The main scope of this thesis is to better understand the physical link between active galactic nuclei (AGNs) and starbursts (SBs) in the central regions of Seyfert galaxies (a low–moderate luminosity class of the AGN populations), as well as their feedback on the surrounding interstellar medium, through high resolution, high sensitivity molecular gas (the dominant form of gas mass in the central \lesssim kpc region of galaxies) observations. The idea that dense molecular medium can be the fuel of supermassive black holes (SMBHs) as well as the stellar nursery, constitutes the basis of this work that uses molecular gas observations. Revealing properties of dust obscured AGNs and SBs, which would keep information on the triggering mechanisms of such activities, is of great importance to obtain a comprehensive view on galaxy evolutions over the cosmic time. Our particular interest is directed towards the ~ 100 pc scale circumnuclear disk (CND) usually found at the centers of galaxies, of which spatial scale has been the missing link in the continuous flow of mass from the host galaxies to the SMBHs. That scale is also the maximum one, at which nuclear energetic sources can significantly alter the chemical composition of the gas either through radiative or kinematic manners.

On the other hand, although molecular gas is an efficient probe of the CND scale activities, previous molecular observations towards active galaxies were mostly conducted with single dish telescopes, which traced the total molecular gas at spatial resolutions of \gtrsim kpc, except for some very nearby galaxies. Moreover, since such studies mostly used CO lines having low critical densities, they could not efficiently or selectively probe the CND scale properties, where the gas density is typically very high. Therefore, in this work, we used the high resolution, high sensitivity measurements of dense gas tracers (HCN(1–0), HCN(4–3), HCO⁺(4–3), and CS(7–6) are specifically used in this work) mainly provided by the Atacama Large Millimeter/submillimeter Array (ALMA), which started its regular operation recently. Adding the data compiled from the archive and the literature, we constructed the large dataset of such emission lines from the CND scale gas.

At first, we attempted to investigate the feedback from AGNs/SBs onto surrounding molecular medium. As an application of revealing any feedback, we tried to construct and propose an energy diagnostic method by utilizing variations in molecular chemistry caused by the different heating sources. The enhanced HCN(4–3)/HCO⁺(4–3) and HCN(4–3)/CS(7–6) ratios in AGNs as compared to SB galaxies (submm-HCN enhancement) revealed in Izumi et al. (2013) was the starting point of our investigation. Based on the analysis of 25 data points (16 galaxies), we found that the similarly high line ratios commonly in AGNs, when the data

was taken at the CND scale, which supports the validity of the combination of those spectral features as an energy diagnostic method. On the other hand, we could not see a clear trend of such enhancements for the data of AGNs taken at the galactic scale apertures (> 1 kpc) with single dish telescopes. This might be due to a significant contamination to the line flux from the surrounding and/or co-existing star forming regions, which is suggestive of the importance of high resolution observations to accurately measure line ratios representative in AGNs.

Non-local thermodynamic equilibrium radiative transfer modelings of the above molecular emission lines involving both collisional and radiative excitation were conducted to investigate the cause of the high line ratios in AGNs as well. We found that enhanced abundance ratios of HCN to HCO⁺ and HCN to CS in AGNs as compared to SB galaxies by a factor of a few to even $\gtrsim 10$ can well reproduce the submm-HCN enhancement. However, we cannot fully discard the possibility that the gas density is systematically higher in AGNs than in SB galaxies, which can also yield the higher line ratios in AGNs, although this seems to be unlikely. Then, we prefer the former scenario, which is indicative of abnormal chemical composition in AGNs, i.e., their feedback on molecular gas. Regarding the actual mechanism to realize the suggested composition, we argue that it is difficult with the conventional gas-phase ionization chemistry in X-ray-dominated regions. We would have to take into account other mechanisms instead, such as neutral-neutral reactions that are efficiently activated in high temperature environments and/or mechanically heated regions, to better reproduce the high line ratios in AGNs.

Although the above topic is related to the CND scale molecular chemistry, we also investigated the possibility of detecting submillimeter hydrogen recombination lines from the ionized broad line regions (BLRs) of AGNs with ALMA, which can be another way to probe the sub-pc scale structure of AGNs as well as to robustly argue the existence of an AGN even in the dust obscured nucleus. However, unfortunately, we proved that such emission lines from BLRs are so faint based on our analytical estimation that it is quite impractical to detect such lines even with ALMA. This speculation is further supported by the actual observational data.

At last, we investigated fueling processes to AGNs at the CND scale. We then analyzed the compiled data of HCN(1 – 0) emission line to estimate the mass of the dense molecular gas (M_{dense}) at the CND scale (10 objects) as well as at the galactic scale (32 objects) of Seyfert galaxies. We found that the M_{dense} of the CNDs are sufficiently large ($\sim 10^{7-8} M_{\odot}$) to keep the current nuclear activity (AGN + SB) for well beyond 10 Myr. Furthermore, we revealed a positive correlation between the M_{dense} and the mass accretion rate onto the SMBHs (\dot{M}_{BH}) estimated by the bolometric luminosities of the AGNs. This is the first time to identify a correlation between the properties of molecular gas and the AGN power at this spatial scale, and the correlation is suggestive of the importance of the CNDs as external source of fuel for (or triggers of) the AGN activities. In CNDs, it has been argued that the \dot{M}_{BH} and the star formation rate (SFR) are positively correlated (AGN–SB connection). As the stars are born from dense gas, the correlation we found would be a reflection of the SFR– \dot{M}_{BH} correlation. By assuming that the correlation is causal, we tried to explain its origin with the supernova-induced turbulent accretion model (Kawakatu & Wada 2008). As a result, we found that the mass inflowing from the CND, and the summation of (i) \dot{M}_{BH} and (ii) mass outflow rate from

an accretion disk, are well balanced, i.e., we might start to dissolve the balance of mass flows at the CND scale for the first time. Although the statistics is still poor, our results will strongly motivate future higher resolution observations that surely resolve the structures of CNDs, to further improve our understanding of the circumnuclear mass transportation.

Declaration

The work in this thesis is based on the research carried out at the Department of Astronomy, The University of Tokyo, Japan. No part of this thesis has been submitted elsewhere for any other degree or qualification.

Takuma Izumi
June 3, 2016

Acknowledgement

First of all, I would like to dedicate my deepest appreciation to Professor Kotaro Kohno, my supervisor, for his kind education on me! He introduced me this incredibly interesting radio-astronomical field. I have been surprising at his deep knowledge and interests over a wide astronomical topics, which enabled me to work on many topics from the nearby to the high(est) redshift universe as well (yes, the apple does not fall far from the tree; a student will grow up to be similar to his/her supervisor, both in behavior and characteristics). You are undoubtedly a great leader; *I hope that I have been a good (at least an interesting) student for you, too.*

I am really thankful for the heart-warming time with the present/former members of the Kohno group: Yoichi Tamura, Shun Ishii, Ryu Makiya, Kenta Suzuki, Soh Ikarashi, Hideki Umehata, Akio Taniguchi, Yuki Yamaguchi, Seiji Fujimoto, Ryo Ando, and Tsuyoshi Ishida. They always give me fruitful insights on various topics, as well as stimulate me to work hard on my study.

The large parts of this thesis are coming from the works with my great collaborators all over the world: Susanne Aalto, Daniel Espada, Kambiz Fathi, Nanase Harada, Bunyo Hatsukade, Pei-Ying Hsieh, Masatoshi Imanishi, Nozomu Kawakatsu, Melanie Krips, Sergio Martín, Satoki Matsushita, David S. Meier, Naomasa Nakai, Kouichiro Nakanishi, Eva Schinnerer, Kartik Sheth, Yuichi Terashima, and Jean L. Turner. I would really appreciate for their enormous cooperation. The intensive discussion with them greatly improved my knowledge and skills on the millimeter/submillimeter astronomy.

I surely learnt a strict and very physical way of approach to dissolve hard obstacles, from the development team of the Transition Edge Sensor Camera for ASTE, especially from Tai Oshima, Tetsuhiro Minamidani, Tatsuya Takekoshi, Tetsuhiro Sato, Max Curran, and Hidemi Ide, which is now the central mind of me, to promote scientific works.

I would like to thank my classmates, especially those who at our Institution of Astronomy (IoA), The University of Tokyo, for intensive discussion on each of our project: Kazushi Okada, Yutaro Kitagawa, Mitsuru Kokubo, and Hiroki Minaguchi.

On a private side, I would like to thank my family, especially for my mother Suzuka Izumi, father Kiyomi Izumi, sister and brother, Haruka and Hayato, my grandparents, and my lovely Candy, for their continuous support and encouragement. I am really grateful to M. Shibata for giving me the brilliant days in these years.

CONTENTS

1	Introduction: The Active Trinity in the Centers of Galaxies	1
1.1	The ISM in Galaxies	4
1.1.1	Molecular Gas in the Central Regions of Galaxies	6
1.2	Feeding Supermassive Black Holes	8
1.3	Star Formation from Molecular ISM	15
1.4	Feedback on Molecular Gas	16
1.4.1	Astrochemistry as a new probe of dust-obscured nucleus	16
1.4.2	Submillimeter hydrogen recombination line as another robust probe of dust-obscured AGNs	22
1.5	This Thesis	24
2	AGN Feedback on the CND-scale Molecular Gas: Submillimeter HCN Enhancement as a New Extinction Free Energy Diagnostic Tool	27
2.1	Context	27
2.2	Data Description	28
2.3	Revised Submm-HCN Diagram	33
2.4	Non-LTE Excitation Analysis	34
2.4.1	Model description	38
2.4.2	Molecular line excitation with photon trapping	39
2.4.3	The $R_{\text{HCN}/\text{HCO}^+}$ and $R_{\text{HCN}/\text{CS}}$ under non-LTE	44
2.4.4	Dependence of the line ratios on gas density	48
2.4.5	Comparison with real galaxies: Case studies of NGC 1097, NGC 1068, and NGC 4418	52
2.4.6	Implication to generic HCN-diagrams	55
2.5	Discussion: Chemical Causes of the HCN Abundance Enhancement	56
2.5.1	Steady-state XDR, PDR, and high temperature chemistry	57
2.5.2	Effects of metallicity and elemental abundance	61
2.5.3	IR-pumping	62
2.5.4	Time-dependent chemistry	63
2.6	Conclusions of This Chapter	63

3	Non-detection of Another Extinction-Free Proxy of Active Nuclei, Submillimeter Hydrogen Recombination Lines	66
3.1	Detectability of Broad Submm-RLs	66
3.2	Comparison with the Actual Data	71
3.3	Results	72
3.4	Conclusions of This Chapter	74
4	CND-scale AGN fueling: Do CNDs Drive the Growth of Supermassive Black Holes?	77
4.1	Context: AGN–SB Connection	77
4.1.1	Scope of This Chapter	78
4.2	Data Description	78
4.2.1	Line selection	81
4.2.2	Interferometric data	81
4.2.3	Single-dish data	85
4.2.4	Comments on the AGN sample	86
4.3	Regression Analysis	88
4.4	Results from the regression analysis	91
4.4.1	Positive $M_{\text{dense}} - \dot{M}_{\text{BH}}$ correlation	91
4.4.2	Virtual equivalence to the SFR – \dot{M}_{BH} correlations	92
4.5	Discussion on the CND-scale fueling	92
4.5.1	Mass loss from evolved stars	95
4.5.2	Angular momentum loss due to SN-driven turbulence	96
4.5.3	Implications for the evolution of AGNs	102
4.6	Conclusions of This Chapter	106
5	Summary and Future Outlook	108
5.1	Summary of This Thesis	108
5.2	Future Outlook	110
A	Notes on individual galaxies used in the submm-HCN diagram	112
A.1	NGC 1068	112
A.2	NGC 1097	113
A.3	NGC 1365	114
A.4	NGC 4945	114
A.5	NGC 7469	115
A.6	NGC 4418	115
A.7	IRAS12127-1412	116
A.8	M82	116
A.9	NGC 253	117
A.10	NGC 1614	117
A.11	NGC 3256	118

A.12 NGC 3628	118
A.13 NGC 7552	118
A.14 IRAS13242-5713	119
A.15 N113	119
A.16 N159	119
B Modifying the background radiation field	120
C Excitation of $\text{HCO}^+(4-3)$ and $\text{CS}(7-6)$ under non-LTE with photon trapping	121
D $J = 1 - 0$ transition measurements of HCN and HCO^+ towards NGC 7469 with ALMA	124
E Archival data of NGC 4579	127

List of Figures

1.1	Co-evolutionary relationships between M_{BH} and the properties of the galactic spheroidal components (Kormendy & Ho 2013)	2
1.2	Various spatial scale of an AGN –from a host galaxy to the center (Robson 1996)	3
1.3	A schematic picture of the active trinity in the centers of galaxies	4
1.4	Schematic outline of mass accumulation histories of both stellar contents and SMBH through gas-rich major mergers (Hopkins et al. 2008)	5
1.5	Various phases of the interstellar gas (Myers 1978)	6
1.6	The molecular mass fraction of several nearby galaxies (Honma et al. 1995) . . .	7
1.7	The typical cooling function of dense photodissociation regions (Hollenbach & Tielens 1999)	7
1.8	Spatial distributions of CO(2 – 1) and HCN(1 – 0) in the central ~ 2 kpc region of NGC 6951 (Krips et al. 2007)	8
1.9	No systematic difference in nuclear morphology between active and inactive galaxies	9
1.10	Molecular and atomic gas mass ratio for Seyfert galaxies and field ones (Maiolino et al. 1997)	10
1.11	Schematic view of the circumnuclear disk (CND) formed by the remaining angular momentum of the inflowing gas from the host galaxy (Kawakatu & Wada 2008) .	11
1.12	Gallery of CNDs in nearby Seyfert galaxies probed by molecular emission lines .	12
1.13	Systematic difference between AGNs and inactive galaxies at the CND-scale (Hicks et al. 2013)	12
1.14	A correlation plot between circumnuclear SFR and \dot{M}_{BH} (Diamond-Stanic & Rieke 2012)	13
1.15	Posterior distributions of the correlation coefficient and the intrinsic scatter in the SFR and \dot{M}_{BH} correlations (Diamond-Stanic & Rieke 2012)	14
1.16	A systematic delay between the onset of nuclear SB and that of AGN activity (Davies et al. 2007)	15
1.17	Correlation plots between properties of star formation and those of molecular gas in galaxies (Kennicutt & Evans 2012)	17
1.18	Extragalactic circumnuclear star formation induced by the gravitational collapse revealed by ALMA (Fathi et al. 2015)	18

1.19	A schematic overview of a photodissociation region = PDR (Hollenbach & Tielens 1999)	19
1.20	Schematic overviews of a ionization, thermal, and chemical structures as well as energy flows in an X-ray dominated region = XDR (Maloney et al. 1996)	20
1.21	Chemical paths expected under the high temperature conditions for HCN and HCO ⁺ (Harada et al. 2010)	21
1.22	Column density distribution of AGNs in the nearby universe (Buchner et al. 2015)	21
1.23	Mm-HCN diagram using HCN(1 – 0)/HCO ⁺ (1 – 0) and HCN(1 – 0)/CO(1 – 0) ratios (Kohno 2005)	22
1.24	Results of multi-transition non-LTE analysis of HCN and HCO ⁺ toward the central 100 pc region of NGC 1097 (Izumi et al. 2013)	23
1.25	The specific optical depth of HI recombination line at various transitions (Scoville & Murchikova 2013)	25
1.26	The expected size of an XDR (Schleicher et al. 2010).	26
2.1	Revised submillimeter-HCN diagram using HCN(4–3)/HCO ⁺ (4–3) and HCN(4–3)/CS(7 – 6) integrated intensity ratios (high resolution sample)	35
2.2	Revised submillimeter-HCN diagram (whole sample)	36
2.3	Excitation temperature (T_{ex}) of HCN(4 – 3) as a function of background temperature (T_{bg})	40
2.4	Line optical depths of HCN(4 – 3), HCO ⁺ (4 – 3), and CS(7 – 6), as a function of T_{bg}	41
2.5	Dependence of $\eta \equiv 1/(\exp(\Delta E_{ul}/T_{\text{bg}})-1)$ of HCN(4 – 3) on T_{bg}	43
2.6	The $R_{\text{HCN}/\text{HCO}^+}$ and the $R_{\text{HCN}/\text{CS}}$ as a function of T_{bg}	45
2.7	Dependence of the $R_{\text{HCN}/\text{HCO}^+}$ and the $R_{\text{HCN}/\text{CS}}$ on T_{ex} and τ_{line}	48
2.8	Same as Figure 2.6, but the models with $n_{\text{H}_2} = 5 \times 10^6 \text{ cm}^{-3}$	51
2.9	Same as Figure 2.4, but the models with $n_{\text{H}_2} = 5 \times 10^6 \text{ cm}^{-3}$	52
2.10	HCN spectral line energy distribution (SLED) of some local galaxies (Knudsen et al. 2007)	53
2.11	Spectral ratio distributions of HCN-to-HCO ⁺ and HCN-to-CS integrated intensity ratios	56
2.12	$R_{\text{HCN}/\text{HCO}^+}$ based on the XDR ionization model (Meijerink et al. 2007)	57
2.13	The steady state abundances of HCN and HCO ⁺ expected in an XDR ionization model (Lepp & Dalgarno 1996)	58
2.14	Spatial distribution of HCN($J = 4 - 3$) to HCO ⁺ ($J = 4 - 3$) integrated intensity ratio inside the CND of NGC 1068 (García-Burillo et al. 2014)	60
2.15	Fractional abundances of HCN, HCO ⁺ , and CS, as a function of the gas-phase metallicity (Bayet et al. 2012)	62
2.16	Steady state fractional abundances of HCN and HCO ⁺ in a molecular disk exposed to AGN radiation under the high temperature chemistry (Harada et al. 2013)	64

LIST OF FIGURES

2.17	Fractional abundances of HCN and HCO ⁺ in a molecular disk exposed to AGN radiation at the shock-crossing time (Harada et al. 2013)	64
3.1	The optical depth of H26 α per unit EM	67
3.2	Expected line to free–free continuum ratios as a function of frequency	70
3.3	The 364 GHz continuum emission of the central region of NGC 1068	73
3.4	The ALMA Band 7 spectrum of NGC 1068 containing H26 α emission line	73
3.5	Radio SED of the nucleus of NGC 1068 (Krips et al. 2011)	75
4.1	Distributions of the bolometric luminosity L_{Bol} , the black hole mass M_{BH} , and the Eddington ratio λ_{Edd} of the sample galaxies	87
4.2	Scatter plot of the spatial resolution and HCN(1 – 0) line luminosity	88
4.3	Scatter plots of $L'_{\text{HCN}} - L_{2-10\text{keV}}$ and $M_{\text{dense}} - \dot{M}_{\text{BH}}$	90
4.4	Distribution of dense gas mass of our sample Seyfert galaxies	91
4.5	Posterior distributions of the regression parameters for the $\log(M_{\text{dense}}) - \log(\dot{M}_{\text{BH}})$ relationship	93
4.6	The spatial coincidence of 2.12 μm H ₂ 1 – 0 S(1) line and cold molecular gas in NGC 1068	99
4.7	Scatter plot of the mass accretion rate from the CNDS predicted by the SN-driven turbulence model and \dot{M}_{BH}	103
4.8	Schematic of the SN-driven turbulent accretion model	104
4.9	Scatter plot of the mass accretion rate from the CNDS and the expected total mass flow rate at the nuclear (accretion disk-scale) region	105
5.1	Summary of the newly revealed properties of the active trinity in this theses	110
5.2	The detailed spatial distributions of dense gas tracers in NGC 1097 (low-luminosity Seyfert) and NGC 1068 (high-luminosity Seyfert)	111
A.1	Spatial distributions of the Band 7 continuum and ¹² CO($J = 3 - 2$) line emissions in the central region of NGC 1068 (García-Burillo et al. 2014; Viti et al. 2014)	113
A.2	Spatial distributions of the Band 7 continuum and HCN($J = 4 - 3$) line emissions in the central region of NGC 1097 (Izumi et al. 2013)	114
A.3	Spatial distributions of HCN($J = 4 - 3$) line emission in the central region of NGC 7469 (Izumi et al. 2015)	116
C.1	Excitation temperature of HCO ⁺ (4 – 3) as a function of background temperature.	122
C.2	Same as Figure C.1, but for the cases of CS(7 – 6).	123
D.1	Spatial distributions of the HCN(1 – 0) and HCO ⁺ (1 – 0) emissions in the central region of NGC 7469	125
D.2	Band 3 spectrum extracted at the nucleus of NGC 7469 containing HCN(1 – 0) and HCO ⁺ (1 – 0) lines	126

E.1 Spatial distribution of HCN(1 – 0) and the underlying continuum emissions in the central 1.2 kpc region of NGC 4579	128
--	-----

List of Tables

- 1.1 Distinctive phases of interstellar gas (Draine 2011) 5
- 2.1 $R_{\text{HCN}/\text{HCO}^+}$ and $R_{\text{HCN}/\text{CS}}$ of the sample galaxies 31
- 2.2 The excitation parameters of HCN(4 – 3), HCO⁺(4 – 3), and CS(7 – 6) line emissions 37
- 2.3 Summary of the typical $X_{\text{HCN}}/X_{\text{HCO}^+}$ of AGN and SB 52
- 3.1 Emission properties at the centre of NGC 1068 75
- 4.1 Properties of the sample galaxies 79
- 4.2 M_{dense} and \dot{M}_{BH} of the sample galaxies 82
- 4.3 Results from the regression analysis 94
- 4.4 Parameters of the CNs for the model prediction 101

Chapter 1

Introduction: The Active Trinity in the Centers of Galaxies

The mass accretion onto a supermassive black hole (SMBH, with a mass of $M_{\text{BH}} \gtrsim 10^6 M_{\odot}$) is commonly believed to produce the enormous amount of energy observed as an active galactic nucleus (AGN, Antonucci 1993; Urry & Padovani 1995), although the physics of the angular momentum transfer of the accreting gas remains unclear (Alexander & Hickox 2012 for a review). SMBHs have been claimed to reside at the centers of galaxies with spheroidal components, showing correlations between M_{BH} and the properties of the spheroidal components, such as bulge mass (M_{bulge}) and stellar velocity dispersion (σ_*). This, a so called *co-evolutionary* relationship (Figure 1.1, Ferrarese & Merritt 2000; Gültekin et al. 2009; Magorrian et al. 1998; Marconi & Hunt 2003; Tremaine et al. 2002; Kormendy & Ho 2013 for a recent review), indicates that galaxies and SMBHs evolved together, by regulating each other, and has become the central issue in the studies on the evolution of galaxies. Therefore, to understand the mechanism of the angular momentum transfer of the accreting gas at various spatial scales (from a host galaxy to an accretion disk; Figure 1.2), which is directly connected to the mass accumulation of an SMBH, is of great importance to unveil the currently unconstrained co-evolutionary mechanism.

From this perspective, we argue the importance of observing cold molecular gas, as it is the dominant phase of the mass of the interstellar medium (ISM) at the central \lesssim kpc regions of galaxies (Section 1.1). That spatial scale, *especially the central 100 pc region of galaxies* (Figure 1.2), is currently *the missing link* in AGN fueling studies (Section 1.2). Furthermore, dense molecular gas is the site of star formation (in the central regions of galaxies, it is specifically referred to as (circumn)nuclear starburst (SB); Section 1.3). In other words, cold molecular gas can be the fuel of both active mass accretion onto SMBHs and circumnuclear SB. Then, revealing the circumnuclear molecular properties will be the key to uncover a potential link between SB and AGN as well (*AGN–SB connection*, or, mass accretion regulated by star formation; Section 1.2).

On the other hand, such heating sources can conversely alter the physical and chemical conditions of their surrounding medium radiatively and/or mechanically in different manners, by reflecting the difference in their spectral energy distributions (SEDs). Hence, the chemical com-

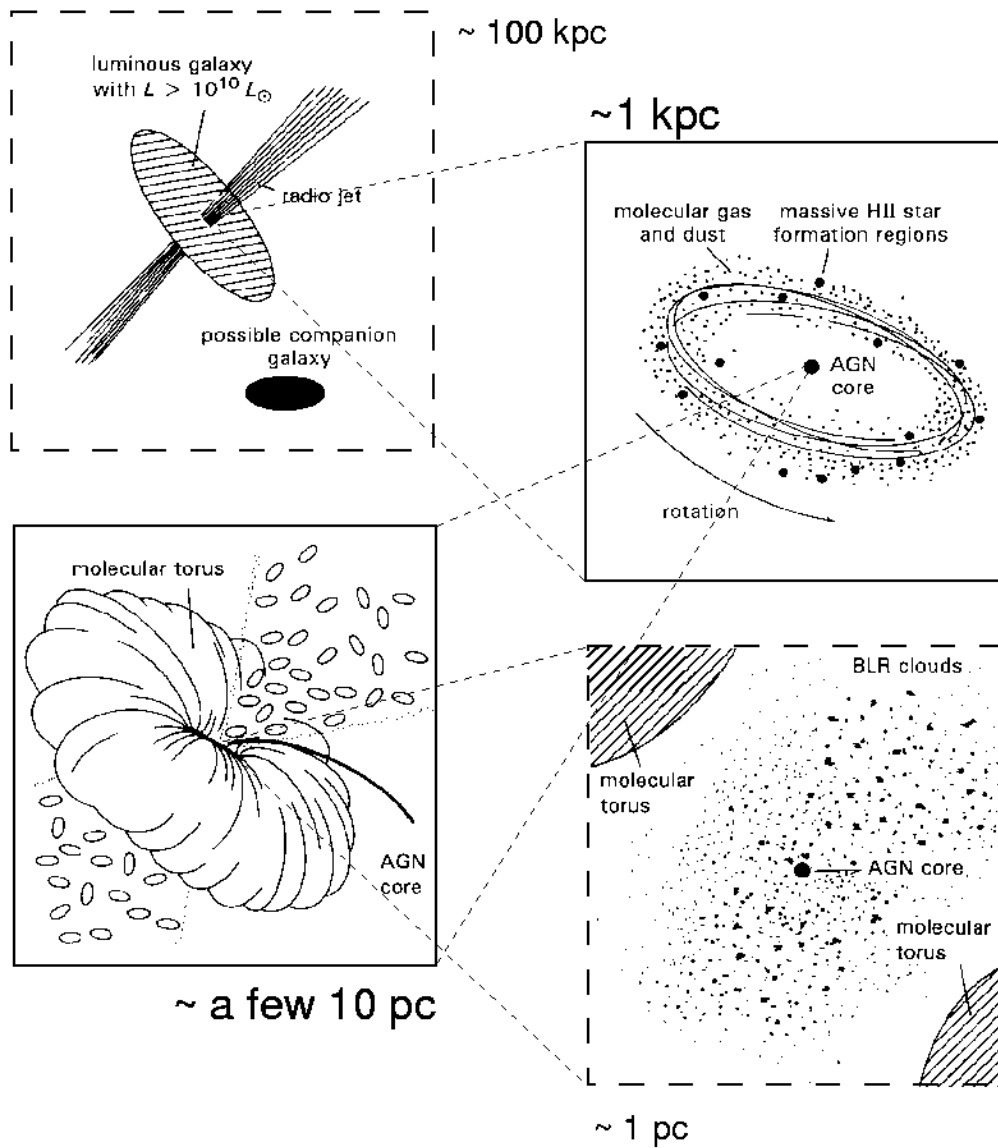


Figure 1.2: A schematic view of various spatial components expected in AGN galaxy, from a galaxy scale to the center (Robson 1996). Among these components, the circumnuclear disk (CND; central 10s–100 pc scale structure), which has not been studied in detail so far, is the target investigated in this thesis.

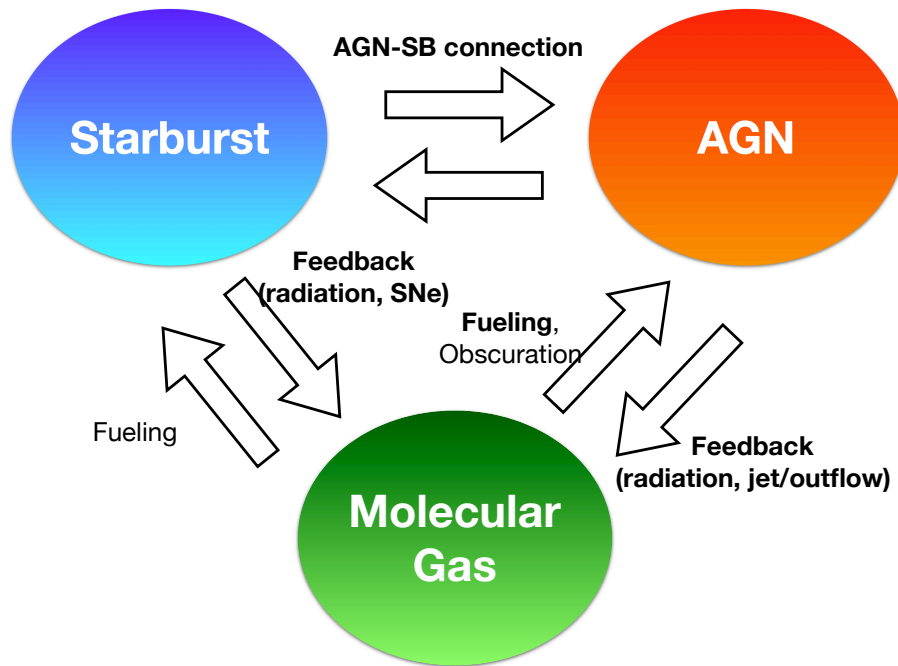


Figure 1.3: The active trinity (active SMBHs = AGNs, starburst = SB, and molecular gas) in the centers of galaxies and their interplay. Revealing the detailed physics of this interplay is our grand scope. The individual topics handled in this thesis are indicated by the bold.

growth at high redshifts even by studying nearby objects.

In the following, we briefly overview the basic properties of the interplay among the active trinity, to provide the background of this thesis.

1.1 The ISM in Galaxies

The ISM is arguably an important component of galaxies as it (especially its molecular form) is the prerequisite material out of which stars are born. Although it is only a minor constituent ($\sim 10\%$) of the present day baryonic mass of large spiral galaxies like the Milky Way, the ISM implicitly controlled the evolution of galaxies as that evolution is predominantly determined by the initial mass function of stars and the star formation rate (SFR), both of which are related to molecular properties of galaxies. Moreover, the ISM can be the fuel onto SMBHs, with releasing huge amount of gravitational energy in accretion disks (AGN). Hence, as the form of both stellar components and AGNs, the ISM is responsible for determining the visible appearance of galaxies.

The ISM consists of gas and dust, with a mass ratio of $\sim 100 : 1$. The temperature of the gas is determined by the balance of the heating and the cooling, whereas the density is determined by the balance of several forces. Figure 1.5 shows the various phases of gas component in the ISM on the density (n)–temperature (T) plane. This distribution is well reproduced by three-phase medium models (e.g., McKee & Ostriker 1977): (1) cold ($T \lesssim 300$ K), dense phase that mostly

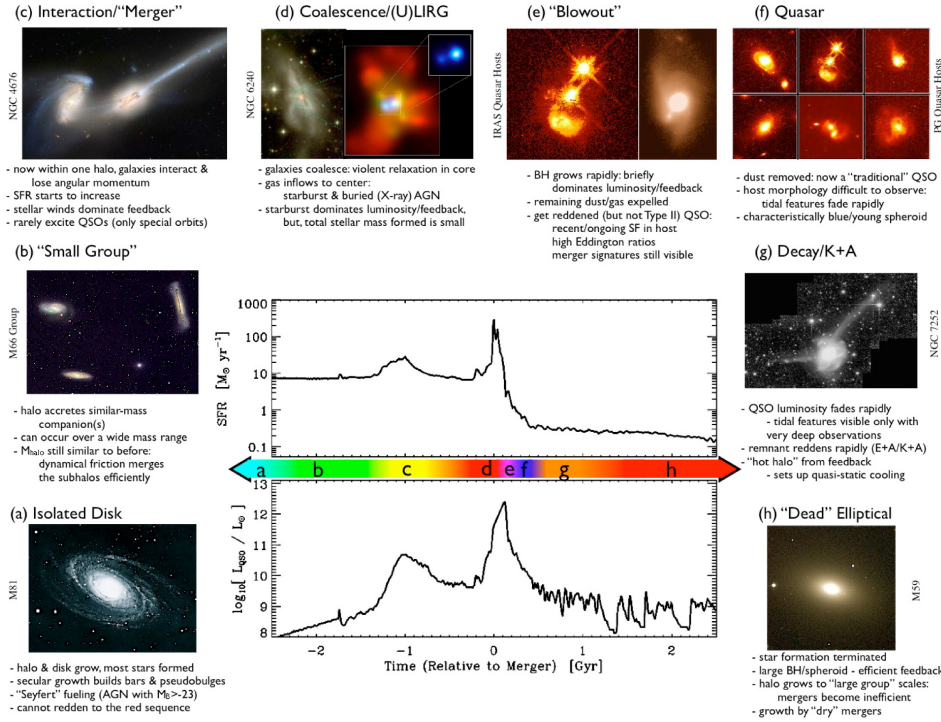


Figure 1.4: Schematic outline of mass accumulation histories of both stellar contents and SMBHs through gas-rich major mergers (top and bottom plots in the central panel, respectively; Hopkins et al. 2008). Galaxy mergers induce mass accretion toward the central region of the merged galaxy, causing prominent starburst and trigger (buried) AGN activity. Once SMBH grows rapidly, its violent radiative feedback blows the surrounding gas out, which makes the AGN a luminous quasar visible at the optical. The AGN feedback terminates the star formation, and after the gas is consumed, the galaxy will become red and dead (elliptical).

Table 1.1: Distinctive phases of interstellar gas (Draine 2011)

ISM phase	Temperature (K)	Density (cm^{-3})	Volume filling factor (%)
Coronal gas	$\gtrsim 10^{5.5}$	~ 0.004	~ 50
HII gas (warm ionized medium)	10^4	$\sim 0.2 - 10^4$	~ 10
Warm HI gas (warm neutral medium)	~ 5000	~ 0.6	~ 40
Cold HI gas (cold neutral medium)	~ 100	~ 30	~ 1
Diffuse H_2 gas	~ 50	~ 100	~ 0.1
Dense H_2 gas	$\sim 10 - 50$	$\sim 10^3 - 10^6$	~ 0.01

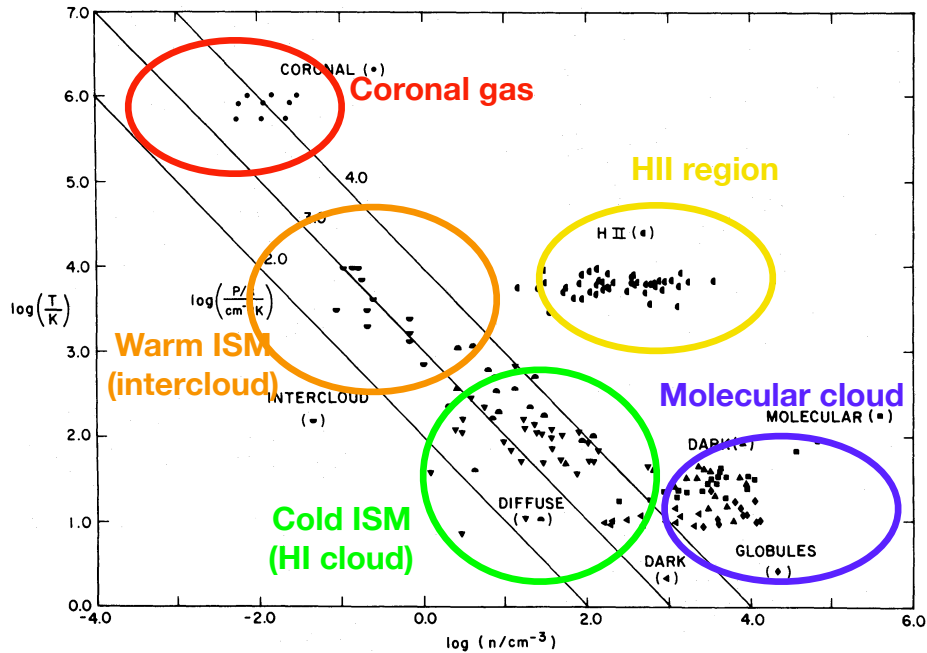


Figure 1.5: Various phases of the interstellar gas (Myers 1978) in the density (n) – temperature (T) plane. As the lines indicate the pressure equilibrium ($P = nk_B T$, k_B is the Boltzmann constant), one can see that, e.g., the intercloud gas (warm ISM) and the diffuse, cold ISM (HI cloud) are in the pressure equilibrium.

consists of neutral clouds of atomic/molecular hydrogen, (2) warm ($T \sim 10^3$ K) intercloud phase that consists of neutral or ionized gas, and (3) hot ($T \sim 10^6$ K) coronal phase that is likely heated by supernova explosions. We list typical properties of each phase in Table 1.1 as well.

1.1.1 Molecular Gas in the Central Regions of Galaxies

Among the various ISM phases, we focus on the molecular phase as it is the dominant carrier of the gas mass in the central kpc regions of galaxies (Figure 1.6, e.g., Honma et al. 1995; but see also Fukui et al. (2015) pointing out that the classical HI mass estimation may underestimate its mass by a factor of a few). The molecular clouds mostly consist of H_2 , with minor contributions from other species such as CO. Owing to the high density (Table 1.1) associating large amount of dust, molecules can survive against the dissociative UV photons from nearby OB stars. It is well known that molecular clouds clearly have supersonic turbulence inside them (e.g., Heyer & Brunt 2004), thus, they are likely to be structured by the balance of the self-gravity and the turbulent pressure.

The molecular clouds, which are heated by, e.g., surrounding massive stars, harsh radiation from AGNs, interstellar shocks, can be cooled down efficiently via molecular rotational lines. As H_2 does not have the eternal dipole moment, abundant species such as CO takes bulk of the cooling instead (Figure 1.7). Hence, properties of cold molecular gas have been mostly probed by CO rotational lines.

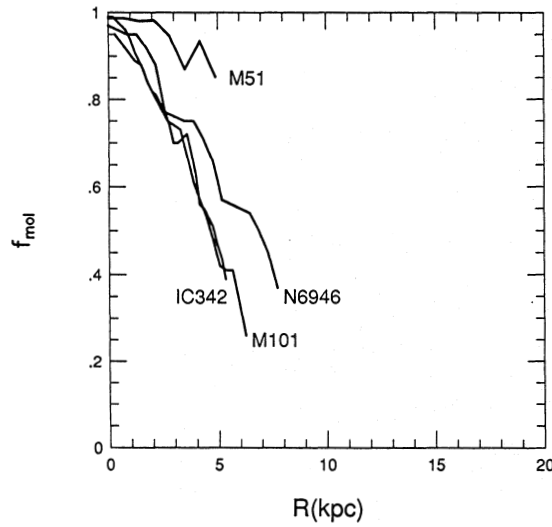


Figure 1.6: The molecular mass fraction, i.e., $f_{\text{mol}} = 2n(\text{H}_2)/(n(\text{H})+2n(\text{H}_2))$, of several nearby galaxies as a function of the galactocentric radius R (Honma et al. 1995). Note that the H_2 mass was calculated from the $\text{CO}(1-0)$ emission line. This plot clearly indicates that the bulk of the gas mass in the central regions of galaxies is dominated by the molecular phase. Although Fukui et al. (2015) predicted more HI mass instead, the dominance of the molecular phase should hold.

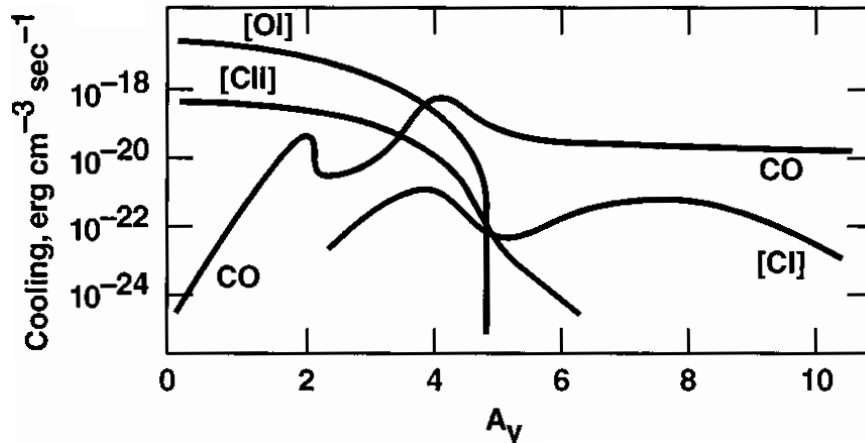


Figure 1.7: A typical cooling function of a dense ($n = 2.3 \times 10^5 \text{ cm}^{-3}$, $G = 10^5 G_0^2$) photodissociation region, plotted against the visual extinction (A_V) of the cloud (Hollenbach & Tielens 1999). While atomic lines carry out the heat at the surface, CO (and H_2O , which is not plotted) is the dominant coolant deeper ($A_V \gtrsim 5$) inside the cloud.

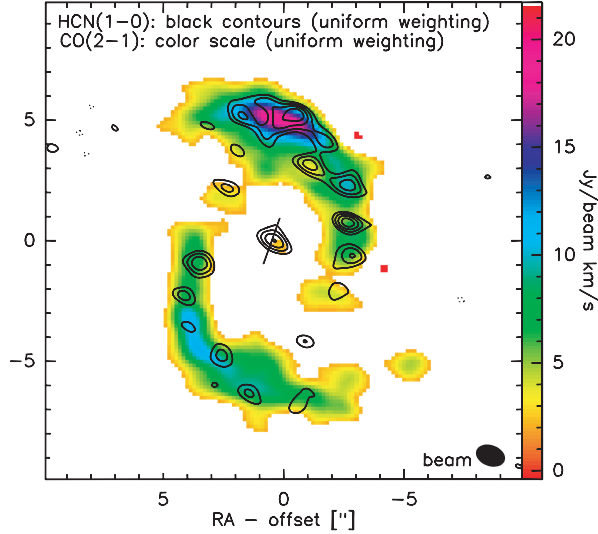


Figure 1.8: Spatial distributions of CO(2 – 1) and HCN(1 – 0) in the central ~ 2 kpc region ($1'' \sim 100$ pc) of NGC 6951 obtained with PdBI (Krips et al. 2007). The contour and the color indicate the distribution of HCN(1 – 0) and CO(2 – 1), respectively. One will find that at the central ~ 100 pc region, CO(2 – 1) is not prominently visible, whereas strong emission of HCN(1 – 0) stems from there.

On the other hand, at the central regions of galaxies, H_2 density starts to exceed the critical density of the conventionally used CO(1 – 0), i.e., $\sim 10^3 \text{ cm}^{-3}$. In such regions, molecular species having larger dipole moments than CO like HCN, HCO^+ , and CS (i.e., dense gas tracer) become prominently visible (Figure 1.8). As stars are born from the densest part of molecular clouds, these dense gas tracers are suitable to probe such regions, and to investigate any link among the active trinity as discussed in the subsequent Chapters.

1.2 Feeding Supermassive Black Holes

Numerical simulations have shown that the radial streaming of gas caused by major mergers can efficiently feed the central SMBH, which triggers a powerful AGN as well as SB (Figure 1.4, e.g., Hopkins et al. 2008; Hopkins & Quataert 2010). While such a violent mechanism would be vital for fueling luminous quasars, rather secular processes induced by, for example, barred gravitational potential, galaxy–galaxy interactions, or even joint effects of star formation and large-scale dynamics (e.g., Barnes & Hernquist 1992; Hopkins & Hernquist 2006; Jogee 2006; Kormendy & Kennicutt 2004; Rocca-Volmerange et al. 2015; Shlosman et al. 1990), or minor mergers (e.g., Kaviraj 2014; Mihos & Hernquist 1994; Taniguchi 1999), would be sufficient to explain lower-luminosity activity, such as that observed in Seyfert galaxies (e.g., Hopkins & Hernquist 2009; Treister et al. 2012). The lack of enhanced signatures of major mergers or strong interactions in local Seyfert galaxies strongly supports this view (Cisternas et al. 2011;

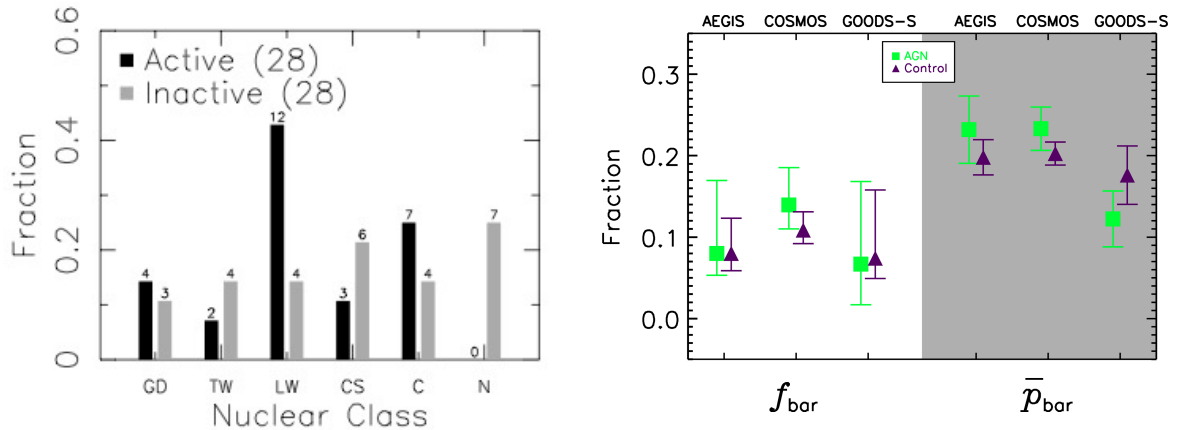


Figure 1.9: (*left*) The distribution of AGNs and inactive galaxies (their host galaxy properties were matched) over a wide range of nuclear morphological classes (Martini et al. 2003). The classes are, GD = grand-design nuclear spiral, TW = tightly wound nuclear spiral, LW = loosely wound nuclear spiral, CS = chaotic spiral, C = chaotic dust structure, and N = no dust structure. Although AGNs seem to reside in dusty environments, the nuclear spiral structure is found with comparable frequency between AGNs and inactive galaxies, indeed. (*right*) The bar fraction (f_{bar}) and the average bar likelihood (\bar{p}_{bar}) of AGNs and control inactive galaxies (Cheung et al. 2015) observed in AEGS, COSMOS, and GOODS-S fields. There are no statistically significant differences in these values between the two groups. Note that this result is based on the Galaxy-Zoo’s Citizen Science: if 25 out of 50 volunteers classified one galaxy as having a bar, then the bar likelihood is $p_{\text{bar}} = 0.5$. The p_{bar} of galaxies in each group is averaged to calculate \bar{p}_{bar} .

Gabor et al. 2009).

In the case of a Seyfert galaxy, although large-scale structures, like a bar, would efficiently transport gases towards the central region (e.g., Sakamoto et al. 1999; Sheth et al. 2005), there is little or no clear difference in that scale morphologies between AGN hosts and inactive galaxies (e.g., Cheung et al. 2015; Cisternas et al. 2015; Martini et al. 2003; Mulchaey & Regan 1997; Simões Lopes et al. 2007), except that AGNs tend to reside in dusty environments. Even for smaller-scale morphologies, such as nuclear bars and nuclear spirals (e.g., Hopkins & Quataert 2010; Shlosman et al. 1990), this trend holds, at least in late-type galaxies (typical hosts of Seyfert nuclei, Figure 1.9, e.g., Hunt & Malkan 2004; Martini et al. 2003). Regarding early type galaxies, on the other hand, Simões Lopes et al. (2007) found that Seyfert nuclei preferentially accompany dusty structures (Figure 1.9). Thus, the presence of a nuclear dusty (equivalently gaseous) structure is necessary but not sufficient to trigger AGNs. From molecular gas observations, again there seems to be no systematic difference in global molecular properties between Seyfert galaxies and non-Seyfert (field) galaxies once a selection effects are accounted for (e.g., Maiolino et al. 1997; see also Figure 1.10). To summarize, there is apparently no unique mechanism (or morphological feature) in Seyfert galaxies at $\gtrsim 100$ pc from the center, and direct trigger(s) of AGN activity should exist at the innermost ~ 100 pc region.

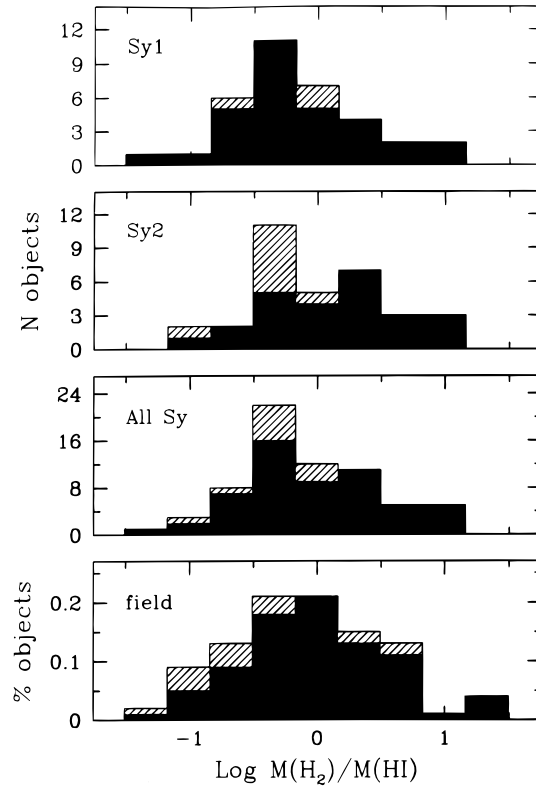


Figure 1.10: Distribution of the ratio of molecular and atomic gas mass for Seyfert (type 1, 2, and all) galaxies and field galaxies (Maiolino et al. 1997). These quantities are measured at the entire galactic scale with single dish telescopes. The filled and the hatched bars indicate the detection and the upper limits, respectively. There is no statistical difference in this qualitative ratio between the Seyferts and the field galaxies.

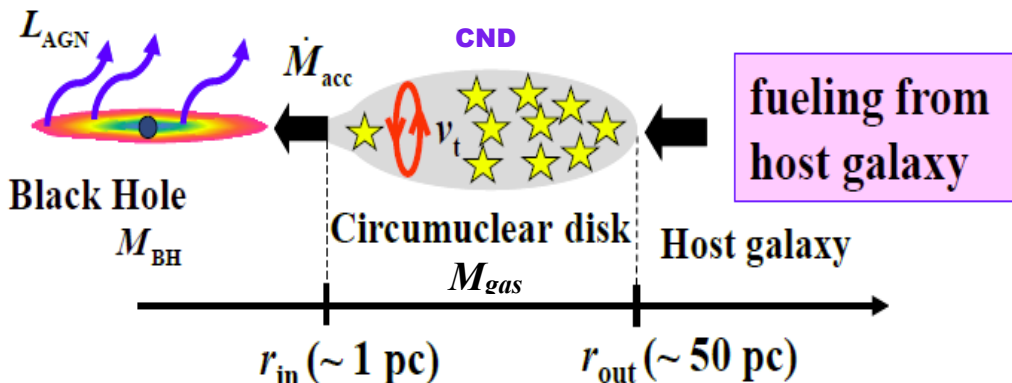


Figure 1.11: Schematic view of the $\sim 100 \text{ pc}$ scale circumnuclear disk (CND) formed by the remaining angular momentum of the inflowing gas from the host galaxy (Kawakatu & Wada 2008). The gas mass of the CND is denoted as M_{gas} . Further mass accretion from the CND with a rate of \dot{M}_{acc} towards the central SMBH (with the mass of M_{BH}) is shown as well. We emphasize that the accretion processes at this CND scale is totally unclear at this moment, which is then the subject of this thesis (Chapter 4).

At the central $\sim 100 \text{ pc}$ scale, many studies have proposed that the inflowing gas from the host galaxies would form a *circumnuclear disk (CND)*³ due to the remaining angular momentum (Figure 1.11, e.g., Ballantyne 2008; Kawakatu & Wada 2008; Thompson et al. 2005; Vollmer et al. 2008). Indeed, such dense molecular gas disks have been found observationally in Seyfert nuclei (e.g., Davies et al. 2012; García-Burillo et al. 2014; Hicks et al. 2013, 2009; Izumi et al. 2013, 2015; Krips et al. 2007; Sani et al. 2012), although few of them have been resolved spatially (Figure 1.12).

Recently, Hicks et al. (2013) reported on systematic differences at the CND-scale between active and inactive galaxies (Figure 1.13): Seyfert galaxies showed more centrally concentrated profiles of both the stellar continuum and $\text{H}_2 1-0 \text{ S}(1)$ line emission with enhanced H_2 luminosity. Therefore, molecular surface brightness is clearly elevated in CNDs of Seyfert galaxies. Moreover, Seyfert galaxies tend to have dynamically colder CNDs, rather than spherical structures with large velocity dispersion, as compared to inactive galaxies, which is also indicative of the existence of disk-like components there. If we regard that the elevated H_2 luminosity is a reflection of enhanced H_2 mass, we can argue that the *surface gas mass density* of the CNDs are systematically higher in Seyfert galaxies than in inactive galaxies.

Because a CND would be a massive reservoir of molecular gas, we can reasonably expect active star formation there. Observationally, prominent (circum-)nuclear SB activities have been found, indeed (e.g., Alonso-Herrero et al. 2013; Cid Fernandes et al. 2004; Davies et al. 2007; Diamond-Stanic & Rieke 2012; Esquej et al. 2014; Heckman et al. 1995; Imanishi & Wada 2004). What is particularly important is that there are correlations between the SFR and the black hole accretion rate (\dot{M}_{BH}) in Seyfert galaxies (Figure 1.14), which are tighter when the

³A CND refers to a massive gaseous disk with sizes of $\sim 1 - 100 \text{ parsec [pc]}$ in this work.

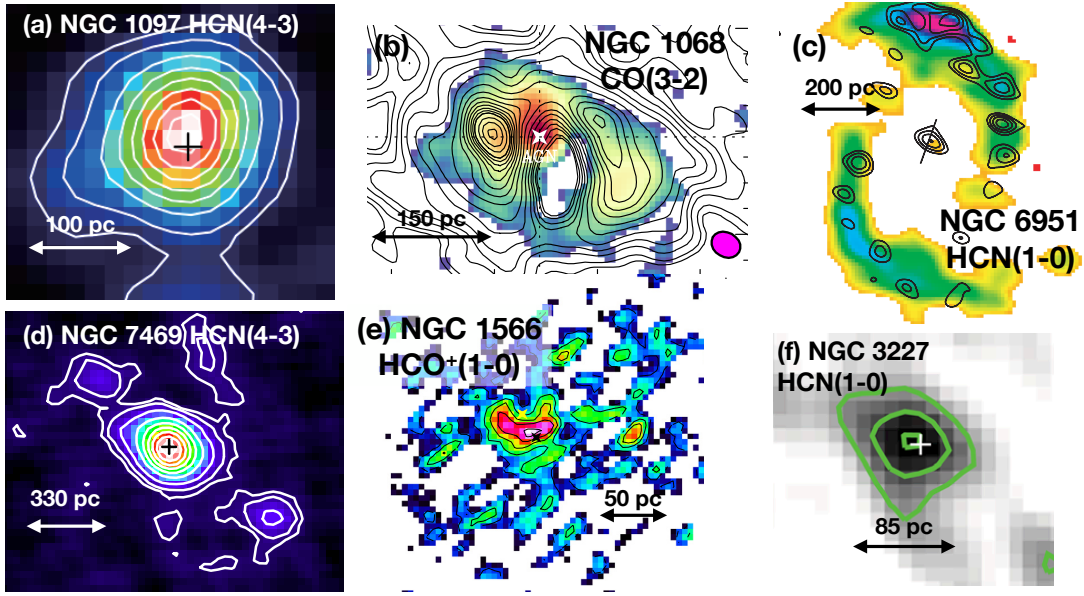


Figure 1.12: The CNDs of (a) NGC 1097 (Izumi et al. 2013), (b) NGC 1068 (García-Burillo et al. 2014), (c) NGC 6951 (Krips et al. 2007), (d) NGC 7469 (Izumi et al. 2015), (e) NGC 1566 (Combes et al. 2014), and (f) NGC 3227 (Sani et al. 2012), probed by molecular emission lines. A ~ 100 pc scale gaseous structure is indeed visible in these Seyfert galaxies.

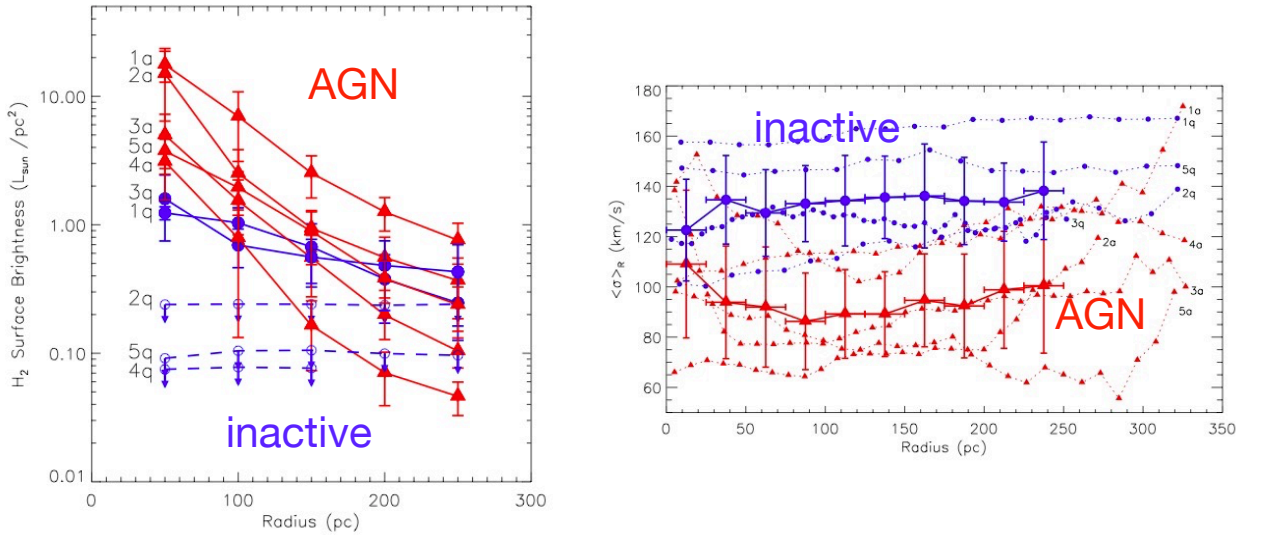


Figure 1.13: Systematic differences between AGNs and inactive galaxies (their host galaxy properties are matched) at the CND-scale (Hicks et al. 2013) in the radial profile of, (left) $2.12 \mu\text{m}$ H_2 surface brightness, and (right) velocity dispersion (σ) of CO absorption line. AGNs show more centrally concentrated H_2 brightness profile in the CND, which can be a reflection of enhanced *mass* surface density, as compared to the cases of inactive galaxies.

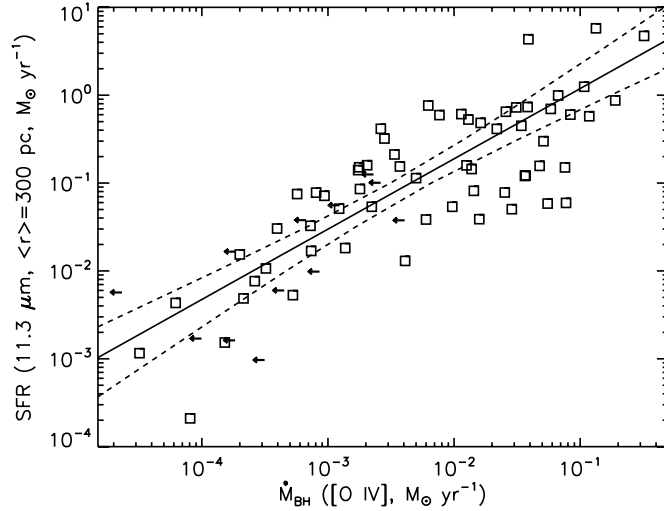


Figure 1.14: A correlation between circumnuclear scale star formation rate (SFR) traced by the $11.3 \mu\text{m}$ polycyclic aromatic hydrocarbon (PAH) emission and mass accretion rate on to SMBH (\dot{M}_{BH}) traced by [OIV] luminosity (Diamond-Stanic & Rieke 2012). The averaged aperture for the PAH measurements is $\langle r \rangle = 300 \text{ pc}$. The positive correlation is suggestive of the AGN–SB connection, where the mass accretion onto the SMBH is somehow controlled by the surrounding star formation.

SFR is measured in closer vicinity to the AGN, whereas it is weaker for larger-scale ($\gtrsim \text{kpc}$) SFR (Figure 1.15, Diamond-Stanic & Rieke 2012; Esquej et al. 2014). Interestingly, similar correlations have been reported in quasars as well (e.g., Drouart et al. 2014; Lutz et al. 2010; Willott et al. 2013).

On the origin of the SFR – \dot{M}_{BH} correlations, we should consider the results of Davies et al. (2007), who suggested a systematic time delay of 50 – 200 Myr between the onset of the latest star formation and that of the AGN activity (Figure 1.16). Similar arguments were raised independently later on (e.g., Schawinski et al. 2009; Wild et al. 2010). That delay might be the compelling evidence of a *causal* connection between those two activities: that star formation provides the fuel for the SMBH, which is the very idea of the AGN–SB connection. As a candidate mechanism to make such a link, Hopkins & Quataert (2010) suggested, for example, the importance of a series of gravitational instability and the resulting stellar gravitational torque on molecular gas based on hydro-dynamic simulations (see also Hopkins 2012). Inside the central $r \lesssim 10 \text{ pc}$, they predicted that an $m = 1$ mode (single-armed spiral) develops, which can efficiently remove the angular momentum of the gas. Indeed, a nuclear trailing spiral (but $m = 2$) was found in the central $\sim 50 \text{ pc}$ of the type 1 Seyfert galaxy NGC 1566 (Combes et al. 2014). However, the prevalence and the practical utility of such spiral(s) in other Seyfert galaxies is still suspicious, considering that there is no systematic morphological difference between active and inactive galaxies at $\gtrsim 100 \text{ pc}$. Furthermore, previous molecular gas observations with Plateau de Bure Interferometer (PdBI) towards nearby AGNs (NUclei of Galaxies = NUGA survey; e.g., García-Burillo et al. 2005, 2003) suggested the limited capability of stellar gravitational torques

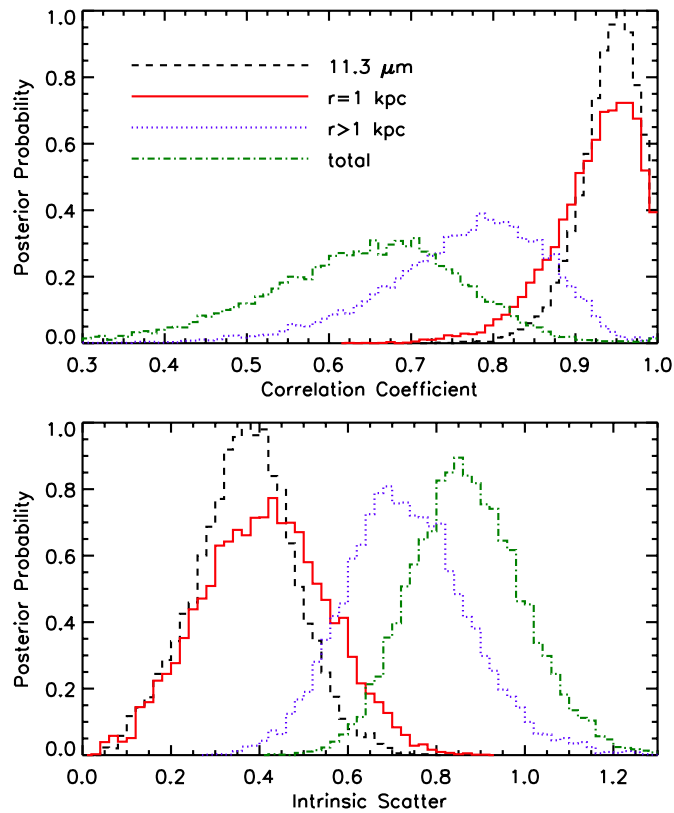


Figure 1.15: Posterior distributions for (*top*) the correlation coefficient and (*bottom*) the intrinsic scatter in the SFR– \dot{M}_{BH} correlations (see Figure 1.14). Here, SFR was measured at different apertures as indicated by different lines (Diamond-Stanic & Rieke 2012). One can find a stronger correlation with smaller scatter for the smaller scale SFR than for the larger/galactic scale one.

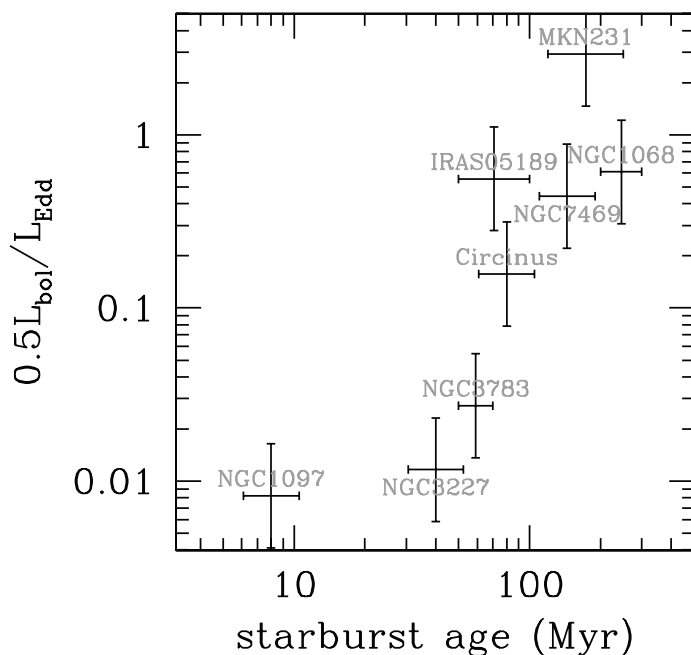


Figure 1.16: A relationship between the age of the most recent episode of nuclear SB and the AGN power (Davies et al. 2007). A systematic delay of $\sim 50 - 100$ Myr between them was suggested for the cases of these Seyfert galaxies. Note that similar arguments were raised independently (e.g., Schawinski et al. 2009; Wild et al. 2010).

on molecular gas to fuel the central $\lesssim 100$ pc region. More directly connected to star formation, on the other hand, mass loss from evolved stars (Ciotti et al. 1991; Davies et al. 2007; Norman & Scoville 1988; Padovani & Matteucci 1993) or angular momentum loss due to supernova (SN)-driven turbulence (Hobbs et al. 2011; Kawakatu & Wada 2008; Wada & Norman 2002; Wada et al. 2009) can also enhance mass accretion, which is indeed the subject of this thesis (Chapter 4).

1.3 Star Formation from Molecular ISM

In the systems unobscured by dust, the standard measure of the SFR would be the UV light or $H\alpha$ emission line, which traces ionizing continuum from OB stars, thus the massive star formation. In this case, we can obtain the total SFR by adopting a certain initial mass function of the stellar populations. On the other hand, if the system is dust-obscured, only a partial fraction of the ionizing photons can escape from the star forming region, which is the case in actual as stars are born from the cores of (dusty) molecular clouds. In this case, the (initially) short-wavelength photons absorbed by dust are re-emitted as far-infrared (FIR) emission. Hence, the combination of the short wavelength emission (e.g., UV continuum) and the FIR continuum is now a good indicator of the SFR. When the system is more deeply obscured by dust, the FIR continuum alone is an indicator of the SFR (e.g., Kennicutt 1998).

At this point, we recall that, because of the necessary fragmentation and collapse of clumps, star formation must take place in the densest parts of the ISM, i.e., molecular gas. This fact constitutes the clear basis of the observable connections between molecular gas mass and SFR. For example, following the original manner by Schmidt (1959), Kennicutt (1998) proposed that the total amount of gas ($\text{H}_2 + \text{HI}$) surface density (Σ_{gas}) is correlated with the surface SFR (Σ_{SFR}) as $\Sigma_{\text{SFR}} \propto \Sigma_{\text{gas}}^N$ ($N \sim 1.4$), which is shown in Figure 1.17a. Note that Σ_{gas} is related to another proxy of star formation, the Toomre-Q parameter (Toomre 1964), as $Q \equiv \Sigma_{\text{crit}}/\Sigma_{\text{gas}}$. Here, if Σ_{gas} exceeds a certain critical density (i.e., $Q < 1$), the gas will become gravitationally unstable and finally collapse to form stars (see Chapter 4 as well).

Regarding the dense(st) gas properties, Gao & Solomon (2004b) revealed a tight and linear correlation even in external galaxies between the mass of dense gas probed by $\text{HCN}(1-0)$ line and the SFR (Figure 1.17b), clearly supporting the view that stars are born from the dense(st) gas (see also Kohno et al. (1999) for the spatial correlation between the $\text{HCN}(1-0)$ emission and the star forming regions). Wu et al. (2005) updated the result, showing that the correlation holds over ~ 8 orders of magnitude in IR luminosity (or SFR), from Galactic star forming regions to ULIRGs. More recently, spatially resolved measurements of dense gas tracers are available thanks to the high resolutions provided by, e.g., ALMA. Thus, now we can obtain more direct, spatially resolved views on the properties of extragalactic star formation such as the gravitational instability of (the associations of) molecular clouds (Figure 1.18), even with relatively faint (as compared to CO lines) dense gas tracers.

1.4 Feedback on Molecular Gas

1.4.1 Astrochemistry as a new probe of dust-obscured nucleus

Recent chemical modelings of ISM predict that the various heating mechanisms will produce different signatures in molecular gas composition. For example, intense UV radiation from massive stars forms photodissociation regions (PDRs; Figure 1.19) around them, and X-ray dominated regions (XDRs; Figure 1.20), which are larger in volume than PDRs due to the higher penetrating capability of the X-ray, are formed at the vicinity of AGNs (e.g., Bayet et al. 2008, 2009; Hollenbach & Tielens 1997, 1999; Maloney et al. 1996; Meijerink & Spaans 2005; Meijerink et al. 2006, 2007). Cosmic rays from frequent supernovae (SNe) and the injection of mechanical energy due to SNe or AGN jet/outflow (mechanical heating) are also important in shaping chemical composition (e.g., Bayet et al. 2011; Kazandjian et al. 2012, 2015; Loenen et al. 2008; Matsushita et al. 2015; Meijerink et al. 2011; Rosenberg et al. 2014a,b). Inclusion of dust grain reactions will influence the chemistry as well (e.g., Charnley & Rodgers 2005; Garrod et al. 2008). It is noteworthy that the temperature of the gas is essentially important for the efficiency of chemical reactions (e.g., Harada et al. 2010, 2013; Nomura & Millar 2004; Rodgers & Charnley 2001); for example, under the high temperature conditions, we can expect an enhanced abundance of HCN due to the activated neutral-neutral reactions from CN, whereas that of HCO^+ will be reduced by reacting with H_2O (Figure 1.21).

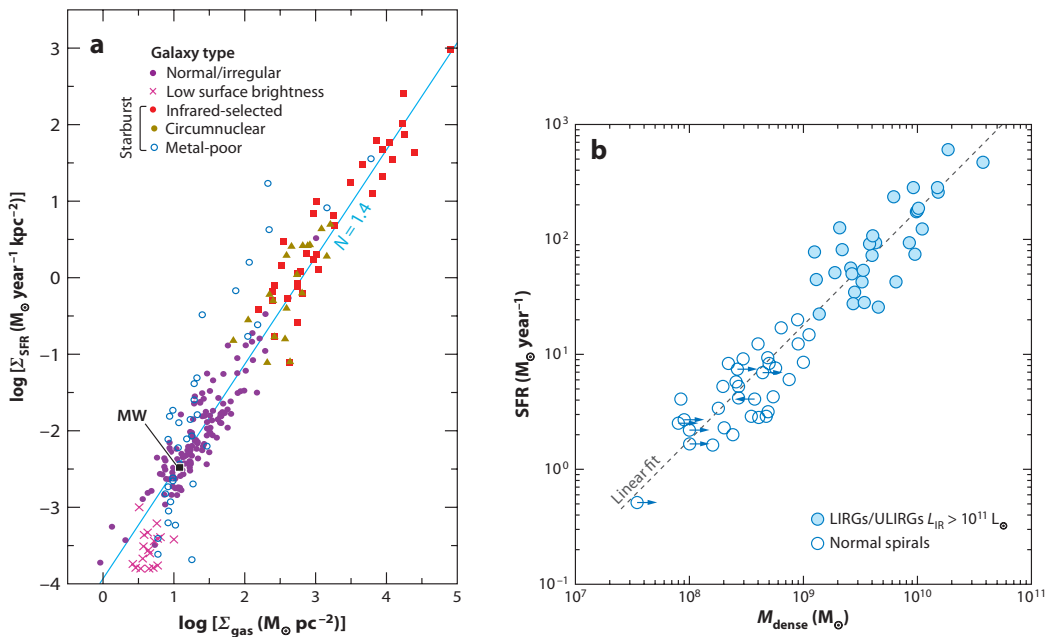


Figure 1.17: Relationships between (a) the surface density of the total ($\text{H}_2 + \text{HI}$) gas mass and that of the SFR (a so-called Schmidt-Kennicutt relation), and (b) the mass of dense molecular gas and the SFR (originally proposed by Gao & Solomon 2004b), from Kennicutt & Evans (2012).

One possible application of identifying different chemical signatures depending on the nuclear energy sources is to construct energy diagnostic methods. Especially, doing that with millimeter/submillimeter spectroscopy is of great importance because these wavelengths *do not suffer from dust extinction*, which is critical to probe dusty nuclear regions totally invisible at optical bands. According to the standard galaxy evolution models (Figure 1.4), such dust-obscured, optically invisible systems (e.g., ultra-luminous infrared galaxies = ULIRGs), which should contain physical information on the triggering mechanisms of AGN, are the progenitors of optically luminous systems (e.g., quasars). Thus, they are important populations to obtain a comprehensive view of galaxy evolution. Furthermore, such obscured systems are said to occupy a large fraction of the total AGN population at least in the nearby universe, based on recent high/deep X-ray observations (e.g., Buchner et al. 2015; Figure 1.22).

With these ideas in mind, many key molecules have been raised so far as useful observational diagnostic tools. Among them, an enhanced intensity of $\text{HCN}(1-0)$, whose critical density (n_{cr}) for collisional excitation with H_2 is $n_{\text{cr}} \sim 10^{4-5} \text{ cm}^{-3}$, with respect to those of $\text{HCO}^+(1-0)$ and/or $\text{CO}(1-0)$ has been proposed as a unique feature to AGNs (e.g., Davies et al. 2012; Imanishi et al. 2007b; Jackson et al. 1993; Kohno 2005; Kohno et al. 1996, 2001; Krips et al. 2008; Matsushita et al. 1998; Sternberg et al. 1994; Tacconi et al. 1994; Usero et al. 2004). Using these line ratios, Kohno et al. (2001) constructed a potential diagnostic diagram (see also Kohno 2005), which was later called as the *mm-HCN diagram* (Figure 1.23). But there are some counter arguments to this diagnostics such that high $\text{HCN}(1-0)/\text{HCO}^+(1-0)$ ratios

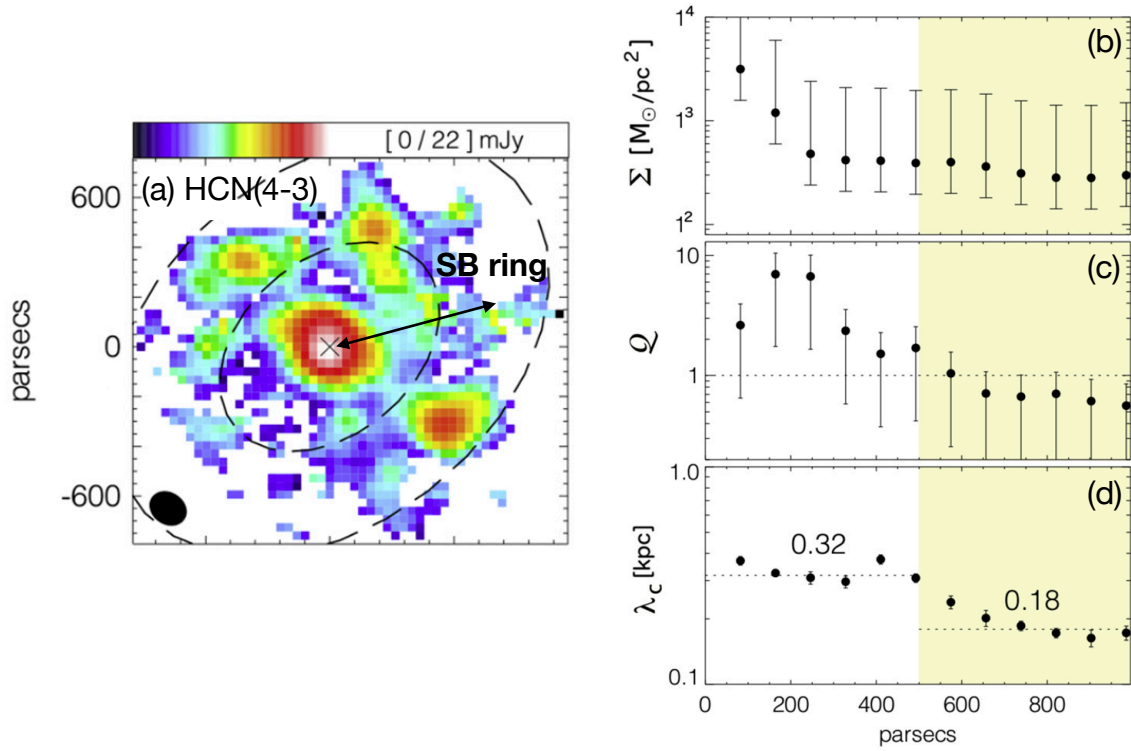


Figure 1.18: (a) Spatial distribution of HCN(4–3) emission in the central ~ 2 kpc region of the type-1 Seyfert galaxy NGC 7469, which consists of the CND and the surrounding SB ring (Fathi et al. 2015). Note that, at least in the SB ring, this emission traces star forming regions. (b)(c)(d) Azimuthally averaged radial profiles of, gas mass surface density, the Toomre- Q parameter, and the characteristic instability scale in NGC 7469 (Fathi et al. 2015). The Q -value drops below unity (i.e., gravitationally unstable) at the SB ring, and the λ_c is comparable to the size of the star forming clumps.

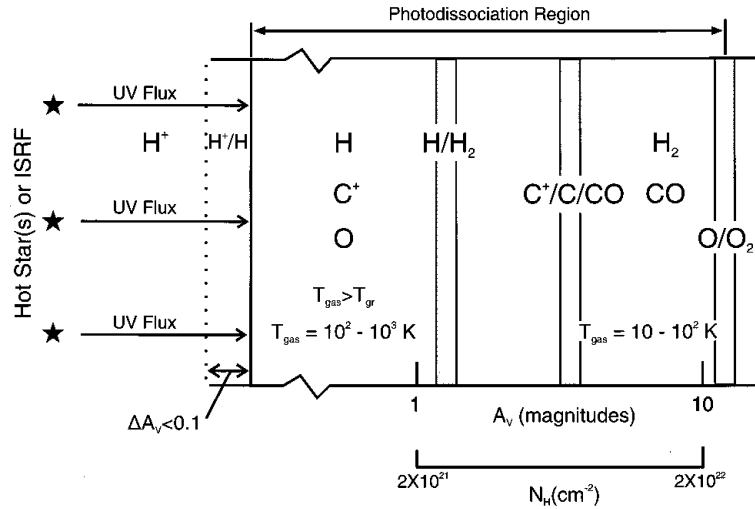


Figure 1.19: A schematic overview of a photodissociation region (PDR; Hollenbach & Tielens 1999). The PDR is illuminated from the left and extends from the predominantly atomic surface to the deeper molecular phase.

observed in non-AGNs (Costagliola et al. 2011; Snell et al. 2011), as well as low $\text{HCN}(1-0)/\text{HCO}^+(1-0)$ in AGNs (e.g., Sani et al. 2012). The latter inconsistency could be due to strong spectral contamination from the likely coexisting SB activities that dilutes emission from an AGN-influenced region. Furthermore, the cause of the enhanced intensity has been unclear because many different mechanisms can contribute to this enhancement; higher gas opacities, densities, and temperatures (excitation conditions), and/or abundance variations caused by different heating mechanisms. A non-collisional excitation, such as infrared (IR)-pumping caused by the re-radiation from UV/X-ray heated dust, could also be important (e.g., Aalto et al. 2002, 2007; Graciá-Carpio et al. 2006; Imanishi & Nakanishi 2013a; Matsushita et al. 2015; Sakamoto et al. 2010), especially in (U)LIRGs.

By getting the idea from the above mentioned $J = 1-0$ measurements, Izumi et al. (2013) found that $\text{HCN}(4-3)/\text{HCO}^+(4-3)$ and $\text{HCN}(4-3)/\text{CS}(7-6)$ integrated intensity ratios seem to be higher in AGNs than in SB galaxies (*submillimeter HCN-enhancement*), and proposed a diagnostic diagram hereafter referred to as a “*submm-HCN diagram*” using those line ratios. One advantage of the submm-HCN diagram over the previous diagnostics using $\text{HCN}(1-0)$ line would be that higher angular resolution is easily achievable at higher- J as compared to $J = 1-0$ transitions, which is essentially important to exclude contamination from SB activity to the line emission from AGN-heated gas. Moreover, it is much more applicable to high-redshift galaxies by using high- J lines because submillimeter lines can be covered with ALMA up to, e.g., $z \sim 3$ for the case of $J = 4-3$ transitions of HCN and HCO^+ (see an example of the detections of such $J = 4-3$ lines from high redshift objects in, e.g., Riechers et al. 2011). These lines can be simultaneously observed with ALMA, which is necessary to obtain accurate line ratios, in terms of both little systematic flux uncertainty and, to a lesser extent, differences in

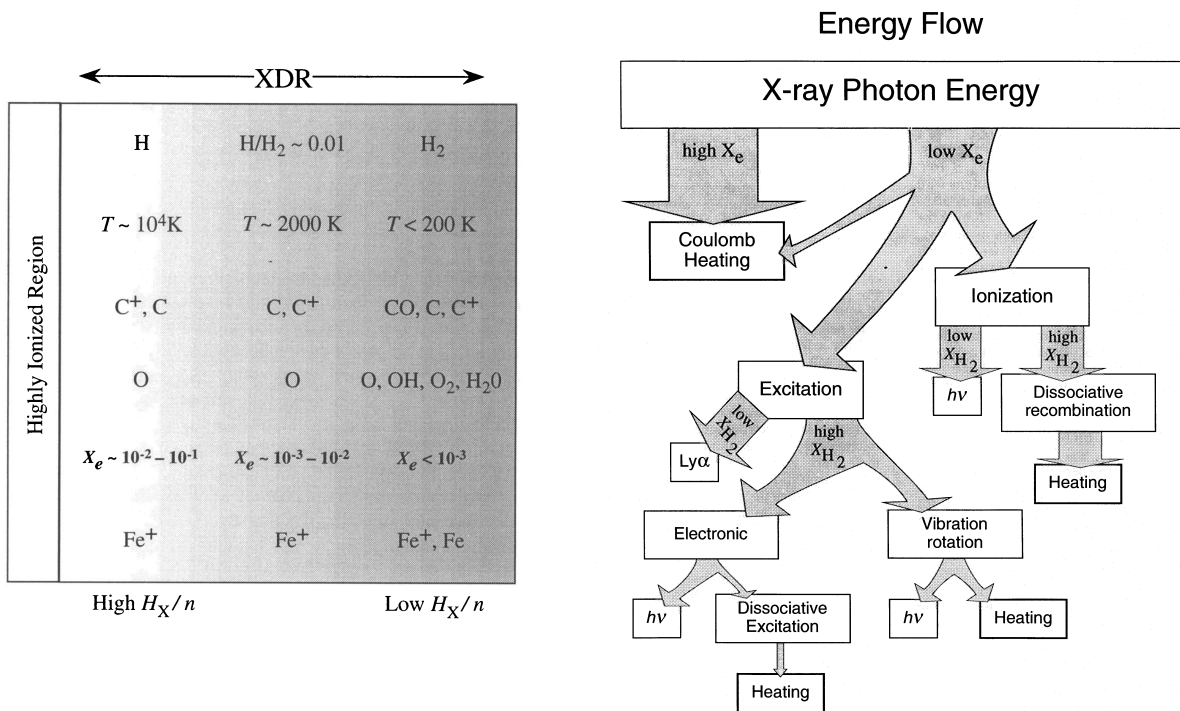


Figure 1.20: Schematic overviews of (*left*) an ionization, thermal, and chemical structures as well as (*right*) energy flows in an X-ray dominated region (XDR; Maloney et al. 1996). In the left, the approximate temperature, chemical composition, and ionization structures are shown as a function of the ratio of the local X-ray energy deposition rate per particle (H_X) to the total hydrogen density (n), which predominantly determines the thermal structure of the system. In the loss-routes for energetic electrons in dense atomic and molecular gas shown in the right, the branching depends on the electron fraction (X_e) and the hydrogen fraction (X_{H_2}).

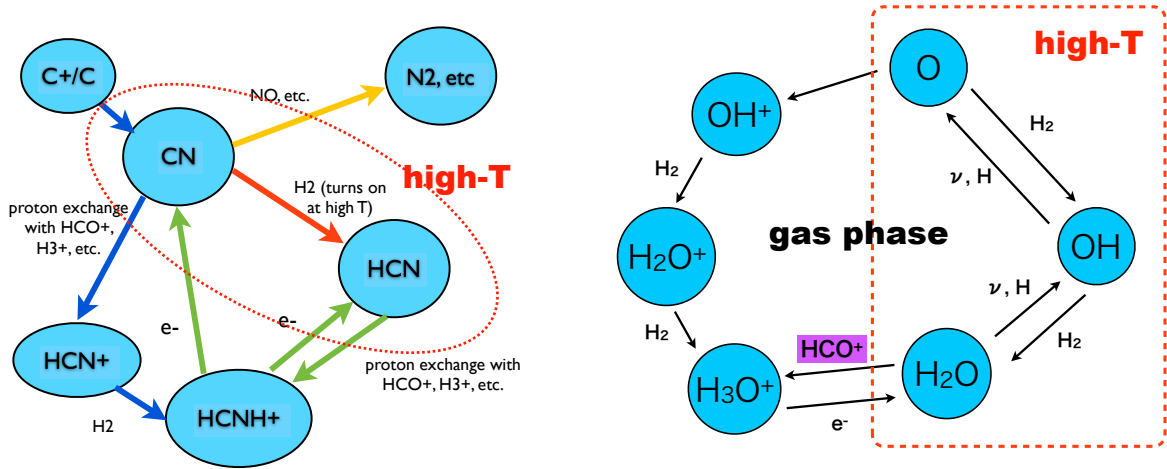


Figure 1.21: Block diagrams of the chemical paths expected under the high temperature environments for (*left*) HCN and (*right*) HCO⁺, as presented by Harada et al. (2010).

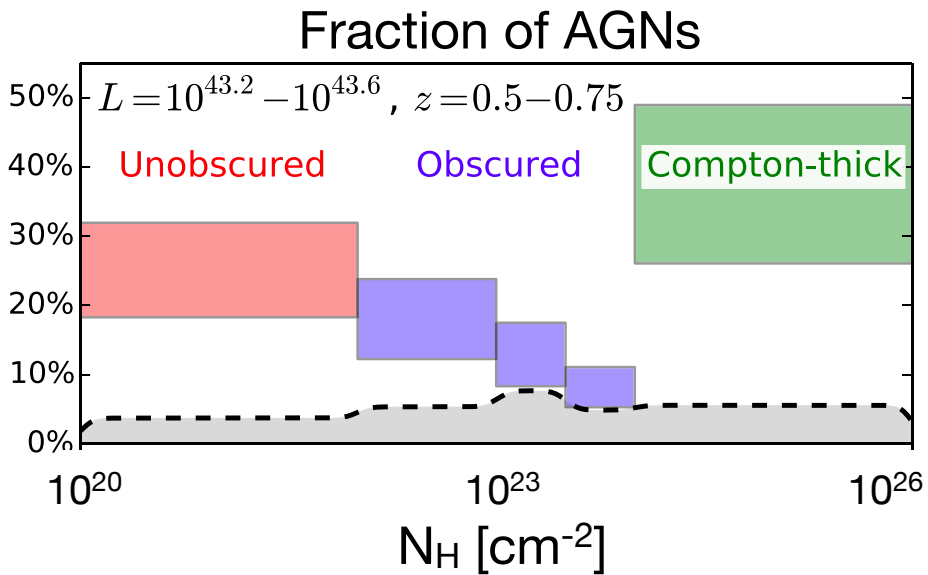


Figure 1.22: Column density distribution of AGNs in the nearby universe inferred from recent deep X-ray observations (Buchner et al. 2015). Three categories, unobscured: $N_H < 10^{22}$ cm⁻², obscured: $N_H = 10^{22-24}$ cm⁻², and Compton-thick: $N_H > 10^{24}$ cm⁻², are shown. One can see that a substantial fraction of the AGN population is obscured.

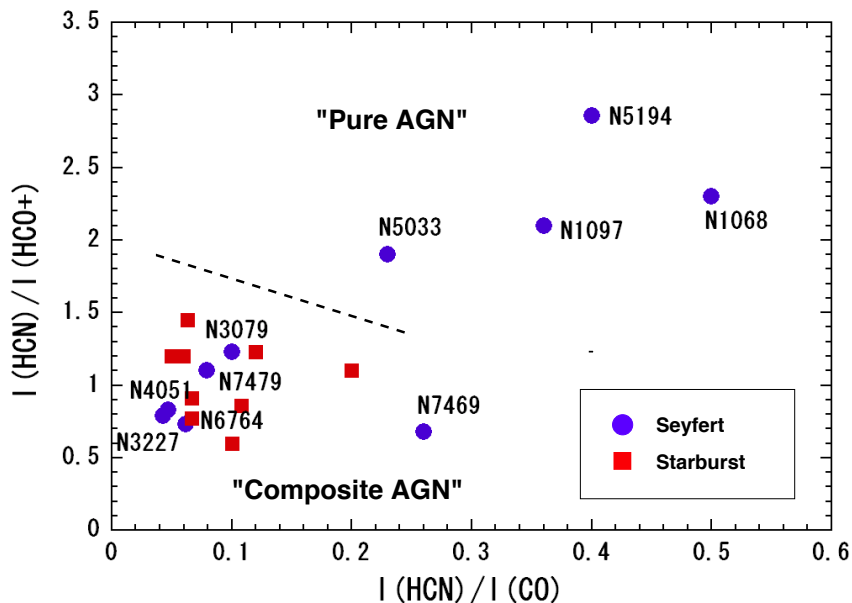


Figure 1.23: The mm-HCN diagram using $\text{HCN}(1-0)/\text{HCO}^+(1-0)$ and $\text{HCN}(1-0)/\text{CO}(1-0)$ ratios (Kohno 2005), which was proposed to distinguish AGNs and SB activities with molecular spectroscopy.

the uv -coverage. In addition, since these transitions have orders of magnitude higher critical densities ($n_{\text{cr}} \sim 10^{6-7} \text{ cm}^{-3}$) than the $J = 1 - 0$ transitions ($n_{\text{cr}} \sim 10^{4-5} \text{ cm}^{-3}$), they are less contaminated by the foreground and/or disk emission, thus are more suitable to probe the densest gas in the obscured nuclear regions of galaxies. However, as is also the case of $J = 1 - 0$ transitions, the cause of this submm-HCN enhancement remains unclear, although Izumi et al. (2013) suggested the possibility of abnormally enhanced HCN abundance in NGC 1097 (one galaxy showing the submm-HCN enhancement) through multi-transition non local thermodynamic equilibrium (non-LTE) analysis of HCN and HCO^+ (Figure 1.24).

1.4.2 Submillimeter hydrogen recombination line as another robust probe of dust-obscured AGNs

As an extension of the way of uncovering dust-obscured nuclei at mm/submm (Section 1.4.1), we focus on tracers of ionized gas too. Since the proposition of the unification scheme of an AGN (Antonucci 1993), it has been supposed that a type 2 AGN contains a type 1 nucleus having a broad line region (BLR; line width $>$ several $\times 1000 \text{ km s}^{-1}$) of ionized material, which is obscured by a dusty torus at short wavelengths such as optical. The detections of the broad HI recombination lines (hereafter RLs) in the polarized light from the prototypical type 2 Seyfert NGC 1068 (e.g., Alexander et al. 1999; Antonucci & Miller 1985) constitute the basis of this classical model. Therefore, in addition to the astrochemical approach mentioned in Section 1.4.1, direct detection of the BLR components (i.e., ionized gas) at the wavelengths least influenced by

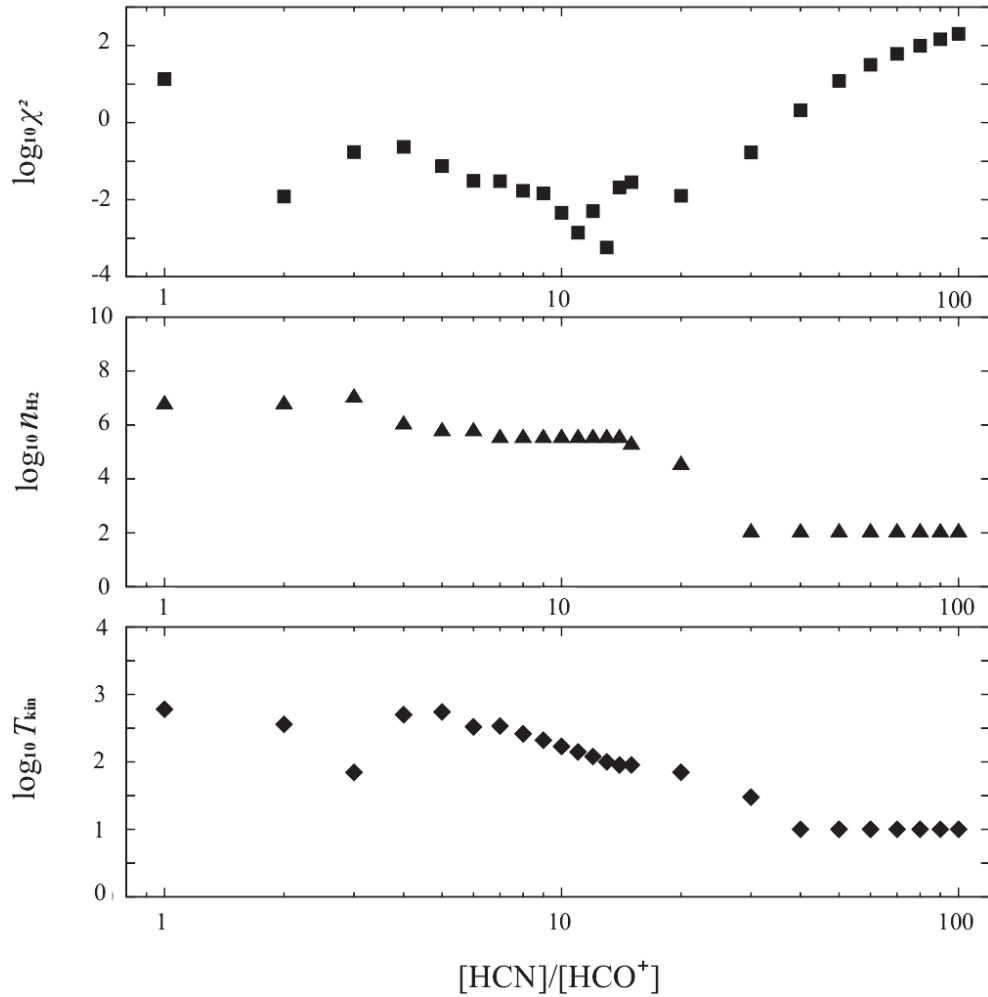


Figure 1.24: χ^2 test results based on line ratios of $J = 1 - 0$, $3 - 2$, and $4 - 3$ HCN and HCO^+ in the central ~ 100 pc region of NGC 1097 (Izumi et al. 2013). They changed $[\text{HCN}]/[\text{HCO}^+]$ abundance ratio from 1 to 100, and observed the response of gas density and temperature, and the reduced χ^2 value showing the goodness of the fit. Molecular gases with high gas density ($n_{\text{H}_2} \sim 10^{5-6} \text{ cm}^{-3}$) and temperature (> 100 K) with high $[\text{HCN}]/[\text{HCO}^+]$ abundance ratio (a few to ~ 30) show good fitness.

the dust attenuation will be another way to robustly identify AGNs obscured by huge amount of dust.

Although some works succeeded in detecting relatively broad ($\sim 1000\text{--}3000 \text{ km s}^{-1}$) RLs (e.g., Goodrich et al. 1994; Lutz et al. 2002; Veilleux et al. 1999, 1997) in type 2 Seyfert galaxies at near-infrared (NIR), these detections seem to be biased towards less-obscured type 2 or intermediate type AGNs (e.g., Lutz et al. 2002, 2000). Here, the ability of penetrating columns of $N_{\text{H}} \lesssim 10^{23\text{--}24} \text{ cm}^{-2}$ expected for the NIR band (e.g., Alonso-Herrero et al. 1997) would be insufficient to probe a sizeable fraction of Compton-thick AGNs ($N_{\text{H}} > 10^{24} \text{ cm}^{-2}$). Indeed, previous studies failed to detect NIR broad RLs firmly from such Compton-thick objects (e.g., Cai et al. 2010; Goodrich et al. 1994; Lutz et al. 2000; Mason et al. 2015). This problem can be severer in probing extremely obscured nuclei whose energy sources are elusive ($N_{\text{H}} \gtrsim 10^{25\text{--}26} \text{ cm}^{-2}$, e.g., Aalto et al. 2015b; Sakamoto et al. 2013). However, at least in the nearby universe, hard X-ray observations suggest that Compton-thick AGNs are comparable or even larger in number density than less obscured AGNs (e.g., Burlon et al. 2011; Lansbury et al. 2015). Therefore, longer wavelengths observations that directly probe those heavily obscured BLRs can be not only a new way to find AGNs but also an approach to better understand the unified scheme in such an extreme population (e.g., Buchner et al. 2015; Davies et al. 2015).

From this perspective, we postulate that submillimeter HI RLs (submm-RLs, hereafter) would provide the way as they do not suffer from dust extinction. Unlike centimeter RLs, submm-RLs would be less affected by potential maser amplification (Gordon & Walmsley 1990) as they are optically thinner than longer wavelengths lines (Figure 1.25). Moreover, it is easy to achieve quite high-velocity resolution at submillimeter that enables us to study kinematics of the nuclear regions in detail. Indeed, Scoville & Murchikova (2013) predicted that both thermal free–free continuum and submm-RL emissions stemming from narrow line regions (NLRs) of luminous nearby galaxies are readily detectable with ALMA.

1.5 This Thesis

The scope of this thesis is to investigate the physical and chemical mechanisms of the interplay of the *active trinity* at the centers of galaxies through high resolution molecular gas observations, which is recently available owing to the advent of ALMA. Our work can be a seed research for future higher resolution, higher sensitivity observations provided by the fully-operating ALMA.

As we mentioned in Section 1.2, the information at the spatial scale of CNDs is currently the missing link in studying the continuous mass flows from the host galaxies to the accretion disks. Considering the fact that there is an extraordinary discrepancy in the spatial scales of the AGN itself (i.e., an accretion disk) and its host galaxy, a CND, which resides between them, would serve as the boundary condition to connect them. Therefore, in this thesis, we try to reveal basic properties of CNDs of Seyfert galaxies with $\sim 100 \text{ pc}$ scale measurements of the dense gas tracer, $\text{HCN}(1-0)$, considering the high gas densities expected there. However, as CNDs are not spatially well resolved at this moment (all the data in this thesis were taken before ALMA cycle 3), we could only probe spatially integrated properties such as molecular mass. Nevertheless,

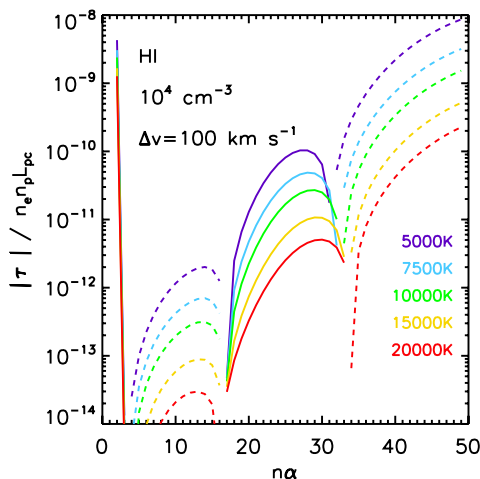


Figure 1.25: The optical depth of HI RLs per unit emission measure (EM; see Equation (3.1) as well), for electron temperature (T_e) = 5000–20000 K with electron density of $n_e = 10^4 \text{ cm}^{-3}$ (Scoville & Murchikova 2013). Here, the EM is defined as $\int N_e N_p dL = N_e N_p L_{\text{pc}}$, where L_{pc} is the line-of-sight path length in the unit of parsec. The solid and the dashed lines indicate that the value of the optical depth is positive and negative, respectively. One can see that for the principal quantum number $n \gtrsim 30$ (long-millimeter to centimeter regime), values are negative, indicative of the maser amplification.

as is described later, we found a link between the masses of the dense gas in CNDs and the AGN powers, which would be another form of the AGN–SB connection. We will also succeed in balancing the mass flow at the CND scale and further inner region, with a supernova driven turbulent accretion model, which would give a basis for the AGN–SB connection.

As a part of the interplay among the active trinity, we will also investigate possible chemical feedback of energy sources on the molecular gas, especially the origin of the submm-HCN enhancement (Izumi et al. 2013) in greater detail in this thesis. Despite the several advantages, the proposed energy diagnostic diagram of Izumi et al. (2013) was very tentative as (1) it was based on as small as 5 galaxy sample, and (2) they mixed galaxies observed at a wide range of spatial resolutions ($\sim 100 \text{ pc}$ to 1 kpc), which would combine flux contributions from various components. In order to assess the potential of the submm-HCN diagram, or the use of molecular spectroscopy as an extinction-free method of energy identification as well as the existence of any chemical feedback on the gas, we need high spatial resolution observations allowing us to isolate the AGN emission from likely contamination due to co-existing SB (e.g., García-Burillo et al. 2014; Izumi et al. 2013, 2015), together with SB samples observed at matched spatial resolutions. To do so, again the CND scale measurements can be the key. Indeed, Schleicher et al. (2010) predicted that a distance out to which AGN-heating with X-ray luminosity of $\sim 10^{43} \text{ erg s}^{-1}$ (a typical value for luminous Seyfert galaxies) dominates in dense gas ($n_{\text{H}_2} \sim 10^{4-5} \text{ cm}^{-3}$) with a soft UV radiation field of $\sim 100 G_0$ is only $\lesssim 100 \text{ pc}$ (Figure 1.26).

The main parts of this thesis is organized as follows: we discuss the nature of the submm-HCN enhancement in greater detail in Chapter 2, by increasing the number of the sample from

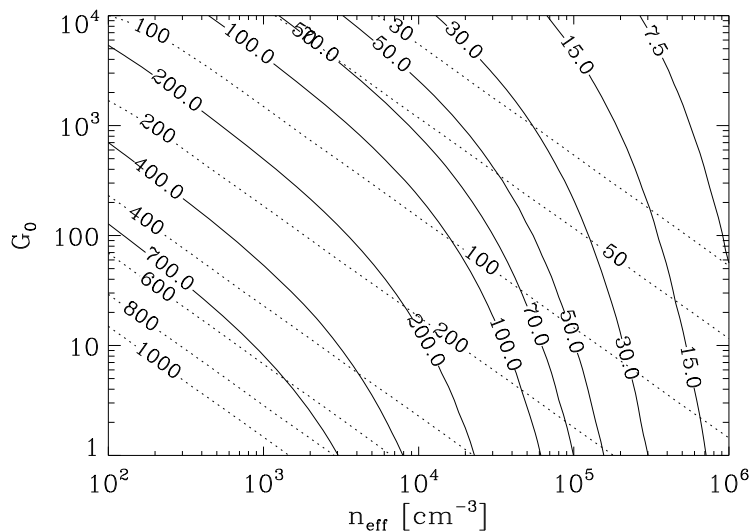


Figure 1.26: The expected size of an XDR [pc], for the SMBH with $10^7 M_{\odot}$, as a function of the UV radiation field and the gas density (Schleicher et al. 2010). The solid lines indicate the cases in which the AGN has the power-law spectrum between 1 and 5 keV, whereas the dashed lines indicate the cases with the power-law spectrum between 1 and 10 keV, respectively.

5 (Izumi et al. 2013) to 25, as well as by discussing the underlying physical and chemical nature responsible for the enhancement. Non-LTE analysis over a relatively wide range of parameters will be presented there, to explore the origin of the enhancement. Several plausible chemical scenarios to explain the inferred abundance variation will be presented as well. Chapter 3 is dedicated to discuss the detectability of submm-RLs, specifically H26 α emission line, which can be a new probe of very nuclear regions of dust-obscured AGNs. We will present simple theoretical considerations, and our prediction will be compared with actual observational data of the well-known type 2 Seyfert galaxy NGC 1068. In Chapter 4, we will then present a link between the mass of dense molecular gas (i.e., stellar nursery) at CNDs of Seyfert galaxies and the accretion rate onto their SMBHs. This is the first case where such a correlation is found at the CND scale. Furthermore, we will also present a scenario of mass accretion at the CND scale to explain the link, as well as the AGN–SB connection there. However, since the number of the sample galaxy is still small (but we constructed the largest sample of CNDs ever made!), this discussion on the accretion scenario is mostly for a demonstrative purpose. Although brief conclusions of each topic are given in each Chapter, at last, we summarize our new points of view regarding the interplay of the active trinity from a broader context spanning over the entire this thesis in Chapter 5, with adding our future outlook in this scientific field.

Chapter 2

AGN Feedback on the CND-scale Molecular Gas: Submillimeter HCN Enhancement as a New Extinction Free Energy Diagnostic Tool

Part of this Chapter has been published as Izumi et al. 2016, ApJ, 818, 42.

2.1 Context

As described in Section 1.4, Izumi et al. (2013) found that $\text{HCN}(4-3)/\text{HCO}^+(4-3)$ and $\text{HCN}(4-3)/\text{CS}(7-6)$ integrated intensity ratios seem to be higher in AGNs than in SB galaxies (*submm-HCN enhancement*), and proposed a diagnostic diagram (*submm-HCN diagram*) using those line ratios. Based on multi-transition non-LTE analysis, they suggested that the abnormally enhanced HCN abundance with respect to those of HCO^+ and CS can explain the enhancement. Hence, a sort of AGN feedback on the molecular chemistry is expected. We again emphasize that identifying unique chemistry around AGNs at millimeter/submillimeter bands can be a new method to dig out AGNs deeply embedded in dust, which is entirely invisible at optical (and even IR) wavelengths. Such obscured AGNs would be a progenitor of optically luminous AGNs (e.g., quasars) according to the standard model predictions (Figure 1.4), thus be an inevitable population to obtain a comprehensive view of the evolution of galaxies. Moreover, as we generally adopt non-LTE approach to infer any abundance variation in molecular phase, we will be able to constrain physical conditions (gas density, temperature) simultaneously (e.g., Izumi et al. 2013; Viti et al. 2014). Those are indeed the parameters to quantitatively assess the conditions of star formation, or, the postulated existence of AGN feedback on star formation.

In this Chapter, we first compile literature and archival data of $\text{HCN}(4-3)$, $\text{HCO}^+(4-3)$, and $\text{CS}(7-6)$ emission lines of various AGNs and SB galaxies to improve the statistics of the submm-HCN diagram, in order to at first gain an insight on its reliability as an energy

diagnostic method. Because multi-transition data is still unavailable for most objects in this work, fine-tuned non-LTE analysis for each galaxy is virtually impossible. Instead, we will survey over wide parameter ranges and reveal rather general trends of the line ratios of our interests on physical/chemical conditions, and speculate upon the origin of the submm-HCN enhancement. Section 2.2 describes the collected data. An up-dated submm-HCN diagram is shown in Section 2.3. Section 2.4 presents simple non-LTE radiative transfer models involving HCN(4 – 3), HCO⁺(4 – 3), and CS(7 – 6). We examine the impact of both line excitation and molecular abundance on the line ratios. In Section 2.5, we discuss possible chemical scenarios to realize the potential abundance variation suggested in Section 2.4. We briefly summarize our outcome of this Chapter in Section 2.6, although our conclusions of this entire thesis are described in Chapter 5.

2.2 Data Description

We first compiled interferometric data of the target emission lines of *extragalactic* objects from literatures. We refer to data obtained with spatial resolutions better than 500 pc as the *high resolution sample*. This threshold resolution of 500 pc is large enough to fully encompass the typical size of CNs in nearby galaxies, as well as small enough to exclude line emission from non-CND components such as circumnuclear SB rings in most cases. These data are further compared with rather lower resolution interferometric data (spatial resolution > 500 pc) and single dish data (typical spatial resolution > 1 kpc) with firm detections of the emission lines (> 5 σ). These data are called *low resolution sample*, and will be used to investigate the impact of different spatial resolution on our diagnostics. As a result, we compiled line emission data of NGC 1068, NGC 1097, NGC 1365, NGC 4945, NGC 7469, NGC 4418, IRAS12127-1412, M82, NGC 253, NGC 1614, NGC 3256, NGC 3628, NGC 7552, IRAS 13242-5713, N113 (LMC), and N159 (LMC). Moreover, in the cases with sufficiently high resolution data, we could measure line ratios at different, representative positions within a single galaxy. The name of each position such as NGC 1097 (AGN) and NGC 1097 (SB ring) is used for them (see also Appendix-A). Note that we classify the data of NGC 4945 obtained with APEX \sim 450 pc (18'') aperture into the low resolution sample, because it hosts a relatively compact circumnuclear SB ring with a radius of 2''.5 (\sim 60 pc) even inside the beam of a small physical size. On the other hand, the spatial resolution of the two LMC objects are orders of magnitude better than the other high resolution sample due to their proximity. We nevertheless keep using their ratios considering the rarity of high resolution extragalactic measurements of the emission lines used in this work. We emphasize that excluding these LMC objects does not change our conclusion at all.

Then, the total number of data points is 16 and 9 for the high and the low resolution sample, respectively. Hence, we improved the statistics significantly (by 5 times for the combined sample) from Izumi et al. (2013). The resultant HCN(4 – 3)/HCO⁺(4 – 3) and HCN(4 – 3)/CS(7 – 6) line ratios of each data point (hereafter we denote as $R_{\text{HCN}/\text{HCO}^+}$ and $R_{\text{HCN}/\text{CS}}$, respectively), are summarized in Table 2.1 with relevant information.

We categorized the target galaxies into three classes of nuclear activities, namely *AGN*, *buried-*

AGN, and SB, based on the following criteria.

- AGN: galaxies with clear broad Balmer lines (including polarized ones), or those with prominent hard X-ray (> 2 keV) point sources with time variability. Therefore, galaxies with *conventional* AGN signatures naturally belong to this category.
- Buried-AGN: galaxies showing little (or no) AGN signatures at X-ray and optical wavelengths, but have been claimed to possess AGNs which are deeply embedded in dust along virtually all sight-lines. These galaxies are identified at infrared wavelength by detections of, e.g., continuum emission from a hot ($\gtrsim 200$ K) dust component, deep silicate absorption feature, and small equivalent width of polycyclic aromatic hydrocarbon (PAH) emission (e.g., Imanishi et al. 2007a).
- SB: galaxies with no clear AGN signature but surely host prominent starbursts at their nuclear regions based on, e.g., BPT-diagram, prominent polycyclic aromatic hydrocarbon (PAH) emission.

Brief descriptions of each galaxy relating the above criteria are presented in Appendix-A. In this classification, we do not take into account the dominance of AGN and SB activities of each galaxy in molecular gas heating. That dominance, which will be a critical quantity to classify galaxies in an actual sense, can be assessed by an equivalent width of PAH emission line or IR color (Section 2.3). In Table 2.1, one can find some high resolution sample only exhibit lower limits in $R_{\text{HCN}/\text{CS}}$ because of the non-detections ($< 3\sigma$) of CS(7 – 6) emission line. However, we include them in our sample taking the rarity of extragalactic interferometric observations of submillimeter dense gas tracers into account. For the data obtained with single dish telescopes, 1σ rms is measured at the channels free of line emission (we quote use values used in the references). For the data obtained with interferometers, that rms is measured at the area free of line emission. The systematic error is also taken into account if mentioned in the references; if not, we adopt 15% for it. We confirmed that the lines from one galaxy mostly show similar line profiles, which is the basis of our non-LTE analysis that assumes that all lines are emitted from the same volume.

As for NGC 1068, which is the nearby best-studied type-2 Seyfert galaxy, we used ALMA band 7 data retrieved from the ALMA Science Archive¹ (ID = 2011.0.00083.S). Although this data was already presented extensively in García-Burillo et al. (2014) and Viti et al. (2014), we re-analyzed the data to obtain high resolution values of the $R_{\text{HCN}/\text{HCO}^+}$ and $R_{\text{HCN}/\text{CS}}$, since the exact values of these ratios are not presented in García-Burillo et al. (2014), and the ratios in Viti et al. (2014) were averaged ones with a 100 pc aperture. We used MIRIAD (Sault et al. 1995) for this analysis. The synthesized beams and the rms noises in channel maps of the target emission lines were typically $0''.5 \times 0''.4$ (corresponds to $35 \text{ pc} \times 28 \text{ pc}$ at the assumed distance of NGC 1068 = 14.4 Mpc) and $2.5 \text{ mJy beam}^{-1}$, respectively. The rms noises and measured fluxes of these lines are in good agreement with the published data. We assume the absolute flux uncertainty to be 15%.

¹<http://almascience.nao.ac.jp/aq/>

At the end of this Section and before constructing an up-dated submm-HCN diagram, we mention the likely-limited applicability of our molecular diagnostics to some buried-AGNs. In most cases, line optical depth at the central regions of galaxies will not be so high (τ is not $\gg 1$) because of strong turbulence there. However, recent high resolution observations of both vibrationally ground ($v = 0$) and excited ($v = 1$) HCN emission lines towards heavily obscured nuclei of ULIRGs revealed severe self- and/or continuum-absorption features at $v = 0$ (Aalto et al. 2015b). In the case of self-absorption, it is hard to extract any physical/chemical information from line ratios. Thus, any kind of energy diagnostics employing such absorbed lines will have a limited power. To date, such self-absorption features in emission lines of our interests have been observed only in heavily obscured nuclei for the case of extragalactic objects (e.g., Arp 220W with the line-of-sight H_2 column density $N_{\text{H}_2} > 10^{25} \text{ cm}^{-2}$; Scoville et al. 2015). Therefore, this can be a central issue in buried-AGNs with steep temperature gradient in gas, whose N_{H_2} are extremely large ($\gtrsim 10^{25-26} \text{ cm}^{-2}$; e.g., Sakamoto et al. 2013). Contrary to these galaxies, we consider such self-absorption will not be a severe problem in non-obscured AGNs primarily because of the low-to-moderate optical depths of the HCN(4–3) emission (\sim a few in NGC 1097 and NGC 7469, Izumi et al. 2013, 2015). This is in clear contrast to the extremely high optical depth ($\gtrsim 100$) in Arp 220W (Scoville et al. 2015). Interestingly, no such absorption feature was found even in the Compton thick AGN of NGC 1068 (total hydrogen column density derived by X-ray observations $N_{\text{H}} \sim 10^{25} \text{ cm}^{-2}$; Marinucci et al. 2016)² when observed at as high as 35 pc resolution (the data used in this work). Clearly, very extreme conditions are required to yield that feature.

With carefully paying attention to these facts, we still keep using our buried-AGN samples in this work because we can not identify such absorption features in their spectrum at this moment (Imanishi & Nakanishi 2014; Sakamoto et al. 2013, 2010). These galaxies are not used for a detailed quantitative discussion, but are used only to see an overall trend of line ratios. On the other hand, our subsequent discussion is mostly based on the high resolution sample of AGNs and SB galaxies. Therefore, inclusion of our buried-AGN samples will not harm our conclusion. Of course, we admit it is plausible that these buried-AGNs would show absorption features when they are observed at higher spatial resolutions, but a quantitative assessment of this point is beyond the scope of this thesis. Note that optically thinner emission and their ratios (e.g., $\text{H}^{13}\text{CN}/\text{H}^{13}\text{CO}^+$ ratio) seem to elucidate the nuclear physical/chemical conditions more straightforwardly in the case of obscured systems. Those isotopic lines can have moderate opacity in heavily obscured systems, hence are bright enough to be detectable with ease. We leave these caveats to future high resolution observations with ALMA.

² The multi-line analysis by Viti et al. (2014) suggested CO column density to velocity width ratio to be $3 \times 10^{17} \text{ cm}^{-2} (\text{km s}^{-1})^{-1}$ (see their Table 6). With the line width of $\sim 200 \text{ km s}^{-1}$ (García-Burillo et al. 2014) and the assumption of CO fractional abundance of 10^{-4} (e.g., Blake et al. 1987), this result corresponds to H_2 column density of $\sim 6 \times 10^{23} \text{ cm}^{-2}$. This value is \sim one order of magnitude smaller than that of the X-ray derived total hydrogen column density (Marinucci et al. 2012, 2016). However, we suggest this inconsistency would not be a problem because the averaged column density over the $\sim 100 \text{ pc}$ beam employed by Viti et al. (2014) would show the lower limit of the nuclear (X-ray) obscuration operating at a much smaller scale.

Table 2.1: $R_{\text{HCN}/\text{HCO}^+}$ and $R_{\text{HCN}/\text{CS}}$ of the sample galaxies

Object ^a	Distance ^b [Mpc]	Type ^c	Telescope ^d	Spatial resolution ^e [pc]	$R_{\text{HCN}/\text{HCO}^+}^f$	$R_{\text{HCN}/\text{CS}}^g$	Reference ^h
High resolution (< 500 pc) sample							
NGC 1068 (AGN)	14.4	AGN	ALMA	35	1.53±0.34	8.84±2.51	(1)
NGC 1068 (E-knot)	14.4	AGN	ALMA	35	2.84±0.60	8.04±1.72	(1)
NGC 1068 (W-knot)	14.4	AGN	ALMA	35	3.19±0.71	11.97±3.45	(1)
NGC 1068 (CND-N)	14.4	AGN	ALMA	35	3.14±0.72	12.79±4.48	(1)
NGC 1068 (CND-S)	14.4	AGN	ALMA	35	2.58±0.19	>4.21	(1)
NGC 1097 (AGN)	14.5	AGN	ALMA	94	2.01±0.29	>12.66	(2)
NGC 7469 (AGN)	70.8	AGN	ALMA	154	1.11±0.13	9.50±3.02	(3)
M82	5.2	SB	JCMT	353	0.41±0.12	4.09±1.14	(2)
NGC 253	3.0	SB	JCMT, APEX	262	1.03±0.22	3.40±0.73	(2)
NGC 1097 (SB ring)	14.5	SB	ALMA	94	0.82±0.17	>1.38	(2)
NGC 1614	69.1	SB	ALMA	468	0.24±0.06	>3.54	(4)
NGC 7469 (SB ring position-B)	70.8	SB	ALMA	154	0.75±0.14	>3.65	(3)
NGC 7469 (SB ring position-C)	70.8	SB	ALMA	154	0.45±0.08	2.50±1.16	(3)
NGC 7469 (SB ring position-D)	70.8	SB	ALMA	154	0.48±0.06	3.03±1.19	(3)
N113 (LMC)	0.05	SB	ASTE	5.3	0.21±0.06	1.30±0.58	(5)
N159 (LMC)	0.05	SB	ASTE	5.3	0.11±0.03	2.16±0.60	(6)
Low resolution (> 500 pc) sample							
NGC 1068 (APEX)	14.4	AGN	APEX	1257	1.85±0.42	5.00±1.47	(7)
NGC 1365	16.9	AGN	APEX	1475	0.59±0.15	2.83±1.17	(7)
NGC 4418	31.3	buried-AGN	SMA	790	1.64±0.25	1.98±0.30	(2)
NGC 4945	5.2	AGN	APEX	454	0.78±0.17	3.21±0.70	(7)

Continue to the next page

Continued from the previous page

Object ^a	Distance ^b [Mpc]	Type ^c	Telescope ^d	Spatial resolution ^e [pc]	$R_{\text{HCN}/\text{HCO}^+}$ ^f	$R_{\text{HCN}/\text{CS}}$ ^g	Reference ^h
IRAS12127-1412	627.4	buried-AGN	ALMA	1667	1.58 ± 0.58	4.32 ± 2.17	(8)
NGC 3256	37.4	SB	APEX	3265	0.39 ± 0.11	1.38 ± 0.51	(7)
NGC 3628	7.7	SB	APEX	672	0.36 ± 0.11	1.80 ± 0.90	(7)
NGC 7552	19.5	SB	APEX	1702	0.54 ± 0.15	2.17 ± 0.92	(7)
IRAS13242-5713	42.0	SB	APEX	3667	1.23 ± 0.29	2.39 ± 0.66	(7)

Note. ^(a)For NGC 1068, we list the data obtained with both ALMA (archival data: ID=2011.0.00083.S) and APEX. The ratios of ALMA data are extracted at the positions of the *AGN*, *E-knot*, *W-knot*, *CND-N*, and *CND-S*. For NGC 1097 and NGC 7469, the ratios extracted both at the AGN position and the circumnuclear SB ring are listed. ^(b)We adopt distances determined by the Tully-Fisher relation (Tully 1988) for most cases. For NGC 4418, NGC 7469, IRAS12127-1412, NGC 1614, and IRAS13242-5713, distances are calculated based on their redshift recorded in NASA/IPAC Extragalactic Database (NED, <http://ned.ipac.caltech.edu>). We adopt $H_0 = 70 \text{ km s}^{-1} \text{ Mpc}^{-1}$, $\Omega_M = 0.3$, and $\Omega_\Lambda = 0.7$ cosmology here. For N113 and N159, the Cepheid-based distance to the LMC (Macri et al. 2006) is used. ^(c)Type of a target galaxy. ^(d)The telescopes used for the observations. ^(e)We separated the sample into two classes based on the spatial resolution of each observation. The resolution of 500 pc is employed here as the threshold, which is sufficient to fully encompass the typical size of CNDs. In the case of NGC 4945, we classified it into the low resolution sample despite the moderate spatial resolution to measure its line ratios ($18'' \sim 450 \text{ pc}$), because this galaxy hosts a relatively compact circumnuclear SB ring ($2''.5$ radius). For interferometric data, we list the geometrical mean of the FWHM of the major and minor axes of the synthesized beams. ^(f)^(g)Integrated intensity ratios of $\text{HCN}(4-3)/\text{HCO}^+(4-3)$ and $\text{HCN}(4-3)/\text{CS}(7-6)$ in the brightness temperature scale. The systematic errors are taken into account. We assume 15% systematic error if it is not mentioned in the references. As for the $R_{\text{HCN}/\text{HCO}^+}$ in NGC 4418, we mention that $0''.5$ observations of Sakamoto et al. (2013) found it to be ~ 2 . ^(h)References for the $R_{\text{HCN}/\text{HCO}^+}$ and $R_{\text{HCN}/\text{CS}}$: (1) This work, but also see García-Burillo et al. (2014) and Viti et al. (2014) for NGC 1068, (2) Izumi et al. (2013) and references therein, (3) Izumi et al. (2015), (4) Imanishi & Nakanishi (2013b), (5) Paron et al. (2014), (6) Paron et al. (2016) (7) Zhang et al. (2014), (8) Imanishi & Nakanishi (2014).

2.3 Revised Submm-HCN Diagram

Based on the data in Table 2.1, we here up-date the submm-HCN diagram first proposed by Izumi et al. (2013). We first show the result using only the high resolution sample (spatial resolution < 500 pc) in Figure 2.1, to avoid strong contamination from the surrounding SB regions to AGN-heated gas as much as possible. As a result, one can find a clear trend that AGNs exhibit higher $R_{\text{HCN}/\text{HCO}^+}$ and/or $R_{\text{HCN}/\text{CS}}$ than SB galaxies, which supports our previous claim in Izumi et al. (2013). Note that the submm-HCN diagram is a scatter plot (or more correctly, this is just a visualization of the two line ratios) and is not a correlation plot. Thus, what we should investigate in the subsequent sections is the origin of the relative enhancement of the individual line ratios in AGNs as compared to SB galaxies.

The influence of spatial resolution on this line diagnostics is investigated in Figure 2.2, with superposing the low resolution sample (spatial resolution > 500 pc). We found SB galaxies continue to show lower $R_{\text{HCN}/\text{HCO}^+}$ and $R_{\text{HCN}/\text{CS}}$ than most AGNs. On the other hand, NGC 1365 and NGC 4945 (both are AGNs) show line ratios fully comparable to SB galaxies, which is in contrast to the trend of the high resolution AGN sample. We suspect that in these two Seyfert galaxies, contamination from co-existing SB regions in line fluxes would be substantial when observed at the APEX $18''$ beam. This scenario can be confirmed by inspecting the energetic dominance of each nuclear activity on the surrounding medium. Indeed, both NGC 1365 and NGC 4945 host a prominent circumnuclear SB ring with a radius of $5''$ – $10''$ (NGC 1365) and $2''.5$ (NGC 4945) associating large amount of molecular gas (Alonso-Herrero et al. 2012b; Chou et al. 2007; Galliano et al. 2005; Marconi et al. 2000; Sakamoto et al. 2007). Regarding the energetics, the equivalent widths of the $11.3 \mu\text{m}$ PAH feature are 432 nm (with $20''.4 \times 15''.3$ aperture; Wu et al. 2009) in NGC 1365 and 358 nm (with $3''.7$ slit; Esquej et al. 2014) in NGC 4945, respectively. These widths are significantly larger than those of NGC 1068 (9 nm with $0''.36$ slit, i.e., similar to the ALMA beam) and NGC 7469 (31 nm with $0''.75$ slit, i.e., similar to the ALMA beam), for example (Esquej et al. 2014). Moreover, the $25 \mu\text{m}$ -to- $60 \mu\text{m}$ *IRAS* colors of NGC 1365 and NGC 4945 are 0.14 and 0.04 , respectively. These equivalent widths and IR-colors are clearly categorized in the SB regime (Wu et al. 2009). Therefore, the low line ratios in NGC 1365 and NGC 4945 compared to the high resolution AGN samples would highlight the importance of high spatial resolution (likely to be $\lesssim 50$ – 100 pc scale: Figure 1.26) to robustly identify low luminosity AGNs accompanying prominent circumnuclear SB based on this diagram. This would reflect the limited spatial extent of energetic influence of AGNs such as XDRs (Izumi et al. 2015; Schleicher et al. 2010).

On the other hand, once we achieve the high resolution, we should carefully treat the spatially resolved measurements of the line ratios because they would reflect very local physics and/or underlying chemistry even within a single AGN environment = single CND (Viti et al. 2014). This is clearly manifested by the case of NGC 1068 (Figure 2.2); both $R_{\text{HCN}/\text{HCO}^+}$ and $R_{\text{HCN}/\text{CS}}$ measured with ALMA ($0''.5$ beam) at the different positions within its CND are different from those with APEX ($18''$ beam). Contrary to this case, spatial resolution seems not to play an important role for the ratios of SB galaxies because both the high and the low resolution

samples exhibit totally comparable line ratios as already mentioned (see also Table 2.1). This could be reconciled if a SB region is an ensemble of massive star forming clumps with similar physical/chemical conditions.

Considering the above, we suggest from Figures 2.1 and 2.2 that (1) galaxies energetically dominated by AGNs show enhanced $R_{\text{HCN}/\text{HCO}^+}$ and/or $R_{\text{HCN}/\text{CS}}$, and (2) those by SB show lower values in both ratios than AGNs. We also point out that the buried-AGNs of our sample tend to exhibit relatively high $R_{\text{HCN}/\text{HCO}^+}$ ($\gtrsim 1.5$) but rather low $R_{\text{HCN}/\text{CS}}$ (\sim a few) which is comparable to SB galaxies. These buried-AGNs belong to our low resolution sample (Figure 2.2). Thus, one concern is that the line ratios will change when observed at a higher resolution. However, at least for NGC 4418, ~ 100 pc scale observations of HCN(4 – 3) and HCO⁺(4 – 3) revealed that the dense molecular gas is well confined in the central ~ 100 pc region (Costagliola et al. 2015; Sakamoto et al. 2013). Therefore, the location of this galaxy will more or less hold in Figure 2.2 even when observed at ~ 100 pc resolution, although we need to increase the high resolution sample of buried-AGNs to examine their overall trend in this diagram.

In the following, we will investigate possible causes for the HCN-enhancement in AGNs, from the perspectives of both *line excitation* and *abundance (ISM chemistry)*. The line ratios of the high resolution samples shown in Figure 2.1 should be the reference for the subsequent discussion as those of the low resolution samples (especially AGNs) are highly likely to be contaminated by the surrounding SB components. We should note that the observed line ratios are the integrated ones over not only some areas but also the line-of-sight columns. Thus, all physical and chemical gradients are integrated.

2.4 Non-LTE Excitation Analysis

In order to investigate the physical origin of the HCN-enhancement, we ran non-LTE radiative transfer models with the RADEX code (van der Tak et al. 2007). The RADEX uses an escape probability approximation to treat optical depth effects and solves statistical equilibrium in a homogeneous (i.e., single temperature and density), one-phase medium. Therefore, all HCN(4 – 3), HCO⁺(4 – 3), and CS(7 – 6) lines are emitted from the same volume in our models. This assumption would not be very crude considering the relatively narrow range of their critical densities (n_{cr} ; Table 2.2) and similar velocity profiles of these lines (e.g., Izumi et al. 2013, 2015; Zhang et al. 2014). As for the cloud geometry, we assumed a spherical one. Other relevant excitation parameters of the target lines are summarized in Table 2.2. We hereafter express line strengths in the brightness temperature scale. Note that we do not intend to mimic an environment of a specific galaxy here. Moreover, one line ratio can be reproduced by various combinations of parameters. Hence the model described below is the result of an educated guess of the parameters, which should be further investigated with future observations of multi-transition lines.

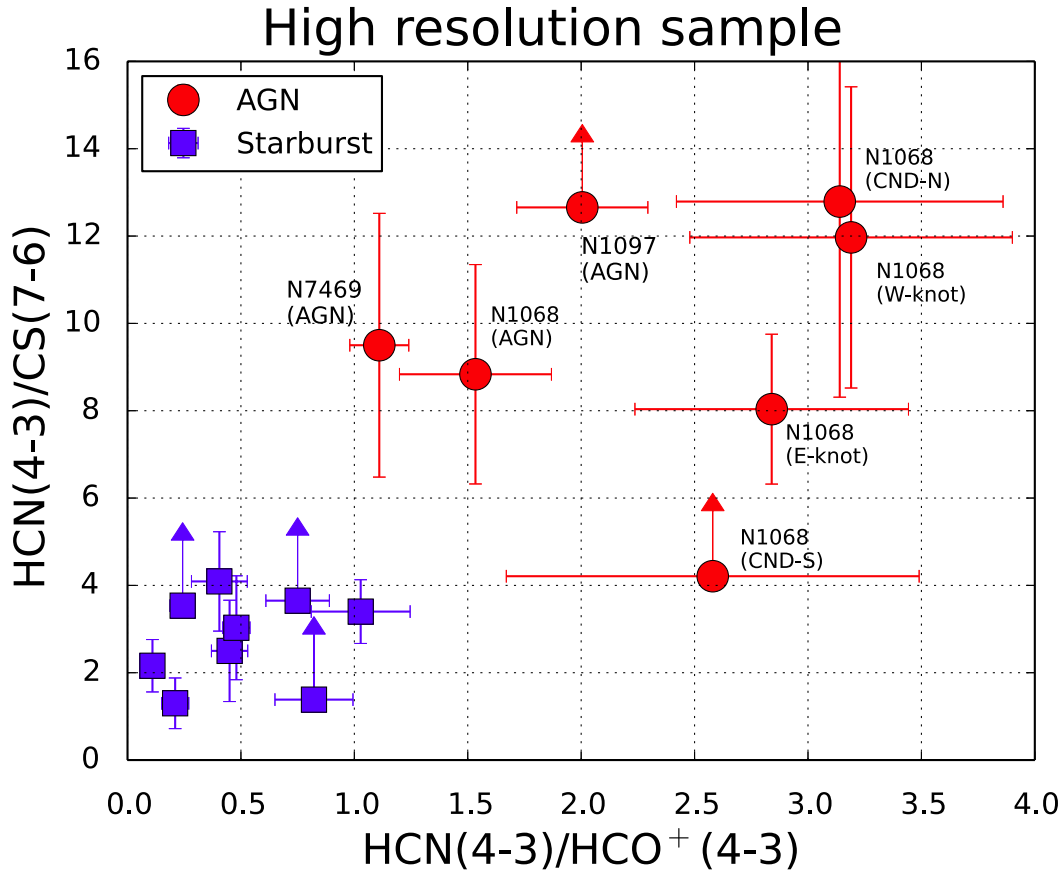


Figure 2.1: Revised submillimeter-HCN diagram using $\text{HCN}(4-3)/\text{HCO}^+(4-3)$ and $\text{HCN}(4-3)/\text{CS}(7-6)$ integrated intensity ratios ($R_{\text{HCN}/\text{HCO}^+}$ and $R_{\text{HCN}/\text{CS}}$ in the text, respectively) in the brightness temperature scale. Only the data obtained with high resolution observations (spatial resolution < 500 pc, except for NGC 4945) are used. The red circles and the blue squares indicate AGNs and SB galaxies, respectively. The abbreviated names of AGNs are shown. Here, the term “AGN” simply means that the galaxy hosts an AGN, regardless of its dominance in the total energy budget of the galaxy. See Table 2.1 for the details of the data. The systematic errors are also included here.

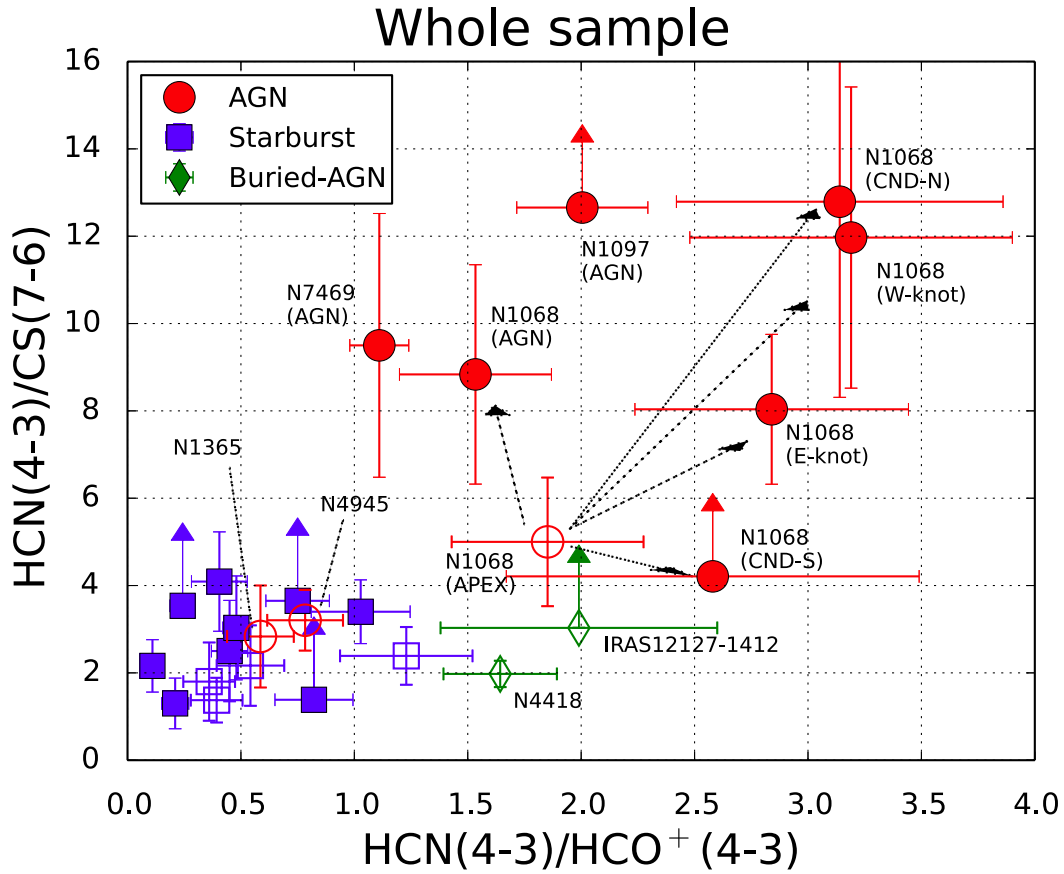


Figure 2.2: Same as Figure 2.1, but the whole sample including both the high resolution (spatial resolution < 500 pc; filled symbol) and the low resolution (spatial resolution > 500 pc; empty symbol) data are plotted. The red circles, green diamonds, and the blue squares indicate AGNs, buried-AGNs, and SB galaxies, respectively (see also Table 2.1). The abbreviated names of AGNs and buried-AGNs are shown. See Table 2.1 for the details of the data. The systematic errors are included here.

Table 2.2: The excitation parameters of HCN(4 – 3), HCO⁺(4 – 3), and CS(7 – 6) line emissions

Line name ^a	ν_{rest} [GHz] ^b	μ [Debye] ^c	E_u/k_B [K] ^d	ΔE_{ul} [K] ^e	A_{ul} [s ⁻¹] ^f	$T_{\text{kin}} = 50$ K	$n_{\text{cr,thin}}$ [cm ⁻³] ^g	$T_{\text{kin}} = 200$ K
HCN($J = 4 - 3$)	354.505	2.99	42.5	17.0	2.054×10^{-3}	1.4×10^7	9.1×10^6	6.1×10^6
HCO ⁺ ($J = 4 - 3$)	356.734	3.93	42.8	17.1	3.627×10^{-3}	2.6×10^6	2.0×10^6	1.6×10^6
CS($J = 7 - 6$)	342.883	1.96	65.8	16.4	8.395×10^{-4}	3.4×10^6	2.6×10^6	2.2×10^6

Note. ^(a)Full name of the line. ^(b)(c)(d)(e)(f)The rest frequency, dipole moment, upper level energy, energy gap between the upper and lower levels, and Einstein A-coefficient of the transition, respectively. These values are extracted from the Leiden Atomic and Molecular Database (*LAMDA*: Schöier et al. 2005). ^(g)Critical density of the line in the optically thin limit without any background radiation, which is calculated for the kinetic temperature (T_{kin}) of 50, 100, and 200 K, using $n_{\text{cr,thin}} = A_{jk}/[\sum_{i<j} \gamma_{ji} + \sum_{i>j} (g_i/g_j) \gamma_{ij} \exp(-(E_i - E_j)/T_{\text{kin}})]$ for the $j \rightarrow k$ transition. Here, γ_{jk} indicates the collision rate of the $j \rightarrow k$ transition. We adopt only H₂ for the collision partner and include collisional de-excitation as well from J_{upper} up to 25. Values for the collision rate γ_{ul} are also extracted from *LAMDA*.

2.4.1 Model description

In our RADEX simulation, we investigated how the following parameters affect the line ratios of our interest.

- Kinetic temperature of the molecular gas (T_{kin}): this affects the rate of the collisional excitation with the target molecules. The cases of 50, 100, and 200 K are investigated. This range mostly covers the T_{kin} suggested for nearby AGNs and SB galaxies (e.g., Davies et al. 2012; Izumi et al. 2013; Krips et al. 2008; Mauersberger et al. 2003; Viti et al. 2014).
- Molecular gas density (n_{H_2}): this also affects the rate of collisional excitation. Two cases of $n_{\text{H}_2} = 10^5$ and $5 \times 10^6 \text{ cm}^{-3}$ will be examined. These values are typical ones suggested in nuclear regions of galaxies (e.g., Izumi et al. 2013; Viti et al. 2014).
- Ratios of molecular fractional abundances with respect to H_2 (X_{mol} , mol = HCN, HCO^+ , and CS): we will show two cases for simplicity, where $X_{\text{HCN}}/X_{\text{HCO}^+}$ (or $X_{\text{HCN}}/X_{\text{CS}}$) = 1 and 10.
- Background radiation temperature (T_{bg}): molecular rotational levels can be radiatively excited through absorbing photons. In this perspective, it is highly likely that the background radiation is stronger around AGNs than in SB environments. In fact, the dust temperature at FIR to submillimeter (i.e., Rayleigh-Jeans regime) is as high as 46 K in the central ~ 400 pc region of NGC 1068 (AGN; García-Burillo et al. 2014), but 29 K in the central 1.2 kpc region of NGC 253 (SB; Weiß et al. 2008), for example. The cases of 2.73 (Cosmic Microwave Background = CMB), 5, 10, 20, 30, 40, 50, and 60 K are studied in this work. We simply adopt the black body approximation to calculate the background radiation field, although this value has a limited meaning as briefly discussed in Appendix-B.
- Optical depth of the line emission (τ): models with different N_{mol}/dV (or equivalently a volume density of the target molecule to a velocity gradient ratio) are employed to test this effect on the line ratios. Here, N_{mol} and dV are a line-of-sight column density and a line velocity width, respectively. N_{HCO^+}/dV (or N_{CS}/dV) = 5.0×10^{12} , 5.0×10^{13} , 5.0×10^{14} , and $5.0 \times 10^{15} \text{ cm}^{-2} (\text{km s}^{-1})^{-1}$ are studied. The N_{HCN}/dV is equated to this N_{HCO^+}/dV (or N_{CS}/dV), or enhanced by 10-times, since now that $X_{\text{HCN}}/X_{\text{HCO}^+}$ (or $X_{\text{HCN}}/X_{\text{CS}}$) = 1 and 10 as already mentioned.

Under these conditions, we ran the RADEX for each set of (T_{kin} , n_{H_2} , $X_{\text{HCN}}/X_{\text{HCO}^+}$, T_{bg} , N_{HCO^+}/dV) and (T_{kin} , n_{H_2} , $X_{\text{HCN}}/X_{\text{CS}}$, T_{bg} , N_{CS}/dV) and took line ratios of $R_{\text{HCN}/\text{HCO}^+}$ and $R_{\text{HCN}/\text{CS}}$. Transitions between vibrational levels through IR-pumping are not included in the models since there is no detection of vibrationally excited HCN emission in our sample galaxies except for NGC 4418 (Sakamoto et al. 2010), although it can be a bit inappropriate treatment in some cases (Section 2.5). Regarding the gas density, we here mention that Krips et al. (2008) suggested systematically lower n_{H_2} in AGNs than in SB galaxies, but their measurements were

based on single dish observations of, e.g., HCN(3–2) to HCN(1–0) line ratio. On the other hand, we need spatially resolved measurements of line ratios to accurately assess n_{H_2} or line excitation (Viti et al. 2014). Moreover, in another work, line excitation is shown to be irrespective of the nuclear energy type (Knudsen et al. 2007). One may expect that an increase in n_{H_2} naturally leads to higher line ratios since n_{cr} of HCN(4–3) is the highest among the target lines. However, this is actually *not so straightforward* as shown later.

In the modelings below, we first fix n_{H_2} to be 10^5 cm^{-3} and investigate the dependence of the line ratios on the other parameters as our fiducial experiments. The case of $n_{\text{H}_2} = 5 \times 10^6 \text{ cm}^{-3}$ will be shown subsequently. Note that our modelling is fundamentally different from the LTE modelings presented by, e.g., Izumi et al. (2013), Viti et al. (2014), and Martín et al. (2015), in the sense that non-LTE processes are treated. Moreover, we also examine the dependence of the line ratios on T_{bg} , which has not been studied in the non-LTE modelings by, e.g., Krips et al. (2011) and Viti et al. (2014). Hence, in addition to the previous key works, we expect that our analysis will provide insights on the underlying physical and chemical conditions in the centers of galaxies from another perspective.

2.4.2 Molecular line excitation with photon trapping

Excitation states of the target lines under the fixed gas density of $n_{\text{H}_2} = 10^5 \text{ cm}^{-3}$ are described here. HCN(4–3) is mainly used for a demonstrative purpose, but the same argument can hold for HCO⁺(4–3) and CS(7–6) as well. Figure 2.3 shows excitation temperature (T_{ex}) of HCN(4–3) as a function of T_{bg} . When the line emission is optically thin or moderately thick (panels-(a) and (b) in Figure 2.3), one can find that the excitation can be dominated by radiative processes, since T_{ex} is very close to T_{bg} especially at $T_{\text{bg}} \gtrsim 10 \text{ K}$. The excitation states of HCO⁺(4–3) and CS(7–6) are presented in Appendix-C. The optical depths of the target lines calculated by the RADEX are shown in Figure 2.4 as a function of T_{bg} .

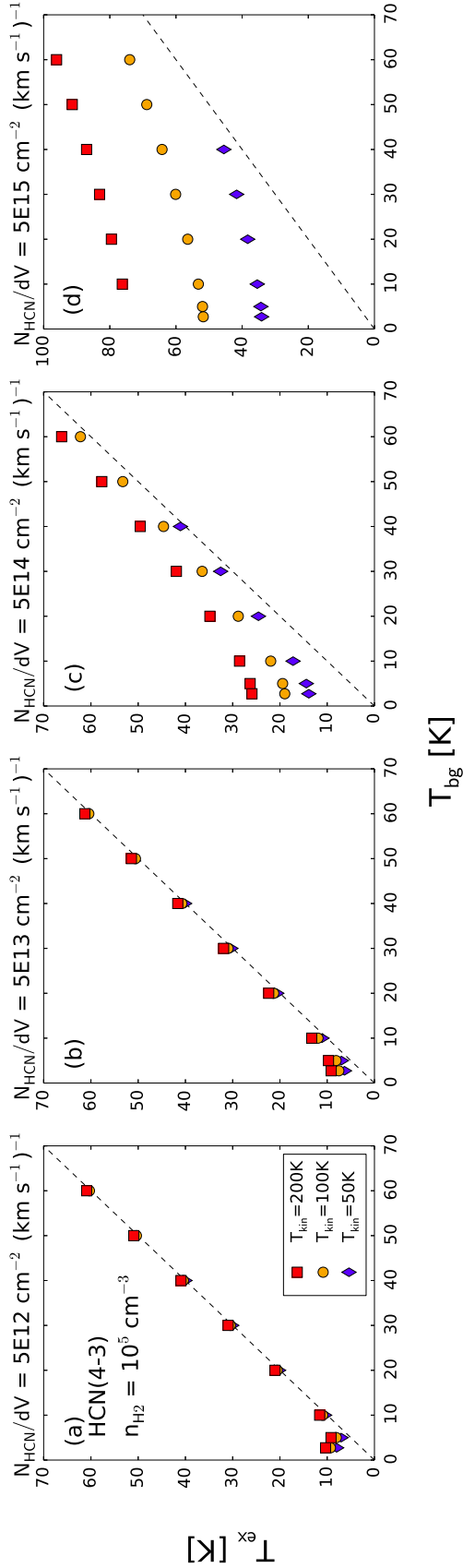


Figure 2.3: Excitation temperature (T_{ex}) of HCN(4 – 3) as a function of background temperature (T_{bg}). The red, orange, blue symbols indicate the models with gas kinetic temperature (T_{kin}) of 200, 100, and 50 K, respectively. We here fixed gas volume density as $n_{\text{H}_2} = 10^5 \text{ cm}^{-3}$. Four cases of the line-of-sight column density to velocity width ratio (N_{HCN}/dV) of (a) 5×10^{12} , (b) 5×10^{13} , (c) 5×10^{14} , and (d) $5 \times 10^{15} \text{ cm}^{-2} (\text{km s}^{-1})^{-1}$ are shown here. Note that the scale of the y-axis in the panel-(d) is different from the others. The dashed line in each panel indicates the $T_{\text{ex}} = T_{\text{bg}}$. One can find that T_{ex} approaches to T_{bg} when $T_{\text{bg}} \gtrsim 10 \text{ K}$ in the panels-(a) and (b). In the panel-(d), optical depth is so large (see also Figure 2.4) that we can expect T_{ex} becomes independent of T_{bg} , and approaches to T_{kin} due to an enhanced photon trapping effect. Note that HCN(5 – 4) (not $J = 4 - 3$) line shows a maser feature ($T_{\text{ex}} < 0$) at $T_{\text{bg}} = 2.73 \text{ K}$ in the panel-(d), and HCN(4 – 3) is also a maser at $T_{\text{bg}} = 5 \text{ K}$ in the same panel, when $T_{\text{kin}} = 200 \text{ K}$. These two extreme cases are excluded from the plot.

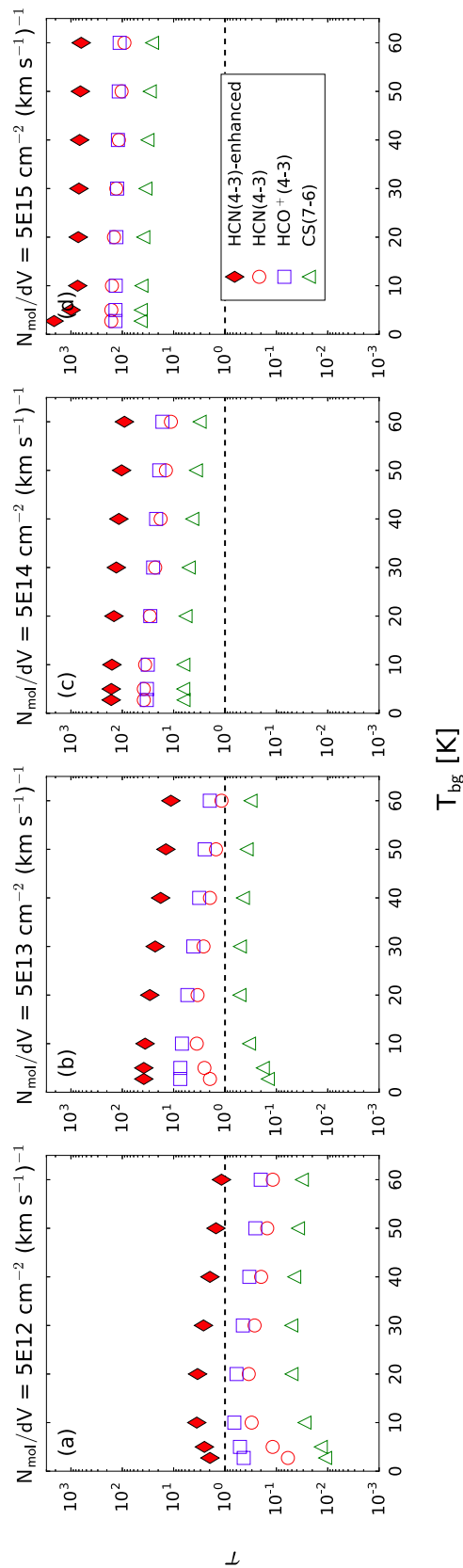


Figure 2.4: Line optical depths of HCN(4 – 3), HCO⁺(4 – 3), and CS(7 – 6), as a function of T_{bg} calculated with the RADEX. The H₂ gas density and the kinetic temperature were fixed to $n_{\text{H}_2} = 10^5 \text{ cm}^{-3}$ and $T_{\text{kin}} = 100 \text{ K}$, respectively. The cases where the molecular column density to the velocity width ratio (N_{mol}/dV , mol = HCN, HCO⁺, and CS) of (a) 5.0×10^{12} , (b) 5.0×10^{13} , (c) 5.0×10^{14} , and (d) $5.0 \times 10^{15} \text{ cm}^{-2} (\text{km s}^{-1})^{-1}$ are presented. In each panel, we also show the optical depth of HCN(4 – 3) calculated after enhancing the abundance of HCN by 10 times (filled diamond) for easier comparison with the subsequent figures. The dashed line indicates $\tau = 1.0$ for an eye-guide.

The excitation state shown in Figure 2.3 can be better understood through a two-level (e.g., HCN $J = 3$ and 4) analytic treatment. Although we conducted full-level statistical equilibrium calculation with the RADEX, this analytic treatment provides us fruitful insights on what is influencing the molecular excitation. Similar approach can be found in, e.g., Scoville et al. (2015) and originally, Scoville & Solomon (1974), but we include background radiation into the analysis as well, which has been usually omitted.

The ratio of the upper to lower level molecular population with the energy gap of ΔE_{ul} can be written as,

$$\begin{aligned} \frac{n_u}{n_l} &= \frac{B_{lu}J_\nu + C_{lu}}{A_{ul} + B_{ul}J_\nu + C_{ul}} = \frac{g_u}{g_l} \frac{\eta A_{ul}\beta_\nu + C_{ul} \exp\left(-\frac{\Delta E_{ul}}{T_{\text{kin}}}\right)}{(1 + \eta)A_{ul}\beta_\nu + C_{ul}} \\ &= \frac{g_u}{g_l} \exp\left(-\frac{\Delta E_{ul}}{T_{\text{ex}}}\right), \end{aligned} \quad (2.1)$$

with

$$\eta \equiv \frac{1}{\exp\left(\frac{\Delta E_{ul}}{T_{\text{bg}}}\right) - 1}. \quad (2.2)$$

Here, the A_{ul} , B_{ul} , and C_{ul} indicate the Einstein coefficients of spontaneous decay, stimulated emission, and collisional de-excitation, respectively. The upwards and downwards collision rates are related assuming a detailed balance in the thermodynamic equilibrium state. The g_u and g_l are statistical weights of the upper and lower levels. The frequency of the line is represented as ν . The internal radiation J_ν is

$$J_\nu = (1 - \beta_\nu)B_\nu(T_{\text{ex}}) + \beta_\nu B_\nu(T_{\text{bg}}), \quad (2.3)$$

where $B_\nu(T)$ is the Planck function at temperature T . Although we should include various mechanisms as the source of the background radiation and solve their radiative transfer individually to achieve the local spectral energy distribution, we represent them by a single Planck function having an equivalent temperature T throughout this paper, for simplicity. The photon escape probability from the model cloud is denoted as β_ν , which is an analytical form of the line optical depth τ as

$$\beta_\nu = \frac{1.5}{\tau} \left[1 - \frac{2}{\tau^2} + \left(\frac{2}{\tau} + \frac{2}{\tau^2} \right) e^{-\tau} \right], \quad (2.4)$$

for a spherical cloud (e.g., Osterbrock & Ferland 2006). The value of β_ν also depends on the assumed geometry. In Equation (2.1), A_{ul} is reduced by β_ν , which means an *effective* n_{cr} of the line ($n_{\text{cr,eff}}$) is lower than the n_{cr} at the optically thin limit ($n_{\text{cr,thin}}$; Table 2.2) due to the *photon trapping effect*, i.e., $n_{\text{cr,eff}} = \beta_\nu \times n_{\text{cr,thin}}$. The background radiation field is included in Equation (2.1) as η . We show the η of HCN(4 – 3) in Figure 2.5, which is almost identical to those of HCO⁺(4 – 3) and CS(7 – 6).

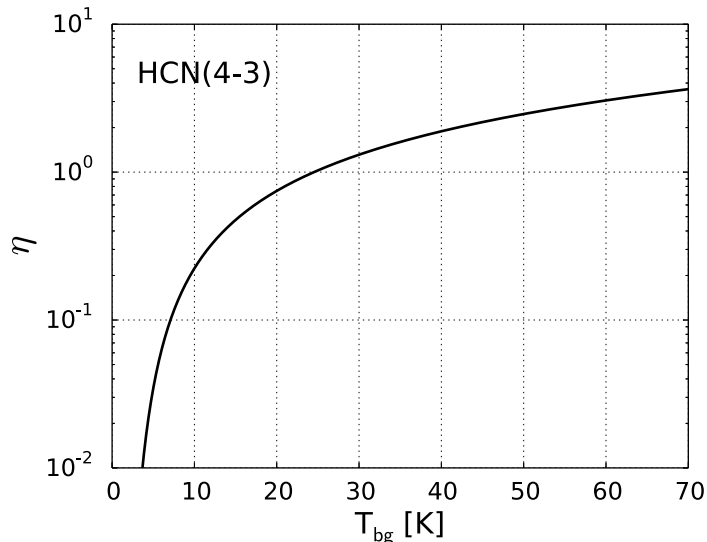


Figure 2.5: Dependence of $\eta \equiv 1/(\exp(\Delta E_{ul}/T_{\text{bg}})-1)$ of HCN(4–3) on T_{bg} . The value of η is almost identical among HCN(4–3), HCO⁺(4–3), and CS(7–6), reflecting their similar energy gaps between the upper and the lower levels (Table 2.2). The radiative excitation can be negligible when $\eta \ll 1$ (compare this plot with Figure 2.3).

By introducing the $n_{\text{cr,eff}}$, Equation (2.1) is reduced to

$$\begin{aligned} \exp\left(-\frac{\Delta E_{ul}}{T_{\text{ex}}}\right) &= \frac{\eta + \left(\frac{n_{\text{H}_2}}{n_{\text{cr,eff}}}\right) \exp\left(-\frac{\Delta E_{ul}}{T_{\text{kin}}}\right)}{(1 + \eta) + \left(\frac{n_{\text{H}_2}}{n_{\text{cr,eff}}}\right)} \\ &\sim \frac{\eta + \left(\frac{n_{\text{H}_2}}{n_{\text{cr,eff}}}\right)}{(1 + \eta) + \left(\frac{n_{\text{H}_2}}{n_{\text{cr,eff}}}\right)}. \end{aligned} \quad (2.5)$$

Here $\exp(-\Delta E_{ul}/T_{\text{kin}})$ commonly takes ~ 1 for HCN(4–3), HCO⁺(4–3), and CS(7–6) at any T_{kin} in our models. With this formula, the molecular excitation in the two extreme cases of β_ν , i.e., $\beta_\nu \rightarrow 1$ (optically thin limit) and $\beta_\nu \rightarrow 0$ (optically thick limit), are discussed in the following for a demonstrative purpose.

(i) optically thin limit—in this limit, we expect $n_{\text{H}_2}/n_{\text{cr,eff}} = n_{\text{H}_2}/n_{\text{cr,thin}} \sim 10^{-2}$ for HCN(4–3), for example (Table 2.2). Taking Figure 2.5 into account as well, one can find both collisional and radiative excitation can contribute to the molecular excitation especially when $T_{\text{bg}} \lesssim 5$ K. On the other hand, the right-hand-side of Equation (2.5) now reduces to $\exp(-\Delta E_{ul}/T_{\text{bg}})$, i.e., molecules are radiatively excited. This trend stands out especially when $T_{\text{bg}} \gtrsim 10$ K, which can be clearly seen in Figure 2.3(a). Therefore, as a general manner, we suggest that radiative excitation should be considered seriously even when we treat line emissions from AGNs, where high T_{bg} is likely expectable.

(ii) optically thick limit—in this limit, by substituting $\beta_\nu \rightarrow 0$ (or $n_{\text{cr,eff}} \rightarrow 0$) to Equation (2.5), one can find that T_{ex} is now identical to T_{kin} and thus independent of T_{bg} . Indeed, T_{ex} is less dependent on T_{bg} and also differs a lot according to T_{kin} (panels-(c) and (d) in Figure 2.3), as HCN(4 – 3) becomes optically thicker (see also Figure 2.4). We note that the output parameters in the RADEX code have a limited meaning at quite high optical depths such as $\tau \gtrsim 100$, since a drastic change of an optical depth over a line profile is not taken into account in the code (van der Tak et al. 2007).

2.4.3 The $R_{\text{HCN/HCO}^+}$ and $R_{\text{HCN/CS}}$ under non-LTE

We then calculated $R_{\text{HCN/HCO}^+}$ and $R_{\text{HCN/CS}}$ based on our non-LTE modelings as a function of T_{bg} . Several cases with different T_{kin} , N_{mol}/dV (or τ), and molecular abundance ratios, are shown in Figure 2.6. Here, we discuss the dependence of each line ratio on the parameters in our models. We guide readers to Martín et al. (2015) for these line ratios calculated under the LTE condition.

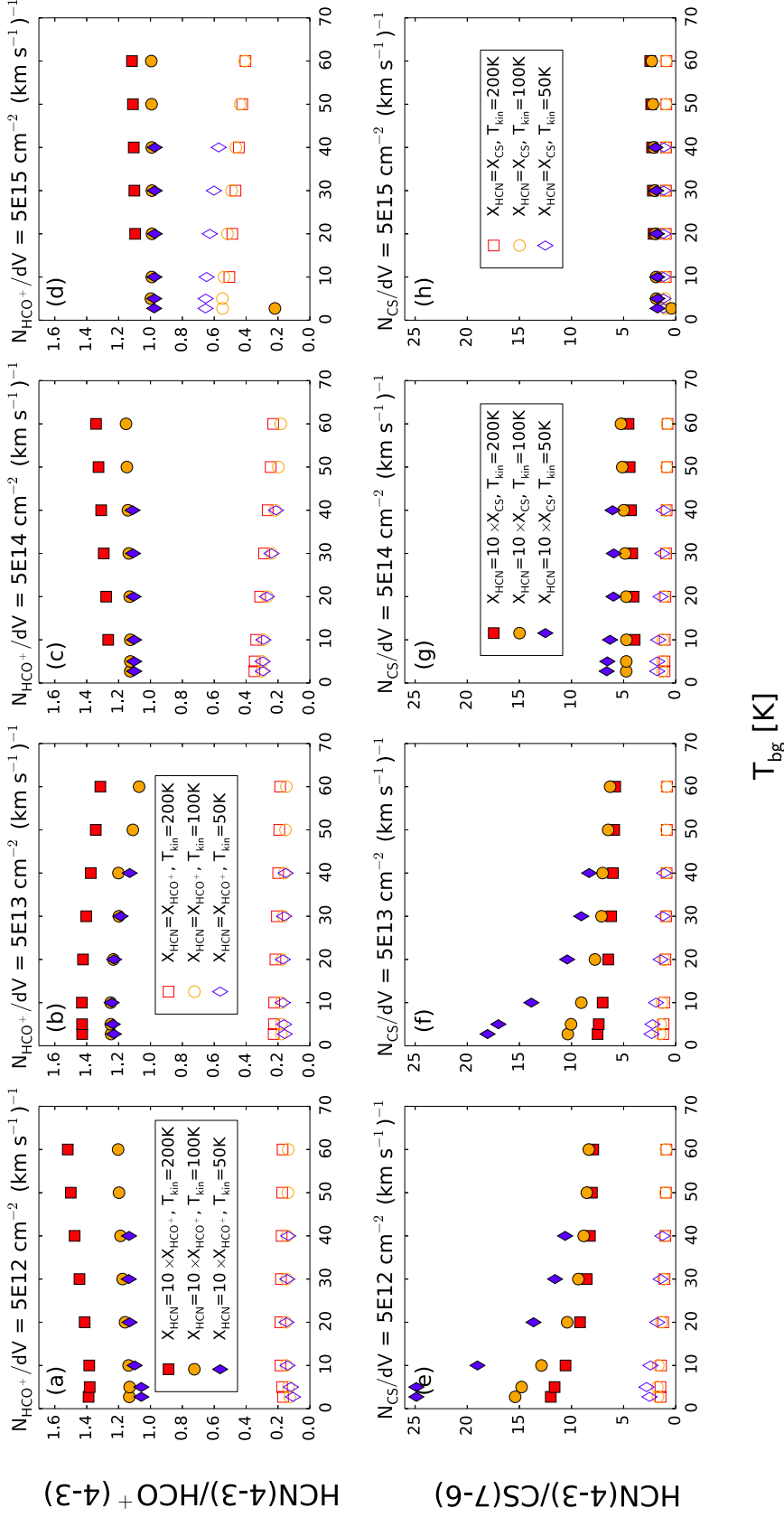


Figure 2.6: The $R_{\text{HCN}/\text{HCO}^+}$ (top panels) and the $R_{\text{HCN}/\text{CS}}$ (bottom panels) as a function of T_{bg} , calculated by our RADEX models. The ratio of line-of-sight molecular column density to velocity width (N_{mol}/dV) varies from 5×10^{12} to $5 \times 10^{15} \text{ cm}^{-2} (\text{km s}^{-1})^{-1}$ for $\text{mol} = \text{HCO}^+$ and CS, respectively. As a result, the left-most panels (a) and (e) display the cases where each emission is optically thin, whereas the right-most panels (d) and (h) show heavily optically thick cases. The opacities of these lines are shown in Figure 2.4 for the case of $T_{\text{kin}} = 100 \text{ K}$. The filled and empty symbols indicate $X_{\text{HCN}}/X_{\text{HCO}^+}$ (or $X_{\text{HCN}}/X_{\text{CS}}$) = 10 or 1, respectively. The colors indicate the gas kinetic temperature (T_{kin}) of 50 K (blue), 100 K (orange), and 200 K (red), respectively.

(i) $R_{\text{HCN}/\text{HCO}^+}$ — one will find in Figure 2.6(a)-(d) that this ratio is not so sensitive to T_{bg} , which is close to T_{ex} when the excitation is dominated by the radiative processes (see also Figure 2.3). To further examine this trend, we rewrite $R_{\text{HCN}/\text{HCO}^+}$ analytically as

$$\frac{T_{\text{ex,HCN}(4-3)} - T_{\text{bg}}}{T_{\text{ex,HCO}^+(4-3)} - T_{\text{bg}}} \cdot \frac{1 - \exp(-\tau_{\text{HCN}(4-3)})}{1 - \exp(-\tau_{\text{HCO}^+(4-3)})} \equiv \xi_{\text{HCN}/\text{HCO}^+} \cdot \zeta_{\text{HCN}/\text{HCO}^+}, \quad (2.6)$$

where $\xi_{\text{HCN}/\text{HCO}^+}$ and $\zeta_{\text{HCN}/\text{HCO}^+}$ correspond to the former and the latter term of the left hand side of Equation (2.6), respectively. Also, we rewrite the optical depth as

$$\tau_{ul} = \frac{c^3}{8\pi\nu^3} \frac{g_u}{g_l} A_{ul} \frac{N_l}{dV} \left(1 - \exp\left(-\frac{\Delta E_{ul}}{T_{\text{ex}}}\right) \right), \quad (2.7)$$

where N_l is the line-of-sight column density at the lower energy level. The resultant $\xi_{\text{HCN}/\text{HCO}^+}$ and $\zeta_{\text{HCN}/\text{HCO}^+}$ are plotted in Figure 2.7(a) for the representative case of $N_{\text{HCO}^+}/dV = 5 \times 10^{13} \text{ cm}^{-2} (\text{km s}^{-1})^{-1}$. At this N_{HCO^+}/dV with $X_{\text{HCN}}/X_{\text{HCO}^+} = 1$, both HCN(4-3) and HCO⁺(4-3) are moderately optically thick, whereas HCN(4-3) can be *heavily* optically thick when $X_{\text{HCN}}/X_{\text{HCO}^+} = 10$ (Figure 2.4). From Figure 2.7(a), one may find that $\xi_{\text{HCN}/\text{HCO}^+}$ and $\zeta_{\text{HCN}/\text{HCO}^+}$ vary towards the opposite direction at $T_{\text{bg}} \lesssim 10 \text{ K}$ (the range where both collisional and radiative processes can influence the excitation), which compensates with each other to keep the $R_{\text{HCN}/\text{HCO}^+}$ more or less constant. At $T_{\text{bg}} \gtrsim 10 \text{ K}$ where $T_{\text{ex}} \sim T_{\text{bg}}$, on the other hand, both $\xi_{\text{HCN}/\text{HCO}^+}$ and $\zeta_{\text{HCN}/\text{HCO}^+}$ are not so sensitive to T_{bg} anymore, as both lines share quite similar excitation conditions. Note that, in the heavily optically thick cases, we can expect $R_{\text{HCN}/\text{HCO}^+}$ converges to ~ 1 as both lines are thermalized at the optically thick limit.

As for the dependence on T_{kin} , one can see that the $R_{\text{HCN}/\text{HCO}^+}$ increases as T_{kin} gets higher in each panel, reflecting the higher n_{cr} of HCN(4-3) than HCO⁺(4-3), except for the case of $X_{\text{HCN}} = X_{\text{HCO}^+}$ in Figure 2.6(d). In that exceptional case, where both lines are quite optically thick, HCO⁺(4-3) is now almost thermalized because of the well reduced $n_{\text{cr,eff}}$ ($\ll n_{\text{H}_2} = 10^5 \text{ cm}^{-3}$) for all data points due to the photon trapping (see also Appendix-C), i.e., $T_{\text{ex}} \sim T_{\text{kin}}$. On the other hand, HCN(4-3) is still sub-thermally excited ($T_{\text{ex}} < T_{\text{kin}}$), and its $T_{\text{ex}}/T_{\text{kin}}$ ratio is higher at $T_{\text{kin}} = 50 \text{ K}$ than at 100 K and 200 K. This somewhat strange feature reflects the significant contribution from radiative processes to the line excitation.

Regarding the molecular abundance ratio, we find $X_{\text{HCN}}/X_{\text{HCO}^+} \gtrsim 10$ is necessary to reproduce $R_{\text{HCN}/\text{HCO}^+} > 1$ observed in AGNs in any T_{kin} and N_{mol}/dV studied here. Enhancing X_{HCN} (equivalently enhancing N_{HCN} in our models) will increase $\tau_{\text{HCN}(4-3)}$ and T_{ex} (photon trapping) under the fixed $(n_{\text{H}_2}, T_{\text{kin}})$, which will result in subsequent enhancement of the $R_{\text{HCN}/\text{HCO}^+}$. The required $X_{\text{HCN}}/X_{\text{HCO}^+}$ is consistent with the previous multi-transitional non-LTE modeling of HCN and HCO⁺ in NGC 1097 (Izumi et al. 2013). We should also mention that Yamada et al. (2007) concluded, based on their three-dimensional radiative transfer simulations, that X_{HCN} must be an order of magnitude higher than X_{HCO^+} in order to account for the observed similarly high HCN(1-0)/HCO⁺(1-0) ratios in AGNs (e.g., ~ 2 in NGC 1068; Kohno et al. 2008). Our results seem to be consistent with their modelings, although we here use $J = 4 - 3$ transitions. Moreover and importantly, *the $X_{\text{HCN}}/X_{\text{HCO}^+}$ required for AGNs ($\gtrsim 10$) are significantly higher*

than that required to reproduce the $R_{\text{HCN}/\text{HCO}^+}$ in SB galaxies, which is typically $X_{\text{HCN}}/X_{\text{HCO}^+} \sim 3$. Therefore, the *boosting factor* (see below) of the abundance ratio in AGNs over that in SB galaxies is at least ~ 3 . This factor can even increase to $\gtrsim 10$ (i.e., $X_{\text{HCN}}/X_{\text{HCO}^+} \gtrsim 30$) to account for the high-end values observed in AGNs (e.g., NGC 1068 (W-knot) in Table 2.1) based on our modelings. Note that, for a convenient discussion, we here define the boosting factor as

$$BF_{\text{HCN}/\text{HCO}^+} = \frac{(X_{\text{HCN}}/X_{\text{HCO}^+})_{\text{AGN}}}{(X_{\text{HCN}}/X_{\text{HCO}^+})_{\text{SB}}}, \quad (2.8)$$

where $(X_{\text{HCN}}/X_{\text{HCO}^+})_{\text{AGN}}$ and $(X_{\text{HCN}}/X_{\text{HCO}^+})_{\text{SB}}$ denote the molecular fractional abundance ratios in AGN and SB galaxies, respectively. The same notation is also used for the case of $X_{\text{HCN}}/X_{\text{CS}}$. We point out that, for the extreme case like NGC 1068 (W-knot), we need to require $N_{\text{HCO}^+}/dV \lesssim 5 \times 10^{13} \text{ cm}^{-2} (\text{km s}^{-1})^{-1}$ because $R_{\text{HCN}/\text{HCO}^+}$ will eventually converge to unity for larger optical depths and will never reach such high values observed as ~ 3 .

(ii) $R_{\text{HCN}/\text{CS}}$ —As is not the case of the $R_{\text{HCN}/\text{HCO}^+}$, $R_{\text{HCN}/\text{CS}}$ shows a steep dive in Figure 2.6(e)(f) as increasing T_{bg} from 2.73 K to 10 K, when $X_{\text{HCN}}/X_{\text{CS}} = 10$. Hence, this line ratio strongly depends on the excitation conditions. This feature is more prominent at lower T_{kin} . All other cases show almost constant $R_{\text{HCN}/\text{CS}}$ against T_{bg} . Following the same manner in Equation (2.6), we express the $R_{\text{HCN}/\text{CS}}$ as

$$\frac{T_{\text{ex,HCN}(4-3)} - T_{\text{bg}}}{T_{\text{ex,CS}(7-6)} - T_{\text{bg}}} \cdot \frac{1 - \exp(-\tau_{\text{HCN}(4-3)})}{1 - \exp(-\tau_{\text{CS}(7-6)})} \equiv \xi_{\text{HCN}/\text{CS}} \cdot \zeta_{\text{HCN}/\text{CS}}. \quad (2.9)$$

The resultant $\xi_{\text{HCN}/\text{CS}}$ and $\zeta_{\text{HCN}/\text{CS}}$ are plotted in Figure 2.7(b) for the case of $N_{\text{CS}}/dV = 5 \times 10^{13} \text{ cm}^{-2} (\text{km s}^{-1})^{-1}$ as a representative example.

In Figure 2.7(b), a rapid drop in $\zeta_{\text{HCN}/\text{CS}}$ (by a factor of ~ 5 when $X_{\text{HCN}}/X_{\text{CS}} = 10$) stands out, which damps the variation of $\xi_{\text{HCN}/\text{CS}}$. We can attribute this dive to the quite different τ between HCN(4–3) and CS(7–6); $\tau_{\text{HCN}(4-3)} = 19.5 - 41.8$, whereas $\tau_{\text{CS}(7-6)} = 0.06 - 0.45$ for the case of Figure 2.7(b). In this case, $\zeta_{\text{HCN}/\text{CS}}$ mostly reflects the variation of $\tau_{\text{CS}(7-6)}$ since $\zeta_{\text{HCN}/\text{CS}}$ is now $\sim 1/\tau_{\text{CS}(7-6)}$. Then, considering the τ of HCN(4–3) and CS(7–6) shown in Figure 2.4, we can deduce that the condition of, “HCN(4–3) is optically thick, whereas CS(7–6) is optically thin,” would be the key to realize the high $R_{\text{HCN}/\text{CS}} \gtrsim 10$ observed in some AGNs. This scenario can explain the dependence of $R_{\text{HCN}/\text{CS}}$ on T_{kin} , as we can expect larger $\tau_{\text{CS}(7-6)}$ (higher $T_{\text{ex,CS}(7-6)}$) at higher T_{kin} , while $\tau_{\text{HCN}(4-3)}$ is already substantially large regardless of any T_{kin} in our models. Note that $R_{\text{HCN}/\text{CS}}$ naturally converges to ~ 1 as both HCN(4–3) and CS(7–6) reach optically thick limit with similar T_{ex} .

Then, we suggest that $N_{\text{CS}}/dV \lesssim 5 \times 10^{13} \text{ cm}^{-2} (\text{km s}^{-1})^{-1}$ and $X_{\text{HCN}}/X_{\text{CS}} \gtrsim 10$ would be necessary conditions to reproduce the observed high $R_{\text{HCN}/\text{CS}}$ in AGNs. The required $X_{\text{HCN}}/X_{\text{CS}}$ for AGNs ($\gtrsim 10$) is again significantly higher than that for SB galaxies (~ 3). Hence the estimated $BF_{\text{HCN}/\text{CS}}$ is at least ~ 3 . This $BF_{\text{HCN}/\text{CS}}$ can even increase to ~ 10 (i.e., $X_{\text{HCN}}/X_{\text{CS}} \sim 30$ in AGNs) to reproduce the high-end values of $R_{\text{HCN}/\text{CS}} \gtrsim 12$ (Figure 2.1) under the conditions of moderately high dust temperature of $\gtrsim 10$ K and high T_{kin} such as 200 K. These boosting factors are roughly consistent with $BF_{\text{HCN}/\text{HCO}^+}$.

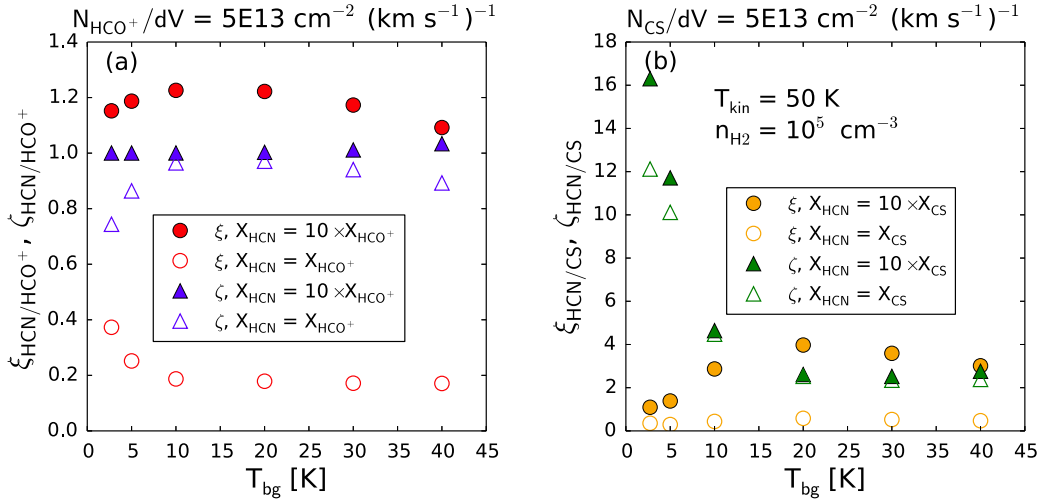


Figure 2.7: Dependence of (a) $\xi_{\text{HCN}/\text{HCO}^+}$ and $\zeta_{\text{HCN}/\text{HCO}^+}$, and (b) $\xi_{\text{HCN}/\text{CS}}$ and $\zeta_{\text{HCN}/\text{CS}}$ on T_{bg} . For the definition of ξ and ζ , see Equations (2.6) and (2.9) in the text. The case of $(T_{\text{kin}}, n_{\text{H}_2}) = (50 \text{ K}, 10^5 \text{ cm}^{-3})$ with $N_{\text{mol}}/dV = 5 \times 10^{13} \text{ cm}^{-2} (\text{km s}^{-1})^{-1}$ are shown (mol = HCO^+ or CS) as the representative ones. The colors indicate (a) red = $\xi_{\text{HCN}/\text{HCO}^+}$, blue = $\zeta_{\text{HCN}/\text{HCO}^+}$, and (b) orange = $\xi_{\text{HCN}/\text{CS}}$, green = $\zeta_{\text{HCN}/\text{CS}}$, respectively. The filled and empty symbols denote $X_{\text{HCN}}/X_{\text{HCO}^+}$ (or $X_{\text{HCN}}/X_{\text{CS}}$) = 10 and 1, respectively.

2.4.4 Dependence of the line ratios on gas density

Recently, Viti et al. (2014) reported that n_{H_2} would vary even inside a single CND. Therefore, the impact of different densities on the line ratios of our interest should be investigated. To this end, we conducted the same analysis as shown in the previous parts but for the case of $n_{\text{H}_2} = 5 \times 10^6 \text{ cm}^{-3}$. This density roughly corresponds to the highest one predicted by Viti et al. (2014) in the CND of NGC 1068. The resultant (model-predicted) line ratios and optical depths are presented in Figures 2.8 and 2.9, respectively.

From Figure 2.8, we found that both $R_{\text{HCN}/\text{HCO}^+}$ and $R_{\text{HCN}/\text{CS}}$ tend to show higher values than those in Figure 2.6 especially when $N_{\text{mol}}/dV \leq 5 \times 10^{13} \text{ cm}^{-2} (\text{km s}^{-1})^{-1}$ (mol = HCO^+ and CS), i.e., cases when emission lines are optically thin or moderately thick. For example, $R_{\text{HCN}/\text{HCO}^+}$ in Figure 2.8(a) exceeds 2.5 at $T_{\text{kin}} \geq 100 \text{ K}$ and $X_{\text{HCN}}/X_{\text{HCO}^+} = 10$, which is comparable to the observed high-end ratios in Table 2.1. The higher values than the former cases with $n_{\text{H}_2} = 10^5 \text{ cm}^{-3}$ directly reflects the highest n_{cr} of $\text{HCN}(4-3)$ among the lines used here. However, when N_{mol}/dV is increased, one can also see that the line ratios converge to unity more quickly than for the cases in Figure 2.6. Enhanced excitation due to the higher n_{H_2} makes each emission line being thermalized and optically thick quicker, leading to this convergence. This is also manifested in the trend that both line ratios are less dependent on T_{bg} , but more sensitive to T_{kin} than the cases in Figure 2.6, which is especially prominent in $R_{\text{HCN}/\text{CS}}$ (this ratio is quite sensitive to the optical depth; Section 2.4.3). Therefore, although it depends on the line opacity, higher n_{H_2} does not necessarily correspond to higher $R_{\text{HCN}/\text{HCO}^+}$ nor $R_{\text{HCN}/\text{CS}}$.

Then, let us speculate more in detail about three cases of gas densities in the following: (i) $n_{\text{AGN}} = n_{\text{SB}}$, (ii) $n_{\text{AGN}} < n_{\text{SB}}$, and (iii) $n_{\text{AGN}} > n_{\text{SB}}$. Here, n_{AGN} and n_{SB} denote *representative*

gas densities in AGN and SB environments, respectively. We focus on two cases of n_{H_2} as are shown in Figures 2.6 (10^5 cm^{-3}) and 2.8 ($5 \times 10^6 \text{ cm}^{-3}$), and focus only on $R_{\text{HCN}/\text{HCO}^+}$ for simplicity. Then, the higher density between n_{AGN} and n_{SB} corresponds to $5 \times 10^6 \text{ cm}^{-3}$, whereas the lower one is 10^5 cm^{-3} .

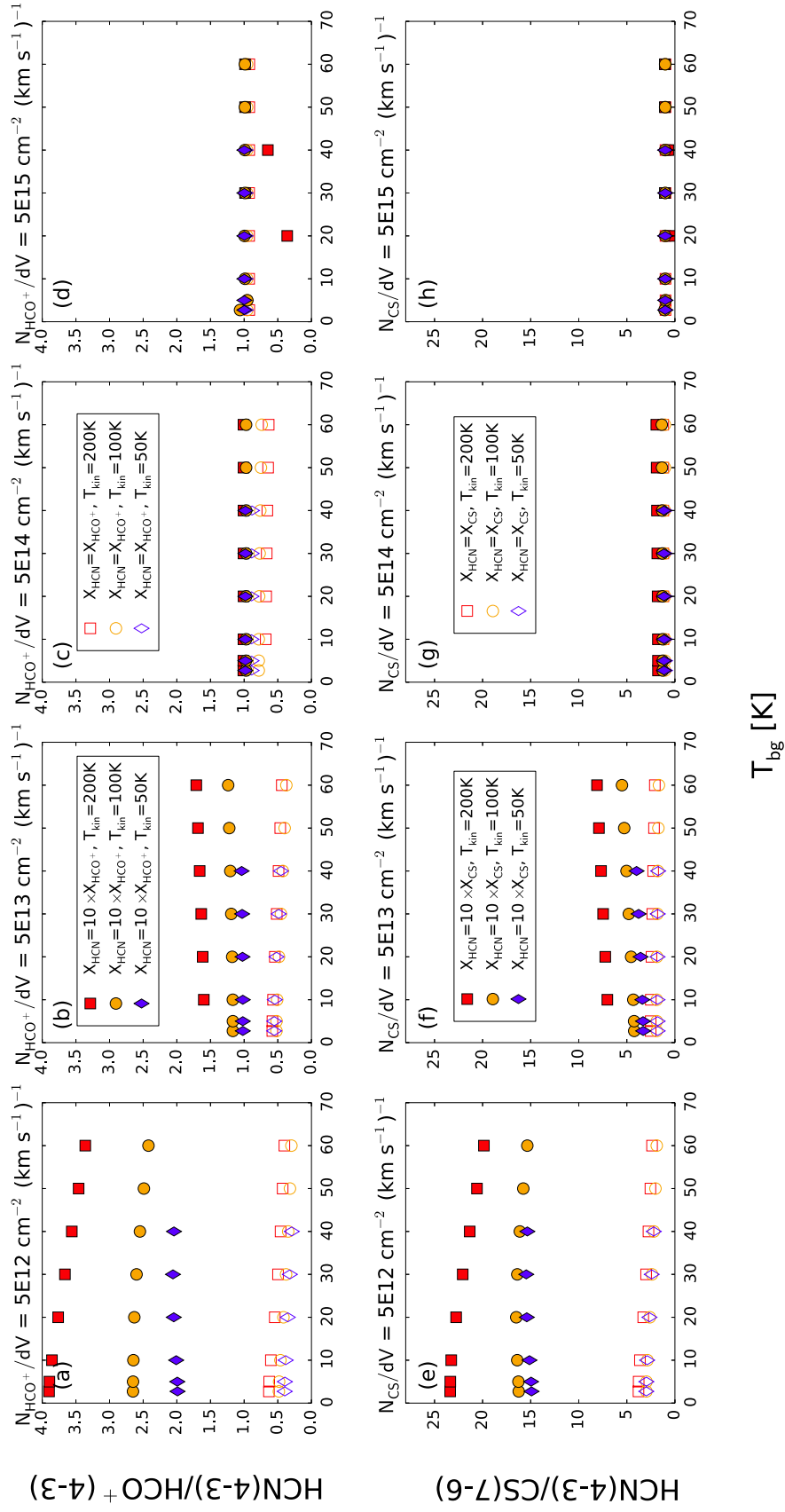
(i) $n_{\text{AGN}} = n_{\text{SB}}$: in the case of $n_{\text{H}_2} = 10^5 \text{ cm}^{-3}$ (Figure 2.6), $X_{\text{HCN}}/X_{\text{HCO}^+}$ is \sim a few for SB galaxies (Section 2.4.3). Then, we request for the boosting factor $BF_{\text{HCN}/\text{HCO}^+}$ to be at least ~ 3 to explain the observed $R_{\text{HCN}/\text{HCO}^+}$ in AGNs. Regarding the high-end value such as $R_{\text{HCN}/\text{HCO}^+} \gtrsim 3$ (e.g., NGC 1068 (W-knot)), $BF_{\text{HCN}/\text{HCO}^+}$ even reaches $\gtrsim 10$ (i.e., $X_{\text{HCN}}/X_{\text{HCO}^+} \gtrsim 30$). When n_{H_2} is increased to $5 \times 10^6 \text{ cm}^{-3}$ (Figure 2.8), $X_{\text{HCN}}/X_{\text{HCO}^+} = 1$ is sufficient to reproduce the $R_{\text{HCN}/\text{HCO}^+}$ in SB galaxies (Figure 2.8). On the other hand, we still need $BF_{\text{HCN}/\text{HCO}^+}$ to be a few to even ~ 10 (depending on the line opacity) in order to account for the $R_{\text{HCN}/\text{HCO}^+}$ in AGNs, especially the high-end values. In either case, we require the enhanced HCN abundance in AGNs to reproduce the observations.

(ii) $n_{\text{AGN}} < n_{\text{SB}}$: As shown above, $X_{\text{HCN}}/X_{\text{HCO}^+} \sim 1$ is sufficient to reproduce the observed $R_{\text{HCN}/\text{HCO}^+}$ in SB galaxies when $n_{\text{H}_2} = 5 \times 10^6 \text{ cm}^{-3}$ (Figure 2.8). However, we need to enhance the $X_{\text{HCN}}/X_{\text{HCO}^+}$ up to ~ 10 ($\gtrsim 30$ for the case of the high-end value) to explain the $R_{\text{HCN}/\text{HCO}^+}$ in AGNs when $n_{\text{H}_2} = 10^5 \text{ cm}^{-3}$. This indicates substantially high $X_{\text{HCN}}/X_{\text{HCO}^+}$ in AGNs with $BF_{\text{HCN}/\text{HCO}^+}$ of as high as $\gtrsim 10$ –30.

(iii) $n_{\text{AGN}} > n_{\text{SB}}$: in the case of $n_{\text{H}_2} = 10^5 \text{ cm}^{-3}$, $X_{\text{HCN}}/X_{\text{HCO}^+} \sim 3$ is sufficient to reproduce the observed $R_{\text{HCN}/\text{HCO}^+}$ in SB galaxies (Figure 2.6). For AGNs having higher gas density of $n_{\text{H}_2} = 5 \times 10^6 \text{ cm}^{-3}$ (Figure 2.8), we have to restrict ourselves to $N_{\text{HCO}^+}/dV \lesssim 5 \times 10^{13} \text{ cm}^{-2} (\text{km s}^{-1})^{-1}$ at first because $R_{\text{HCN}/\text{HCO}^+}$ converges to unity for higher column density (or τ) and thus never reaches $\gtrsim 2$. Under these conditions, we found $X_{\text{HCN}}/X_{\text{HCO}^+} \sim 3$ –5 can indeed yield a high $R_{\text{HCN}/\text{HCO}^+}$ of ~ 1.5 –2.5 (see an example in Figure 2.8(a)). In this case, $BF_{\text{HCN}/\text{HCO}^+}$ is only ~ 1 –1.5, i.e., *virtually no abundance variation between AGNs and SB galaxies*. Note that, even with this high n_{H_2} , it is still a bit challenging to reproduce the observed highest $R_{\text{HCN}/\text{HCO}^+}$ of $\gtrsim 3$. To do so, we might need to require $BF_{\text{HCN}/\text{HCO}^+}$ to be \sim a few even with the high n_{H_2} in AGNs. On the other hand, when $N_{\text{HCO}^+}/dV \sim 5 \times 10^{13} \text{ cm}^{-2} (\text{km s}^{-1})^{-1}$, we can not avoid increasing $BF_{\text{HCN}/\text{HCO}^+} \gtrsim$ a few to yield the high-end $R_{\text{HCN}/\text{HCO}^+}$ in AGNs (Figure 2.8(b)).

As the summary of our non-LTE modelings with both $n_{\text{H}_2} = 10^5 \text{ cm}^{-3}$ and $5 \times 10^6 \text{ cm}^{-3}$ (see Table 2.4.4), we suggest that $X_{\text{HCN}}/X_{\text{HCO}^+}$ would be enhanced in AGNs as compared to SB galaxies by several times to $\gtrsim 10$ times when n_{H_2} in AGNs are comparable to or lower than those in SB galaxies. Another plausible origin might be a systematically higher gas density in AGNs than in SB galaxies. In this case, an almost comparable $X_{\text{HCN}}/X_{\text{HCO}^+}$ is expected between AGNs and SB galaxies, i.e., there is no abundance variation. However, the existence of such a systematic difference in gas density is unclear at this moment. Although Viti et al. (2014) suggested such differences between the kpc scale SB ring and the 100 pc scale CND of NGC 1068, what we are treating here is the rather smaller, *circumnuclear scale* ($\lesssim 100 \text{ pc scale}$) components located at the centers of both AGN and SB galaxies; recall that we made Figure 2.1 only based on the high resolution samples in Table 2.1. Hence, the contrast in gas density between AGN and circumnuclear SB environments would be smaller than in the case between

AGN and kpc scale SB environments. Moreover, ~ 30 pc scale measurements of HCN(4 – 3) and HCN(1 – 0) revealed HCN(4 – 3)/HCN(1 – 0) integrated intensity ratio is ~ 0.7 – 1.0 in the central region of NGC 253 (the brightness temperature scale, Meier et al. 2015; Sakamoto et al. 2011), which is comparable to those obtained for the CND of NGC 1068 (Viti et al. 2014), i.e., they have similar excitation conditions. As stated before, Knudsen et al. (2007) also proposed that the line excitation is independent of nuclear types (Figure 2.10), although this argument was based on *single dish* measurements of the HCN spectral energy distribution (SLED). These results suggest that the degree of line excitation at the nuclear region of a galaxy would not depend on the specific nuclear type of that galaxy. Therefore, we prefer the scenario that the variation of underlying molecular abundances between AGNs and SB galaxies as the prime cause of the HCN-enhancement.


 Figure 2.8: Same as Figure 2.6, but the models with $n_{\text{H}_2} = 5 \times 10^6 \text{ cm}^{-3}$ are shown.

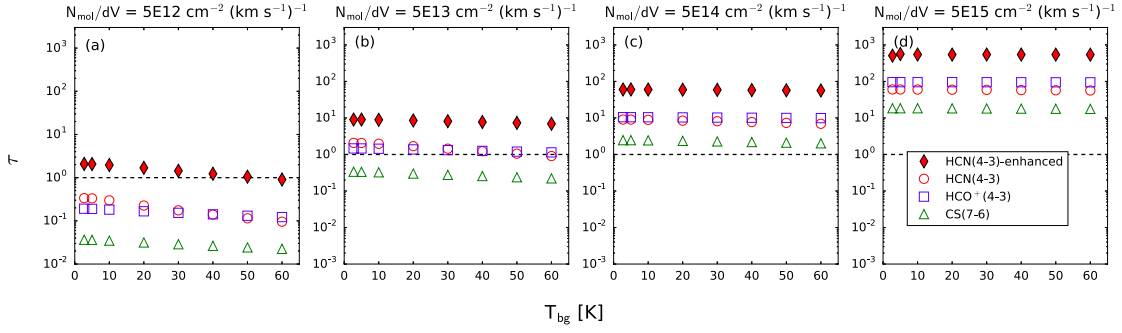


Figure 2.9: Same as Figure 2.4, but the models with $n_{\text{H}_2} = 5 \times 10^6 \text{ cm}^{-3}$ are shown. The dashed line indicates $\tau = 1.0$ for an eye-guide.

Table 2.3: Summary of the typical $X_{\text{HCN}}/X_{\text{HCO}^+}$ of AGN and SB

	H_2 density	
	10^5 cm^{-3}	$5 \times 10^6 \text{ cm}^{-3}$
AGN	> 10	a few
SB	a few	~ 1

2.4.5 Comparison with real galaxies:

Case studies of NGC 1097, NGC 1068, and NGC 4418

In this Section, we briefly compare our model calculations with the observed $R_{\text{HCN}/\text{HCO}^+}$ and/or $R_{\text{HCN}/\text{CS}}$ of two instructive AGNs and one buried-AGN, namely NGC 1097, NGC 1068, and NGC 4418. See their line ratios in Table 2.1 and Figure 2.1 as the references. The characteristics of these galaxies are presented in Appendix-A. Models with $n_{\text{H}_2} = 10^5 \text{ cm}^{-3}$ (Figure 2.6) are employed here, but those with $n_{\text{H}_2} = 5 \times 10^6 \text{ cm}^{-3}$ yield essentially the same (qualitative) arguments. As these models were not constructed to mimic an environment of a specific galaxy, our immediate objective here is to roughly check consistency between the model-predicted line ratios and the observed values.

NGC 1097 (AGN): Hsieh et al. (2008) estimated $N_{\text{H}_2} = 5.9 \times 10^{22} \text{ cm}^{-2}$ from CO interferometric observations. Assuming $X_{\text{CS}} = 2.5 \times 10^{-9}$ (the value of OMC-1 Extended Ridge where $N_{\text{H}_2} = 3 \times 10^{23} \text{ cm}^{-2}$; Blake et al. 1987) and the line width of 250 km s^{-1} (FWZI of HCN(4-3); Izumi et al. 2013), N_{CS}/dV is estimated to be $\sim 6 \times 10^{11} \text{ cm}^{-2} (\text{km s}^{-1})^{-1}$. Then, judging from Figure 2.4, we can expect CS(7-6) emission is totally optically thin ($\tau_{\text{CS}(7-6)} \ll 0.1$). This is consistent with the non-detection of CS(7-6) emission in our previous observations with ALMA (Izumi et al. 2013). Even if we increase X_{CS} by 10 times, the situation is the same. On the other hand, non-LTE analysis by Izumi et al. (2013) suggested N_{HCN}/dV in NGC 1097 is $\sim \text{a few} \times 10^{13} \text{ cm}^{-2} (\text{km s}^{-1})^{-1}$, thus HCN(4-3) would be moderately optically thick (Figure 2.4; a similar depth is deduced from H^{12}CN -to- H^{13}CN ratio as well). The resultant X_{HCN} in this case is $\sim 10^{-7}$, which is close to the value observed in Galactic hot cores and is significantly higher than that observed in, e.g., OMC-1 Extended Ridge (5.0×10^{-9} ; Blake et al. 1987). Therefore, the situation is similar to the panel-(e) of Figure 2.6 with a high $X_{\text{HCN}}/X_{\text{CS}}$ of \gtrsim

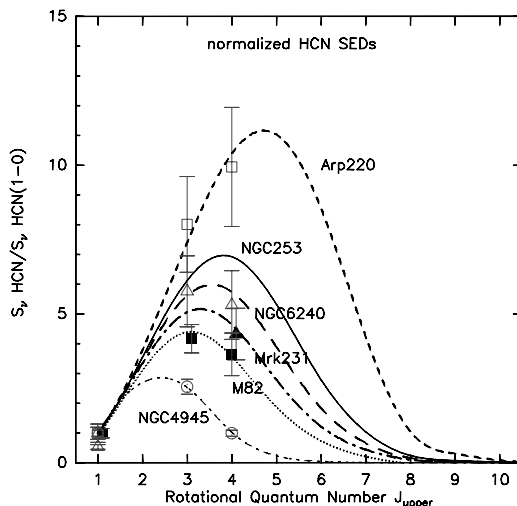


Figure 2.10: HCN spectral energy distribution of some local galaxies, including both AGNs (NGC 4945, Mrk 231, NGC 6240, and likely Arp 220) and pure SB galaxies (M82 and NGC 253), which shows the degree of line excitation (Knudsen et al. 2007). There is no clear trend of systematic difference in excitation between AGNs and SB galaxies.

10. Indeed, our model using the above values shows $R_{\text{HCN}/\text{CS}} \gtrsim 20$, which matches the observed value ($R_{\text{HCN}/\text{CS}} > 12.7$).

However, our estimated abundance ratios such as $X_{\text{HCN}}/X_{\text{HCO}^+} \sim 10$ are significantly higher than those obtained by Martín et al. (2015) through LTE analysis, which are ~ 3 . As long as we adopt a gas density that is not high enough to thermalize all of the HCN(4–3), HCO⁺(4–3), and CS(7–6) emission lines (e.g., $n_{\text{H}_2} = 10^5 \text{ cm}^{-3}$ in Figure 2.6), we should require highly enhanced abundance ratios to overcome the inefficient excitation of the HCN(4–3) line (this line has the highest n_{cr} among the target lines; Table 2.2) and yield high line ratios. In the case of higher n_{H_2} such as $5 \times 10^6 \text{ cm}^{-3}$, the required abundance ratio can be as low as ~ 3 for optically thin emission lines (Figure 2.8-(a)(e)). This ratio is consistent with the estimated LTE values (Martín et al. 2015), because now the conditions of (i) LTE and (ii) optically thin emission are mostly satisfied. For optically thicker cases, we will again see discrepancy between our model predictions and those by Martín et al. (2015). Therefore, whether our model-predictions are consistent or not with the previous LTE results, strongly depends on the assumed n_{H_2} and line optical depth.

NGC 1068: In this galaxy, both the $R_{\text{HCN}/\text{HCO}^+}$ and $R_{\text{HCN}/\text{CS}}$ at the precise AGN position are lower than those of NGC 1097 (AGN). We suppose this is due likely to a larger N_{mol} than that of NGC 1097 (AGN), i.e., the lines are optically thicker than those of NGC 1097 (AGN). Actually, the N_{H_2} towards this AGN can be $\sim 6 \times 10^{23} \text{ cm}^{-2}$ based on the CO multi-line non-LTE analysis by Viti et al. (2014), which is ~ 10 times larger than that of NGC 1097 (AGN). In this case, again by applying the $X_{\text{CS}} = 2.5 \times 10^{-9}$ (Blake et al. 1987) and $dV \sim 200 \text{ km s}^{-1}$ (García-Burillo et al. 2014), we estimate $N_{\text{CS}}/dV \sim 1 \times 10^{13} \text{ cm}^{-2} (\text{km s}^{-1})^{-1}$. For this N_{CS}/dV , CS(7–6) emission is still (moderately) optically thin ($\tau_{\text{CS}} \sim 0.1$; Figure 2.4), but

is significantly thicker than the case of NGC 1097 (AGN). The same speculation can also be applied to HCN(4 – 3) and HCO⁺(4 – 3) emission lines. As shown in Figure 2.6, it is natural for line ratios to converge to unity when the paired lines get optically thick. Moreover, since $R_{\text{HCN/CS}}$ is sensitive to T_{bg} , we can expect a lower value of this ratio in NGC 1068 (AGN) than in NGC 1097 (AGN) even when they share the same $X_{\text{HCN}}/X_{\text{CS}}$, considering the much higher AGN luminosity of NGC 1068 than NGC 1097 (Liu et al. 2014; Marinucci et al. 2012). Therefore, despite the rather lower $R_{\text{HCN/HCO}^+}$ and $R_{\text{HCN/CS}}$ than NGC 1097 (AGN), we can still expect underlying $X_{\text{HCN}}/X_{\text{HCO}^+}$ and $X_{\text{HCN}}/X_{\text{CS}}$ are high (e.g., ~ 10) in NGC 1068 (AGN).

As for the *knots* of the CND of NGC 1068, panels-(a)(b)(e)(f) of Figure 2.6 would be good approximations for their situations if we adopt the estimated N_{H_2} by Viti et al. (2014). If $T_{\text{kin}} > 100$ K, we need the abundance ratios of $\gtrsim 30$ under $n_{\text{H}_2} = 10^5 \text{ cm}^{-3}$. As shown before, we cannot discard the possibility of no abundance enhancement in the cases of the panels-(a) and (e) in Figure 2.8 ($n_{\text{H}_2} = 5 \times 10^6 \text{ cm}^{-3}$). However, if $N_{\text{mol}}/dV \gtrsim 5 \times 10^{13} \text{ cm}^{-2} (\text{km s}^{-1})^{-1}$ is true, i.e., line emissions are at least moderately optically thick, we still need to enhance the abundance ratios to be $\gtrsim 30$ even with $n_{\text{H}_2} = 5 \times 10^6 \text{ cm}^{-3}$ to reproduce the high-end values observed in these knots (e.g., $R_{\text{HCN/HCO}^+} \gtrsim 3$). Note that we can find consistent abundance ratios, with those suggested above, in previous works of multi-line, multi-species non-LTE analysis (e.g., Table 8 of Viti et al. 2014). On the other hand, there seems to be an inconsistency with the predicted abundance ratios from an LTE analysis (Table 5 of Viti et al. 2014), which are ~ 5 for both $X_{\text{HCN}}/X_{\text{HCO}^+}$ and $X_{\text{HCN}}/X_{\text{CS}}$. For the fiducial n_{H_2} of 10^5 cm^{-3} (Figure 2.6), again we should enhance X_{HCN} to overcome the inefficient excitation of HCN(4 – 3). For the higher n_{H_2} of $5 \times 10^6 \text{ cm}^{-3}$ (Figure 2.8), our results are consistent with those from the LTE analysis as long as emission lines are optically thin or moderately thick (see also Figure 2.9), but the discrepancy becomes prominent for optically thicker cases because now the condition of *optically thin emission* assumed in the LTE analysis breaks. In such optically thick cases, we eventually require enhanced ratios, e.g., $X_{\text{HCN}}/X_{\text{HCO}^+}$ of $\gtrsim 30$, as already addressed.

NGC 4418: The same argument of the optical depth effect as for NGC 1068 (AGN) holds with a stronger basis for this galaxy, because this hosts a heavily obscured compact nucleus ($N_{\text{H}_2} \gtrsim 10^{26} \text{ cm}^{-2}$; Sakamoto et al. 2013). The distinctively lower $R_{\text{HCN/CS}}$ than optically-detectable AGNs favors this view as this ratio is highly sensitive to the optical depth of CS(7 – 6) emission line (Figure 2.7). Regarding $R_{\text{HCN/HCO}^+}$, we mention this ratio is slightly increased to ~ 2 when observed at $0''.5 \sim 80$ pc resolution (Sakamoto et al. 2013), which is a comparable value to other AGNs. However, whether an enhanced $X_{\text{HCN}}/X_{\text{HCO}^+}$ such as 10 is really necessary to account for this relatively high ratio is unclear, because this galaxy exhibits a prominent $v = 1$ state HCN emission line (IR-pumping; Sakamoto et al. 2010). Radiative transfer modelings involving the IR-pumping are thus inevitable to elucidate the validity of our diagram in such a deeply embedded nucleus that the IR-pumping is highly likely affecting the ratio.

2.4.6 Implication to generic HCN-diagrams

At the last of Section 2.4, we predict HCN-to-HCO⁺ and HCN-to-CS integrated intensity ratios at other transitions based on our RADEX modelings, by varying $X_{\text{HCN}}/X_{\text{HCO}^+}$ and $X_{\text{HCN}}/X_{\text{CS}}$. Illustrative cases are shown in Figure 2.11 as a function of the upper rotational state (J_{u}) of HCN. As for CS, we coupled a transition with the closest frequency to each HCN transition (e.g., HCN(1 – 0) and CS(2 – 1), HCN(4 – 3) and CS(7 – 6)). We hereafter call this type of diagram as a spectral ratio distribution (SRD). Note that we do not intend to predict a line ratio of a specific galaxy in Figure 2.11, but to understand a qualitative feature of these ratios at various transitions.

By inspecting the SRD, one can see that enhanced $X_{\text{HCN}}/X_{\text{HCO}^+}$ (or $X_{\text{HCN}}/X_{\text{CS}}$) correspondingly produces higher line ratios at any transition. Therefore, if $X_{\text{HCN}}/X_{\text{HCO}^+}$ and $X_{\text{HCN}}/X_{\text{CS}}$ are truly enhanced in AGNs than in SB galaxies, and if they share the comparable excitation (e.g., n_{H_2} and T_{kin}), we predict AGNs would show higher line ratios not only at a single transition but also at other transitions than SB galaxies. Indeed, NGC 1097 and NGC 1068 show higher HCN(1 – 0)/HCO⁺(1 – 0) and HCN(1 – 0)/CS(2 – 1) ratios than SB galaxies (e.g., Kohno et al. 2008; Martín et al. 2015; Nakajima et al. 2011).

From this perspective, remarkable inconsistency can stem from NGC 7469, which shows HCN(1 – 0)/HCO⁺(1 – 0) ratio of ~ 0.6 when observed with Nobeyama Millimeter Array at a $\sim 6'' = 2$ kpc aperture (Kohno 2005), whereas it shows HCN(4 – 3)/HCO⁺(4 – 3) = 1.1 at a ~ 150 pc aperture (Table 2.1). This inconsistency can be reconciled when we measure $J = 1 - 0$ lines at a higher resolution to selectively probe the CND of NGC 7469 as much as possible, because this galaxy hosts a prominent SB ring with ~ 1 kpc in diameter that can be a strong source of spectral contamination; HCN(4 – 3)/HCO⁺(4 – 3) ratio at the SB ring is as low as ~ 0.5 . In fact, ~ 150 pc aperture (i.e., almost identical one to that used for observing $J = 4 - 3$ transitions; Table 2.1) measurements of $J = 1 - 0$ transitions newly obtained with ALMA reveals HCN(1 – 0)/HCO⁺(1 – 0) > 1 at the AGN position (Izumi et al. in prep., see also Appendix-D). This improved spatial resolution is still larger than, but more close to the expected size of the XDR in NGC 7469 (~ 80 pc in diameter; Izumi et al. 2015).

With this in mind, we here suppose that the low HCN(1 – 0)/HCO⁺(1 – 0) ratio (< 1) observed in NGC 2273 and NGC 4051 (both are AGNs; Sani et al. 2012) would be (at least partly) due to severe spectral contamination from the surrounding SB regions. This can be the same situation as we discussed for NGC 1365 and NGC 4945 in Section 2.3. These low line ratios were measured in the central $3''$ regions (Sani et al. 2012), which correspond to 390 pc for NGC 2273 and 150 pc for NGC 4051, respectively. Indeed, the equivalent widths of the $11.3 \mu\text{m}$ PAH emission in NGC 2273 (330 nm with ~ 500 pc slit; Alonso-Herrero et al. 2014) and NGC 4051 (95 nm with 25 pc slit; Alonso-Herrero et al. 2016) are significantly larger than those of NGC 7469 or NGC 1068 (Section 2.3). Moreover, the 2 – 10 keV X-ray luminosity of NGC 2273 ($\log(L_{2-10\text{keV}}/\text{erg s}^{-1}) = 42.7$; Marinucci et al. 2012) and NGC 4051 ($\log(L_{2-10\text{keV}}/\text{erg s}^{-1}) = 41.1$; Liu et al. 2014) are ~ 3 and ~ 130 times smaller than that of NGC 7469 ($\log(L_{2-10\text{keV}}/\text{erg s}^{-1}) = 43.2$; Liu et al. 2014), respectively. Thus, we can expect that the spatial

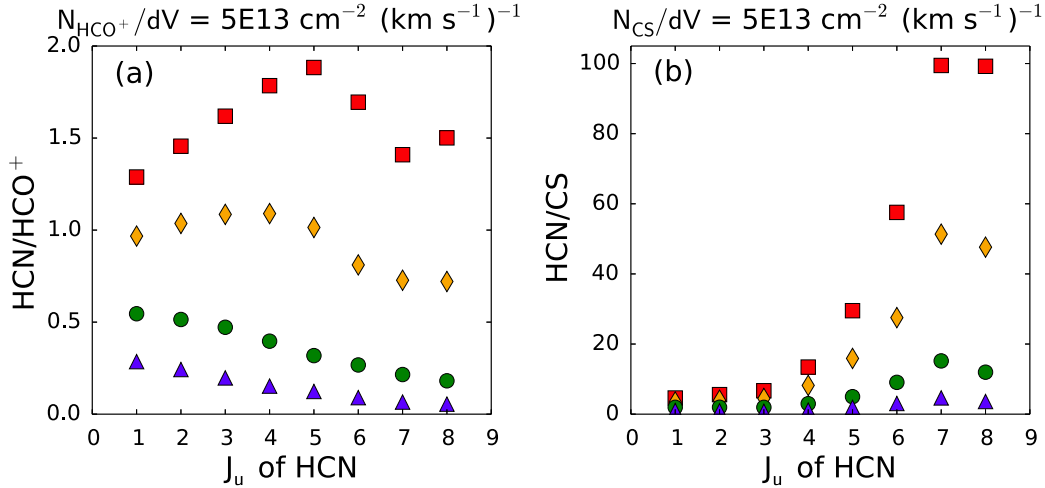


Figure 2.11: An example of spectral ratio distribution of (a) HCN to HCO⁺ and (b) HCN to CS integrated intensity ratios in the brightness temperature scale, as a function of the upper rotational state J_u of HCN. The value of each ratio is calculated based on our RADEX simulation, assuming $n_{\text{H}_2} = 10^5 \text{ cm}^{-3}$, $T_{\text{kin}} = 100 \text{ K}$, $T_{\text{bg}} = 10 \text{ K}$. The case of N_{HCO^+}/dV (or N_{CS}/dV) = $5 \times 10^{13} \text{ cm}^{-2} (\text{km s}^{-1})^{-1}$ is shown. We set molecular abundance ratios to be $X_{\text{HCN}}/X_{\text{HCO}^+}$ (or $X_{\text{HCN}}/X_{\text{CS}}$) = 20 (red square), 10 (orange diamond), 3 (green circle), and 1 (blue triangle), respectively. As for CS, the transition with the closest frequency to each HCN(J_u - J_l) is used. At any transition, enhanced X_{HCN} correspondingly produces higher line ratios (i.e., blue < green < orange < red).

extent of an XDR, or, AGN-heated gas, is much smaller in NGC 2273 and NGC 4051 than in NGC 7469 (Izumi et al. 2015). Hence, the above mentioned 3'' areas are too large to measure line ratios that are representative in AGN environments of these galaxies.

2.5 Discussion: Chemical Causes of the HCN Abundance Enhancement

In this Section, we present several plausible scenarios for the molecular abundance variation (or, HCN-enhancement in AGNs) as suggested in Section 2.4, from the perspective of ISM chemistry. We here focus on the $R_{\text{HCN}/\text{HCO}^+}$ of AGNs and SB galaxies, since this ratio is less sensitive to the line excitation than $R_{\text{HCN}/\text{CS}}$ (Figures 2.6 and 2.8). Hence, we discuss chemical causes for enhancing $X_{\text{HCN}}/X_{\text{HCO}^+}$ hereafter. Line ratios of buried-AGNs are not considered because they would be (at least partly) affected by IR-pumping. However, even focusing on the $X_{\text{HCN}}/X_{\text{HCO}^+}$ only, one will find that it is still difficult to tightly constrain the various possibilities due to insufficient amount of data currently available. We hope future high resolution, multi-line, and multi-species observations will settle the issue.

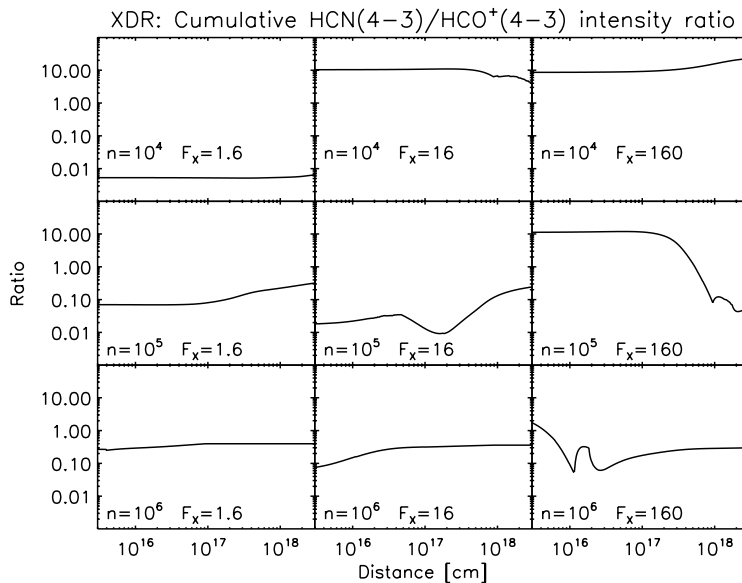


Figure 2.12: $R_{\text{HCN}/\text{HCO}^+}$ based on the XDR ionization model by Meijerink et al. 2007. One can find that $R_{\text{HCN}/\text{HCO}^+}$ exceed unity only at the limited parameter space, which reflects the wider range of ionization rate over which X_{HCO^+} is high as compared to X_{HCN} (see also Figure 2.13).

2.5.1 Steady-state XDR, PDR, and high temperature chemistry

It has been suggested that the enhanced HCN(1–0) intensity observed in AGNs is due to abnormal chemistry realized in XDRs (e.g., Kohno 2005; Krips et al. 2008). The molecular abundances and the resultant *column-integrated* line intensities of our target molecules under steady state gas-phase XDRs and PDRs were extensively modeled by Meijerink & Spaans (2005) and Meijerink et al. (2007). In their XDR models, $R_{\text{HCN}/\text{HCO}^+}$ can exceed unity only at the surface ($N_{\text{H}} \lesssim 10^{22.5} \text{ cm}^{-2}$)³ of low-to-moderate density gas ($n_{\text{H}} \lesssim 10^5 \text{ cm}^{-3}$) exposed to an X-ray emitting source, where a high X-ray flux (e.g., $F_{\text{X}} \gtrsim 10 \text{ erg s}^{-1} \text{ cm}^{-2}$) can be expected (Figure 2.12). However, for a larger N_{H} where F_{X} is attenuated, they predicted $R_{\text{HCN}/\text{HCO}^+} < 1$. This is due to the fact that the range of the ionization rate over which X_{HCO^+} is high is much wider than that of HCN under X-ray ionization chemistry (Lepp & Dalgarno 1996; Figure 2.13). One weak point in this model, on the other hand, would be that the predicted line intensities are considerably low at the surface region of $N_{\text{H}} \lesssim 10^{22.5} \text{ cm}^{-2}$ (Meijerink et al. 2006, 2007), which seems to be inconsistent with the prominent HCN(4–3) and HCO⁺(4–3) emission lines observed in AGNs.

Another possible scenario is a high temperature gas-phase chemistry, under which neutral-neutral reactions with high reaction barriers are enhanced in general (e.g., Harada et al. 2010). This kind of chemistry is thus efficient in, e.g., hot core-like regions and mechanically dominated regions (MDRs). For example, a formation path of $\text{CN} + \text{H}_2 \rightarrow \text{HCN} + \text{H}$, which has a barrier

³ N_{H} includes both atomic and molecular hydrogen here, i.e., $N_{\text{H}} = N_{\text{HI}} + 2 \times N_{\text{H}_2}$.

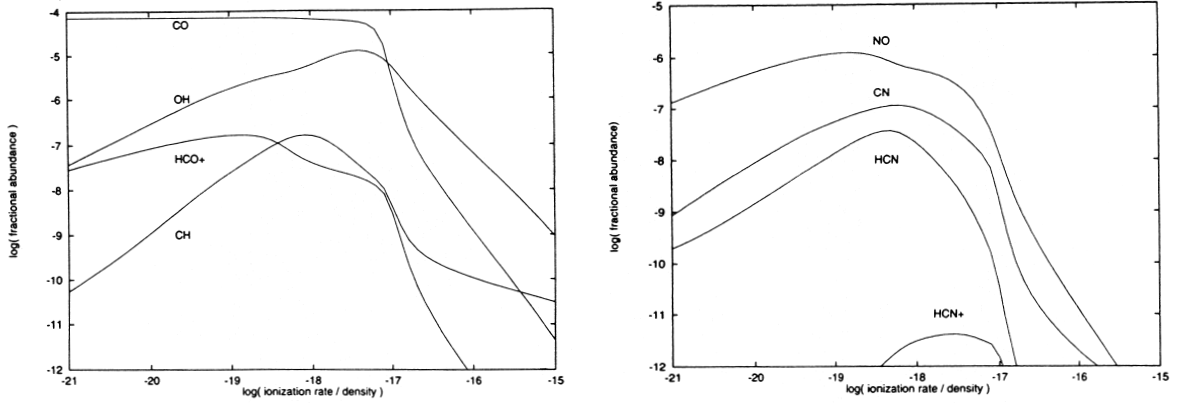


Figure 2.13: The steady state abundances of some molecular species including (*left*) HCO^+ and (*right*) HCN , as a function of the ratio of ionization rate and gas density (Lepp & Dalgarno 1996). One can see that HCO^+ is abundant (e.g., $X_{\text{HCO}^+} \gtrsim 10^{-8}$) over wider range of the x -axis as compared to HCN , which makes $R_{\text{HCN}/\text{HCO}^+} > 1$ difficult as shown in Figure 2.12.

of ~ 960 K (KIDA⁴), can be efficient at $T_{\text{kin}} \gtrsim 300$ K (Harada et al. 2010; Figure 1.21). Indeed, according to KIDA, the rate coefficient of the above HCN -forming reaction is $\sim 2 \times 10^{-12} \text{ cm}^{-3} \text{ s}^{-1}$ at 300 K (we assume $n_{\text{H}_2} = 10^5 \text{ cm}^{-3}$ and $X_{\text{CN}} = 10^{-8}$). On the other hand, rate coefficients of reactions destructing CN (e.g., $\text{CN} + h\nu \rightarrow \text{C} + \text{N}$, $\text{CN} + \text{N} \rightarrow \text{C} + \text{N}_2$) are well below $10^{-13} \text{ cm}^{-3} \text{ s}^{-1}$. Hence, we can expect the rapid formation of HCN from CN in this case.

Such a high temperature ($\gtrsim 300$ K) can likely be expected in AGNs (e.g., Davies et al. 2012; Krips et al. 2008). At that temperature, X_{HCO^+} will be somewhat reduced due to an activated reaction with H_2O to form H_3O^+ (Figure 1.21). Moreover, these chemical reactions can be complemented to conventional X-ray induced ionization models (Harada et al. 2013); we can expect much higher gas temperature in XDRs than in SB environments (PDR), indeed. Interestingly, recent high resolution VLA observations revealed a higher fractional abundance of NH_3 in the very nuclear region of NGC 3079 (type-2 AGN; Miyamoto et al. 2015) than in SB galaxies (Takano et al. 2013, and references therein). NH_3 is also a typical molecule efficiently formed in high temperature environments, which supports our view on the importance of the high temperature chemistry.

Keeping these models in mind, we hereafter present possible interpretation of the $R_{\text{HCN}/\text{HCO}^+}$ in three instructive AGNs and two SB galaxies, namely NGC 7469, NGC 1068, NGC 1097, NGC 253, and M82.

(i) NGC 7469—We first discuss the $R_{\text{HCN}/\text{HCO}^+}$ measured at the AGN position of NGC 7469 (denoted as *N7469 (AGN)* in Figure 2.1), which is comparable to the ratios of some SB galaxies such as NGC 253. No morphological and kinematic signatures of a jet-ISM interaction has been found in the CND of NGC 7469 through the high resolution observations of H_2 and $\text{Br}\gamma$ emission lines (Hicks et al. 2009; Müller-Sánchez et al. 2011) and then mechanical heating might not play an important role in this galaxy, although Lonsdale et al. (2003) found a compact radio

⁴<http://kida.obs.u-bordeaux1.fr>

components at the nucleus, which can be either core jet components or supernova remnants. Regarding the origin of the relatively low $R_{\text{HCN}/\text{HCO}^+}$, Izumi et al. (2015) pointed out the compactness of the XDR. They estimated the spatial extent of the XDR to be ~ 42 pc in radius. Therefore, not a poor but a still relatively large observing beam employed for the NGC 7469 observations (~ 150 pc; Table 2.1) might have picked up line fluxes emanating from the extended SB region, which would have resulted in reducing the $R_{\text{HCN}/\text{HCO}^+}$ of this AGN.

(ii) NGC 1068—The X-ray luminosity of this AGN ($\log L_{2-10\text{keV}} = 43.0$; Marinucci et al. 2012) is quite comparable to that of NGC 7469 ($\log L_{2-10\text{keV}} = 43.2$; Liu et al. 2014). The degree of contamination from PDRs and SNe (i.e., stellar feedback) to the observed line ratio is unclear, although we expect it to be low by considering the moderate stellar age inside the CND (200-300 Myr; Davies et al. 2007). This age is much older than those of SB galaxies in this work, e.g., NGC 253 (~ 6 Myr; Fernández-Ontiveros et al. 2009) and M82 (~ 10 Myr; Förster Schreiber et al. 2003). We found a relatively high $R_{\text{HCN}/\text{HCO}^+}$ of ~ 1.5 at its precise AGN position (denoted as *N1068 (AGN)* in Figure 2.1), which value is well consistent with the results in García-Burillo et al. (2014). The ratio was measured with a single synthesized beam of 35 pc. García-Burillo et al. (2014) also reported a positive correlation between the spatially resolved HCN(4 – 3) to CO(3 – 2) intensity ratio ($\equiv R_{\text{HCN}/\text{CO}}$) and the 6 – 8 keV X-ray flux to CO(3 – 2) intensity ratio ($\equiv R_{\text{X-ray}/\text{CO}}$) across the CND of NGC 1068. The same trend can also be found with HCO⁺(4 – 3), SiO(2 – 1), and CN(2 – 1) (García-Burillo et al. 2010, 2014), which suggests that the whole CND is a giant XDR. However, again according to Meijerink et al. (2007), to reproduce $R_{\text{HCN}/\text{HCO}^+} > 1$ at this AGN position is quite difficult by their XDR ionization models since the N_{H_2} towards the AGN position is as high as $\sim 6 \times 10^{23} \text{ cm}^{-2}$ (Viti et al. 2014), which is inconsistent with the model-required N_{H_2} to yield a high $R_{\text{HCN}/\text{HCO}^+}$ (Meijerink et al. 2007). To interpret the high $R_{\text{HCN}/\text{HCO}^+}$ of *N1068 (AGN)* from the perspective of pure XDR ionization reactions is thus not straightforward. We might have to add some other processes such as high temperature chemistry (Harada et al. 2010, 2013) to forcibly enhance X_{HCN} .

As for the $R_{\text{HCN}/\text{HCO}^+}$ measured at other positions, namely, at the East/West-knots of the CND of NGC 1068 (listed as *N1068 (E-knot)* and *N1068 (W-knot)* in Figure 2.1), we found the ratios are 2 times higher than that at *N1068 (AGN)* as shown in Figure 2.14. This is a bit surprising result *since the ratio increases as receding from the nucleus* (= the X-ray peak). We speculate the cause of this enhancement at the E/W-knots is likely related to that for the prominent 2.12 μm H₂ emission there (e.g., Müller Sánchez et al. 2009). The $R_{\text{HCN}/\text{CO}} - R_{\text{X-ray}/\text{CO}}$ correlation shown above and the very uniform distribution of the H₂ $\lambda 2.25 \mu\text{m}/\lambda 2.12 \mu\text{m}$ ratio across the entire CND (Riffel et al. 2014) seem to support a scenario that these emissions are primarily due to non-directional X-ray heating (see also Galliano et al. 2003). Note that the H₂ line ratio at the CND (~ 0.1) is a typical value for thermal processes by X-ray and/or shock heating (Mouri 1994). In this scenario, we might be observing HCN and HCO⁺ emissions emerged from molecular clouds directly illuminated by X-ray radiation (i.e., clouds directly seen by the AGN itself, not severely intercepted by a dusty torus) at the East/West-knots, considering the geometry of the type-2 nucleus (the position angle of the almost edge-on H₂O maser disk is

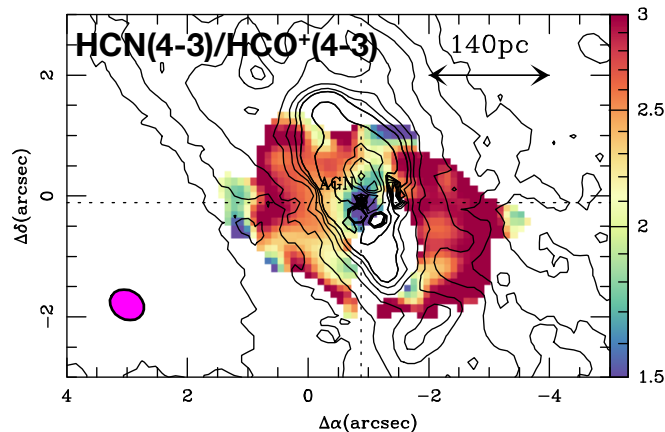


Figure 2.14: The spatial distribution of $R_{\text{HCN}/\text{HCO}^+}$ inside the CND of NGC 1068 (García-Burillo et al. 2014). One can see that the ratio is ~ 1.5 at the AGN position, whereas it increases to ~ 3 at the East- and the West-knot of the CND.

-45° ; Greenhill et al. 1996) and the surrounding CND. In this case, the X-ray fluxes received at the East/West-knots can be quite high because of little attenuation, which will result in an efficient X-ray heating and thus high $X_{\text{HCN}}/X_{\text{HCO}^+}$ due to, e.g., high temperature reactions (Harada et al. 2010, 2013). Indeed, if there is no attenuation, we can expect F_X is as high as $\sim 100 \text{ erg s}^{-1} \text{ cm}^{-2}$ even at 30 pc away from the nucleus. According to the model calculation by Meijerink et al. (2007), this high X-ray flux can heat up the gas with $n_{\text{H}_2} = 10^{5-6} \text{ cm}^{-3}$ to $\gg 100 \text{ K}$.

On the other hand, the radial expansion of the CND of NGC 1068 (Barbosa et al. 2014; Krips et al. 2011). would support the existence of shocks and/or a jet-ISM (and possibly, outflow-ISM) interaction, which can also contribute to excite the H_2 molecule. We especially mention that García-Burillo et al. (2014) suggested that as much as $\sim 50\%$ of $\text{CO}(3-2)$ emission stems from the outflowing component, which extends out to $\sim 400 \text{ pc}$ away from the nucleus. Hence, there is at least a certain portion of a region dominated by mechanical heating (e.g., Kazandjian et al. 2012, 2015; Meijerink et al. 2011) in the CND. Again high gas temperature chemistry would be responsible for the high $R_{\text{HCN}/\text{HCO}^+}$ in this case. Indeed, we can expect the maximum temperature of $n_{\text{H}_2} = 10^5 \text{ cm}^{-3}$ gas should reach as high as $\sim 2500 \text{ K}$ for C-shock when the shock velocity is $> 20 \text{ km s}^{-1}$ (Flower & Pineau des Forêts 2013), which is high enough to produce prominent H_2 emission. Such a high temperature is well beyond the reaction barrier of HCN formation from CN, thus HCN can be abnormally abundant. According to the model calculation of molecular abundances in MDRs by Kazandjian et al. (2012), $X_{\text{HCN}}/X_{\text{HCO}^+}$ can well exceed 100 when the input mechanical energy is $\gtrsim 10^{-18} \text{ erg s}^{-1} \text{ cm}^{-3}$, which is large enough to produce high $R_{\text{HCN}/\text{HCO}^+}$. Interestingly, the $R_{\text{HCN}/\text{CO}}-R_{\text{X-ray}/\text{CO}}$ correlation in NGC 1068 has large scatter at lower $R_{\text{X-ray}/\text{CO}}$, i.e., away from the AGN (García-Burillo et al. 2014), suggesting the importance of other heating mechanisms than X-ray radiation for driving the underlying chemistry. Indeed, the line velocity dispersion is high at the East/West-knots (García-Burillo

et al. 2014), indicating the existence of a strong turbulence. In this scenario, it would also be probable that the outflow/shock velocity is so high at *N1068 (AGN)* that the shock wave provides ionized gas to increase ions (e.g., Dickinson et al. 1980; Elitzur 1983; Koo & Moon 1997; Rawlings et al. 2004), which would potentially result in a depressed $X_{\text{HCN}}/X_{\text{HCO}^+}$ near the nucleus.⁵

(iii) *NGC 1097*—Another remarkable example is the $R_{\text{HCN}/\text{HCO}^+}$ measured at the AGN position of *NGC 1097 (N1097 (AGN))* in Figure 2.1). As we stated in Section 2.4.5, we would need an enhanced $X_{\text{HCN}}/X_{\text{HCO}^+}$ compared to SB galaxies to yield the high $R_{\text{HCN}/\text{HCO}^+}$ when $n_{\text{H}_2} \sim 10^5 \text{ cm}^{-3}$ (Izumi et al. 2013). However, judging from the very low X-ray luminosity ($\log L_{2-10\text{keV}} = 40.8$; Liu et al. 2014), the XDR chemistry seems not to play an important role in *NGC 1097* (Izumi et al. 2013). Radiative feedback from SB activity would be discarded as well considering the high gas temperature ($\gtrsim 100 \text{ K}$) suggested for the molecular phase (Beirão et al. 2012; Izumi et al. 2013). On the other hand, mechanical heating can be another choice, which is supported by the detection of a compact radio jet (largest beam-convolved and projected size is $\sim 90 \text{ pc}$; Thean et al. 2000). A tentative gradient of $\text{HCN}(1-0)/\text{HCO}^+(1-0)$ line ratio inside the CND (lower towards the center, and higher towards the outer edge of the CND; Martín et al. 2015) would also support this scenario, although Martín et al. (2015) did not fully resolve the CND. Note that an inferred SNe rate is quite low as $O(10^{-4}) \text{ yr}^{-1}$ (Davies et al. 2007), thus we can neglect its influence on the chemistry. We also comment that it would be difficult to identify shock-heated dust emission by SED modelling, as it has been said that a dusty torus disappears in a low-luminosity AGN (e.g., Elitzur & Shlosman 2006). We alternatively need to identify direct evidence of shock heating, such as SiO emission line, which is observed in this nucleus (Martín et al. 2015), as well as to model gas properties (n_{H_2} , T_{kin}) through multi-transition non-LTE analysis.

(iv) *NGC 253 and M82*—As for the SB galaxies, the predicted $R_{\text{HCN}/\text{HCO}^+}$ in Meijerink et al. (2007) is higher than the observed values by a factor of a few. This can be explained by an enhanced cosmic ray ionization rate due to frequent supernovae (SNe), which would increase X_{HCO^+} even in a dense molecular cloud (e.g., Aladro et al. 2013; Bayet et al. 2011; Meijerink et al. 2011). The lower $R_{\text{HCN}/\text{HCO}^+}$ in M82 than in *NGC 253* follows this scenario well considering the younger SB phase in *NGC 253* than in M82 (Izumi et al. 2013; Krips et al. 2008), although we might be able to construct some counter arguments (Papadopoulos 2007; Zhang et al. 2014). We mention that mechanical heating seems to be responsible for the relatively high $R_{\text{HCN}/\text{HCO}^+}$ in young SB galaxy *NGC 253* (SB age $\sim 6 \text{ Myr}$; Fernández-Ontiveros et al. 2009), whose ratio is totally comparable to those of *N7469 (AGN)* and *N1068 (AGN)*, as that heating mechanism is claimed to be important there (Rosenberg et al. 2014a).

2.5.2 Effects of metallicity and elemental abundance

The chemistry of PDRs in high metallicity (i.e., $Z \geq Z_{\odot}$ where Z_{\odot} denotes the solar metallicity) environments was modeled by, e.g., Bayet et al. (2012). They showed X_{HCN} increases with

⁵There is a counter argument, i.e., efficiently produced electrons due to shocks would reduce the HCO^+ abundance by recombination (Papadopoulos 2007).

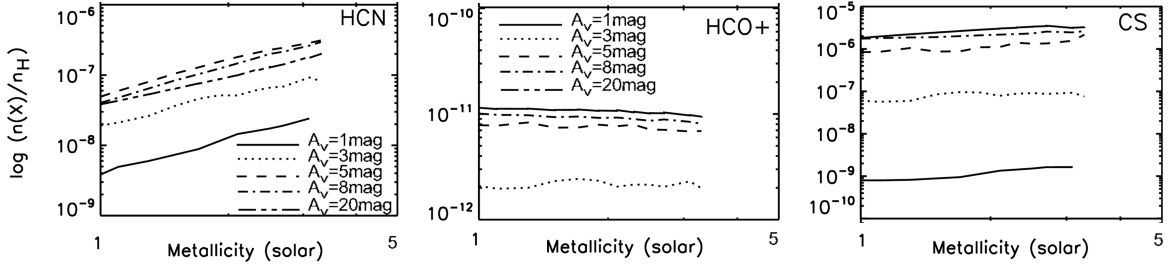


Figure 2.15: Fractional abundances of (*left*) HCN, (*middle*) HCO⁺, and (*right*) CS, with respect to the total number of H atoms, as a function of the gas-phase metallicity (Bayet et al. 2012).

metallicity, whereas X_{HCO^+} and X_{CS} are insensitive to the variation, when FUV radiation field and cosmic ray ionization (mimicking X-ray ionization) rate are fixed (Figure 2.15). From the observational side, Davis et al. (2013) found a positive correlation between gas-phase metallicity and $N_{\text{HCN}}/N_{\text{CS}}$ in the sample of early type galaxies, metal-rich spirals, and SB galaxies, which would support the Bayet et al.’s prediction. However, if we regard $12 + \log [\text{O}/\text{H}]$ as an indicator of the gas phase metallicity, NGC 1068, NGC 1097, NGC 253, and M82 show almost the same value (Galliano et al. 2008, and references therein). Thus, we suggest that the metallicity is not an important factor for the submm-HCN diagram at least when we treat already chemically evolved systems such as the central regions of nearby galaxies studied in this work. We should take this parameter into account when we consider less-evolved systems such as high redshift galaxies. Interestingly, the $R_{\text{HCN}/\text{HCO}^+}$ is \sim a few times smaller in the LMC (SB) than in other massive SB galaxies (Table 2.1). Although this would be partly reconciled by the different gas density in each galaxy, we can also expect that the sub-solar metallicity in the LMC (Hunter et al. 2009) would have decreased $X_{\text{HCN}}/X_{\text{HCO}^+}$.

On the other hand, metal compositions will influence the line ratios: it seems likely that an overabundance of elemental nitrogen observed in AGNs (e.g., Storchi-Bergmann 1991) contributes to the HCN-enhancement, since X_{HCN} depends on the elemental abundance of nitrogen (Bayet et al. 2008).

2.5.3 IR-pumping

This mechanism must be vital for vibrationally excited lines of these dense gas tracers such as HCN($v_2 = 1^1_f$, $J = 4 - 3$), since their energy levels (~ 1000 K) are too high to be collisionally excited. Although the small number of the detections of the vibrationally excited lines from extragalactic objects (Aalto et al. 2015a; Imanishi & Nakanishi 2013a; Imanishi et al. 2016; Sakamoto et al. 2010) limit our discussion on this topic, it would be at least influencing the rotational population and thus the line intensity of HCN in NGC 4418 (Sakamoto et al. 2010). Meanwhile, HCN($v_2 = 1^1_f$, $J = 4 - 3$) emission was not detected in NGC 7469 (Izumi et al. 2015) in spite of its high IR luminosity of $L_{8-1000\mu\text{m}} = 10^{11.4} L_{\odot}$, which is comparable to that of NGC 4418 (Sanders et al. 2003). This would be due to the optical depth effect; we can not

detect a fully optically thin emission even if it is surely existing. The column density of $\text{HCN}(v_2 = 1^1_f, J = 4 - 3)$ would not be so large along the line of sight towards the CND of NGC 7469 that the emission is optically thin. We speculate that the vibrationally excited lines can only be visible in compact (i.e., close to a warm IR-source), heavily obscured (i.e., high column density) nuclei such as in NGC 4418, where we can expect $\text{HCN}(v_2 = 1^1_f, J = 4 - 3)$ line emission is (moderately) optically thick. Moreover, Imanishi et al. (2016) suggested that, even taking the IR-pumping into account, an enhanced $X_{\text{HCN}}/X_{\text{HCO}^+}$ is eventually required to reproduce a high $\text{HCN}(J = 3 - 2)$ to $\text{HCO}^+(J = 3 - 2)$ line ratio in (buried-AGN of) IRAS 20551-4250.

2.5.4 Time-dependent chemistry

This can be important since the $X_{\text{HCN}}/X_{\text{HCO}^+}$ is predicted to be highly time-dependent with possible variations of orders of magnitude (e.g., Meijerink et al. 2013). The time-evolution is typically studied via time clock molecules such as sulfur bearing species. Indeed, while $N_{\text{CS}}/N_{\text{SO}}$ in the CNDs of NGC 1097 and NGC 1068 estimated in LTE analysis are ~ 2 -3 (Martín et al. 2015; Nakajima et al. 2015), it is only ~ 0.2 in the Orion hot core (Table 2 in Esplugues et al. 2014). If we assume that the above CNDs are influenced by mechanical heating, and the abundances of these species in NGC 1097 and NGC 1068 depend on the evolution of hot core-like systems, this result indicates that NGC 1097 and NGC 1068 are more time-evolved systems than the Orion hot core (e.g., Charnley 1997; Esplugues et al. 2014).

At this point, we should mention that, according to the CND-scale modelings of the molecular composition under the high temperature conditions by Harada et al. (2013), $X_{\text{HCN}}/X_{\text{HCO}^+}$ would not be so high once the chemically steady state is achieved (Figure 2.16). However, we guess that the shock induced by AGN jet/outflow will circumvent this problem, as it will be a dissociative one, i.e., it will initialize the physical/chemical conditions of the system and thus the chemically-steady state will not be achieved. Indeed, $X_{\text{HCN}}/X_{\text{HCO}^+}$ predicted for the CND at the shock-crossing time (or dissipation time scale of shock waves that will reset molecular physical/chemical conditions; $\sim 10^5$ yr) can be as high as ~ 100 (Harada et al. 2013; Figure 2.17). Future sensitive and systematic study of time clock species as well as shock-related species (e.g., SiO) will help us understand the chemical evolution in AGNs.

2.6 Conclusions of This Chapter

The submm-HCN diagram was up-dated to construct a robust energy diagnostic method that is especially useful to identify dust-obscured activities (AGN and SB). We also invested the possible origins of the enhanced $\text{HCN}(4 - 3)$ intensity with respect to $\text{HCO}^+(4 - 3)$ and $\text{CS}(7 - 6)$ in AGNs (i.e., HCN-enhancement). The achieved outcomes are then as follows:

- Compiling data from the literature and the ALMA archive, the submm-HCN diagram is presented (Figures 2.1 and 2.2). As was supposed by Izumi et al. (2013), we found a trend that AGNs tend to show higher $R_{\text{HCN}/\text{HCO}^+}$ and/or $R_{\text{HCN}/\text{CS}}$ than SB galaxies especially when these samples are observed at high resolutions enough to separate regions

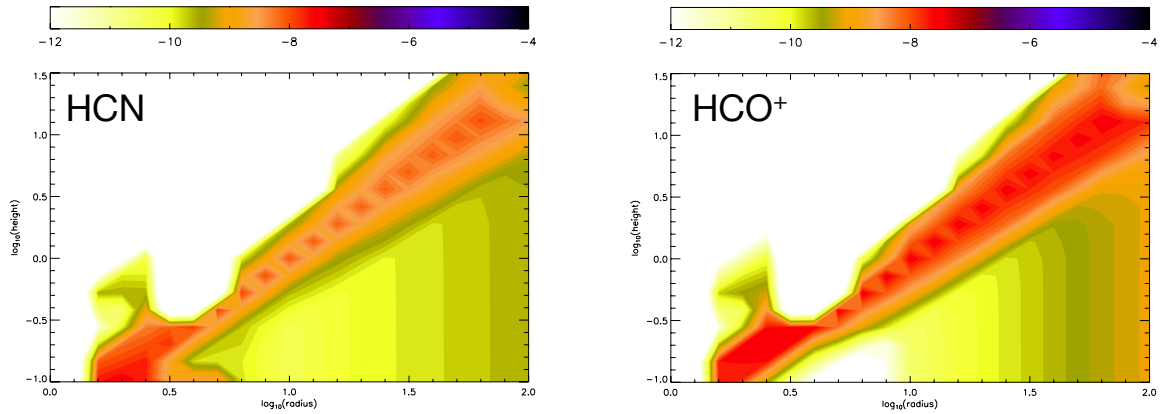


Figure 2.16: Radial and height dependence of the fractional abundances of (*left*) HCN and (*right*) HCO^+ at the steady state, expected under the high temperature chemistry (Harada et al. 2013). An AGN is located at the bottom-left corner. Both species are abundant at the surface layer of the disk exposed to the AGN radiation.

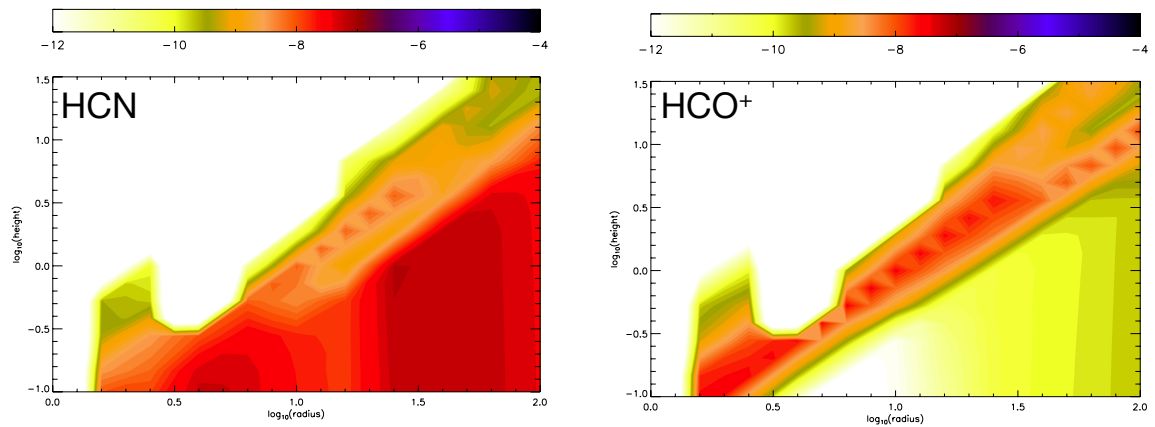


Figure 2.17: Same as Figure 2.17, but at the shock-crossing time (Harada et al. 2013).

energetically dominated by AGNs (e.g., XDR and/or MDR) from those contaminated by co-existing SB activities (e.g., circumnuclear SB ring). When AGNs are observed at low resolutions ($\gtrsim 1$ kpc), the energetics within the beam seems to be dominated by surrounding SB activities, which would result in reduced line ratios.

- Simple non-LTE radiative transfer modelings involving both collisional and radiative excitation were conducted with the RADEX code. Under the constant density of $n_{\text{H}_2} = 10^5 \text{ cm}^{-3}$, we found $R_{\text{HCN}/\text{HCO}^+}$ is not so sensitive to excitation, whereas $R_{\text{HCN}/\text{CS}}$ strongly depends on it, especially when CS(7 – 6) is optically thin and HCN(4 – 3) is thick.
- From the above non-LTE modelings, we suggest that both $X_{\text{HCN}}/X_{\text{HCO}^+}$ and $X_{\text{HCN}}/X_{\text{CS}}$ would be significantly enhanced in AGNs by several to even $\gtrsim 10$ times than those in SB galaxies, to reproduce their line ratios. From this perspective, we suggest that the variation of molecular abundances would drive the HCN-enhancement in AGNs.
- On the other hand, we could not fully discard the possibility that the systematically higher gas density in AGNs than in SB galaxies is the cause of the HCN-enhancement, which was revealed by modifying n_{H_2} to a higher value (here $5 \times 10^6 \text{ cm}^{-3}$), although the existence of such a systematic difference is unclear within the central ~ 100 pc regions of galaxies.
- We also investigated HCN/HCO⁺ and HCN/CS line ratios at other transitions based on our RADEX models. As a result, we found enhanced $X_{\text{HCN}}/X_{\text{HCO}^+}$ and $X_{\text{HCN}}/X_{\text{CS}}$ subsequently result in high line ratios at any transition, that seems to be consistent with observations.
- Various possible chemical scenarios for the high $X_{\text{HCN}}/X_{\text{HCO}^+}$ in AGNs are discussed. Although it is still far from being well understood, we suppose it would be difficult to explain the high line ratios in AGNs solely by conventional X-ray ionization models. We suggest that some additional mechanisms, e.g., high temperature chemistry (likely related to mechanical heating), seem to be necessary to fully explain the observations.

We preferred the scenario of enhanced HCN abundance with respect to those of HCO⁺ and CS, rather than a systematically higher gas density in AGNs than in SB galaxies (Section 2.4). However, the latter scenario was not fully discarded because of the simplified modelings in this work. Indeed, the observed line ratios can be obtained by using some sets of physical and chemical conditions. To disentangle these, we have to conduct multi-line, multi-species non-LTE modelings for both AGNs and SB galaxies, with sufficiently high resolution data to spatially resolve their CNDs, as was recently conducted by Viti et al. (2014). Moreover, as presented in Section 2.5, there are still various competing chemical interpretations for the HCN-enhancement. Higher resolution observations of not only typical and relatively bright dense molecular gas tracers (e.g., HCN, HCO⁺, HNC, and CS), but also rarer species which are more susceptible to the variation of the underlying chemistry (e.g., NH₃, CH₃CN, HNCO, CH₃OH, and SiO) will be inevitable to test them.

Chapter 3

Non-detection of Another Extinction-Free Proxy of Active Nuclei, Submillimeter Hydrogen Recombination Lines

Part of this Chapter has been published as Izumi et al. 2016, MNRAS, 459, 3629.

In this Chapter, we discuss the general detectability of submm-RL from AGNs with a simple theoretical calculation. We will compare our prediction with the results of our ALMA Cycle 2 observations of the submm-RL, H26 α ($\nu_{\text{rest}} = 353.62$ GHz), towards the center of NGC 1068 ($D = 14.4$ Mpc; Tully 1988). This galaxy is well known to host a type 2 (and Compton-thick with $N_{\text{H}} \sim 10^{25}$ cm $^{-2}$; e.g., Marinucci et al. 2016) AGN, thus is one of the best targets to demonstrate the capability of submm-RLs to probe dust-obscured nuclei. Note that several attempts have been done so far towards this AGN to detect broad HI RLs: Lutz et al. (2000) observed Br β 2.63 μm and Pf α 7.46 μm emission but could not detect broad lines likely due to severe dust extinction. No significant emission of H40 α ($\nu_{\text{rest}} = 99.02$ GHz) and H53 α ($\nu_{\text{rest}} = 42.95$ GHz) lines were detected with single dish measurements as well at least partly due to insufficient sensitivity (Puxley et al. 1991).

3.1 Detectability of Broad Submm-RLs

Although the electron volume density (N_e) and line optical depths will be extremely large in BLRs compared to those in typical HII regions (Peterson 1997), previous studies support a fairly good resemblance between the observed line flux ratios and the theoretical values under the Case-B condition (see Netzer 1990 and references therein). Therefore, we adopted the model-calculated parameters of HI RLs under the Case-B condition by Storey & Hummer (1995) as our best estimate. Their values were used in Scoville & Murchikova (2013) as well for the cases of N_e

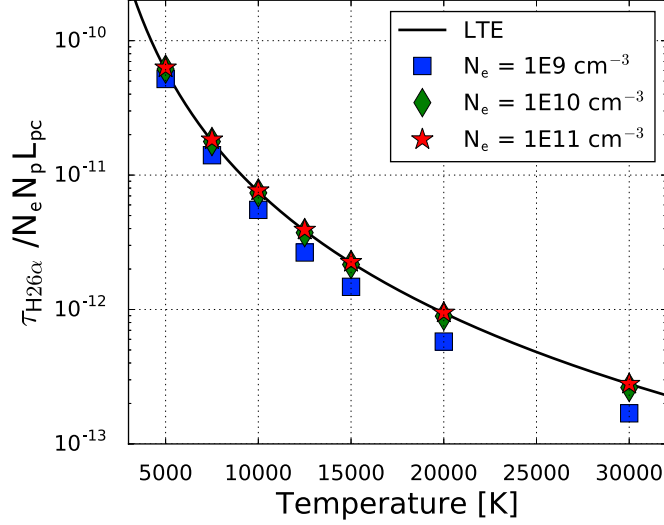


Figure 3.1: The optical depth of H26 α per unit EM, $\Omega_{\text{H26}\alpha}$, defined in Equation (3.1), for electron temperature (T_e) = 5000–30000 K. Three cases of electron density, $N_e = 10^9$, 10^{10} , and 10^{11} cm^{-3} (typical values expected for BLRs; Peterson 1997), as well as the LTE solution are plotted. No significant difference is found among these values. The line center optical depth can be achieved by multiplying this value by the EM = $\int N_e N_p dL = N_e N_p L_{\text{pc}}$, where L_{pc} is the line-of-sight path length in the unit of parsec.

$\leq 10^8 \text{ cm}^{-3}$: we expand their theoretical basis towards higher N_e in this work. We investigate several cases of gas density and temperature as BLRs likely to have clouds with various physical conditions. We will mainly speculate upon the detectability of *submm* recombination lines, especially H26 α line, as a demonstrative purpose. We will not take millimeter lines into account as they usually suffer maser amplification. Note that we use N to express the volume density to avoid confusion with the principal quantum number n .

At the high densities suggested in BLRs ($N_e \gtrsim 10^8 \text{ cm}^{-3}$), one can expect level populations are in the local thermal equilibrium (LTE) for large n . Indeed, the departure coefficient from the LTE (b_n) clearly shows ~ 1 at $N_e \gtrsim 10^8 \text{ cm}^{-3}$ for $n \gtrsim 20$ ($\lambda \gtrsim$ submillimeter), i.e., no departure from the LTE (collisional process). Fig. 3.1 shows the optical depth parameter $\Omega_{n,n'}$ of H26 α calculated by Storey & Hummer (1995) as a function of N_e and electron temperature (T_e), which is related to the line center optical depth of the $n \rightarrow n'$ transition as

$$\tau_{n,n'} = N_e N_p \Omega_{n,n'} L, \quad (3.1)$$

where L is the line-of-sight path length. Thus, the $\Omega_{n,n'}$ gives the optical depth per unit emission measure (EM), which is defined as

$$\text{EM} = \int N_e N_p dL. \quad (3.2)$$

N_p is the proton volume density. The thermal Doppler width ($\sim 21.5 \text{ km s}^{-1}$ at $T_e = 10^4 \text{ K}$ for H I) is assumed in Fig. 3.1 as we would like to primarily treat a single cloud existing in BLRs. Although this width shall be regarded as just the first-order approximation (e.g., Dietrich et al. 1999; Peterson 1997), we suppose that a line width up to \sim a few 100 km s^{-1} would not alter our conclusions drastically. Note that $\tau_{n,n'}$ is almost inversely proportional to the line width.

As is expected from the quasi-LTE condition, we can see from Fig. 3.1 that the line optical depth is approaching to the following LTE solution under the ionization equilibrium:

$$\tau_{\text{line,LTE}} = 2.7 \times 10^3 \times \left(\frac{T_e}{\text{K}}\right)^{-3} \times \left(\frac{\text{EM}}{\text{cm}^{-6} \text{ pc}}\right) \times \left(\frac{\nu}{\text{GHz}}\right)^{-1}. \quad (3.3)$$

Hence, we will discuss under the LTE condition hereafter. Substituting typical values supposed for BLRs (e.g., Dietrich et al. 1999; Ferland et al. 1992; Osterbrock & Ferland 2006; Peterson 1997), namely, $N_e = N_p = 10^9 \text{ cm}^{-3}$, $T_e = 10^4 \text{ K}$, and $L = 20 \text{ r}_\odot = 4.5 \times 10^{-7} \text{ pc}$ (the path length of a single cloud; radius is thus 10 r_\odot in this case), we obtain an optical depth of H26 α as $\tau_{\text{H26}\alpha} \sim 3.4$, i.e., the line emission is (moderately) optically thick in this case. This, reflecting the quite high EM in BLRs adopted here, is a striking difference from the cases in H II regions, where the submm-RLs are always optically thin.

On the other hand, in the thermal plasma with $T_e \sim 10^4 \text{ K}$, the thermally averaged Gaunt factor (Lang 1980) is,

$$\bar{g}_{\text{ff}} = \frac{\sqrt{3}}{\pi} \left[\ln \frac{(2k_B T_e)^{3/2}}{4.23\pi e^2 \nu m_p^{1/2}} \right] = 0.55 \left[17.7 + \ln \left(\frac{T_e^{3/2}}{\nu} \right) \right]. \quad (3.4)$$

With this formula, an optical depth of the free–free emission is

$$\tau_{\text{ff}} = 0.082 \times \left(\frac{T_e}{\text{K}}\right)^{-1.35} \times \left(\frac{\nu}{\text{GHz}}\right)^{-2.1} \times \left(\frac{\text{EM}}{\text{cm}^{-6} \text{ pc}}\right). \quad (3.5)$$

Substituting the above-adopted parameters, we obtain $\tau_{\text{ff}} \sim 0.65$ at 350 GHz for the BLR emission, i.e., thermal free–free emission is moderately optically thin. Therefore, we can expect a relatively high peak line flux to continuum flux ratio,

$$R_{\text{lc}} \equiv \frac{T_e(1 - e^{-(\tau_{\text{line}} + \tau_{\text{ff}})})}{T_e(1 - e^{-\tau_{\text{ff}}})} - 1 \quad (3.6)$$

of ~ 1.0 in this case. We used the formalism by, e.g., Bell & Seaquist (1978), for this estimation. A stimulated emission due to the background *non-thermal* radiation (i.e., synchrotron) is neglected for simplicity. The high $R_{\text{lc}} > 0$ seems to open a way to detect the broad submm-RL, if clouds with $N_e \sim 10^9 \text{ cm}^{-3}$ are the dominant contributor to the BLR flux at submillimeter. Moreover, as both $\tau_{\text{H26}\alpha}$ and τ_{ff} are functions of T_e and EM, we can estimate one parameter when the other is known independently. *However, that situation is disfavoured in an actual observational sense as discussed hereafter.*

We then estimate the peak flux density of H26 α line to the observer ($F_{\text{H26}\alpha,\text{obs}}$). Under the

conditions described above, the (continuum-subtracted) peak brightness temperature of H26 α line is ~ 5000 K. Suppose that a single blackbody cloud (radius = $10 r_{\odot}$) is radiating at this temperature, an expected peak flux density from the cloud is 1.48×10^{-14} Jy for the case of NGC 1068 ($D = 14.4$ Mpc). As we have assumed that a single cloud has the thermal width of 21.5 km s^{-1} , an expected integrated intensity under the Gaussian line profile is then $S_{\text{H26}\alpha, \text{cl}} = 3.38 \times 10^{-13} \text{ Jy km s}^{-1}$. This value will be multiplied by a number of BLR clouds contributing to the observed flux to estimate $F_{\text{H26}\alpha, \text{obs}}$.

To do so, we first estimate the effective source size of the line-emitting region in the BLR. Reverberation mapping observations towards type 1 AGNs revealed that the innermost radius of a dusty torus, $r_{\text{in, dust}}$, is proportional to the square root of the AGN luminosity (e.g., Suganuma et al. 2006). To estimate the $r_{\text{in, dust}}$ of NGC 1068, we first used [OIV] luminosity, which is considered to be an isotropic proxy of the AGN power (e.g., Diamond-Stanic et al. 2009), thus is more likely to be applicable to type-2 AGNs. Using the compiled data in Diamond-Stanic et al. (2009), we find that $r_{\text{in, dust}}$ of NGC 1068 would be ~ 1.5 times larger than that of the type 1 Seyfert NGC 7469. These AGNs have comparable (absorption corrected) X-ray luminosities (Liu et al. 2014; Marinucci et al. 2016), which supports the view that they have accretion disks with a similar condition. As the reverberation mapping by Koshida et al. (2014) revealed that $r_{\text{in, dust}}$ of NGC 7469 is ~ 100 light-days, we deduce that of NGC 1068 would be ~ 150 light-days (0.13 pc).

For optically thick emission, an area-covering factor (f_a), rather than a volume-filling factor, is important to estimate the effective source size and line fluxes. So far, simple speculation on the equivalent width of Ly α yields $f_a \sim 0.1$ in BLRs (Peterson 1997). Therefore, the total H26 α flux expected for NGC 1068 can be,

$$S_{\text{H26}\alpha, \text{cl}} \times \frac{f_a \pi r_{\text{in, dust}}^2}{\pi (10 r_{\odot})^2} \sim 0.011 \text{ Jy km s}^{-1}. \quad (3.7)$$

This value can be an upper limit as we do not take into account an overlap of clouds in the velocity space. On the other hand, we will achieve a 1σ sensitivity¹ of $\sim 5 \mu\text{Jy}$ even with 100 days on-source integration at a velocity resolution of 100 km s^{-1} . Therefore, it is virtually impossible to achieve a high sensitivity enough to detect the above flux significantly (e.g., 10σ detection) even with ALMA, as the expected peak flux density is \sim a few – $10 \mu\text{Jy}$.

When the electron density is higher ($N_e \gtrsim 10^{10} \text{ cm}^{-3}$), the situation becomes essentially different since both the H26 α line and the underlying free–free continuum emissions are now optically thick. In this case, $R_{\text{lc}} \sim 0$ is realized, whereas the continuum emission is maximally emitted as the blackbody (full thermal equilibrium). Hence, again one can never detect the line component from such extremely high-density clouds. For clouds with the low-end N_e expected for BLRs ($\sim 10^8 \text{ cm}^{-3}$), where both the H26 α line and the free–free emissions are optically thin, we find that $R_{\text{lc}} \sim 5$. However, the low line optical depth ($\tau_{\text{H26}\alpha} = 0.03$) leads the emission to be totally transparent, which cannot be detected at all.

¹<https://almascience.nrao.edu/proposing/sensitivity-calculator>

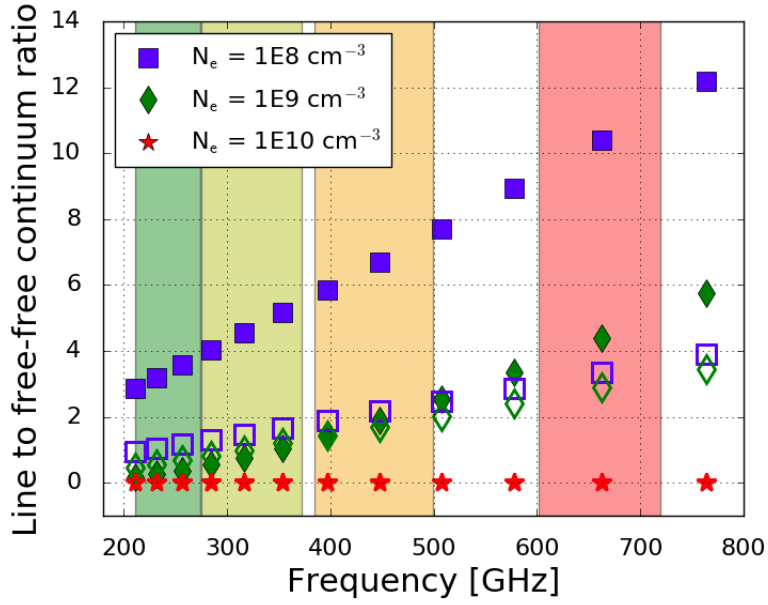


Figure 3.2: Expected line to free–free continuum ratios as a function of frequency. Three different cases of N_e are displayed for twelve submm-RLs (H31 α to H20 α), i.e., $N_e = 10^8$ (blue-square), 10^9 (green-diamond), and 10^{10} (red-star) cm^{-3} . The filled and open symbols indicate that $T_e = 10^4$ K and 2×10^4 K, respectively. As we fixed $L = 20 r_\odot$ in this calculation, $N_e = 10^9 \text{ cm}^{-3}$ corresponds to $EM = 4.5 \times 10^{11} \text{ cm}^{-6} \text{ pc}$. The shaded regions denote the frequency coverages of the ALMA bands, from Band 6 (green) to Band 9 (red).

Under the LTE condition, we expand the above speculations to other submm-RLs that are observable with ALMA (redshift = 0 is assumed here). The resultant R_{lc} of H31 α to H20 α , as well as the frequency coverages of the ALMA Bands 6 to 9 are shown in Fig. 3.2. Lower frequency lines (e.g., H40 α) are not displayed since their R_{lc} approach to ~ 0 even for $N_e \gtrsim 10^9 \text{ cm}^{-3}$ due to large optical depths. We varied N_e and T_e , whereas L is fixed to $20 r_\odot$. Thus, $N_e = 10^9 \text{ cm}^{-3}$ corresponds to $EM = 4.5 \times 10^{11} \text{ cm}^{-6} \text{ pc}$. As already explained, one can see that $R_{lc} > 0$ for $N_e = 10^8 \text{ cm}^{-3}$ and 10^9 cm^{-3} but $R_{lc} \sim 0$ for $N_e = 10^{10} \text{ cm}^{-3}$ (or higher), for these submm-RLs. We note, however, that submm-RLs from $N_e = 10^8 \text{ cm}^{-3}$ clouds are totally optically thin and are hard to be detectable. Therefore, BLR clouds with $N_e \sim 10^9 \text{ cm}^{-3}$ should be the dominant contributor to the H $n\alpha$ flux ($n \gtrsim 20$). Even so, however, we again find that the line fluxes of any H $n\alpha$ are intrinsically as extremely faint as calculated above, for virtually all imaginable sets of physical parameters in BLRs. *Hence, we suppose that it is very impractical to detect submm-RLs of the BLR-origin even with ALMA.*

At centimeter wavelengths, on the other hand, one would expect to see BLR lines as absorption against bright synchrotron emission with $T_B \gg 10^4 \text{ K}$, if a synchrotron source (e.g., jet core) is embedded in the BLR, which is an analogous to the observations of HI absorption line at 21 cm (e.g., Momjian et al. 2003). This detection requires a quite high resolution (e.g., sub-pc scale) because otherwise the surrounding jet component would contaminate the continuum level. While Very Long Baseline Interferometry systems seem to have this capability ($n \gtrsim 90$ RLs shall be observed), their narrow bandwidths are eventually problematic in actual observations of broad lines. Moreover, if the synchrotron emission of an AGN has an electron-scattered nature as suggested by Krips et al. (2011) for NGC 1068, the absorption feature would be outshone by that scattered light. Therefore, it would be quite difficult to detect the BLR components at centimeter bands.

3.2 Comparison with the Actual Data

Then, we roughly compare our prediction described in Section 3.1 with the actual observational data of NGC 1068. The H26 α line of NGC 1068 was circumstantially observed with ALMA on 2015 June 15 with 37 antennas as a part of our Cycle 2 science program (ID = 2013.1.00188.S, PI: M. Imanishi). The baseline length spans from 21.4 to 783.5 m, which corresponds to the uv range of 25.0 to 914.2 k λ at 350 GHz. The nuclear region of NGC 1068² was entirely covered with a single pointing with an 18'' field of view. The receiver was tuned to cover the redshifted HNC(4 – 3) line ($\nu_{\text{rest}} = 362.63 \text{ GHz}$) in the upper side band (USB), and the redder side of H26 α line ($\nu_{\text{rest}} = 353.62 \text{ GHz}$) relative to the systemic velocity ($V_{\text{sys}} = 1137 \text{ km s}^{-1}$; Huchra et al. 1999) in the lower side band (LSB). Each of four spectral windows (Spw 0, 1 = USB and Spw 2, 3 = LSB) has a bandwidth of 1.875 GHz, which yields $\sim 7.5 \text{ GHz}$ width in total. Note that we could not cover the entire velocity range of the hypothesized broad H26 α line because the LSB has only $\sim 3180 \text{ km s}^{-1}$ width in total for it. Actually, this observation was not tuned

²The location of the AGN is set to ($\alpha_{J2000.0}, \delta_{J2000.0} = 02^{\text{h}}42^{\text{m}}40^{\text{s}}710, -00^{\circ}00'47''938$), which is defined by the high-resolution interferometric observations at 6 cm (e.g., Gallimore et al. 2004).

ideally to detect H26 α as this program was intended to cover HCN(4 – 3), HCO⁺(4 – 3), and HNC(4 – 3) of this galaxy.

The velocity spacing of the LSB was originally 0.42 km s⁻¹ per channel, but 120 channels were binned to improve the signal-to-noise ratio, which resulted in the final velocity resolution of $dV \sim 50$ km s⁻¹. This is high enough to resolve the hypothesized broad line component, which has a full width at zero intensity (FWZI) of ~ 7500 km s⁻¹ as seen in the polarized spectrum of H β (Antonucci & Miller 1985). It is also enough to moderately resolve the typical width of NLR-lines of NGC 1068 (~ 500 km s⁻¹; Müller-Sánchez et al. 2011). The bandpass, phase, and flux were calibrated with J0224+0659, J0239+0416, and Ceres, respectively. The total on-source time was ~ 35 min.

The reduction, calibration, and subsequent analysis were conducted with CASA version 4.3 (McMullin et al. 2007) in standard manners. All images were reconstructed by the CASA task CLEAN. Continuum subtraction can be problematic in the LSB because all channels could contain the BLR component considering the limited band width. Therefore, we show the spectrum of the LSB without continuum subtraction in this work. The information on the continuum emission is extracted from the USB instead. The full width at the half-maximum (FWHM) of the achieved synthesized beam was $\theta_{\text{maj}} \times \theta_{\text{min}} = 0''.37 \times 0''.31$, which corresponds to 26 pc \times 22 pc at the distance of NGC 1068. The 1σ sensitivity is 0.42 mJy beam⁻¹ at $dV = 50$ km s⁻¹ for the LSB (estimated from the areas free from emission), whereas $1\sigma = 0.19$ mJy beam⁻¹ for the USB continuum emission, which is surely free from the contamination of the broad H26 α line.

3.3 Results

Fig. 3.3 shows the spatial distribution of the USB continuum emission centred at $\nu_{\text{rest}} = 364$ GHz towards the nuclear region of NGC 1068. This distribution is well consistent with that of the 349 GHz (García-Burillo et al. 2014). The emission is clearly detected and peaks at the precise AGN position (11.72 mJy beam⁻¹), which suggests this is of AGN origin. Fig. 3.4 displays the LSB spectrum extracted at the AGN position with a single aperture. The plotted velocity range (adjusted for the ν_{rest} of H26 α line) corresponds to almost the redder half of the FWZI of the polarized broad H β (Antonucci & Miller 1985).

In order to estimate the line flux, we try to determine the continuum level at the LSB using that at the USB. To date, three models have been mainly proposed to explain the centimeter to submillimeter nuclear SED of NGC 1068 (Krips et al. 2011 and references therein; see also Figure ??): (i) pure synchrotron model, (ii) thermal free–free model³, and (iii) electron-scattered synchrotron model. These models consider a significant contribution from the thermal dust emission as well. Among them, previous observations supported the models (ii) and (iii) equally (e.g., García-Burillo et al. 2014; Krips et al. 2011), but disfavoured the model (i). However, we find that even these preferred two models overestimate our USB continuum level by ~ 2 times,

³The origin of this free–free emission was modelled (Hönig et al. 2008) to have a modest electron density (8×10^5 cm⁻³) and a very high temperature (1.3×10^6 K). Hence, we guess that the dominant origin would not be the BLR clouds.

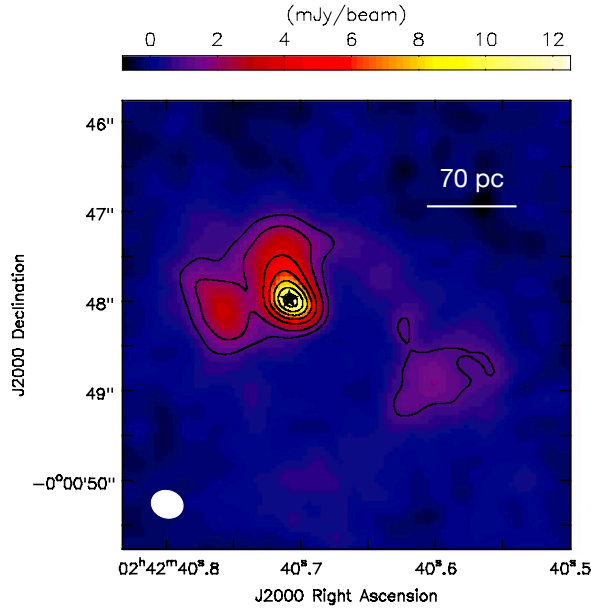


Figure 3.3: The USB continuum emission of the central region of NGC 1068 centred at $\nu_{\text{rest}} = 364$ GHz. The white ellipse denotes the synthesized beam of $0''.37 \times 0''.31$ ($1'' = 70$ pc) with P.A. = $73^\circ 64$. The contour indicates 5, 10, 20, . . . , and 60σ , where $1\sigma = 0.19$ mJy beam $^{-1}$. The flux density at the AGN position (central star; Gallimore et al. 2004) is 11.72 mJy beam $^{-1}$.

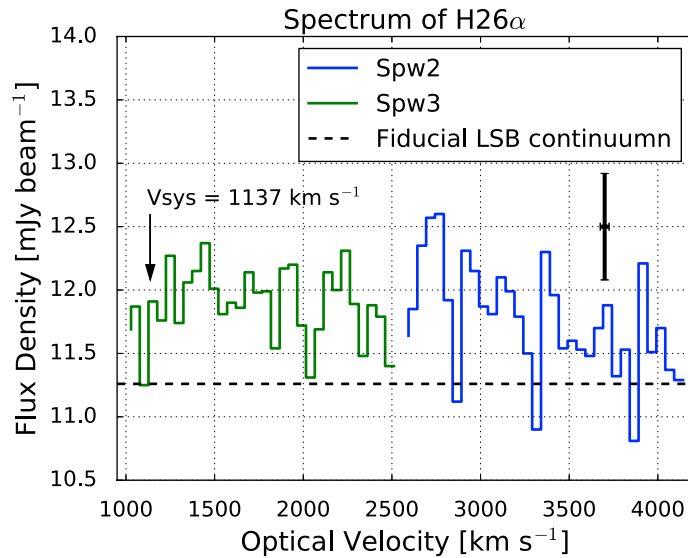


Figure 3.4: The LSB spectrum ($\nu_{\text{rest}} = 350.08 - 353.85$ GHz) extracted at the AGN position of NGC 1068. This frequency range must contain the H26 α emission from the BLR. The vertical solid line shows the $\pm 1\sigma$ sensitivity (0.42 mJy) at the velocity resolution of 50 km s $^{-1}$. The label of the x -axis is expressed as the LSR velocity of H26 α in the optical convention. The systemic velocity of NGC 1068 is indicated by the arrow, whereas the horizontal dashed line denotes our fiducial estimate of the LSB continuum level (11.26 mJy; see the text for details).

judging from their proposed (best-fit) formulations. The lack of high-resolution photometry at FIR, as well as different apertures used in previous works, altogether make the accurate SED modelling quite difficult. A highly time variable nature of AGN-originated emission even at millimeter to submillimeter (e.g., Baldi et al. 2015) also hinders such a challenge.

We then simply give a crude estimate on the LSB continuum level by assuming that the USB continuum emission is composed of (1) thermal dust emission from both the dusty torus and the extended cold dust (50 per cent contribution to the total USB emission), (2) thermal free–free emission from both the BLR and the NLR (25 per cent), and (3) synchrotron emission from the jet (25 per cent). Indeed, García-Burillo et al. (2014) suggested that ~ 50 per cent continuum at the ALMA Band 7 stems from non-dust components. Assuming typical slopes (α) of the flux scaling ($flux \propto \nu^\alpha$) that are 3.5, -0.15 , -1.0 for the above three components, respectively (e.g., Draine 2011), we estimate the LSB continuum level to be $11.26 \text{ mJy beam}^{-1}$. Note that varying the relative contributions of the free–free and synchrotron emissions only slightly modifies this estimation, which does not influence our arguments. Moreover, the free-free continuum levels at the USB and the LSB are almost identical irrespective of its contribution to the total continuum flux and its spectral index.

Back to Fig. 3.4 with keeping this fiducial continuum level in mind, one would see that there seems to be some excess in the flux over a wide velocity range, which can be the broad H26 α emission line. However, this excess in each channel is still below the 3σ limit of our observations ($1.26 \text{ mJy beam}^{-1}$). Moreover, the amount of the excess strongly depends on the actual continuum level, which is hard to determine at this moment. Considering this situation, we regard this marginal excess at the LSB as *non-detection*. Although this view is not conclusive, we summarize our current estimates in Table 3.1. From this Table, one can see that, although it can be modified with other sets of parameters, our prediction is consistent with this non-detection of the broad H26 α line, which is primarily due to the limited sensitivity of ALMA.

We also mention that the above argument can be applied for the non-detection of the H26 α line of the NLR-origin. Suppose that the ionized gas with NLR-like parameters (e.g., $T_e = 10^4$ K, $N_e = N_p = 10^4 \text{ cm}^{-3}$) is filling a spherical volume within our observing beam (~ 24 pc in radius), Equations (11), (13), and (17) of Scoville & Murchikova (2013) yields an integrated H26 α intensity to be $\sim 135 \text{ Jy km s}^{-1}$. This is > 200 times larger than our 3σ detection limit of $\sim 0.67 \text{ Jy km s}^{-1}$ (500 km s^{-1} FWHM is assumed; Müller-Sánchez et al. 2011). Considering that submm-RLs of NLR-origin are likely to be optically thin (Scoville & Murchikova 2013), this discrepancy can be largely attributed to a small volume-filling factor of ionizing clouds. Conversely, from our observations, that factor can thus be constrained to be $< 5 \times 10^{-3}$, which is consistent with the canonical value for NLRs, $< 10^{-2}$ (Peterson 1997).

3.4 Conclusions of This Chapter

As it manifests the existence of dust-obscured AGNs straightforwardly, we tried to examine the detectability of submillimeter HI recombination lines (submm-RLs) stemming from the broad line region (BLR) of AGNs. From this perspective, our key results can be summarized as follows:

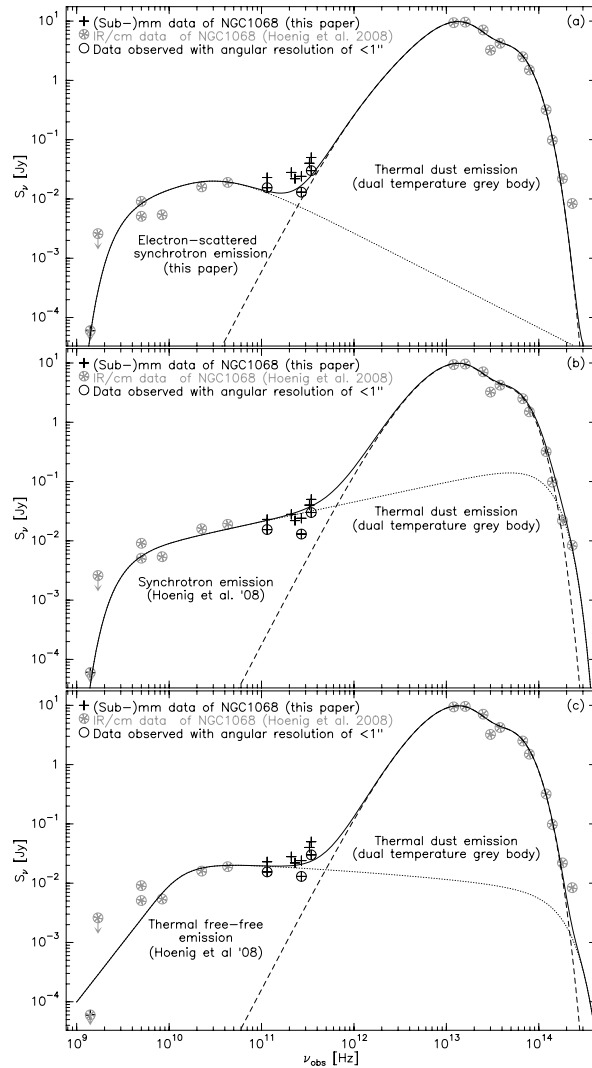


Figure 3.5: Radio SED of the nuclear continuum emission of NGC 1068 (Krips et al. 2011). The dotted line represents for the ratio continuum emission either (a) electron-scattered synchrotron emission, (b) synchrotron emission, and (c) thermal free-free emission. The dashed line represents the thermal dust emission. The data obtained with $< 1''$ aperture are additionally marked with a circle. Among the models, the case (b) is relatively disfavoured because it overestimates the submillimeter flux. However, we should pay attention to the prominent time variability of the AGN continuum as well as the different apertures used to obtain the data plotted here.

Table 3.1: Emission properties at the centre of NGC 1068

Emission	ν_{rest} (GHz)	Peak flux (mJy beam $^{-1}$)	Peak flux (mK)	S (Jy beam $^{-1}$ km s $^{-1}$)	S (K km s $^{-1}$)
H26 α (red side)	353.62	< 1.26	< 107	< 4.02	< 342
Continuum (USB)	363.98	11.26 ± 0.19	956 ± 15	—	—

Note. For H26 α , we list 3σ upper limit on the peak values that are appropriate for both the broad and the narrow components at the velocity resolution of 50 km s $^{-1}$. The integrated intensity was calculated by assuming the Gaussian profile with the FWHM of 3000 km s $^{-1}$ (Alexander et al. 1999), having the peak flux of the above 3σ value.

- We investigated the nature of BLR clouds that can potentially emit broad submm-RLs under the LTE condition. As a result, we suggest $N_e \sim 10^9 \text{ cm}^{-3}$ (typical value for BLRs) components mostly contributes to line emission. From clouds with other densities, we will not see broad submm-RLs because the system is in the full thermal equilibrium or the lines are totally transparent. However, an expected line flux of this $N_e = 10^9 \text{ cm}^{-3}$ case is extremely faint, which is impractical to detect even with ALMA.
- We predicted line-to-continuum ratios of various $Hn\alpha$ lines at submillimetre to investigate whether the line components can appear. As a result, although some combinations of parameters can yield the broad line component in principle, again we cannot detect them due to the limited sensitivity of currently available submillimeter instruments including ALMA.
- Admitting the uncertainty in the continuum level, our model predictions are consistent with the non-detections of both broad and narrow $H26\alpha$ emission lines (3σ sensitivity of 1.26 mJy at $dV = 50 \text{ km s}^{-1}$) from the central region of the type-2 Seyfert galaxy NGC 1068, according to the results of our ALMA Cycle 2 observations.

Considering the speculation in Section 3.1, as well as the limited column penetrating capability at NIR wavelength, one possible way to directly detect obscured BLR lines is to use sensitive mid-IR observations. Such a chance will be provided with the Mid-infrared Instrument (MIRI)⁴ on board the *James Webb Space Telescope (JWST)*⁵. That instrument can cover $n = 5 - 8$ HI RLs at redshift zero, with the 10σ detection limit of $\sim 1 \times 10^{-20} \text{ W m}^{-2}$ for a point source (at $\sim 10 \mu\text{m}$, with 10 000 s). However, careful treatment on the departure from the LTE as well as the influence from both thermal (from an accretion disc and a dusty torus) and non-thermal continuum radiation is necessary to predict the detectability.

⁴<http://jwst.nasa.gov/miri.html>

⁵<http://www.jwst.nasa.gov>

Chapter 4

CND-scale AGN fueling: Do CNDS Drive the Growth of Supermassive Black Holes?

Part of this Chapter will be published in ApJ in August, 2016.

4.1 Context: AGN–SB Connection

With the AGN–SB connection introduced in Section 1.2 in mind, we argue that determining the properties of cold molecular gas (e.g., mass, distribution, kinematics) is essential for further progress because it takes the bulk of the gas mass in the nuclear region of galaxies (Section 1.1). Such dense gas could be a source of fuel to an SMBH as well as a stellar nursery. Thus, it should contain information on the origin of the AGN–SB connection. From this perspective, the pioneering work of Yamada (1994) showed a linear correlation between X-ray luminosity and CO(1–0) luminosity in some AGNs, with measuring CO(1–0) line with single dish telescopes (i.e., spatial resolution $>$ kpc). Monje et al. (2011) updated that result with improved statistics, again based on single-dish measurements. However, the origin of these correlations is still unclear as is the case for the SFR – \dot{M}_{BH} correlations. Moreover, whether there is any dependence of the correlation strength on the probed spatial scale has not yet been investigated. Here, we note that, if we use dense gas tracers for our investigation rather than the conventional CO(1–0) line that traces total molecular gas, including diffuse and/or foreground ones, we can expect less contamination from, e.g., the foreground component such as galactic disks. Moreover, dense gas is indeed the source of massive star formation. Hence, to achieve new insights on the AGN–SB connection more straightforwardly and to understand the underlying mass accretion processes at the CND scale, it would be desirable to establish a correlation between AGN activity and some molecular properties based on emission lines that faithfully trace star forming regions. Then, as next steps, we would proceed to check the variation of any correlation upon the spatial scale probed, and to explore the origin of the correlations with theoretical backgrounds.

4.1.1 Scope of This Chapter

Motivated by the idea above, we explored the possible correlation between \dot{M}_{BH} and the mass of the CNL-scale molecular gas as a natural extension of the previous galactic scale measurements (Monje et al. 2011; Yamada 1994). The mass of *dense* molecular gas (M_{dense}) was investigated preferentially for the above-mentioned reasons. Thus, we compiled currently available data for a typical dense gas tracer at the millimeter band, specifically, the HCN(1–0) emission line (Section 4.2.1). This allows us to straightforwardly compare results with the SFR – \dot{M}_{BH} correlations, because M_{dense} is directly convertible to SFR (e.g., Gao & Solomon 2004b). *This is the first observational study to probe any physical link between molecular properties and AGN accretion at the CNL-scale.* The detailed spatial distribution (or gas surface density) and kinematics of dense molecular gas, however, will not be discussed at this moment as most CNLs have not been well resolved spatially. Such a study will be possible with future high-resolution observations provided by ALMA.

The rest of this thesis is organized as follows. In Section 4.2, we describe the details of the data and derivation of each physical parameter used. Section 4.3 describes our regression analysis. The resulting correlation plots between HCN(1 – 0) luminosity and 2 – 10 keV X-ray luminosity, or, almost equivalently, between M_{dense} and \dot{M}_{BH} , are presented in Section 4.4. Section 4.5 is dedicated to discuss CNL-scale mass accretion mechanisms, especially supernova-driven turbulent accretion model (Kawakatu & Wada 2008) for demonstrative purposes, although this is not definitive. Our conclusions of this Chapter is summarized in Section 4.6, although we will discuss the progress by our work with our future prospects in Chapter 5.

4.2 Data Description

Here, we describe the details of the emission line, sample galaxies, and the procedure to estimate the physical quantities used. The results are listed in Tables 4.1 and 4.2. Cosmology with $H_0 = 70 \text{ km s}^{-1} \text{ Mpc}^{-1}$, $\Omega_{\text{M}} = 0.3$, $\Omega_{\Lambda} = 0.7$ was adopted. We included galaxies classified as Seyfert 1.5, 1.8, and 1.9 into the Seyfert 1 category to maintain consistency with Esquej et al. (2014), who provided a high resolution SFR– \dot{M}_{BH} correlation.

Table 4.1: Properties of the sample galaxies

Target (1)	D_L (2)	Morphology (3)	AGN type (4)	$\log(L_{2-10\text{keV}})$ (5)	Ref. 1 (6)	$\log(L'_{\text{HCN}})$ (7)	θ_{res} (8)	Ref. 2 (9)	$\log(M_{\text{BH}})$ (10)	Ref. 3 (11)
Interferometric data (IT-sample)										
NGC 1068	16.3	(R)SA(rs)b	2	43.02±0.30	(1)	7.40±0.07	0.38	(7)	6.96±0.02	(24), maser
NGC 1097	18.2	SB(s)b	1	40.84±0.30	(2)	6.71±0.06	0.16	(8)	8.15±0.10	(25), gas
NGC 2273	26.4	SB(r)a	2	42.73±0.30	(1)	6.70±0.05	0.38 [‡]	(9)	6.89±0.02	(26), maser
NGC 3079	16.0	SB(s)c edge-on	2	42.02±0.30	(1)	6.94±0.04	0.39 [‡]	(10)	7.90±0.63	(27,28), $M_{\text{BH}} - \sigma_*$
NGC 3227	16.6	SAB(s)a pec	1.5	42.07±0.30	(2)	6.32±0.08	0.24 [‡]	(9)	7.18±0.30	(29), stellar
NGC 4051	10.0	SAB(rs)bc	1.5	41.13±0.30	(2)	5.58±0.05	0.14 [‡]	(9)	6.13±0.14	(30), reverberation
NGC 4579	21.8	SAB(rs)b	1.5	41.33±0.30	(2)	5.93±0.13	0.20	(11)	7.76±0.45	(27,28), $M_{\text{BH}} - \sigma_*$
NGC 5033	12.5	SA(s)c	1.9	40.91±0.30	(2)	5.87±0.05	0.18 [‡]	(10)	7.38±0.46	(27,28), $M_{\text{BH}} - \sigma_*$
NGC 6951	20.4	SAB(rs)bc	2	- [‡]	- [‡]	6.24±0.04	0.30 [‡]	(9)	7.10±0.50	(27,28), $M_{\text{BH}} - \sigma_*$
NGC 7469	70.8	(R')SAB(rs)a	1.2	43.17±0.30	(2)	7.44±0.04	0.19	(12)	6.97±0.05	(30), reverberation
Single dish data (SD-sample)										
Cen A	7.8	S0 pec	2	41.90±0.30	(3)	7.24±0.07	1.1	(13)	7.65±0.04	(31), gas
Circinus	6.2	SA(s)b	2	42.62±0.30	(1)	7.24±0.07	1.7	(14)	6.23±0.08	(32), maser
IRAS 05189-2524	188.2	-	2	44.20±0.30	(4)	8.71±0.08	26	(15)	7.42±0.40	(27,28), $M_{\text{BH}} - \sigma_*$
Mrk 273	166.5	pec	2	42.87±0.30	(2)	8.81±0.14	23	(16)	9.17±0.05	(33), maser
Mrk 331	80.3	Sa	2	40.70±0.30	(4)	8.53±0.15	27	(17)	6.81±0.47	(27,28), $M_{\text{BH}} - \sigma_*$
NGC 34	85.3	pec	2	42.00±0.30	(4)	8.02±0.07	12	(15)	7.71±0.52	(27,28), $M_{\text{BH}} - \sigma_*$
NGC 660	12.2	SB(s)a pec	2	39.40±0.30	(4)	7.31±0.11	1.7	(18)	7.12±0.47	(27,28), $M_{\text{BH}} - \sigma_*$
NGC 931	72.2	SAbc	1	43.29±0.30	(2)	<8.06	15	(19)	7.54±0.60	(27,28), $M_{\text{BH}} - \sigma_*$
NGC 1068	16.3	(R)SA(rs)b	2	43.02±0.30	(1)	8.13±0.02	2.2	(20)	6.96±0.02	(24), maser
NGC 1097	18.2	SB(s)b	1	40.84±0.30	(2)	7.54±0.09	1.7	(21)	8.15±0.10	(25), gas
NGC 1365	23.5	SB(s)b	1.8	42.25±0.30	(2)	8.26±0.10	6.4	(19)	7.50±0.51	(27,28), $M_{\text{BH}} - \sigma_*$
NGC 1667	65.7	SAB(r)c	2	42.37±0.30	(5)	8.71±0.11	14	(19)	7.82±0.45	(27,28), $M_{\text{BH}} - \sigma_*$
NGC 2273	26.4	SB(r)a	2	42.73±0.30	(1)	6.96±0.22	5.5	(19)	6.89±0.02	(26), maser
NGC 3079	16.0	SB(s)c edge-on	2	42.02±0.30	(1)	7.91±0.10	5.5	(17)	7.90±0.63	(27,28), $M_{\text{BH}} - \sigma_*$
NGC 3147	40.3	SA(rs)bc	2	41.40±0.30	(4)	7.96±0.07	5.5	(22)	7.42±0.50	(27,28), $M_{\text{BH}} - \sigma_*$
NGC 4258	6.4	SAB(s)bc	1.9	40.57±0.30	(2)	6.09±0.04	0.9	(16)	7.56±0.03	(34), maser
NGC 4388	36.3	SA(s)b edge-on	2	43.20±0.30	(2)	6.88±0.25	4.9	(16)	6.92±0.01	(26), maser
NGC 4593	38.8	(R)SB(rs)b	1	42.80±0.30	(2)	7.05±0.28	5.3	(16)	6.89±0.09	(30), reverberation
NGC 4945	8.6	SB(s)cd edge-on	2	42.22±0.30	(6)	8.15±0.09	2.2	(23)	6.46±0.03	(35), maser

Continue on next page

Continued from the previous page

NGC 5005	13.5	SAB(rs)bc	2	40.02±0.30	(2)	7.75±0.12	4.7	(17)	7.84±0.45	(27,28), $M_{\text{BH}} - \sigma_*$
NGC 5033	12.5	SA(s)c	1.9	40.91±0.30	(2)	7.21±0.09	2.6	(19)	7.38±0.46	(27,28), $M_{\text{BH}} - \sigma_*$
NGC 5135	59.3	SB(s)ab	2	43.10±0.30	(1)	8.11±0.10	16	(19)	7.24±0.46	(27,36), $M_{\text{BH}} - \sigma_*$
NGC 5194	6.6	SA(s)bc pec	2	41.54±0.30	(1)	6.63±0.02	9.0	(20)	6.60±0.49	(27,28), $M_{\text{BH}} - \sigma_*$
NGC 5347	33.6	(R')SB(rs)ab	2	42.39±0.30	(1)	<7.06	7.0	(19)	6.73±0.55	(27,28), $M_{\text{BH}} - \sigma_*$
NGC 5506	26.6	Sa pec edge-on	1.9	43.01±0.30	(2)	6.50±0.46	3.6	(16)	7.87±0.49	(27,28), $M_{\text{BH}} - \sigma_*$
NGC 5548	74.5	(R')SA(s)0/a	1.2	43.42±0.30	(2)	<6.69	10	(16)	7.73±0.12	(30), reverberation
NGC 6814	22.4	SAB(rs)bc	1.5	42.18±0.30	(2)	7.10±0.12	6.2	(19)	7.05±0.06	(30), reverberation
NGC 6951	20.4	SAB(rs)bc	2	- [†]	- [†]	7.43±0.01	2.8	(20)	7.10±0.50	(27,28), $M_{\text{BH}} - \sigma_*$
NGC 7130	70.0	Sa pec	1.9	43.10±0.30	(1)	8.26±0.11	19	(19)	7.48±0.46	(27,36), $M_{\text{BH}} - \sigma_*$
NGC 7469	70.8	(R')SAB(rs)a	1.2	43.17±0.30	(2)	8.46±0.16	15	(19)	6.97±0.05	(30), reverberation
NGC 7479	34.2	SB(s)c	2	41.17±0.30	(5)	7.99±0.12	12	(17)	7.61±0.46	(27,28), $M_{\text{BH}} - \sigma_*$
NGC 7582	22.6	(R')SB(s)ab	1	42.60±0.30	(4)	7.65±0.12	3.1	(18)	7.56±0.51	(27,28), $M_{\text{BH}} - \sigma_*$

Note. Column 1: name of the sample galaxy. Column 2: luminosity distance to the object in [Mpc]. Column 3: morphology of the host galaxy recorded in the NED. Mrk 331 is classified to Sa based on the record in HyperLeda (no record in the NED). Column 4: AGN type. We follow the classification of Maiolino & Rieke (1995) for the RSA Seyfert samples. For the non-RSA Seyfert samples, we mostly adopt the classification by the NED. Columns 5 and 6: the logarithmic scale value of absorption corrected 2 – 10 keV luminosity in [erg s^{-1}] and its reference. Zero padding is applied to some data. [†]We used [OIV] line luminosity to estimate L_{Bol} (Diamond-Stanic et al. 2009; Rigby et al. 2009). Columns 7, 8, and 9: the logarithmic scale value of $\text{HCN}(1-0)$ line luminosity in [$\text{K km s}^{-1} \text{pc}^2$], the aperture used to measure the luminosity in [kpc], and the reference for them. [‡]For NGC 2273, NGC 3227, NGC 4051, and NGC 6951 in the IT-sample, we used the line fluxes measured for the central 3'' region as reported in Sani et al. (2012). Similarly, for NGC 3079 and NGC 5033, 5'' and 3'' apertures are used as shown in Lin et al. (2016). Systematic uncertainty is included. We assume 10% and 15% for the statistical and systematic uncertainties unless mentioned in the reference. Columns 10 and 11: the logarithmic scale value of black hole mass in [M_{\odot}] with the reference and the method for the estimation. References: (1) Marinucci et al. (2012), (2) Liu et al. (2014), (3) de Rosa et al. (2012), (4) Brightman & Nandra (2011), (5) Panessa et al. (2006), (6) Lutz et al. (2004), (7) Kohno et al. (2008), (8) Martín et al. (2015), (9) Sani et al. (2012), (10) Lin et al. (2016), (11) from ALMA archive (this work), (12) Izumi et al. in preparation, (13) Wild & Eckart (2000), (14) Curran et al. (2001), (15) Privoon et al. (2015), (16) Jiang et al. (2011), (17) Gao & Solomon (2004a), (18) Baan et al. (2008), (19) Curran et al. (2000), (20) Krips et al. (2008), (21) Kohno et al. (2003), (22) Solomon et al. (1992a), (23) Wang et al. (2004), (24) Lodato & Bertin (2003), (25) Onishi et al. (2015), (26) Kuo et al. (2011), (27) Gültekin et al. (2009), (28) HyperLeda, (29) Davies et al. (2006), (30) Bentz & Katz (2015) and references therein, (31) Neumayer (2010), (32) Greenhill et al. (2003), (33) Klöckner & Baan (2004), (34) Miyoshi et al. 1995, (35) Greenhill et al. (1997), (36) Garcia-Rissmann et al. (2005)

4.2.1 Line selection

We used the HCN(1 – 0) emission line ($\nu_{\text{rest}} = 88.631$ GHz) as a proxy for M_{dense} . The critical density for collisional excitation with H₂ (n_{cr}) is $\sim 10^5$ cm⁻³ in the optically thin limit. This line is one of the brightest ones in the 3 mm wavelength band in nearby galaxies after CO(1 – 0). Unlike CO(1 – 0) which traces total molecular gas (i.e., both dense and diffuse/foreground gas; $n_{\text{cr}} \sim 10^{2-3}$ cm⁻³), the HCN(1 – 0) emission emanates selectively from dense molecular gas where stars are born (Gao & Solomon 2004a,b; Wu et al. 2005). Thus, using HCN(1 – 0) may be more suitable physically to investigate any possible link between circumnuclear star formation and AGN activity.

Indeed, substantial fraction of the molecular gas at a CND would be typically so dense and warm ($n_{\text{H}_2} \gtrsim 10^{4-5}$ cm⁻³, kinetic temperature $\gtrsim 100$ K; e.g., Davies et al. 2012; Izumi et al. 2013; Viti et al. 2014) that CO is readily excited to higher rotational states (e.g., Kamenetzky et al. 2014). However, converting the line flux of high- J CO into that of CO(1 – 0) would cause large uncertainty, unless spatially resolved multi-transitions are available. Thus, it is better to continue to use the $J = 1 - 0$ transition line that can selectively trace dense gas, such as HCN(1 – 0), to estimate M_{dense} .

The HCN(1 – 0) line becomes more intense in AGNs with respect to the CO, HCO⁺, and CS emission lines, compared to SB galaxies, i.e., HCN-enhancement as shown in Chapters 1 and 2 (see also, e.g., Davies et al. 2012; Krips et al. 2008). This may be a consequence of either an abnormal chemical composition due to AGN feedback, excitation (gas density, temperature), optical depth, infrared-pumping, or even a combination of them. One might concern that abundance variation will make the mass estimation quite difficult. However, the line optical depth of HCN(1 – 0) is almost always (well) beyond the unity in most objects (i.e., the line intensity gets saturated even if HCN abundance is substantially enhanced in AGNs). Thus, the potential variation in abundance will not severely affect our conclusions as long as we estimate M_{dense} from HCN(1 – 0) line luminosity via the virial theorem. Using a mass conversion factor specifically estimated for AGNs (Krips et al. 2008) will also help to reduce this uncertainty.

4.2.2 Interferometric data

We compiled high-resolution (aperture < 500 pc) interferometric data for the HCN(1 – 0) emission line from the literature and the ALMA archive to estimate M_{dense} of CNDs of nearby Seyfert galaxies. There is currently very little information on such high-resolution HCN(1 – 0) data, which ultimately limits the number of our sample galaxies (called the *interferometric sample* \equiv *IT sample*). The data were obtained with the Plateau de Bure Interferometer = PdBI (NGC 2273, NGC 3227, NGC 4051, and NGC 6951: Sani et al. 2012 and references therein, NGC 3079 and NGC 5033: Lin et al. 2016), the Nobeyama Millimeter Array = NMA (NGC 1068: Kohno et al. 2008), and ALMA (NGC 1097¹: Martín et al. 2015, NGC 4579²: ALMA archive, and

¹ID = 2011.0.00108.S

²ID = 2012.1.00456.S

Table 4.2: M_{dense} and \dot{M}_{BH} of the sample galaxies

Target (1)	$\log (M_{\text{dense}})$ (2)	$\log (\dot{M}_{\text{BH}})$ (3)
Interferometric data (IT-sample)		
NGC 1068	8.40 ± 0.31	-1.55 ± 0.42
NGC 1097	7.71 ± 0.30	-4.10 ± 0.42
NGC 2273	7.70 ± 0.30	-1.91 ± 0.42
NGC 3079	7.94 ± 0.30	-2.76 ± 0.42
NGC 3227	7.32 ± 0.31	-2.70 ± 0.42
NGC 4051	6.58 ± 0.30	-3.78 ± 0.42
NGC 4579	6.93 ± 0.33	-3.56 ± 0.42
NGC 5033	6.87 ± 0.30	-4.02 ± 0.42
NGC 6951	7.24 ± 0.30	-3.29 ± 0.42
NGC 7469	8.44 ± 0.30	-1.36 ± 0.42
Single Dish data (SD-sample)		
Cen A	8.24 ± 0.31	-2.91 ± 0.42
Circinus	8.24 ± 0.31	-2.05 ± 0.42
IRAS 05189-2524	9.71 ± 0.31	-0.03 ± 0.42
Mrk 273	10.27 ± 0.32	-1.74 ± 0.42
Mrk 331	9.53 ± 0.34	-4.25 ± 0.42
NGC 34	9.02 ± 0.31	-2.79 ± 0.42
NGC 660	8.31 ± 0.32	-5.59 ± 0.42
NGC 931	< 9.06	-1.21 ± 0.42
NGC 1068	9.13 ± 0.30	-1.55 ± 0.42
NGC 1097	8.54 ± 0.31	-4.10 ± 0.42
NGC 1365	9.26 ± 0.32	-2.48 ± 0.42
NGC 1667	9.71 ± 0.32	-2.34 ± 0.42
NGC 2273	7.96 ± 0.37	-1.91 ± 0.42
NGC 3079	8.91 ± 0.32	-2.76 ± 0.42
NGC 3147	8.96 ± 0.31	-3.48 ± 0.42
NGC 4258	7.09 ± 0.30	-4.39 ± 0.42
NGC 4388	7.88 ± 0.39	-1.32 ± 0.42
NGC 4593	8.05 ± 0.41	-1.82 ± 0.42
NGC 4945	9.15 ± 0.31	-2.52 ± 0.42
NGC 5005	8.75 ± 0.32	-4.96 ± 0.42
NGC 5033	8.21 ± 0.31	-4.02 ± 0.42
NGC 5135	9.11 ± 0.32	-1.45 ± 0.42
NGC 5194	7.63 ± 0.30	-2.50 ± 0.42
NGC 5347	< 8.06	-2.32 ± 0.42
NGC 5506	7.50 ± 0.55	-1.56 ± 0.42
NGC 5548	< 7.69	-1.04 ± 0.42
NGC 6814	8.10 ± 0.32	-2.58 ± 0.42
NGC 6951	8.43 ± 0.30	-3.29 ± 0.42
NGC 7130	9.26 ± 0.32	-1.45 ± 0.42
NGC 7469	9.46 ± 0.34	-1.36 ± 0.42
NGC 7479	8.99 ± 0.32	-3.73 ± 0.42
NGC 7582	8.65 ± 0.32	-2.07 ± 0.42

Note. Column 1: name of the target galaxy. Columns 2 and 3: logarithmic values of $M_{\text{dense}} [M_{\odot}]$ and $\dot{M}_{\text{BH}} [M_{\odot} \text{ yr}^{-1}]$. Numbers in Table 4.1 are used to estimate these values (see the derivation in Section 4.2).

NGC 7469³: T. Izumi et al. in prep.). We guide a reader for the detailed data analysis to those references. Regarding each of the PdBI sources, the line flux/luminosity in the literature was measured with an aperture ($3'' - 5''$), rather than a single synthesized beam. This enabled us to cover the entire area of each CND in all cases. In NGC 1097, NGC 4579, and NGC 7469, although the line flux/luminosity measured with single synthesized beams placed at the AGN positions were used, their CNDs were not resolved with the adopted beams. Thus, we covered almost the entire area of each CND in these samples as well. For NGC 1068, there are higher resolution (~ 100 pc) data with PdBI (García-Burillo et al. 2008; Viti et al. 2014). Nevertheless, we used the NMA data mentioned above (380 pc resolution), considering the relatively large CND of this galaxy (~ 300 pc in diameter; García-Burillo et al. 2014). This enabled us to make a fair comparison among the targets because we could then compile the line fluxes/luminosities from the entire area of each CND. Note that the ALMA data (NGC 4579 and NGC 7469) were analyzed further with the Common Astronomy Software Applications (CASA: McMullin et al. 2007; Petry & CASA Development Team 2012). The data analysis of NGC 7469 was already presented in Appendix-D (to discuss the generic HCN-diagram in Section 2.4.6), and that of NGC 4579 can be found in the Appendix-E. We excluded galaxies showing an absorption feature in the HCN(1 – 0) line from the IT sample. Indeed, NGC 4945 and Centaurus A (both in the ALMA archive) showed prominent absorption features at their nuclei. We also excluded NGC 5194 (M51) from the IT sample because it exhibited a possible feature of maser amplification in the HCN(1 – 0) emission (Matsushita et al. 2015).

Thus, we assessed the HCN(1 – 0) line flux/luminosities for a total of 10 Seyfert galaxies (six type 1 and four type 2). The median distance of the samples was 17.4 Mpc. For each AGN from the literature, we used the line flux/luminosity listed in the reference, measured with an aperture sufficient to encompass the whole CND, as noted above. Thus, the sampled spatial scale differed among galaxies (median value $\theta_{\text{med}} = 220$ pc). Note that the angular sizes of the target CNDs were at most a few arcseconds (e.g., Izumi et al. 2013, 2015), which is well below the maximum recoverable angular scale of the interferometers mentioned above. Consequently, the missing flux is not a major problem.

Line luminosity of HCN(1 – 0)

HCN(1 – 0) line luminosity L'_{HCN} was calculated as

$$\left(\frac{L'_{\text{HCN}}}{\text{K km s}^{-1} \text{ pc}^2} \right) = 3.25 \times 10^7 \left(\frac{S\Delta v}{\text{Jy km s}^{-1}} \right) \left(\frac{\nu_{\text{rest}}}{\text{GHz}} \right)^{-2} \cdot \left(\frac{D_L}{\text{Mpc}} \right)^2 (1+z)^{-1}, \quad (4.1)$$

where $S\Delta v$, D_L , and z indicate the velocity-integrated line flux of HCN(1 – 0), the luminosity distance to the object, and the redshift of the object, respectively (Solomon et al. 1992b; Solomon & Vanden Bout 2005). For the data taken from the literature, we simply used the listed $S\Delta v$

³ID = 2012.1.00165.S

after correcting D_L . For NGC 4579 and NGC 7469, we measured $S\Delta v$ in a zeroth moment map, which was computed with the CASA task `immoments` without any clipping after subtracting the underlying continuum emission. The velocity ranges for the integration were chosen carefully to fully cover the full width at zero intensity of the HCN(1 – 0) lines, but not to be so large as to introduce unnecessary noise. The RMS noises for these maps were measured in areas free of HCN(1 – 0) emissions.

Mass of dense molecular gas

Assuming that the HCN(1 – 0) emission is emanating from an ensemble of virialized, non-shadowing (in space and velocity) clouds, we can estimate M_{dense} of the CND as (e.g., Solomon et al. 1990),

$$\begin{aligned} \left(\frac{M_{\text{dense}}}{M_{\odot}}\right) &= 2.1 \left(\frac{n_{\text{H}_2}}{\text{cm}^{-3}}\right)^{1/2} \left(\frac{T_{\text{b}}}{\text{K}}\right)^{-1} L'_{\text{HCN}} \\ &\equiv X_{\text{HCN}} \cdot L'_{\text{HCN}}, \end{aligned} \quad (4.2)$$

where T_{b} is the brightness temperature of the emission line. We direct readers to Papadopoulos et al. (2012) for a more sophisticated formalism that accounts for the departure from the assumptions above. Although the conversion factor (X_{HCN}) would span a wide range, we adopt $X_{\text{HCN}} = 10 M_{\odot} (\text{K km s}^{-1} \text{ pc}^2)^{-1}$ throughout this work. This factor was specifically estimated for nearby AGNs through a multi-transitional non-LTE analysis of the single dish-based data (IRAM 30m; Krips et al. 2008). We adopted 0.30 dex uncertainty for this factor, as estimated by those authors, which dominates the total uncertainty of M_{dense} .

Black hole mass

M_{BH} is used to discuss AGN properties (Section 4.2.4) and mass accretion mechanisms (Section 4.5). We favored values derived from stellar or gas kinematics (NGC 1097 and NGC 3227), Very Long Baseline Interferometry (VLBI) maser observations (NGC 1068 and NGC 2273), and reverberation mapping (NGC 4051 and NGC 7469). We fixed a virial factor of $f = 4.3$ for the reverberation method (Bentz & Katz 2015; Grier et al. 2013⁴). For the other galaxies, the σ_* compiled in HyperLeda⁵ (Makarov et al. 2014) were applied to the $M_{\text{BH}} - \sigma_*$ relationship constructed by Gültekin et al. (2009). An intrinsic scatter (0.44 dex) accompanying the relation was also taken into account when estimating the total uncertainty in M_{BH} .

Bolometric luminosity and mass accretion rate

An absorption-corrected 2 – 10 keV hard X-ray luminosity ($L_{2-10\text{keV}}$) catalogued in published papers was considered a proxy for the bolometric luminosity of the AGN (L_{Bol} ; e.g., Ho 2008). The bolometric correction of Marconi et al. (2004) was applied to the $L_{2-10\text{keV}}$. The uncertainties in the L_{Bol} would be mainly driven by the scatter on the correction and the time variability of

⁴<http://www.astro.gsu.edu/AGNmass/>

⁵<http://leda.univ-lyon1.fr>

the $L_{2-10\text{keV}}$, which, generally, are significantly larger than the statistical error in the $L_{2-10\text{keV}}$. We adopted 0.30 dex uncertainty for each, which is likely to be sufficient. Adding these in quadrature, 0.42 dex uncertainty was set for L_{Bol} .

The mass accretion rate onto an SMBH was subsequently estimated using the following relationship (Alexander & Hickox 2012),

$$\left(\frac{\dot{M}_{\text{BH}}}{M_{\odot} \text{ yr}^{-1}}\right) = 0.15 \left(\frac{0.1}{\eta}\right) \left(\frac{L_{\text{Bol}}}{10^{45} \text{ erg s}^{-1}}\right) \quad (4.3)$$

where $\eta = 0.1$ is a typical value for mass-to-energy conversion efficiency in the local universe (Marconi et al. 2004). Any uncertainty accompanying this relationship was not taken into account for simplicity. Thus, the total uncertainty of \dot{M}_{BH} is the same as that of L_{Bol} , i.e., 0.42 dex. Note that models predict a drop of the η in a low accretion phase (Narayan & Yi 1995) due to advection of matter in an accretion disk. In that case, the estimated value above would be the lower limit of \dot{M}_{BH} . We ignore this potential influence here, but that may be a subject of future studies.

Regarding NGC 6951, we could not find an absorption-corrected $L_{2-10\text{keV}}$ in the literature. However, rather than discarding this valuable sample with high-resolution HCN(1–0) measurements, we used another proxy for L_{Bol} , namely an [O IV] line luminosity ($L_{[\text{OIV}]}$). The line flux collected by Diamond-Stanic et al. (2009) and the bolometric correction of $L_{\text{Bol}} = 810 \times L_{[\text{OIV}]}$ (for type 2 Seyfert galaxies; Rigby et al. 2009) were applied. The uncertainty in this L_{Bol} was assumed to be at the same level as that derived from $L_{2-10\text{keV}}$ for simplicity: i.e., 0.42 dex.

4.2.3 Single-dish data

To investigate the impact of an aperture for sampling L'_{HCN} in this study (Section 4.3), we compiled HCN(1–0) flux data for nearby Seyfert galaxies obtained with single-dish telescopes from the literature. Again, the number of HCN(1–0) detections limited the total number of our sample (the *single-dish sample* \equiv *SD sample*). We excluded merging galaxies from our sample, because we could not judge from which galaxy (or both) the line emission came in most cases, considering the coarse spatial resolutions. The angular resolutions of the telescopes were, 29'' (IRAM 30 m), 57'' (SEST), 44'' (OSO), 72'' (NRAO 12 m), 62'' (FCRAO 14 m), and 19'' (NRO 45 m), respectively, at the ν_{rest} of HCN(1–0). These resolutions typically correspond to more than a few kpc and sometimes even reach > 10 kpc at the distance of the sample galaxies. This indicates that these observations traced dense molecular gas existing over a bulge-scale (typically a few kpc) or larger (i.e., an entire galaxy). We should also emphasize that the spatial resolution of \sim a few kpc is insufficient to separate a CND (100 pc scale) from other components in that central region, such as a kpc-scale circumnuclear SB ring (e.g., Izumi et al. 2013, 2015; see also the Figures in Appendix-A).

We adopted the same procedure described in Section 4.2.2 to achieve M_{dense} , M_{BH} , L_{Bol} , and \dot{M}_{BH} . In most cases, we had no choice but to use the $M_{\text{BH}} - \sigma_*$ relationship (Gültekin et al. 2009) to estimate M_{BH} . This σ_* was collected mainly from HyperLeda, and otherwise from

the literature. A total of 32 samples (12 type 1 and 20 type 2) were assessed. Their median distances and spatial resolutions were 26.5 Mpc and 5.5 kpc, respectively.

4.2.4 Comments on the AGN sample

We first note that neither the IT nor SD sample is homogeneous, because they were simply compiled from the literature or the archive. Around 75% and 60% of our IT and SD samples, respectively, belong to the revised Shapley-Ames (RSA) catalog (Maiolino & Rieke 1995; Sandage & Tammann 1987), which includes Seyfert galaxies brighter than $B_T = 13$ mag. The RSA sample is a magnitude-limited one, sensitive to low-luminosity AGNs. However, as shown in Table 4.1, the morphology of our sample was mostly the barred spiral (SAB or SB type), which clearly contrast against the broader distribution of the whole RSA Seyfert sample. Efficient gas transportation towards the center by a bar would be related to this morphological bias.

Figure 4.1 shows the distribution of the L_{Bol} , M_{BH} , and λ_{Edd} of our sample AGNs. Here, λ_{Edd} denotes the Eddington ratio ⁶. The logarithmic median values of $(L_{\text{Bol}}, M_{\text{BH}}, \lambda_{\text{Edd}})$ are (42.80, 7.14, -2.43) and (43.41, 7.42, -2.08) for the IT and SD samples, respectively. The resulting λ_{Edd} is distributed over a wide range: i.e., ~ 5 orders of magnitude. This might suggest the limited applicability of Equation (4.3) for all of our samples under the fixed value of $\eta = 0.1$, because it has been predicted that the accretion disk will change its state at $\lambda_{\text{Edd}} \sim 10^{-3}$ (e.g., Abramowicz & Fragile 2013). We nevertheless stick to the current estimation of \dot{M}_{BH} because the actual η is not observationally constrained for low- λ_{Edd} objects. This point should be improved in future succeeding works both from theoretical and observational aspects.

Based on these data, the SD sample seems to be slightly biased towards higher-luminosity objects than the IT sample, likely because there are few high-luminosity (or high λ_{Edd}) AGNs in the very nearby universe (e.g., $D_L \lesssim 20$ Mpc), where the CND could be spatially well separated from, for example, the surrounding SB ring, at the HCN(1 – 0) emission line in past interferometric observations. However, we could not clearly reject the null hypothesis that both the IT and the SD samples are drawn from the same distribution. Indeed, the Kolmogorov–Smirnov (KS) test of the IT and SD distributions shown in Figure 4.1 returned marginal (or even high) p -values, which were (0.33, 0.75, 0.75) for $(L_{\text{Bol}}, M_{\text{BH}}, \lambda_{\text{Edd}})$, respectively. Thus, admitting the poor statistics of the sample and the relatively large uncertainty for each parameter, we ignored any (possible) systematic difference in the intrinsic AGN properties between the two sample groups. In this way, one critical difference between the two sample groups that dominantly influences our study is M_{dense} , which directly reflects the orders-of-magnitude different spatial scales for HCN(1 – 0) measurements (Figure 4.2). Indeed, our whole sample exhibits a positive correlation between the spatial resolution and the HCN(1 – 0) line luminosity with a correlation coefficient of $0.71_{-0.08}^{+0.07}$ (excluding the upper limits on L'_{HCN} ; see Section 4.3 for the method of the correlation analysis).

⁶ $\lambda_{\text{Edd}} = L_{\text{Bol}}/L_{\text{Edd}}$, where $L_{\text{Edd}} [\text{erg s}^{-1}] = 1.26 \times 10^{38} M_{\text{BH}} [M_{\odot}]$.

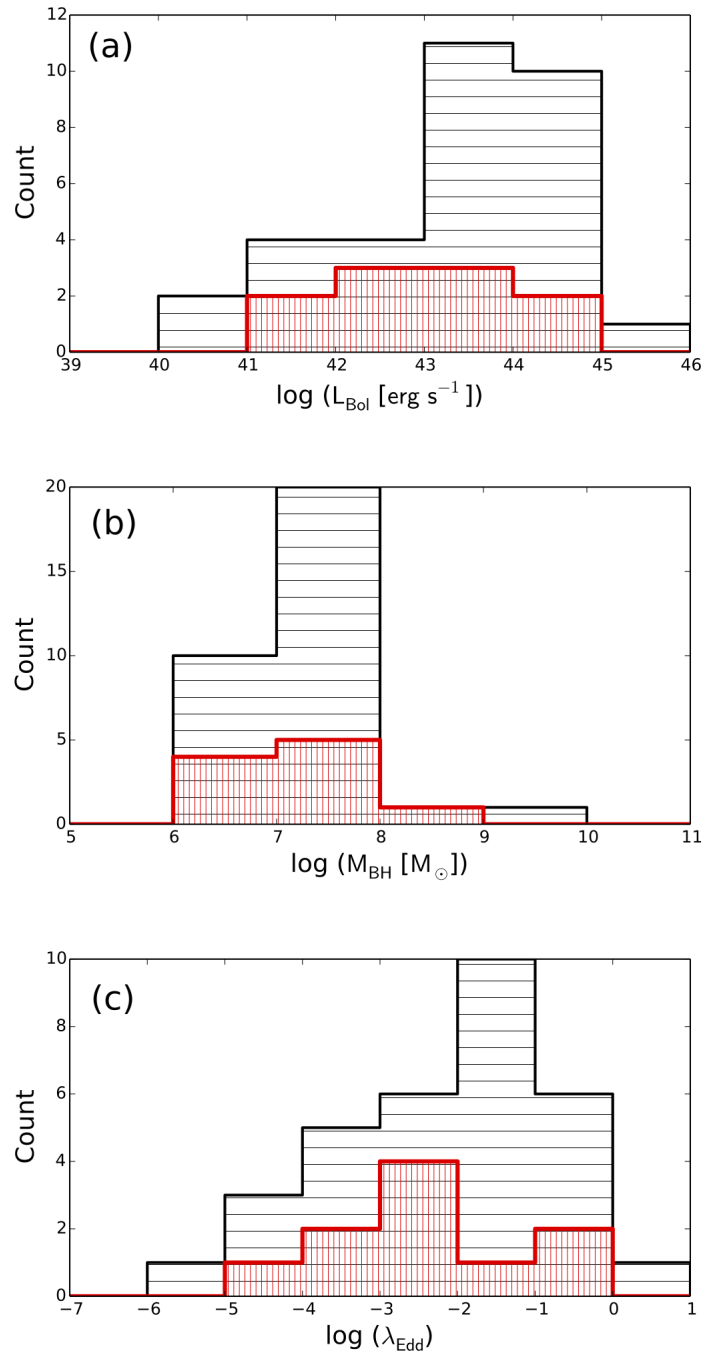


Figure 4.1: Distributions of (a) bolometric luminosity L_{Bol} , (b) black hole mass M_{BH} , and (c) Eddington ratio λ_{Edd} of the sample galaxies. Data obtained with interferometers (IT sample: red, vertical line) and single-dish telescopes (SD sample: black, horizontal line) are shown.

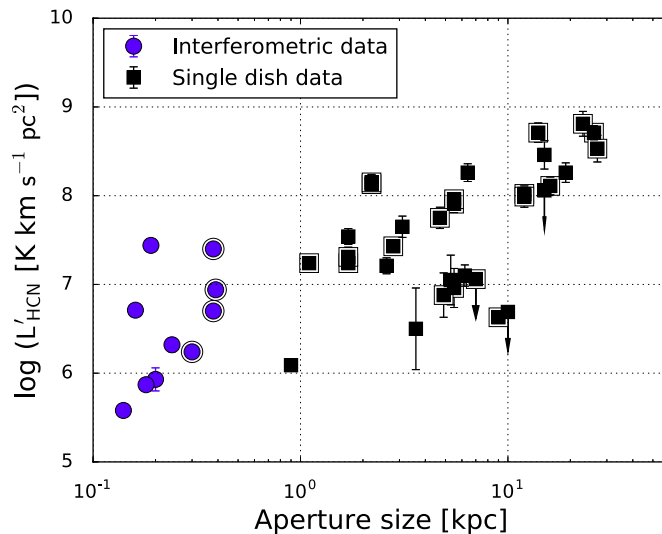


Figure 4.2: Scatter plot of the spatial resolution and HCN(1–0) line luminosity including both the IT sample (blue circle) and the SD sample (black square). There is a positive correlation between these two quantities (correlation coefficient = $0.71^{+0.07}_{-0.08}$). The doubled symbols denote type 2 AGNs.

4.3 Regression Analysis

Figure 4.3 shows the observed scatter plots of the quantities in Tables 4.1 and 4.2, indicating the maximum number of data points currently available. Excluding those with upper limits, the median values of $(L'_{\text{HCN}}, L_{2-10\text{keV}}, M_{\text{dense}}, \dot{M}_{\text{BH}})$ were (6.51, 42.02, 7.51, -3.03) and (7.75, 42.37, 8.75, -2.41) for the IT and SD samples, respectively, on a logarithmic scale. Regarding the IT sample, one might see a trend of positive correlations in both plots, indicating the importance of CNDs as an *external driver* of AGN activity. To study such a view more quantitatively, we applied the linear regression method developed by Kelly (2007) for the two sets of variables: $(L'_{\text{HCN}}, L_{2-10\text{keV}})$ and $(M_{\text{dense}}, \dot{M}_{\text{BH}})$. Because we used the same X_{HCN} and the fixed η in Equation (4.3) for all sample galaxies, and the conversion factors from $L_{2-10\text{keV}}$ to L_{Bol} (Marconi et al. 2004) are eventually comparable among our sample, these two sets produce virtually equivalent correlations. However, we should also note that any uncertainty in η and the conversion from L_{Bol} to \dot{M}_{BH} were not taken into account, which could have influenced our results. Nevertheless, we argue that our work is an important step to better understand the physical link between the content of circumnuclear molecular gas and the AGN event.

The procedure for the analysis is available from the IDL Astronomy User’s Library ⁷ as `linmix_err`. This is a Bayesian-based algorithm that can handle errors on both axes, upper limits on the dependent variable, and the intrinsic scatter. It also returns a linear correlation

⁷<http://idlastro.gsfc.nasa.gov>

strength. The assumed formula for the regression is

$$\log \zeta = \alpha + \beta \times \log \xi + \epsilon, \quad (4.4)$$

where α , β , and ϵ are the intercept, slope, and intrinsic scatter of a two-dimensional regression line for variables (ξ, ζ) . Here, ϵ is assumed to follow a Gaussian distribution with a mean zero and a constant variance of σ_{int}^2 (we show values of σ_{int} as the intrinsic scatter). However, each measurement (labeled by i) for the variable (ξ, ζ) can be expressed as (x_i, y_i) , which have random measurement errors $(\epsilon_{x,i}, \epsilon_{y,i})$. Thus, $x_i = \xi_i + \epsilon_{x,i}$ and $y_i = \zeta_i + \epsilon_{y,i}$.

The `linmix_err` procedure uses a Markov-chain Monte Carlo (MCMC) technique to draw random parameter sets from the probability distributions constructed from the measured data: it returns posterior parameter distributions. In this work, we regard the posterior mode and the range around it that encompasses the 68% fraction of the distribution as our *best-fit value* and *uncertainty* for each regression parameter. We used 3×10^4 random draws returned by the MCMC sampler with the Metropolis-Hastings algorithm. Note that the `linmix_err` models the prior distribution of the independent variable using a weighted mixture of K -Gaussians. Although Kelly (2007) recommended using $K = 3$ to be flexible enough for a wide variety of distributions, we instead used $K = 1$, considering the small numbers of samples. Note that Figure 4.4 supports the distribution of $\log(M_{\text{dense}})$ of the samples, which supports the validity of our simple modeling of the prior distribution. The canonical Spearman rank correlation coefficient and the corresponding null-hypothesis probability were also derived with `r_correlate` in IDL to simplify the results.

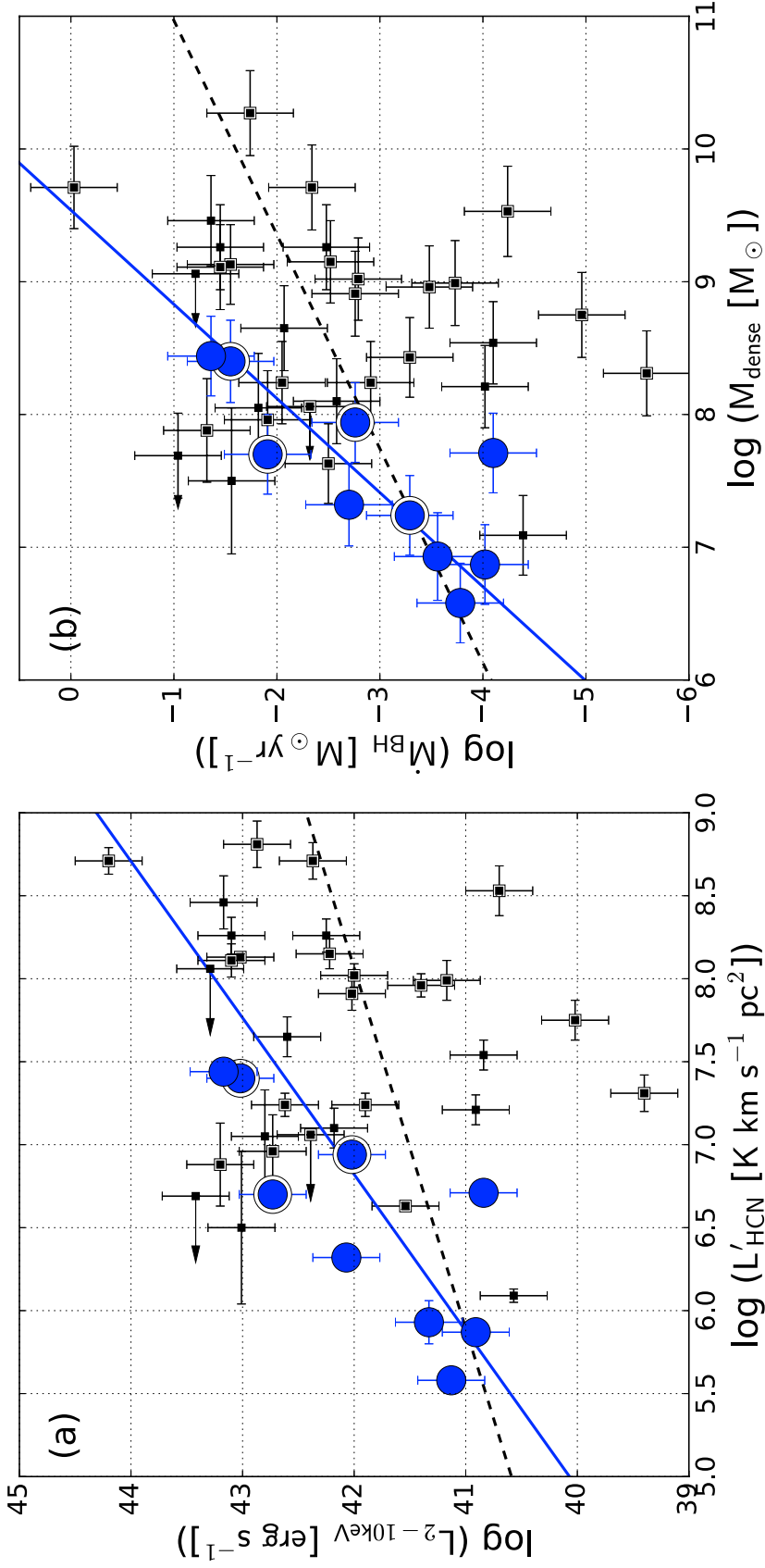


Figure 4.3: Observed scatter plot of (a) $L'_{\text{HCN}} - L_{2-10\text{keV}}$ and (b) $M_{\text{dense}} - \dot{M}_{\text{BH}}$, on a logarithmic scale. Blue circles and black squares indicate that the $\text{HCN}(1-0)$ emission was obtained with interferometers (median aperture $\theta_{\text{med}} = 220$ pc; IT sample) and single-dish telescopes ($\theta_{\text{med}} = 5.5$ kpc; SD sample), respectively. The best-fit regression lines are shown by the blue solid and the black dashed line for the IT and SD samples, respectively. See also Section 4.2 for the derivation of each parameter and Section 4.3 for the details of the regression analysis. The best-fit regression parameters can be found in Table 4.3. Note that the interferometric data of NGC 6951 was not plotted in (a) because of the lack of absorption-corrected 2 – 10 keV X-ray luminosity in the literature. The doubled symbols denote type-2 AGNs.

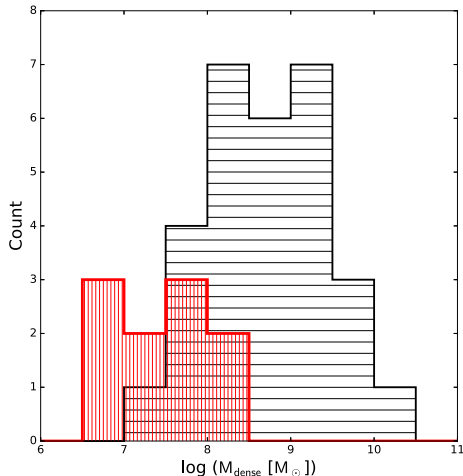


Figure 4.4: Distribution of $\log(M_{\text{dense}})$ of the IT sample (red, vertical line) and the SD sample (black, horizontal line). One may understand that their distributions can be approximated as single Gaussians. This supports the validity of our modeling of the prior distributions in the regression analysis (Section 4.3).

4.4 Results from the regression analysis

4.4.1 Positive $M_{\text{dense}} - \dot{M}_{\text{BH}}$ correlation

Based on the method described in Section 4.3, we achieved the posterior distribution of each regression parameter defined in Equation (4.4). For example, Figure 4.5 shows the distributions for the $M_{\text{dense}} - \dot{M}_{\text{BH}}$ correlation. The resulting best-fit parameters are summarized in Table 4.3 and the regression lines constructed with these values are overlaid on Figure 4.3 as our best-fit lines. We hereafter focus on the $M_{\text{dense}} - \dot{M}_{\text{BH}}$ correlation because it gives more physically meaningful information than the $L'_{\text{HCN}} - L_{2-10\text{keV}}$ correlation, although both will yield the same conclusions. We confirmed a similar correlation in the flux-flux plane as well.

The estimated parameters for both the IT and SD samples have relatively wide ranges, reflecting their limited statistics. Nevertheless, there is a positive correlation between these two quantities, particularly for the IT sample, as supported by the positive slope, the high correlation coefficient (>0.77) and the low intrinsic scatter; that is, *the more gas, the more active the AGN*. Here, the canonical null-hypothesis probability returned by `r_correlate` (0.033) also showed statistical significance at the 5% level. Because \dot{M}_{BH} is seemingly independent of M_{BH} (Collin & Kawaguchi 2004), our results suggest the importance of CNDs as the external drivers of AGN activity.

4.4.2 Virtual equivalence to the SFR – \dot{M}_{BH} correlations

To ignite and maintain AGN activity, a sufficient amount of molecular gas (= fuel) and the presence of physical mechanisms to cause/keep mass accretion are required. The former condition is surely satisfied for our sample because the measured M_{dense} of the CND is enough to keep the current \dot{M}_{BH} well beyond 100 Myr. Given the low \dot{M}_{BH} ($\lesssim 0.1 M_{\odot} \text{ yr}^{-1}$) and the likely prevalence of dusty, compact structures in the central regions of Seyfert galaxies (Martini et al. 2003; Simões Lopes et al. 2007) that indicates the coexistence of gaseous CNDs, the first condition could be satisfied in most Seyfert galaxies as well.

However, measured circumnuclear (i.e., $\lesssim 100$ pc scale) SFRs tend to far exceed \dot{M}_{BH} , by more than ~ 10 times, in Seyfert galaxies (e.g., Diamond-Stanic & Rieke 2012). This indicates that most of the dense gas in the CNDs would be consumed by such star formation. Even so, M_{dense} is massive enough to keep the current nuclear activity (i.e., $\dot{M}_{\text{BH}} + \text{SFR}$) over $\sim 10 - 100$ Myr so long as there is no massive in/outflow. From this perspective, we can state that the $M_{\text{dense}} - \dot{M}_{\text{BH}}$ correlation in Figure 4.3 is virtually equivalent to the SFR – \dot{M}_{BH} correlations (Diamond-Stanic & Rieke 2012; Esquej et al. 2014). In that sense, our results support the existence of the SFR – \dot{M}_{BH} correlation in an individual way. One advantage of using cold molecular gas measurements is that, today, we can achieve quite high resolutions with ALMA. This is essential in probing the CND scale of relatively distant galaxies. Less spectral contamination from an AGN itself is expected at millimeter/submillimeter bands than at optical/IR ones as well. Furthermore, quite high velocity resolutions necessary for kinematic modelings are easily achievable with ALMA, which is essential to study detailed gas transportation at the CND scale. Note that we can reproduce the slope of the SFR – \dot{M}_{BH} correlations at the CND using that of the $M_{\text{dense}} - \dot{M}_{\text{BH}}$ correlation and the linear conversion from M_{dense} to SFR (Gao & Solomon 2004b).

Our regression analysis also revealed that the correlation was tighter for the IT sample than the SD sample in a statistical sense (Figure 4.5, Table 4.3). That is, the IT sample showed a smaller scatter ($\sigma_{\text{int}} = 0.52^{+0.34}_{-0.29}$ dex) and a higher correlation coefficient ($\rho > 0.77$) than the SD sample ($\sigma_{\text{int}} = 1.19^{+0.18}_{-0.21}$ and $\rho = 0.35^{+0.18}_{-0.24}$), in the $M_{\text{dense}} - \dot{M}_{\text{BH}}$ plane. This dependence again traces that of the SFR – \dot{M}_{BH} correlations (Figure 1.15) and indicates that CND-scale gas can be an external regulator of mass accretion further inward, whereas an entire galactic-scale does not.

4.5 Discussion on the CND-scale fueling

In the previous Sections, we showed that there is a positive and fairly strong correlation between M_{dense} and \dot{M}_{BH} at CNDs, indicating that a more active AGN resides in a more gas-rich CND. However, as is also the case for the SFR – \dot{M}_{BH} correlation, this result does not manifest the physical mechanism(s) of mass accretion at this spatial scale. Thus, motivated by the arguments for the causal AGN–SB connection, here we try to speculate on accretion mechanisms (or the triggers of AGN activity). This could lead to important progress in the study of AGN fueling because accretion processes (even the dominant one) at $\sim 1 - 100$ pc scale region remain

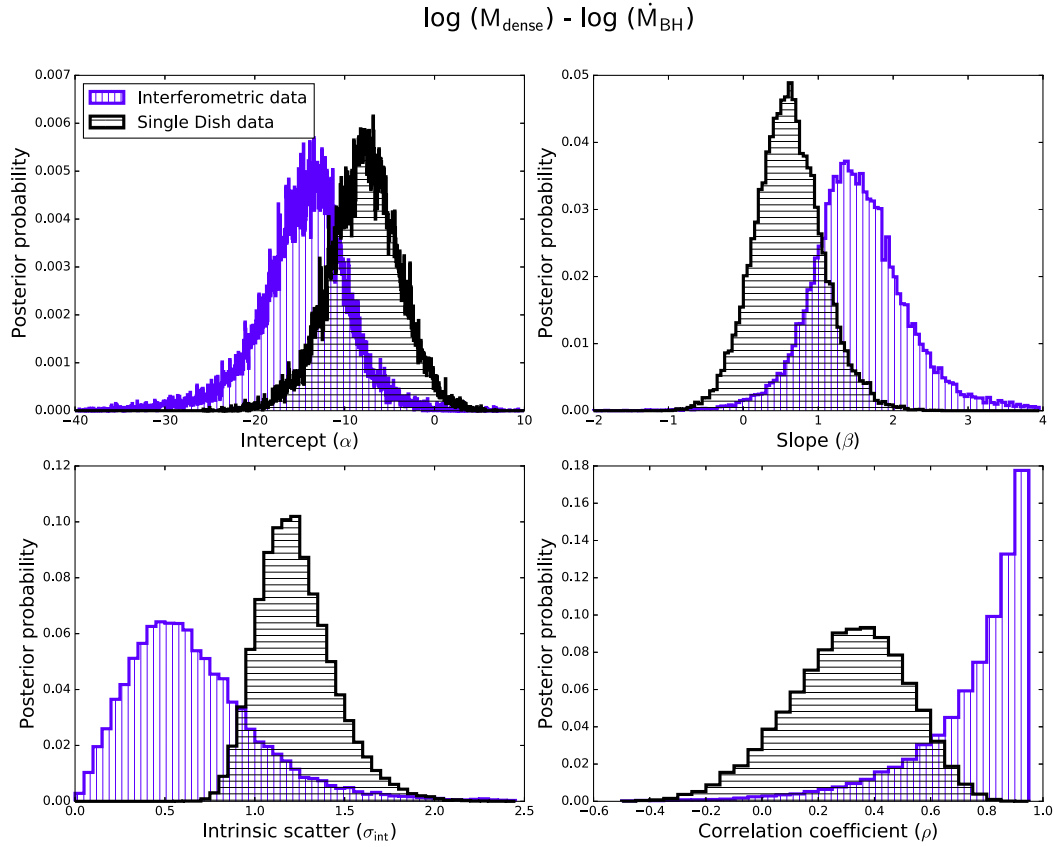


Figure 4.5: Posterior distributions for the intercept (α), slope (β), intrinsic scatter (σ_{int}), and correlation coefficient (ρ) for the $\log(M_{\text{dense}}) - \log(\dot{M}_{\text{BH}})$ relationship (Figure 4.3b). Colors indicate the IT (blue, vertical line) and SD (black, horizontal line) samples, respectively. The width of each bin is fixed to 0.05 in these plots. Note that the regression analysis for the $\log(L'_{\text{HCN}}) - \log(L_{2-10\text{keV}})$ yields essentially similar parameter distributions.

Table 4.3: Results from the regression analysis

Data	Median aperture	N_{sample}	α	β	σ_{int}	ρ	p
(1)	(2)	(3)	(4)	(5)	(6)	(7)	(8)
$\log(L'_{\text{HCN}}) - \log(L_{2-10\text{keV}})$ correlation							
IT-sample	220 pc	9	$34.77^{+2.64}_{-2.63}$	$1.06^{+0.40}_{-0.39}$	$0.59^{+0.30}_{-0.23}$	$0.89^{+0.07}_{-0.23}$	0.058
SD-sample	5.5 kpc	28	$38.29^{+2.52}_{-2.52}$	$0.46^{+0.33}_{-0.32}$	$1.04^{+0.19}_{-0.14}$	$0.31^{+0.19}_{-0.19}$	0.210
$\log(M_{\text{dense}}) - \log(\dot{M}_{\text{BH}})$ correlation							
IT-sample	220 pc	10	$-13.45^{+3.90}_{-5.25}$	$1.41^{+0.70}_{-0.56}$	$0.52^{+0.34}_{-0.29}$	>0.77	0.033
SD-sample	5.5 kpc	29	$-7.80^{+3.77}_{-3.76}$	$0.62^{+0.42}_{-0.52}$	$1.19^{+0.18}_{-0.21}$	$0.35^{+0.18}_{-0.24}$	0.270

Notes. We assumed the formulation of $\log \zeta = \alpha + \beta \times \log \xi + \epsilon$ (Section 4.3) for two regression pairs of $(\xi, \zeta) = (L'_{\text{HCN}}, L_{2-10\text{keV}})$ and $(M_{\text{dense}}, \dot{M}_{\text{BH}})$. Column 1: type of the sample. Column 2: the median aperture for HCN(1–0) measurement. Column 3: number of the sample used for the analysis. Data with an upper limit on L'_{HCN} (or M_{dense}) are excluded. Columns 4–7: the intercept (α), slope (β), intrinsic scatter (σ_{int}), and correlation coefficient (ρ) of the regression. The quoted values correspond to the mode of the posterior distribution and the range around it that encompasses 68% fraction of the distribution, based on the estimation from the IDL code `linmix_err` (Kelly 2007). Note that the distribution of ρ of the IT-sample does not show a clear turnover for the case of $\log(M_{\text{dense}}) - \log(\dot{M}_{\text{BH}})$ correlation. We thus show the lower limit of ρ instead, i.e., $0.77 \leq \rho \leq 1.00$ contains 68% of the posterior distribution. Column 8: null-hypothesis probability returned by the IDL code `r.correlate`.

unknown. Note that simple Eddington-limited accretion does not explain these Seyfert galaxies because the observed λ_{Edd} are well below unity (Figure 4.1).

As introduced in Section 4.1, to date, one of the most compelling pieces of evidence for a *causal* connection between AGN and (circumnuclear) starburst activities would be the observed $\sim 50 - 100$ Myr time delay between the onset of each activity (Davies et al. 2007; Schawinski et al. 2009; Wild et al. 2010). This supports the view that the preceding star formation event subsequently provides fuel for the AGN. With this in mind, we pick up the following two scenarios showing a *direct* connection between AGN and SB: *mass loss from evolved stars* (e.g., Ciotti et al. 1991; Davies et al. 2007; Norman & Scoville 1988; Padovani & Matteucci 1993) and *angular momentum loss due to SN-driven turbulence* (e.g., Kawakatu & Wada 2008; Wada & Norman 2002; Wada et al. 2009). Because of this simple treatment, as well as of insufficient observational constraints currently available, we emphasize that our discussion will not provide a complete view of CND-scale accretion. Rather, we seek to demonstrate one possible approach to tackle the fueling problem at this spatial scale, which should be expanded much greater detail with future high-resolution, high-sensitivity observations provided by ALMA.

4.5.1 Mass loss from evolved stars

The time delay between the SB and AGN activities can be reconciled by the scenario that winds from AGB stars accrete onto the SMBH (e.g., Norman & Scoville 1988) through the Bondi accretion (Bondi 1952). The relatively low speed of the winds (v_{wind}) from AGB stars is essential in this mechanism. Winds from OB stars or SNe are too fast to efficiently accrete through the Bondi mechanism as it indicates (Davies et al. 2007),

$$\dot{M}_{\text{BH}} \sim \frac{G^2 M_{\text{BH}}^2 \dot{M}_{\text{wind}}}{(v_{\text{wind}}^2 + c_s^2)^{3/2} v_{\text{wind}} R_*^2}, \quad (4.5)$$

where we can roughly expect $\dot{M}_{\text{BH}} \propto v_{\text{wind}}^{-4}$. Here, G is the gravitational constant, \dot{M}_{wind} is the mass-loss rate from AGB stars, c_s ($\sim 1 \text{ km s}^{-1}$) is the sound speed, and R_* is the distance from the star to the SMBH.

However, we suppose that there are two caveats on this mass loss scenario as follows.

- *Insufficient star formation*: models predict that galactic-scale $\text{SFR}/\dot{M}_{\text{BH}}$ to be ~ 1000 over the almost entire growth event for the mass loss scenario to provide sufficient fuel for the AGN (Wild et al. 2010), although the observed ratio at the CND scale is ~ 10 (e.g., Diamond-Stanic & Rieke 2012). Given that the star formation is usually a centrally-concentrated activity (Esquej et al. 2014), this discrepancy is hard to be reconciled. Note that, however, this scenario strongly depends on the evolutionary model of star forming activity, and Davies et al. (2007) provided a plausible one to explain both the time delay and the rather low $\text{SFR}/\dot{M}_{\text{BH}}$.
- *Ellipticals are the red and dead systems*: ellipticals are the systems of old stars typically hosting massive-end black holes ($M_{\text{BH}} > 10^8 M_{\odot}$; Kormendy & Ho 2013). Under this

situation, we can expect enhanced mass loss from evolved AGB stars (and more efficient Bondi accretion as that mechanism indicates $\dot{M}_{\text{BH}} \propto M_{\text{BH}}^2$). However, this type of galaxies usually show a quite low-level activities in actual.

With these caveats, rather than discarding this mass loss scenario, we push a SN-driven accretion scenario forward as described in the following. We also comment that recent high resolution observations show that the gas and stars form a disk-like structure rather than a spherical structure (e.g., Fathi et al. 2013; Hicks et al. 2013), which will reduce the \dot{M}_{BH} expected in the Bondi accretion. The currently observed low SFR/ \dot{M}_{BH} would not be in line with the radiation pressure supported disk model as well (Thompson et al. 2005), which requires SFR/ $\dot{M}_{\text{BH}} \sim 1000$.

4.5.2 Angular momentum loss due to SN-driven turbulence

Type II SNe occur after a certain time delay from the onset of the SB episode. That delay is 10 – 50 Myr for an SB event with an e -folding time scale (τ_{SB}) of 10 Myr (Davies et al. 2007). The delay naturally becomes longer as τ_{SB} increases. Indeed, along with large uncertainty, τ_{SB} can be as long as $\gtrsim 100$ Myr (e.g., Alonso-Herrero et al. 2013; Schawinski et al. 2009; Wild et al. 2010). Thus, SN-driven accretion will explain the observed $\sim 50 - 100$ Myr delay between the onsets of SBs and AGNs.

According to the numerical simulations of Wada & Norman (2002) and Wada et al. (2009), SNe inject strong turbulence into a CND, which effectively removes the angular momentum of the gas and increases \dot{M}_{BH} . From the observational side, a circumnuclear SFR is typically $0.1 - 1 M_{\odot} \text{ yr}^{-1}$ (Diamond-Stanic & Rieke 2012) for the IT sample. Integrating the Salpeter initial mass function over a stellar mass range of $0.1 - 125 M_{\odot}$ yields a type II SN rate of ~ 0.007 SFR (Wada et al. 2009). Then, the current SN rate of the IT sample is $\sim 10^{-3} - 10^{-2} \text{ yr}^{-1}$. Because even a CND with a low SN rate ($5.4 \times 10^{-5} \text{ yr}^{-1}$) shows a highly turbulent motion in the numerical simulation (Wada et al. 2009), it would seem reasonable to expect turbulence-driven accretion to occur in the sample CNDs. Moreover, kinematic analysis of the $\text{H}_2 1 - 0 \text{ S}(1)$ emission line clearly revealed that CNDs are highly turbulent, with a velocity dispersion of $\gtrsim 50 \text{ km s}^{-1}$ (or, an aspect ratio of the *warm* molecular disk ~ 1 ; Hicks et al. 2009).

Then we applied an analytical form of the SN-driven accretion model developed by Kawakatu & Wada (2008) to our observations. A typical SFR/ \dot{M}_{BH} is a few–10 in this model (see also Kawakatu & Wada 2009), which is consistent with the observations. Based on the viscous accretion model (Pringle 1981), they derived a mass accretion rate expected at the innermost radius (r_{in}) of a CND as

$$\left(\frac{\dot{M}_{\text{acc}}(r_{\text{in}})}{M_{\odot} \text{ yr}^{-1}} \right) = 3\pi\alpha_{\text{SN}}\mu_{\text{SN}}E_{\text{SN}}C_{*}\Sigma_{\text{dense}}(r_{\text{in}}) \left(\frac{r_{\text{in}}^3}{GM_{\text{BH}}} \right). \quad (4.6)$$

In this model, the turbulent pressure is assumed to be in the hydrodynamical equilibrium with gravity in the vertical direction. The so-called viscous-alpha parameter was invoked to express the viscous coefficient as $\nu_t(r) = \alpha_{\text{SN}}v_t(r)h(r)$, where $v_t(r)$ and $h(r)$ are the turbulent velocity and the scale height of the disk at the radius r from the center. E_{SN} is the total energy injected

by a single SN ($\sim 10^{51}$ erg), and μ_{SN} is the heating efficiency per unit mass that bridges E_{SN} and the kinetic energy of the gaseous matter. This energy input from SNe is balanced with dissipation due to the turbulence. C_* , Σ_{dense} , and G are the star formation efficiency ($\equiv \text{SFR}/M_{\text{dense}}$), the gas surface-density of the disk⁸, and the gravitational constant, respectively.

Regarding the dependence of Equation (4.6) on each parameter, we emphasize the following two points that match observations well.

- *H₂ surface brightness*: Recent VLT observations of the 2.12 μm H₂ 1 – 0 S(1) emission line revealed that CNDs of AGNs show systematically higher H₂ surface brightness than those of inactive galaxies (Hicks et al. 2013). If we assume enhanced H₂ is a reflection of gas mass, this is consistent with the form of $\dot{M}_{\text{acc}} \propto \Sigma_{\text{dense}}$.
- *Black hole mass*: From Tables 4.1 and 4.2, we found that, for example, NGC 1097 and NGC 2273 have comparable M_{dense} , whereas their \dot{M}_{BH} are totally different: NGC 1097 shows a ~ 150 times smaller value. However, NGC 1097 has a ~ 20 times larger M_{BH} than NGC 2273. Thus, we expect that including M_{BH} in a negative form into \dot{M}_{BH} like $\propto M_{\text{BH}}^{-1}$ would better reproduce the trend in \dot{M}_{BH} . This is indeed the proposed formulation of \dot{M}_{acc} .

These points provided our motivation to apply Equation (4.6) to the actual observations. The negative dependence on M_{BH} indicates that a suppressed scale height of the disk, due to strong gravity from the SMBH itself, reduced the turbulent viscosity inside the disk, and \dot{M}_{acc} accordingly. We also note that Equation (4.6) does not necessarily disagree with the results of Collin & Kawaguchi (2004), who claimed that \dot{M}_{BH} seemed to be independent of M_{BH} , because we now include not only M_{BH} but also Σ_{dense} as controlling parameters of mass accretion.

One might question whether ongoing star formation can have a direct link with the ongoing AGN activity in terms of the time scale. The viscous time scale from the radius r of the CND ($\tau_{\text{vis,CND}}$) can be determined by the viscous coefficient ν_t as

$$\tau_{\text{vis,CND}} = \frac{r^2}{\nu_t} = \frac{r^2}{\alpha_{\text{SN}} v_t(r) h(r)} \quad (4.7)$$

Putting $r = 30$ pc, $v_t(r = 30 \text{ pc}) = 50 \text{ km s}^{-1}$, $h(r = 30 \text{ pc}) = 30$ pc (these are typically observed values in H₂ 1 – 0 S(1) disks; Hicks et al. 2009) and $\alpha_{\text{SN}} = 1$ as our fiducial values, we obtain $\tau_{\text{vis,CND}} \sim 1$ Myr, which is comparable to the dynamical time. On the other hand, using the free-fall time from the radius r' to the center (τ_{ff}), the viscous time scale inside the accretion disk ($\tau_{\text{vis,disk}}$) is

$$\tau_{\text{vis,disk}} \sim \frac{\tau_{\text{ff}}}{\alpha_{\text{disk}} (h/r')^2}, \quad (4.8)$$

where α_{disk} denotes the viscous alpha-parameter in the accretion disk (Pringle 1981; Shakura & Sunyaev 1973). We consider the accretion disk with $r' = 0.1$ pc (typical size of water maser disks, hence the upper limit on the size of the AGN accretion disks; Kuo et al. 2011) around

⁸We use the subscript *dense* considering the high densities of the CNDs.

the SMBH with $10^7 M_\odot$. Numerical simulations reported $\alpha_{\text{disk}} = 0.01 - 0.1$ due to magneto-rotational instability in the disk (e.g., Machida & Matsumoto 2003). Thus, putting $\alpha_{\text{disk}} = 0.1$ and $(h/r') = 0.01$ (typical value assumed in standard disk models) in Equation (4.8), we obtain $\tau_{\text{vis,disk}} \sim 20$ Myr. Consequently, we suggest that the total accretion time scale from the CND to the center is at most a few $\times 10$ Myr. This is comparable to, or even smaller than, the typical $\tau_{\text{SF}} (\gtrsim 10 - 100$ Myr, Alonso-Herrero et al. 2013; Schawinski et al. 2009; Wild et al. 2010). Therefore, it does seem to be plausible for CNDs and the star formation that occurs inside them to have a *causal* link with on-going AGN activities.

Comparison with observations

Next we compared the model-predicted accretion rates with the observed values. We restricted the analysis to the IT sample only, because galactic-scale molecular gas would have no relevance to current AGN activity, as we saw in Section 4.4. Again, we note that this discussion is rather speculative with large uncertainties, and should be tested with larger samples based on future observations. One important issue is that most of the CNDs are not resolved spatially at the HCN(1 – 0) emission line, so we cannot measure Σ_{dense} directly. Thus, we simply assume that the dense gas is uniformly distributed within a CND and then reduce Equation (4.6) to

$$\left(\frac{\dot{M}_{\text{acc}}(r_{\text{in}})}{M_\odot \text{ yr}^{-1}} \right) \sim 0.13 \left(\frac{\alpha_{\text{SN}}}{1} \right) \left(\frac{r_{\text{in}}}{3 \text{ pc}} \right)^3 \left(\frac{r_{\text{out}}}{30 \text{ pc}} \right)^{-2} \cdot \left(\frac{C_*}{10^{-7} \text{ yr}^{-1}} \right) \left(\frac{M_{\text{dense}}}{M_{\text{BH}}} \right). \quad (4.9)$$

Here, the model-simulated fiducial values of $\mu_{\text{SN}} = 10^{-3} M_\odot^{-1}$ and $\alpha_{\text{SN}} \sim 1$ are used (Wada & Norman 2002).

Regarding the outer radii (r_{out}) of disks, we assume that they are identical to the HWHM of the H₂ 1 – 0 S(1) emission disks (Hicks et al. 2009). The values are listed in Table 4.4 after correcting the distance to each object. A basis of this assumption is the fact that a 100 pc scale spatial distributions of the H₂ 1 – 0 S(1) emission line and those of the CO and HCN emission lines are almost identical in NGC 1068 (Figure 4.6). With this constraint, we will focus on the IT sample with the high-resolution H₂ 1 – 0 S(1) information in Hicks et al. (2009), namely, NGC 1097, NGC 3227, NGC 4051, and NGC 7469, in the following analysis. Note that we excluded NGC 1068 from this specific investigation because the innermost ~ 10 pc scale regions of its CND show considerably complex substructures that are likely reflecting strong AGN feedback events (Hicks et al. 2009), which violates our assumption of the uniform gas distribution inside a CND as stated above.

For the disk inner radius (r_{in}), Kawakatu & Wada (2008) defined it as the dust sublimation radius, which we believe has limited meaning. Because we are now trying to apply the *SN-driven* turbulence model, star formation must occur prior to SN explosions. However, we would not expect star formation in the gas disk with a temperature as high as, for example, > 1000 K. Alternatively, we consider two other radii. The first is the radius at which the fractional

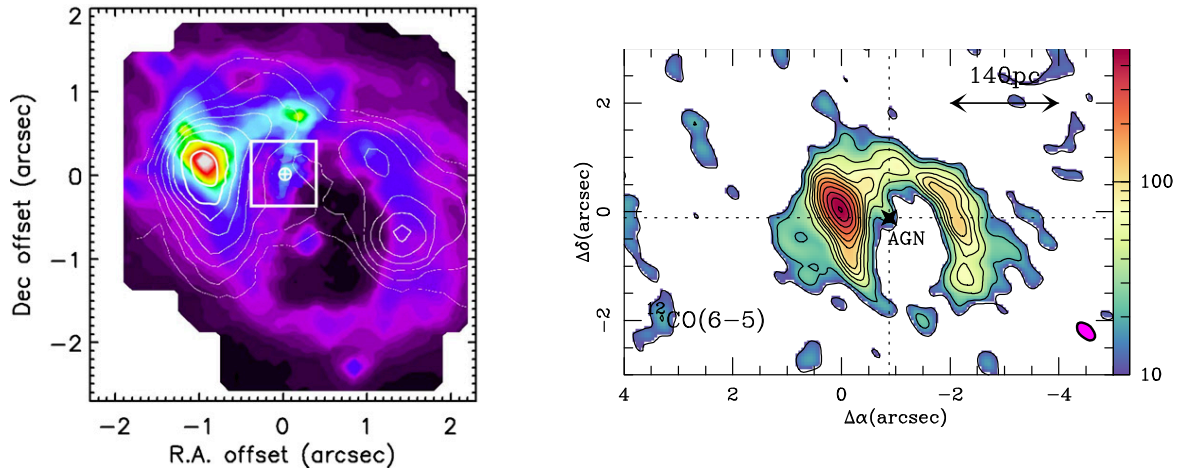


Figure 4.6: Spatial distributions of (*left*) $2.12 \mu\text{m}$ H_2 $1-0$ S(1) line (color; Müller Sánchez et al. 2009) and (*right*) $^{12}\text{CO}(J = 6 - 5)$ line ($\text{Jy beam}^{-1} \text{ km s}^{-1}$ unit, García-Burillo et al. 2014) in the CND of NGC 1068. Their distributions, especially at the outer envelope, resemble well with each other, which constitutes the basis of our assumption of the similar co-spatial distribution of these emission lines in other Seyfert galaxies.

abundance (f) of H_2 becomes equivalent to that of HI, i.e., $f(\text{H}_2) = f(\text{HI})$. We argue this because stars are born from molecular gas. In close vicinity to AGNs, strong X-ray irradiation can substantially alter gas physics and chemistry (XDR; Lepp & Dalgarno 1996; Maloney et al. 1996). Thus, we calculate this radius (denoted as r_X) following Equation (2) of Maloney et al. (1996). According to their calculation, we can estimate r_X as the radius at which the ratio of X-ray energy deposition rate per particle takes $\log(H_X/n_H) = -27.5$. Note that in the region with $\log(H_X/n_H) < -27.5$, the gas temperature is $\sim 10\text{s} - 100$ K. A gas volume density of $n_{\text{H}_2} = 10^6 \text{ cm}^{-3}$ (here, we regard $n_H = n_{\text{H}_2}$) is adopted based on a recent high-resolution multi-transitional study towards the center of NGC 1068 (Viti et al. 2014), although another value in the range of $n_{\text{H}_2} \sim 10^{5-7} \text{ cm}^{-3}$ would not change our argument. The X-ray luminosity in Table 4.1 was used here to derive r_X , listed in Table 4.4. However, even if molecular hydrogen exists, stars cannot be formed unless the gas becomes gravitationally unstable. Thus, we estimated the radius at which the Toomre-Q parameter (e.g., Toomre 1964) became unity, i.e.,

$$Q \equiv \frac{\kappa(r)c_s}{\pi G \Sigma_{\text{dense}}} = 1, \quad (4.10)$$

where κ is the epicyclic frequency, c_s ($\sim 1 \text{ km s}^{-1}$) is the sound speed, and G is the gravitational constant. The spatially averaged gas surface density $\Sigma_{\text{dense}} \sim M_{\text{dense}}/\pi r_{\text{out}}^2$ was used. The radius r_Q in Table 4.4 was derived in this way. Using these two radii, we regard the *effective* innermost radius as $r_{\text{in,eff}} = \max[r_X, r_Q]$.

To obtain C_* , we used SFR measured with a comparable aperture to that of the $\text{HCN}(1-0)$ measurements, as $C_* = \text{SFR}/M_{\text{dense}}$. This SFR was estimated with the $11.3 \mu\text{m}$ PAH emission

(Diamond-Stanic & Rieke 2012; Esquej et al. 2014). Because of the mechanism invoked by the model, we consider that there is no star formation inside $r_{\text{in,eff}}$.

Following the above, we estimated \dot{M}_{acc} with Equation (4.9), as tabulated in Table 4.4. The uncertainty was assumed to be primarily driven by that of $M_{\text{dense}}/M_{\text{BH}}$ for simplicity, because those of the other parameters are not well constrained. Note that this \dot{M}_{acc} is now an accretion rate at $r_{\text{in,eff}}$. Figure 4.7 compares the resulting \dot{M}_{acc} with the observed \dot{M}_{BH} . According to this SN-driven accretion model, one can find $\dot{M}_{\text{acc}} \sim \dot{M}_{\text{BH}}$ in NGC 7469 and NGC 3227, indicating that most of the mass accreted from their $r_{\text{in,eff}}$ goes to black hole accretion directly. In contrast to these objects, \dot{M}_{BH} was only $\sim 10\%$ or less of \dot{M}_{acc} in NGC 1097 and NGC 4051, respectively. Thus, only a small fraction of the accreting gas from the CND contributed to growing the SMBH in these galaxies. In the latter case, we need some other process(es) to account for the missing mass flows.

Table 4.4: Parameters of the CNDs for the model prediction

Target (1)	r_{out} (2)	r_{X} (3)	r_{Q} (4)	SFR/aperture (5)	Ref. (6)	C_* (7)	$\log(M_{\text{acc}})$ (8)	$\log(M_{\text{wind}})$ (9)	Ref. (10)
NGC 1097	28.8	0.38	2.1	0.14/250	1	2.7×10^{-9}	-3.32 ± 0.32	-	-
NGC 3227	34.9	0.95	2.0	0.07/60	2	3.4×10^{-9}	-2.87 ± 0.43	-	-
NGC 4051	7.6	0.46	0.43	0.11/140	1	2.9×10^{-8}	-2.22 ± 0.33	-2.39	3,4
NGC 7469	30.8	2.2	0.84	1.19/260	2	6.0×10^{-9}	-1.20 ± 0.30	-1.22	5

Notes. Column 1: name of the sample galaxy that has both the interferometric HCN(1 – 0) emission data and high resolution H₂ 1 – 0 S(1) data (Hicks et al. 2009). Column 2: the outermost radius of the CND [pc]. Column 3: the critical radius [pc] that satisfies the condition of $f_{\text{H}_2} = f_{\text{HI}}$ from XDR calculations (Maloney et al. 1996). Column 4: the critical radius [pc] that satisfies the condition of $Q = 1$. Column 5: estimated SFR [$M_{\odot} \text{ yr}^{-1}$] based on the 11.3 μm PAH emission and the (geometrically averaged) circular aperture [pc] for the measurement. Column 6: reference for Column 5. Column 7: estimated SFE [yr^{-1}] by using SFR in Column 5 and M_{dense} of the CND as $C_* = \text{SFR}/M_{\text{dense}}$. Column 8: logarithmic scale value of mass accretion rate [$M_{\odot} \text{ yr}^{-1}$] at $r_{\text{in,eff}} = \max[r_{\text{Q}}, r_{\text{X}}]$ based on the SN-driven turbulence model (Kawakatu & Wada 2008). We assume that the uncertainty is driven by that of $M_{\text{dense}}/M_{\text{BH}}$ for simplicity. Columns 9 and 10: logarithmic scale value of the observed mass outflow rate [$M_{\odot} \text{ yr}^{-1}$] in the X-ray warm absorber and UV absorber found in literature, and the reference for them. References: (1) Diamond-Stanic & Rieke (2012), (2) Esquej et al. (2014), (3) Krongold et al. (2007), (4) Kraemer et al. (2012), (5) Blustin et al. (2007).

Other components of the mass budget—gaseous outflow

In a more realistic situation, we suggest $\dot{M}_{\text{acc}} \neq \dot{M}_{\text{BH}}$ in general, because the accreted mass from the CND can be expelled in other ways, such as nuclear winds (e.g., Genzel et al. 2010). Such winds may compensate for the discrepancy between \dot{M}_{acc} and \dot{M}_{BH} in NGC 1097 and NGC 4051. In this scenario, if the mass flow at the accretion disk scale can be solely ascribed to either black hole accretion (\dot{M}_{BH}) or the winds (\dot{M}_{wind}), the following relation should hold:

$$\dot{M}_{\text{acc}} = \dot{M}_{\text{BH}} + \dot{M}_{\text{wind}} \equiv \dot{M}_{\text{nuclear}}. \quad (4.11)$$

This situation is described schematically in Figure 4.8.

Unfortunately, among our sample, \dot{M}_{wind} is available only for NGC 7469 and NGC 4051 (Table 4.4) in the literature. Here, we considered the winds observed as X-ray/UV warm absorbers only, because these components are highly likely to be located in close vicinity to the accretion disks. However, AGN winds observed in atomic or molecular lines would be emanating from regions far outside the BLR, of which \dot{M}_{wind} are substantially mass-loaded by the surrounding ISM.

Finally, we compare \dot{M}_{acc} with \dot{M}_{nuclear} in Figure 4.9. Only the uncertainty of \dot{M}_{BH} is shown here because that of \dot{M}_{wind} is not clearly stated in the references. However, we note that the uncertainty of \dot{M}_{wind} may be quite large because it critically depends on the currently unconstrained nuclear geometry and volume filling factor of the outflowing gas. That aside, it is remarkable that both NGC 7469 and NGC 4051 show good agreement of $\dot{M}_{\text{CND}} \sim \dot{M}_{\text{nuclear}}$ (Figure 4.9). Note that NGC 7469 already showed $\dot{M}_{\text{CND}} \sim \dot{M}_{\text{BH}}$, i.e., \dot{M}_{wind} is not so prominent compared to \dot{M}_{BH} for this object.

Based on these results, it seems that we are likely describing the balance of mass flows at the nuclear regions of Seyfert galaxies (Equation (4.11)). However, our results are tentative due to the small sample size, and are based on simplified assumptions. Moreover, not all of the expected uncertainties are included in Figures 4.7 and 4.9, largely due to exact uncertainties are not constrained at this moment. Thus, high-resolution observations of dense molecular gas with ALMA to measure Σ_{dense} directly, and for example, high-sensitivity UV/X-ray spectroscopy to measure \dot{M}_{wind} robustly, are needed to further improve our understanding of circumnuclear mass accretion processes, including other mechanisms beyond this SN-driven accretion model.

4.5.3 Implications for the evolution of AGNs

As shown in Equations (4.6) and (4.9), \dot{M}_{acc} in the SN-driven accretion model depends negatively on M_{BH} , i.e., $\dot{M}_{\text{acc}} \propto M_{\text{BH}}^{-1}$. This is a totally different dependence from those assumed in Eddington-limited accretion ($\propto M_{\text{BH}}$) and Bondi accretion ($\propto M_{\text{BH}}^2$). Because of this dependence, for a given M_{dense} (or Σ_{dense}), it becomes more difficult for an SMBH to grow as its M_{BH} becomes larger. Observationally, under this SN-driven scenario, the growth factor of M_{BH} in the coming ~ 100 Myr would be at most ~ 2 for our samples, considering the low \dot{M}_{BH} currently observed, unless massive inflows occur from the host galaxies into the CNDs to forcibly enhance

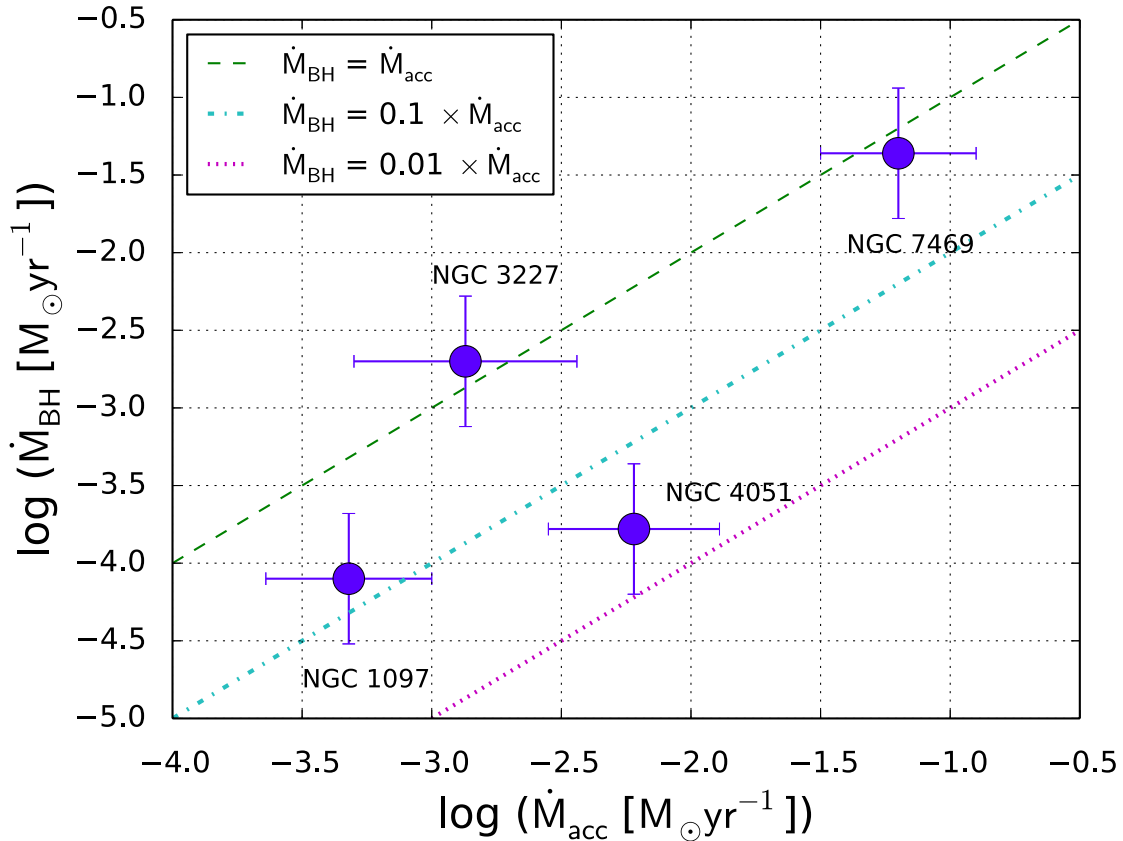


Figure 4.7: Scatter plot of the mass accretion rate at the *effective* innermost radius ($r_{\text{in,eff}}$) of the CNDs (\dot{M}_{acc}) predicted by the SN-driven turbulence model (Kawakatu & Wada 2008), and the black hole accretion rate (\dot{M}_{BH}). The overlaid lines indicate that \dot{M}_{BH} is 100% (green, dashed), 10% (cyan, dot-dashed), and 1% (magenta, dotted) of \dot{M}_{acc} . In NGC 3227 and NGC 7469, we found $\dot{M}_{\text{BH}} \sim \dot{M}_{\text{acc}}$, indicating that most of the mass accreted from $r_{\text{in,eff}}$ directly went to the black hole accretion. However, $\dot{M}_{\text{BH}} \ll \dot{M}_{\text{acc}}$ in NGC 1097 and NGC 4051. Although not all of the uncertainties are explicitly included in both \dot{M}_{acc} and \dot{M}_{BH} , this discrepancy would suggest other sources of mass flow, e.g., disk winds (see also Figures 4.8 and 4.9).

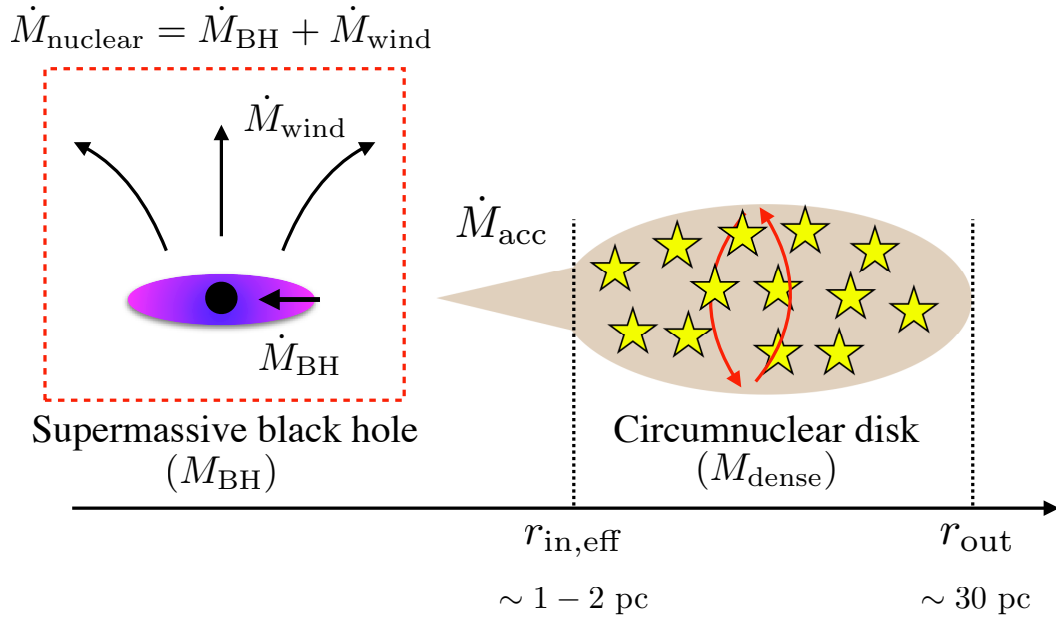


Figure 4.8: Schematic of the SN-driven turbulent accretion model, describing the parameters used for Figures 4.7 and 4.9. The vertical height of the circumnuclear disk (CND) is supported by the turbulent pressure due to SN explosions. $r_{\text{in,eff}}$ and r_{out} are the effective innermost radius and the outermost radius, respectively, of the CND (see Section 4.5.2 for details). This CND, with a gas mass of M_{dense} , fuels the nuclear (accretion disk-scale) events at the rate of \dot{M}_{acc} in the form of either black hole mass accretion (\dot{M}_{BH}) or nuclear wind (\dot{M}_{wind}). We combine these two events into \dot{M}_{nuclear} .

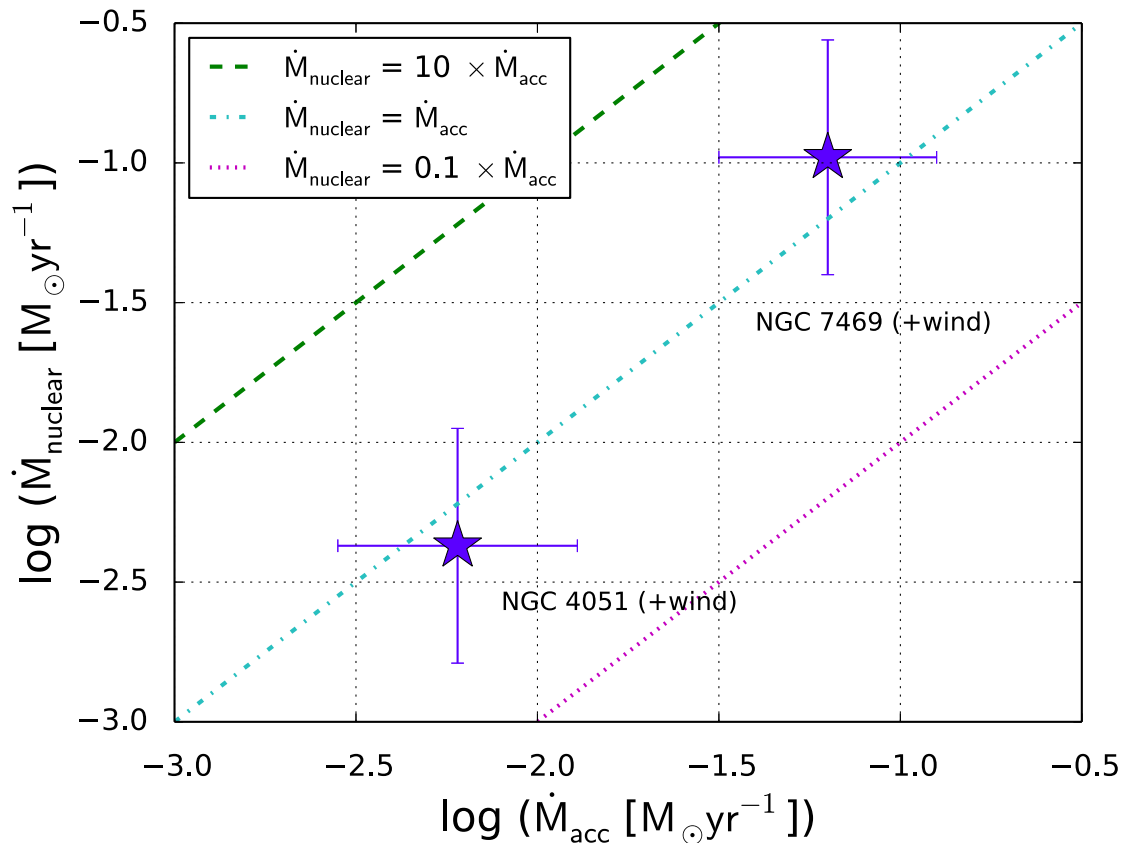


Figure 4.9: Scatter plot of the mass accretion rate at the *effective* innermost radius ($r_{\text{in,eff}}$) of the CNDs (\dot{M}_{acc}) predicted by the SN-driven turbulence model (Kawakatu & Wada 2008), and the total mass flow rate at the nuclear (accretion disk-scale) region ($\dot{M}_{\text{nuclear}} \equiv \dot{M}_{\text{BH}} + \dot{M}_{\text{wind}}$; see also Figure 4.8). The overlaid lines indicate that \dot{M}_{nuclear} is 1000% (green, dashed), 100% (cyan, dot-dashed), and 10% (magenta, dotted) of \dot{M}_{acc} . There is remarkable agreement between \dot{M}_{nuclear} and \dot{M}_{acc} in NGC 4051 and NGC 7469.

Σ_{dense} . Because the total lifetime of AGNs would be $\sim 10^{8-9}$ yr (e.g., Marconi et al. 2004), most of the SMBH accretion would have occurred in the distant past, at the early epoch of their evolution, when $M_{\text{BH}} \ll M_{\text{dense}}$ was surely satisfied. Kawaguchi et al. (2004) claimed that most growth of SMBHs occurred in the super-Eddington phase when they were young, whereas the growth rate in the sub-Eddington phase is small. Such a super-Eddington accretion can be allowed in this SN-driven model, for example, for an SMBH with $M_{\text{BH}} = 10^{5-6} M_{\odot}$ embedded in a CND of $M_{\text{dense}} \gtrsim 10^8 M_{\odot}$, judging from Equation (4.9).

However, it is highly challenging to form SMBHs with $M_{\text{BH}} \gtrsim 10^9 M_{\odot}$ typically found in local elliptical galaxies (e.g., Kormendy & Ho 2013) and high redshift quasars even at $z > 6 - 7$ (e.g., Mortlock et al. 2011) with this SN-driven accretion. If such black holes accumulated their mass within 10^9 yr (Marconi et al. 2004), the average mass accretion rate would be $\sim 1 M_{\odot} \text{ yr}^{-1}$. Even if we assume a quite high C_* , such as 10^{-7} yr^{-1} , which is an upper value observed in submillimeter galaxies (Solomon & Vanden Bout 2005), $\gtrsim 10^{10} M_{\odot}$ molecular gas should be accumulated in the CND within 10^9 yr and should remain there for almost over the entire period of SMBH growth. This mass is comparable to the total (i.e., galactic scale) amount of dense molecular gas observed in high redshift quasars (e.g., Wang et al. 2011) as well as nearby galaxies (see the case of the SD sample in Figure 4.3b). This, in turn, indicates the difficulty forming high mass-end SMBHs because it is highly unlikely for a galaxy to confine all of its molecular gas inside the CND (central ~ 100 pc).

Regarding lower-mass SMBHs, by assuming $\sim 10\%$ of the total dense molecular gas of the galaxy is in the CND, it would be possible to form an SMBH with $\sim 10^8 M_{\odot}$, based on the same speculation described above. Moreover, the formation of black holes in this mass range ($M_{\text{BH}} \lesssim 10^8 M_{\odot}$) could have followed a downsizing trend (Ueda et al. 2014, 2003) because high-redshift galaxies tend to show higher C_* (Solomon & Vanden Bout 2005), which controls \dot{M}_{acc} . To make high mass-end SMBHs ($M_{\text{BH}} \gtrsim 10^9 M_{\odot}$), we need some other mechanism(s), such as mergers of black holes or long-lasting mass inflows from intergalactic space.

4.6 Conclusions of This Chapter

Motivated by the $\text{SFR} - \dot{M}_{\text{BH}}$ correlation, (e.g., Diamond-Stanic & Rieke 2012; Esquej et al. 2014), we investigated the correlation between the mass of dense molecular gas (M_{dense}) traced by the HCN(1–0) emission line and the black hole mass accretion rate (\dot{M}_{BH}) in nearby Seyfert galaxies, with a Bayesian-based regression analysis. Most of the data were compiled from the literature and/or the ALMA archive. Because of the high spatial resolution provided by the interferometers (PdBI, NMA, and ALMA), we could probe molecular gas at the CND-scale. Our main conclusions are summarized as follows.

- There is a positive correlation between M_{dense} and \dot{M}_{BH} at the CND-scale. Because dense molecular gas is the site of star formation, this correlation is virtually equivalent to the (nuclear) $\text{SFR} - \dot{M}_{\text{BH}}$ correlations found so far. Thus, it seems that we succeeded in rebuilding the $\text{SFR} - \dot{M}_{\text{BH}}$ correlations individually from the perspective of cold molecular

gas observations.

- The $M_{\text{dense}} - \dot{M}_{\text{BH}}$ correlation is significantly tighter for the sample where the HCN(1–0) emission line was measured at the CND scale (IT sample; $\theta_{\text{med}} = 220$ pc) than for the sample measured at the galactic scale (SD sample; $\theta_{\text{med}} = 5.5$ kpc). This is again consistent with the trend found in the SFR – \dot{M}_{BH} correlations, suggesting that CND-scale molecular gas plays an important role in fueling AGNs, whereas the galactic-scale molecular gas does not.
- Assuming that star formation in CNDs directly provides fuel for AGNs, we adopted an SN-driven turbulent accretion scenario (Kawakatu & Wada 2008). Although there are still large observational uncertainties in the parameters needed for the model (and not all of the uncertainties are explicitly addressed in this study), direct comparisons of the model-predicted \dot{M}_{acc} (= mass accretion rate at the innermost radius of the CND to further inwards) with \dot{M}_{BH} were conducted. We found that only a partial fraction (from $\lesssim 10\%$ to $\sim 100\%$) of \dot{M}_{acc} was converted into \dot{M}_{BH} in general.
- On the other hand, we also found good agreement between $\dot{M}_{\text{nuclear}} = \dot{M}_{\text{BH}} + \dot{M}_{\text{wind}}$ (mass outflow rate as nuclear winds) and model-predicted \dot{M}_{acc} in NGC 4051 and NGC 7469. This result would suggest that we now might be describing the balance of mass flow in the nuclear regions of these Seyfert galaxies, although this view is based on the tentative and simplified assumptions in this work. We suggest that high-resolution observations of dense molecular gas with ALMA to accurately measure Σ_{dense} , as well as, for example, high-sensitivity spectroscopic observations of nuclear winds in the UV/X-ray bands are needed to better understand the validity of this SN-driven accretion model.

Because we used the SN-driven accretion model as a demonstration of one possible approach for studying CND-scale accretion processes in the ALMA era, we should, of course, test other models (e.g., mass-loss from evolved stars) quantitatively by increasing the number of high-resolution measurements of CND-scale dense gas.

Chapter 5

Summary and Future Outlook

5.1 Summary of This Thesis

The main scope of this thesis is to better understand physical links between AGNs and SBs in the central regions of Seyfert galaxies, as well as their feedback on the surrounding ISM, through high resolution, high sensitivity molecular gas observations (Figure 1.3). Particular interest has been directed towards the ~ 100 pc scale CNDs frequently found at the centers of galaxies, of which spatial scale has been the missing link in the continuous flow of mass from the host galaxies to the SMBHs.

Despite its importance in probing the CND scale activities, previous observations of molecular gas towards active galaxies were mostly conducted with single dish telescopes, which traced the total molecular gas at spatial resolutions of \gtrsim kpc, except for some very nearby galaxies. Moreover, since such studies mostly used CO lines having low critical densities, they could not efficiently or selectively probe the properties of the CND scale, where the gas density is typically very high. Motivated by these facts, in this work, we used the high resolution, high sensitivity measurements of dense gas tracers mainly provided by ALMA. Adding the data compiled from the archive and the literature, we established the large dataset of such emission lines from the CND scale gas.

At first, we attempted to construct and propose an energy diagnostic method by picking up potential variations in molecular chemistry caused by different heating sources. The enhanced $\text{HCN}(4-3)/\text{HCO}^+(4-3)$ and $\text{HCN}(4-3)/\text{CS}(7-6)$ ratios in AGNs as compared to SB galaxies (submm-HCN enhancement) revealed in Izumi et al. (2013) with a small number of the sample was the starting point of our investigation. Based on the analysis of 25 data points (16 galaxies), we found that the similarly high line ratios commonly in AGNs, when the data was taken at the CND scale, which supports the validity of the combination of those spectral features as an energy diagnostic method. On the other hand, we could not see a clear trend of such enhancements for the data of AGNs taken at the galactic scale apertures (> 1 kpc) with single dish telescopes. This might be due to a significant contamination to the line flux from the surrounding and/or co-existing star forming regions, which is suggestive of the importance of high resolution observations to accurately measure line ratios representative in AGNs.

In order to investigate the cause of the high line ratios in AGNs, we conducted non-LTE radiative transfer modelings of the above molecular emission lines involving both collisional and radiative excitation as well. Then, we found that enhanced $X_{\text{HCN}}/X_{\text{HCO}^+}$ and $X_{\text{HCN}}/X_{\text{CS}}$ in AGNs as compared to SB galaxies by a factor of a few to even ~ 10 are required to reproduce the submillimeter HCN-enhancement. Note that, although a systematically higher gas density in AGNs than in SB galaxies can also reproduce the trend, it would be unlikely considering the fact that the excitation states of these dense gas tracers in galaxies having various nuclear types have no clear trend. Hence, we suggest that the abnormal chemical composition in AGNs would be the prime cause of the submillimeter-HCN enhancement. Regarding the actual mechanism to realize the chemical composition with enhanced X_{HCN} , we suggest that it is difficult with the conventional gas-phase ionization chemistry expected in XDRs. We would have to take into account other mechanisms instead, such as neutral-neutral reactions that are efficiently activated in high temperature environments and/or mechanically heated regions, to better reproduce the high line ratios in AGNs.

While the above topic is related to the CND scale molecular chemistry, we also investigated the possibility of detecting submillimeter HI RLs from the ionized BLRs of AGNs with ALMA, which can be another way to probe the sub-pc scale structure of AGNs as well as to robustly argue the existence of an AGN even in the dust obscured nucleus. However, unfortunately, we found that such emission lines from BLRs are so faint based on our analytical estimation that it is quite impractical to detect them even with ALMA. This speculation is further supported by the actual data showing the non-detection of H26 α line from NGC 1068.

At last, we analyzed the compiled set of HCN(1–0) emission line data to estimate the M_{dense} at the CND scale (10 objects) as well as at the galactic scale (32 objects) of Seyfert galaxies. We found that the M_{dense} of the CNDs are sufficiently large ($\sim 10^{7-8} M_{\odot}$) to keep the current nuclear activity (AGN + SB) for more than 10 Myr. Furthermore, we revealed a positive correlation between the M_{dense} and the \dot{M}_{BH} onto the SMBHs. Note that this is the first time to identify a correlation between the properties of molecular gas and the AGN power at this spatial scale, and the correlation is suggestive of the importance of the CNDs as external sources of fuel for (or triggers of) the AGN activities. At the CND scale, it has been argued that the \dot{M}_{BH} and the star formation rate (SFR) there are positively correlated, suggestive of that the mass accretion onto SMBHs are regulated by star formation (AGN–SB connection). As the stars are born from dense gas, the correlation we found would be a reflection of the SFR– \dot{M}_{BH} correlation. Then, by assuming that the correlation is causal, we tried to explain its origin with the SN-induced turbulent accretion model (Kawakatu & Wada 2008). As a result, we found that only a partial fraction of the mass from the CND (\dot{M}_{acc}) is accreting onto the SMBH. However, we also found that \dot{M}_{acc} and the summation of (i) \dot{M}_{BH} and (ii) mass outflow rate from an accretion disk (\dot{M}_{wind}), are well balanced, i.e., $\dot{M}_{\text{acc}} \simeq \dot{M}_{\text{BH}} + \dot{M}_{\text{wind}}$. This indicates that we might start to dissolve the balance of mass flows at the CND scale for the first time.

Therefore, as an overall result from the thesis, we succeeded in (1) catching the trends of the feedback from AGNs on the molecular gas (especially chemistry) that is applicable to a new energy diagnostic method free from dust extinction, (2) reproducing the AGN–SB connection

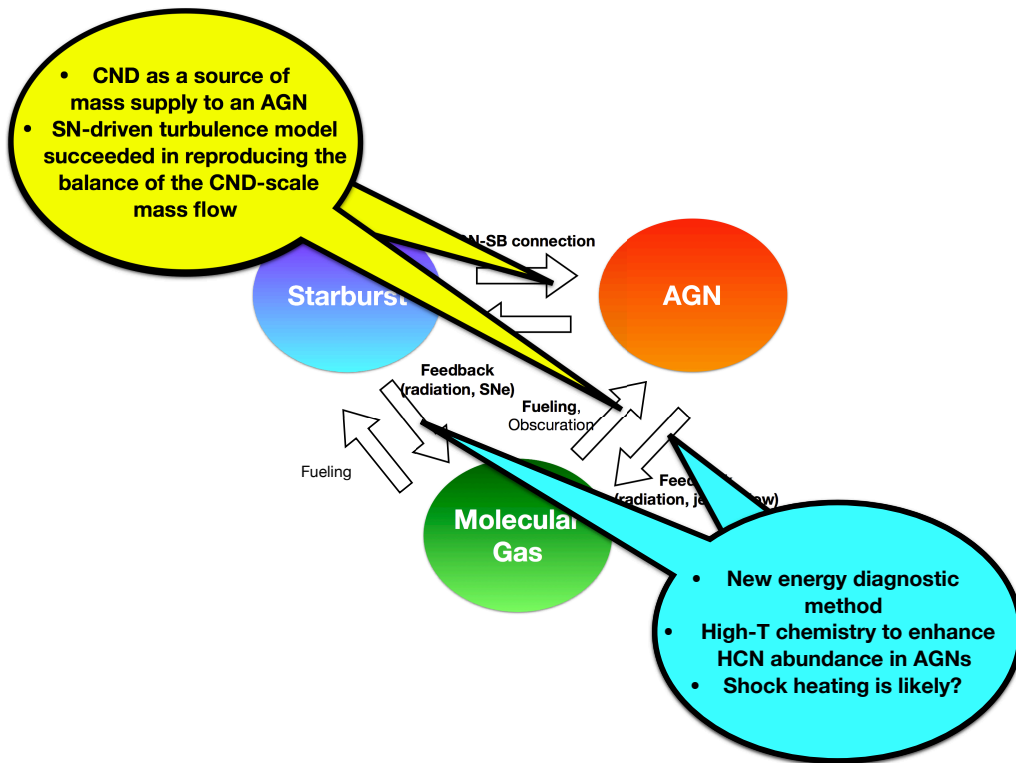


Figure 5.1: Summary of the newly revealed properties of the active trinity in this theses. Our new achievements are commented on the original figure shown in Figure 1.3

individually from molecular observations, and (3) balancing of mass flows at the CND scale by invoking the SN-driven turbulence model. In other words, we could show observationally supported mechanisms of the interplay among the active trinity, which is indeed the subject of this thesis (Figure 5.1).

5.2 Future Outlook

Although the statistics of our last result, which shows the balance of the mass flow at the CND scale, is still poor, our results will strongly motivate future higher resolution observations that surely resolve the (innermost) structures of CNDs, which are necessary to further improve our understanding of the circumnuclear mass transportation, e.g., from the perspective of AGN–SB connection.

One possible and straightforward approach is to measure Σ_{dense} directly by molecular observations. According to the prediction by the SN-driven turbulent accretion model (Kawakatu & Wada 2008), the mass accretion rate from the CND to further inward (\dot{M}_{acc}) is proportional to Σ_{dense} , as indicated in Equation (4.6). Interestingly, recent very high resolution measurements of dense gas tracers in CNDs of Seyfert galaxies revealed that the little HCN(4 – 3) emission is stemming from the close vicinity of the low-luminosity Seyfert NGC 1097, whereas prominent

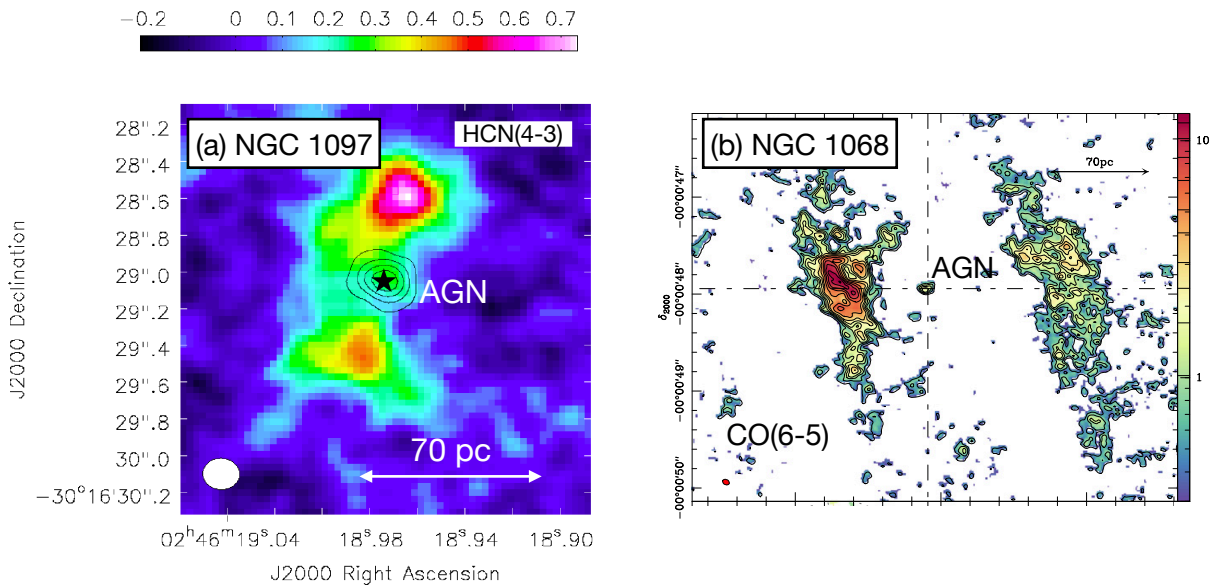


Figure 5.2: The spatial distributions of dense gas tracers, namely, (*left*) HCN(4 – 3) (color; contour = 350 GHz continuum) in the central region of the low-luminosity Seyfert NGC 1097 ($\theta = 0''.20 \times 0''.17$; K. Kohno et al. in prep.), and (*right*) CO(6 – 5) in the central region of the high-luminosity Seyfert NGC 1068 ($\theta = 0''.07 \times 0''.05$; García-Burillo et al. 2016), respectively. The spatial scale is $1'' = 70$ pc for both galaxies. The colors are coded in $\text{Jy beam}^{-1} \text{ km s}^{-1}$ unit. One can see that the emission of the dense gas tracer does not peak at the nucleus of NGC 1097, whereas it does at the nucleus of NGC 1068, clearly indicating that the Σ_{dense} of these nuclei are totally different.

central-concentration of CO(6 – 5) was found in the high-luminosity Seyfert NGC 1068 (Figure 5.2). As these transitions have more or less comparable n_{cr} , Figure 5.2 clearly indicates that their Σ_{dense} are totally different (NGC 1068 \gg NGC 1097), which is well in concordance with the model prediction (Kawakatu & Wada 2008).

As ALMA starts to provide the capability of very high resolutions from its Cycle 3 (2015~) period, now we can systematically obtain similar resolution image to those in Figure 5.2. Such photometric measurements, as well as non-LTE modelings using multi-transition data to accurately estimate physical conditions of the gas, will surely enable us to obtain accurate Σ_{dense} , which should open up a new way to investigate CND scale mass flows in the ALMA era.

Appendix A

Notes on individual galaxies used in the submm-HCN diagram

This Appendix provides some basic information on the individual galaxies collected in Table 2.1 and Figures 2.1 and 2.2, reported in previous studies. The information was compiled mainly from the perspective of nuclear energetics as mentioned in Section 2.2.

A.1 NGC 1068

Undoubtedly this is one of the best studied Seyfert galaxies hosting a luminous type-2 AGN ($L_{2-10\text{keV}} = 10^{43.0}$ erg s $^{-1}$; Marinucci et al. 2012). Broad Balmer emission lines are observed in the polarized light (Antonucci & Miller 1985), which is a supportive evidence for the unified model of AGNs (Antonucci 1993). In X-rays, this AGN is known to be substantially Compton thick with $N_{\text{H}} \sim 10^{25}$ cm $^{-2}$ along the line of sight (e.g., Marinucci et al. 2012, 2016; Matt et al. 2000). NGC 1068 also hosts a ring- or arm-like SB region with a diameter of $\sim 30''$ (Telesco & Decher 1988). Several unbiased line surveys with single dish telescopes and/or interferometric observations of individual molecular line emissions at millimeter/submillimeter have been conducted towards this AGN (e.g., Aladro et al. 2013; García-Burillo et al. 2014; Krips et al. 2011; Nakajima et al. 2015; Takano et al. 2014; Usero et al. 2004). The CNM is bright not only in CO but also, and more distinctively, in dense gas tracers such as HCN and HCO $^{+}$ lines (e.g., García-Burillo et al. 2014; Kohno et al. 2008; Schinnerer et al. 2000). This CNM mainly consists of two bright knots, namely, East and West knots, which are ~ 100 pc away from the exact location of the AGN (Figure A.1). Interestingly, HCN(4-3)/HCO $^{+}$ (4-3) line ratio is two times higher at these knots than at the AGN location (García-Burillo et al. 2014). NGC 1068 is also known to possess a radio jet, ionized outflow, and prominent molecular outflow, which might be interacting with the CNM (e.g., Krips et al. 2011).

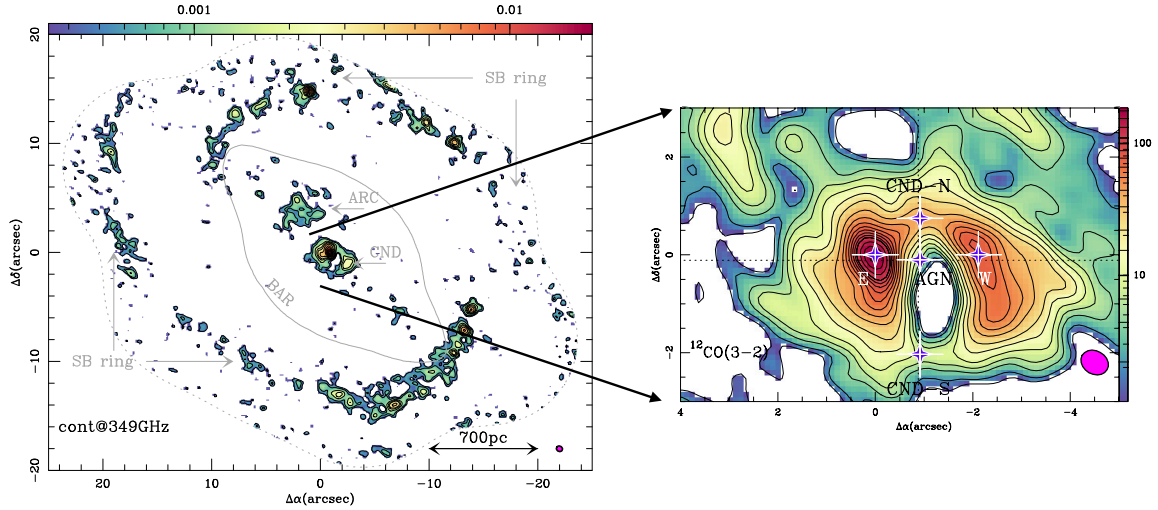


Figure A.1: (*left*) Spatial distribution of ALMA Band 7 (349 GHz) continuum emission in the central ~ 3 kpc region of NGC 1068 (Jy beam^{-1} unit, García-Burillo et al. 2014). $1'' = 70$ pc in this galaxy. The central CND is surrounded by the kpc scale circumnuclear SB ring. (*right*) The zoomed-up view of the CND at $^{12}\text{CO}(J = 3 - 2)$ emission line ($\text{Jy beam}^{-1} \text{ km s}^{-1}$ unit, Viti et al. 2014). Names of representative positions are overlaid, where we measured line ratios in Chapter 2.

A.2 NGC 1097

This galaxy hosts a low luminosity type-1 AGN (LLAGN, $L_{2-10\text{keV}} = 10^{40.8} \text{ erg s}^{-1}$; Liu et al. 2014) as evidenced by double-peaked broad Balmer emission lines with time variability (FWHM $\sim 7500 \text{ km s}^{-1}$; Storchi-Bergmann et al. 1997). Interestingly, NGC 1097 also showed a transient phenomenon from a LINER nucleus to a type-1 AGN. This LLAGN and the CND are surrounded by a circumnuclear SB ring with a radius of $\sim 10'' = 700 \text{ pc}$ (Barth et al. 1995). At infrared, Mason et al. (2007) reported the absence of $3.3 \mu\text{m}$ PAH feature at sub-arcsec scale measurements of the CND, which is typical for strong radiation field. But attempts to fit the IR-data with clumpy torus models failed, which led Mason et al. (2007) to conclude that the torus is absent or weak. Alternatively, they argued a nuclear star-forming cluster, which is likely co-existing with this LLAGN (Storchi-Bergmann et al. 2005) would be dominant in MIR energetics. We emphasize that the dominant heating source at submillimeter to infrared remains unknown. Both ADAF + truncated disk model and jet synchrotron model can reproduce the nuclear SED similarly well (Nemmen et al. 2011). Regarding the molecular properties, both the CND and the SB ring accompany large amount of molecular gas prominent at e.g., CO, HCN, HCO^+ emissions (e.g., Hsieh et al. 2012, 2008; Izumi et al. 2013; Kohno et al. 2003; Figure A.2). It has been claimed that the CND is warm even in the molecular phase (\sim several hundreds K; Beirão et al. 2012; Izumi et al. 2013), which would be heated by the AGN.

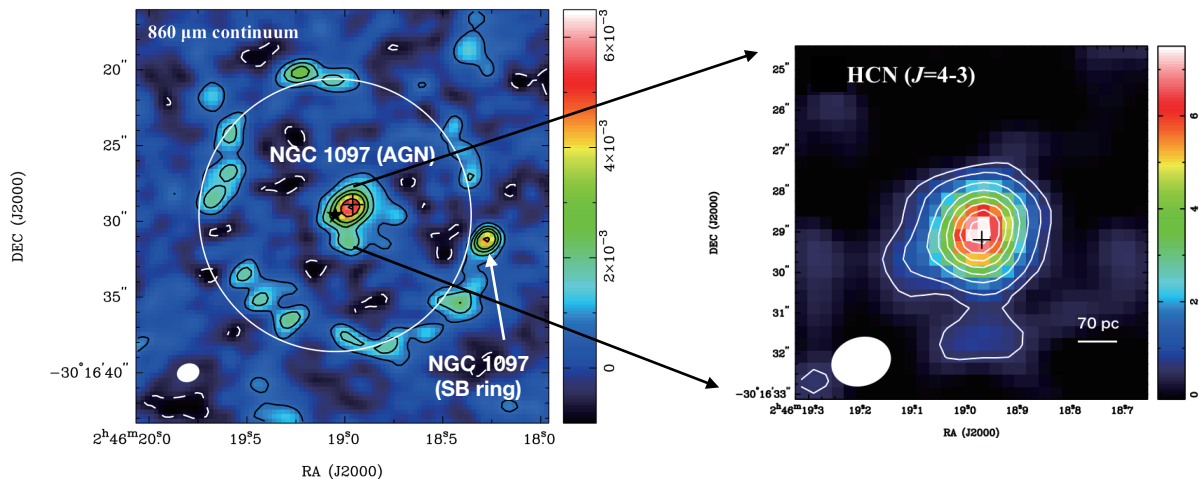


Figure A.2: (*left*) Spatial distribution of ALMA Band 7 (349 GHz) continuum emission in the central ~ 2 kpc region of NGC 1097 (Jy beam^{-1} unit, $1'' = 70$ pc), and (*right*) the zoomed-up view of the CND at HCN($J = 4 - 3$) emission line ($\text{Jy beam}^{-1} \text{ km s}^{-1}$ unit), respectively (Izumi et al. 2013). As is also the case in NGC 1068 (Figure A.1), the CND is surrounded by the kpc scale circumnuclear SB ring. Names of representative positions are overlaid, where we measured line ratios in Chapter 2.

A.3 NGC 1365

This archetypal barred spiral galaxy hosts both a Seyfert 1.5 nucleus ($L_{2-10\text{keV}} = 10^{42.3} \text{ erg s}^{-1}$; Liu et al. 2014) with time variability (Walton et al. 2014) and a circumnuclear SB ring with a radius of $5''-10''$. Several star clusters are embedded inside the SB ring (Galliano et al. 2005). A comprehensive review of this galaxy can be found in Lindblad (1999). Alonso-Herrero et al. (2012b) estimated that the AGN contributes only $\sim 5\%$ of the total IR emission in the central ~ 5 kpc, although it seems to dominate the energetics at $\lambda \lesssim 24 \mu\text{m}$. Previous CO multi-transition observations revealed that most of their emissions comes from the SB ring, and little is from the vicinity of the Seyfert nucleus (Sakamoto et al. 2007). This suggests that the primary heating source of molecular gas is the SB activity, rather than the AGN, although the spatial distribution of dense gas tracers such as HCN and HCO^+ is currently unknown. High resolution observations of them are thus desirable.

A.4 NGC 4945

This galaxy contains an AGN as evidenced by its strong and rapidly variable X-ray emission (Guainazzi et al. 2000; Puccetti et al. 2014). The intrinsic 2-10 keV luminosity is estimated to be $L_{2-10\text{keV}} = 10^{42.5} \text{ erg s}^{-1}$ (Guainazzi et al. 2000). The AGN is classified as Seyfert 2 with a large amount of obscuring material ($N_{\text{H}} = 10^{24.5} \text{ cm}^{-2}$; Puccetti et al. 2014). It has also been found that NGC 4945 exhibits a prominent SB activity including a large IR luminosity and

IRAS color similar to a giant HII region, but almost an edge-on view ($i = 78^\circ$) and the resultant severe dust attenuation have prevented detailed study at optical wavelengths. Marconi et al. (2000) reported that the spatial distribution of the SB region is ring-like with a radius of $\sim 2.5''$ (50 pc), which is clearly visible most in a Pa α map. Chou et al. (2007) argued that this SB activity, rather than the AGN, is the dominant heating source for dust in the nuclear region. Furthermore, interferometric HCN(1 – 0), HCO⁺(1 – 0), and HNC(1 – 0) observations revealed that these dense gas tracers are emitted from an inclined rotating disk-like component with a radius of $\sim 4''$ (Cunningham & Whiteoak 2005), i.e., emanating from both around the AGN and the SB ring. Higher resolution observations are thus necessary to obtain reliable spectrum of each component.

A.5 NGC 7469

The existence of a type-1 AGN ($L_{2-10\text{keV}} = 10^{43.2}$ erg s⁻¹; Liu et al. 2014) in this galaxy is evidenced by broad Balmer emission lines (FWHM ~ 4370 km s⁻¹; Peterson et al. 2014) with time variability (Bonatto & Pastoriza 1990; Collier et al. 1998). Time variability is also confirmed by UV and X-ray observations (e.g., Nandra et al. 2000; Scott et al. 2005). A core jet-like structure or supernova remnants (Lonsdale et al. 2003) and ionized outflows (Blustin et al. 2007) have been found, while high resolution H₂ observations could not detect any signature of jet-ISM (or outflow-ISM) interaction in the CND (e.g., Hicks et al. 2009). Similar to some other Seyfert galaxies, the AGN and the CND of NGC 7469 are surrounded by a prominent SB ring with a radius of 1.5''-2.5'' (Díaz-Santos et al. 2007; Soifer et al. 2003), which accounts for two-thirds of the bolometric luminosity of the entire galaxy (Genzel et al. 1995). Inside the nuclear $r \lesssim 130$ pc region, Davies et al. (2007) reported an existence of star clusters with modest ages of 110-190 Myr. As for the molecular phase, Izumi et al. (2015) reported the significant concentration of HCN(4 – 3), HCO⁺(4 – 3), and CS(7 – 6) line emissions towards the CND (Figure A.3).

A.6 NGC 4418

This is a luminous infrared galaxy (LIRG) with an infrared luminosity of $L_{8-1000\mu\text{m}} \sim 10^{11} L_\odot$ (Imanishi et al. 2004). NGC 4418 shows no clear AGN signature at optical and X-ray (Armus et al. 1989; Maiolino et al. 2003), However, the 5-23 μm MIR spectrum shows a typical feature of an obscured AGN (Spoon et al. 2001). Furthermore, Imanishi et al. (2004) found that the nuclear star forming activity estimated from PAH emission can account for only 1/50 of the total IR luminosity, suggesting the primary energy source is deeply embedded in dust and gas. Indeed, Sakamoto et al. (2013) estimated the dust continuum opacity at 860 μm is surprisingly as large as $\tau_{860\mu\text{m}} \sim 1$, suggesting a large hydrogen column density of $N_{\text{H}_2} \sim 10^{26}$ cm⁻². As for the hidden energy source, Imanishi et al. (2004) also suggested that the observed large equivalent width of H₂ emission and a high HCN(1 – 0)/HCO⁺(1 – 0) ratio at the nucleus can be well explained by the presence of a strong X-ray source such as an AGN. Note that shock heating due

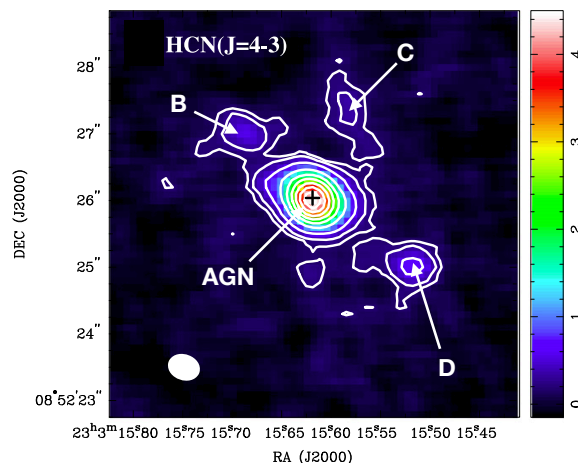


Figure A.3: The spatial distribution of HCN($J = 4 - 3$) line emission in the central ~ 2 kpc region of NGC 7469 ($\text{Jy beam}^{-1} \text{ km s}^{-1}$ unit, Izumi et al. 2015). Again, the CNB is surrounded by the kpc scale circumnuclear SB ring ($1'' = 330$ pc in this galaxy). Names of the representative positions, where we measured line ratios (Chapter 2) are indicated as well.

to in/outflows detected by molecular observations (e.g., González-Alfonso et al. 2012; Sakamoto et al. 2013) would also influence these features. Considering the above, we classify this galaxy as a buried-AGN in this paper, although the evidence is still tentative.

A.7 IRAS12127-1412

This is a ULIRG with $L_{8-1000\mu\text{m}} = 10^{12.1} L_{\odot}$ (Imanishi et al. 2006), consists of two nuclei with a separation of $\sim 10''$ (Kim et al. 2002). Optical spectroscopy classified this object as a non-Seyfert (LINER or HII region; Veilleux et al. 1999), but the nuclear source is obscured as indicated by a large silicate optical depth of $\sim 2.5 - 3.0$ (Imanishi et al. 2007a). IR observations, on the other hand, suggest that the energy source of the North-East nucleus is very compact, which is further characterized by weak PAH emissions and a steep temperature gradient (Imanishi et al. 2007a, 2006). These are characteristic features to buried-AGNs, thus we classify this object as such. Note that IRAS12127-1412 has a 1.4 GHz radio luminosity that is ~ 4 times brighter than the value expected for a star forming galaxy (Spoon & Holt 2009), suggesting the existence of an AGN-jet. This hypothesized jet may explain the observed outflow signatures in [NeIII] line (Spoon & Holt 2009) as well.

A.8 M82

This galaxy, as well as NGC 253, is one of the best studied galaxies after the Milky Way. It is famous for its intense star formation ($\text{SFR} \sim 10 M_{\odot} \text{ yr}^{-1}$; Förster Schreiber et al. 2003) and a prominent superwind at many wavelengths (e.g., Bregman et al. 1995; Ohya et al. 2002). The current SB region extends over ~ 500 pc centered on the nucleus (*SB core*), which consists

of four high surface brightness clumps (O’Connell & Mangano 1978). The bolometric luminosity of the SB core is $\sim 10^{10.8} L_{\odot}$, half of which is emanating from OB stars (Förster Schreiber et al. 2003). Higher resolution HST observations revealed that ~ 200 super star clusters exist in that region (e.g., Melo et al. 2005). The SB history was extensively modeled by Rieke et al. (1993) and Förster Schreiber et al. (2003), who predicted that the bursts occurred ~ 10 and 5 Myr ago each lasting for a few Myr. The estimated age is consistent to the observed molecular properties suggesting M82 hosts an evolved SB whose energetics is dominated by radiative processes (i.e., PDRs) rather than shocks (e.g., Aladro et al. 2011).

A.9 NGC 253

The star forming region of this nearest and IR-brightest SB galaxy is located in the central $r \lesssim 500$ pc (e.g., Scoville et al. 1985). High resolution millimeter/submillimeter observations revealed that molecular gas in the nuclear region is distributed along a 700×200 pc bar-like structure containing several dense clumps (e.g., Paglione et al. 1995; Sakamoto et al. 2011, 2006b). The SB activity has been taking place for at least a few Myr, producing an IR luminosity of $\sim 10^{10.5} L_{\odot}$ (Telesco & Harper 1980), or a SFR of $\sim 5 M_{\odot} \text{ yr}^{-1}$ assuming a Kennicutt-Schmidt relation (Kennicutt 1998). The nuclear region consists of a number of massive stellar clusters (e.g., Fernández-Ontiveros et al. 2009), some of which have a radio counterpart (Ulvestad & Antonucci 1997). Assuming an instantaneous SB, the age of the stellar clusters is estimated to be ~ 6 Myr, whereas they would consist of young ($\lesssim 4$ Myr) and old (~ 10 Myr) populations in actual (Fernández-Ontiveros et al. 2009). Prominent ionized and molecular outflows are emerging from this region as well (e.g., Bolatto et al. 2013; Weaver et al. 2002). Considering the relatively young stellar age ($\lesssim 4$ Myr), NGC 253 would be in an early phase of a SB evolution. Indeed, Martín et al. (2006) suggested that the low-velocity shocks rather than UV radiation would dominate the molecular chemistry in NGC 253.

A.10 NGC 1614

The merging system NGC 1614 is classified as a LIRG ($L_{8-1000\mu\text{m}} = 10^{11.6} L_{\odot}$; Imanishi & Nakanishi 2013b), which has a bright optical center and two spiral arms at scales of a few kpc. At optical wavelengths, it is classified as a SB galaxy (Veilleux et al. 1995; Véron-Cetty & Véron 2010). Indeed, the IR spectrum features including prominent $3.3 \mu\text{m}$ PAH emission, $4.05 \mu\text{m}$ Br α emission (and their ratios to IR luminosity), and $2.3 \mu\text{m}$ stellar CO absorption, are typical of SB galaxies (Alonso-Herrero et al. 2001; Brandl et al. 2006; Imanishi et al. 2010). There is no clear indication of an AGN activity as well. The star forming activity is significantly concentrated towards the nuclear region as indicated by a SB ring with a radius of ~ 300 pc clearly visible at Pa α emission (Alonso-Herrero et al. 2001) and radio emission (e.g., Olsson et al. 2010). A low HCN(1 – 0)/HCO⁺(1 – 0) ratio is also supportive of dominance of SB activity (Costagliola et al. 2011).

A.11 NGC 3256

The late-stage merging system NGC 3256 is the most luminous galaxy within 40 Mpc with $L_{8-1000\mu\text{m}} = 10^{11.6} L_{\odot}$ (Sanders et al. 2003), which has a double nucleus with a separation of $\sim 5'' = 850$ pc. The existence of the double nucleus has been revealed at radio, NIR, X-ray, as well as molecular line emission (Kotilainen et al. 1996; Lira et al. 2002; Norris & Forbes 1995; Sakamoto et al. 2006a). Although NGC 3256 is luminous in X-ray ($L_{0.5-10\text{keV}} \sim 10^{42}$ erg s^{-1} ; Lira et al. 2002), the presence of an AGN is not supported by a considerable amount of observational evidence (Jenkins et al. 2004; Lípari et al. 2000; Lira et al. 2002). The relatively strong X-ray emission would be stellar origin since hundreds of young stellar clusters have been found in the central region of this system (Alonso-Herrero et al. 2002; Zepf et al. 1999). Indeed, the above mentioned X-ray luminosity is consistent with the boundary to separate AGNs from SB galaxies found in deep X-ray surveys (e.g., Alexander et al. 2005). Therefore, we classify this object as a SB galaxy in this work.

A.12 NGC 3628

The SB galaxy NGC 3628 ($L_{8-1000\mu\text{m}} = 10^{10.3} L_{\odot}$; Sanders et al. 2003) is a member of the Leo Triplet (Arp 317), including NGC 3627 and NGC 3623 as well. Radio observations of both continuum and hydrogen recombination line emissions revealed this galaxy possesses a SB in its central ~ 500 pc region (Condon et al. 1982; Zhao et al. 1997). A large scale galactic wind, relating this SB, has been detected in X-ray and $\text{H}\alpha$ emissions (Strickland et al. 2001, 2004). In addition, a sub-kpc scale molecular outflow is also found (Tsai et al. 2012). Note that an X-ray point source ($L_{0.3-8.0\text{keV}} \sim 10^{40}$ erg s^{-1}), which is a candidate of an intermediate mass black hole, was discovered in this galaxy (Strickland et al. 2001). But the location of the object is at least $20''$ away from the nucleus. Thus, it would have no contribution to the molecular line observations with APEX $18''$ beam used in this paper (Zhang et al. 2014).

A.13 NGC 7552

A nearly face-on barred spiral galaxy NGC 7552 ($L_{8-1000\mu\text{m}} = 10^{10.9} L_{\odot}$; Sanders et al. 2003) has been classified as a LINER galaxy due to its weak [OI] emission (Durret & Bergeron 1988). It hosts a prominent circumnuclear ring with a radius of $\sim 2.5''$ or 250 pc, which is the powering source of a SB activity (e.g., Brandl et al. 2012; Schinnerer et al. 1997). This SB ring is occupied by a number of young stellar clusters (Brandl et al. 2012), which would be formed about 10 Myr ago (Schinnerer et al. 1997). Inside the SB ring, neither X-ray (Liu & Bregman 2005) nor NIR (Forbes et al. 1994) observations have shown a clear evidence of a nuclear activity. Therefore, this galaxy is genuinely a SB galaxy. High resolution observations revealed that dense molecular gas is mainly concentrated to the SB ring (Pan et al. 2013).

A.14 IRAS13242-5713

Unlike other sample galaxies, observational information on this LIRG ($L_{8-1000\mu\text{m}} = 10^{11.0} L_{\odot}$; Sanders et al. 2003) is currently very limited. However, based on the MIR observations with *Spitzer* IRS, Alonso-Herrero et al. (2012a) reported that an AGN, if it exists, has almost no contribution to the MIR spectrum. Indeed, [Ne V] 14.32 μm , which is an indicator of an existence of an AGN, was not detected (Alonso-Herrero et al. 2012a). Then, although the observational evidence is lacked, we conclude that an AGN is absent, or at least negligible to the energy budget in this galaxy, and classify this to be a SB galaxy.

A.15 N113

This is an HII region in the Large Magellanic Cloud (LMC) associated with a clumpy molecular cloud (Seale et al. 2012) with a mass of a few $\times 10^5 M_{\odot}$ in total (Wang et al. 2009). The molecular clouds are the site of massive star formation, as evidenced by several embedded young stellar objects (YSOs) (e.g., Carlson et al. 2012; Seale et al. 2009, 2012). N113 hosts the most intense H_2O maser of the Magellanic Clouds (e.g., Oliveira et al. 2006) and OH maser as well (Brooks & Whiteoak 1997). This region (and the LMC as well) is characterized by its low-metallicity ISM ($Z \sim 1/3 Z_{\odot}$; e.g., Hunter et al. 2009). Therefore, this is an appropriate object to investigate the effect of metallicity on molecular chemistry.

A.16 N159

This is also one of the best-studied HII regions in the LMC, close to the evolved starburst of 30 Doradus. The N159 complex is a type-III giant molecular cloud as classified by Fukui et al. (2008), i.e., a GMC with HII regions and young star clusters. Indeed, this region is known to host many YSOs, OH maser sources, and ultra-compact HII regions (e.g., Chen et al. 2010). Extensive studies of molecular material have been conducted for this region (e.g., Bolatto et al. 2000; Minamidani et al. 2011; Mizuno et al. 2010; Okada et al. 2015; Paron et al. 2016). The total mass of clumps visible at $^{12}\text{CO}(3-2)$ emission is $\sim 6 \times 10^5 M_{\odot}$ (Minamidani et al. 2008). Recent non-LTE modelings of high density gas tracers such as HCN, HCO^+ and CS revealed the existence of warm ($T_{\text{kin}} \sim 80 \text{ K}$) and dense ($n_{\text{H}_2} \sim 5 \times 10^5 \text{ cm}^{-3}$) gas (Paron et al. 2016). As is the case of N113 (and LMC), this region is also a site with low-metallicity.

Appendix B

Modifying the background radiation field

In the non-LTE radiative transfer modelings in Section 2.4, we assumed that the background radiation is the black body at temperature T_{bg} . In the RADEX code, this means that the radiation fills the sky like the cosmic microwave background (CMB), hence, by using the Planck function (B_ν), the background intensity (I_ν^b) is written as $I_\nu^b = B_\nu(T_{\text{bg}})$.

On the other hand, the background radiation seen by the observer should be

$$I_\nu^b = B_\nu(T_{\text{CMB}}) + B_\nu(T_d)(1 - e^{-\tau_d}). \quad (\text{B.1})$$

Here T_d and τ_d indicate the dust temperature and the optical depth of that dust emission, respectively. We only consider the thermal dust radiation for simplicity, as we primarily focus on the submillimeter spectroscopy in Chapter 2. We need to further modify this to the background radiation seen by the molecules. In the optically thin case, it can be written as

$$I_\nu^{b,thin} = B_\nu(T_{\text{CMB}}) + \eta B_\nu(T_d)(1 - e^{-\tau_d}), \quad (\text{B.2})$$

where η represents the dilution of the surrounding dust emission due to geometrical effects. Hence, η takes values between 0 and 1. Except for the cases of compact, heavily obscured nuclei having $N_{\text{H}_2} \gtrsim 10^{25-26} \text{ cm}^{-2}$ such as Arp 220 and NGC 4418 (e.g., Martín et al. 2016; Sakamoto et al. 2013), submillimeter dust emission is always optically thin. Thus, in some cases, we can expect that the value of the Equation (B.3) is smaller than that of $B_\nu(T_d)$ alone (adopted value in the modelings in Chapter 2). That is, the modelled cases with high T_{bg} such as $\gtrsim 20$ K would have a limited meaning in an actual observational sense.

Note that, in the optically thick case, Equation (B.3) should replace the $B_\nu(T_{\text{bg}})$ in Equation (2.3), and the internal radiation felt by a molecule becomes,

$$I_\nu^{b,thick} = (1 - \beta_\nu)B_\nu(T_{\text{ex}}) + \beta_\nu[B_\nu(T_{\text{CMB}}) + \eta B_\nu(T_d)(1 - e^{-\tau_d})]. \quad (\text{B.3})$$

Appendix C

Excitation of $\text{HCO}^+(4-3)$ and $\text{CS}(7-6)$ under non-LTE with photon trapping

The molecular excitation temperature (T_{ex}) of $\text{HCO}^+(4-3)$ and $\text{CS}(7-6)$ are shown in Figures C.1 and C.2, as a function of the background radiation temperature (T_{bg}), respectively. The overall trend is totally similar to the case of $\text{HCN}(4-3)$ as shown in Figure 2.3; T_{ex} approaches T_{bg} at $T_{\text{bg}} \gtrsim 10$ K, when the line is optically thin to moderately thick (left two panels). On the other hand, in the optically thick cases, T_{ex} is getting close to the gas kinetic temperature (T_{kin}) and independent of T_{bg} , due to an efficient photon trapping effect.

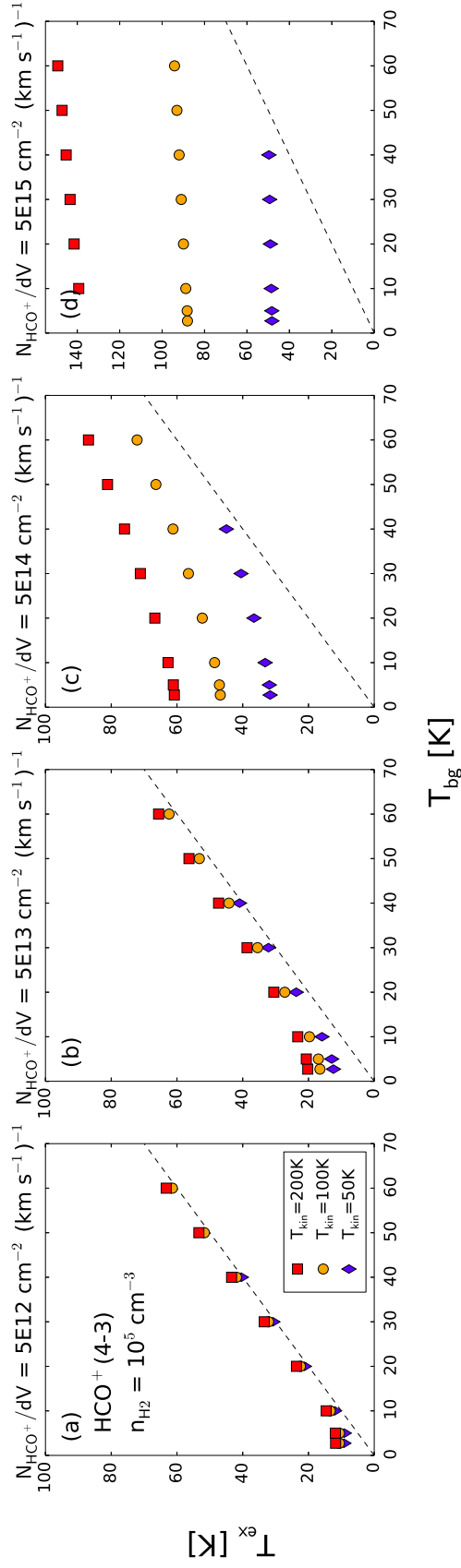


Figure C.1: Excitation temperature (T_{ex}) of $\text{HCO}^+(4-3)$ as a function of background temperature (T_{bg}). The red square, orange circle, and blue diamond symbols indicate the models with gas kinetic temperature (T_{kin}) of 200, 100, and 50 K, respectively. We here fixed gas volume density (n_{H_2}) to 10^5 cm^{-3} . Four cases of the line-of-sight column density (N_{HCO^+}/dV) of (a) 5×10^{12} , (b) 5×10^{13} , (c) 5×10^{14} , and (d) $5 \times 10^{15} \text{ cm}^{-2} (\text{km s}^{-1})^{-1}$ are shown. Note that the scale of the y -axis in the panel-(d) is different from the others. The dashed line in each panel indicates the $T_{\text{ex}} = T_{\text{bg}}$. Some cases where the line emission shows a maser feature are excluded. The overall trend is similar to that of $\text{HCN}(4-3)$ as shown in Figure 2.3.

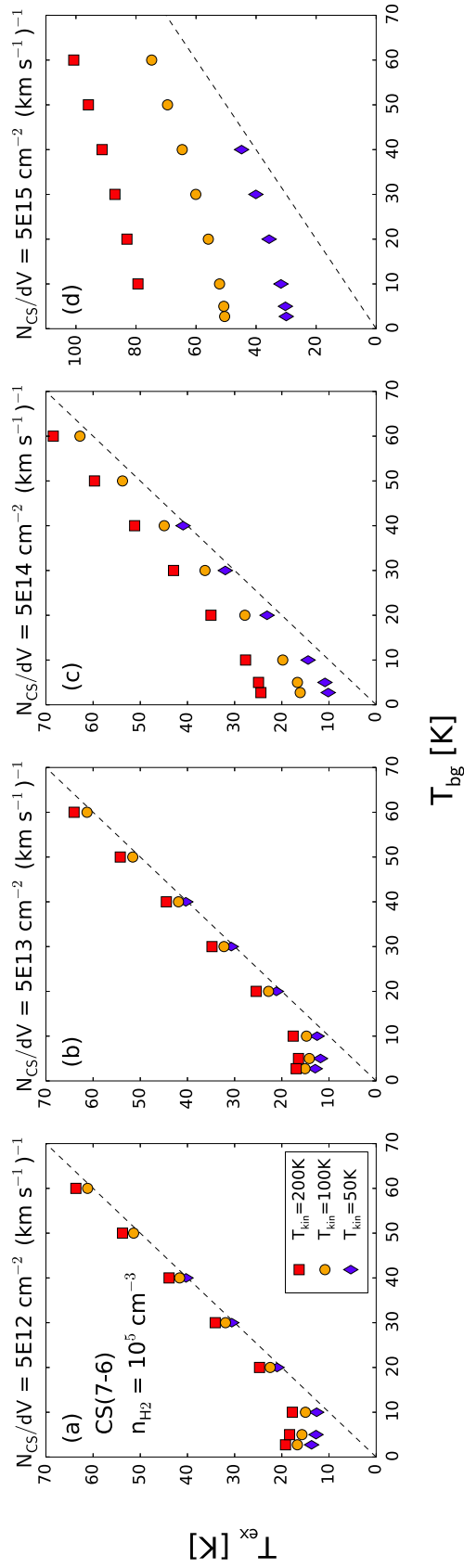


Figure C.2: Same as Figure C.1, but for the cases of CS(7 – 6).

Appendix D

$J = 1 - 0$ transition measurements of HCN and HCO^+ towards NGC 7469 with ALMA

The $J = 1 - 0$ transitions of HCN and HCO^+ from NGC 7469 (luminosity distance = 70.8 Mpc) was observed with ALMA on 2015 July 1 and 2, with 43 (the first day) and 42 (the second day) antennas as a Cycle 1 early science program (ID = 2012.1.00165.S, PI = T. Izumi). Baseline lengths range from 43 m to 1.6 km. The observations were conducted in a single pointing with a $\sim 60''$ field of view, which fully covered the nuclear region of this galaxy. The phase tracking center was set to $(\alpha_{\text{J2000.0}}, \delta_{\text{J2000.0}}) = (23^{\text{h}}03^{\text{m}}15.64^{\text{s}}, +08^{\circ}52'25.80'')$. Both the HCN($1 - 0$) and $\text{HCO}^+(1 - 0)$ emission lines, as well as $\text{C}_2\text{H}(1 - 0)$ line were covered in the lower side band (LSB), whereas CS($2 - 1$) line was in the upper side band (USB), respectively. Both side bands in total covered ~ 7.5 GHz width. The velocity spacing was originally $\sim 1.6 \text{ km s}^{-1}$ (488 kHz), but we binned 20 channels to achieve 20 km s^{-1} resolution to improve the signal to noise ratio. The bandpass, phase, and absolute flux were calibrated with 3C454.3, J2232+1143, and Neptune, respectively. The total on-source time was ~ 1.5 hr and the typical system temperature was $\sim 50 - 80$ K.

The reduction and calibration of the data were conducted with CASA version 4.2.2 (McMullin et al. 2007; Petry & CASA Development Team 2012) in standard manners. The raw visibility data was reduced by the pipeline in the CASA. The line data cubes were reconstructed with the CASA task CLEAN (gain = 0.1, threshold = 1.2 mJy, weighting = natural). The achieved synthesized beam was $0''.77 \times 0''.66$ (254 pc \times 218 pc) with P.A. = -42.12° . The rms noise in the channel map was $\sim 0.27 \text{ mJy beam}^{-1}$ after the primary beam correction, which was measured at the areas free of line emission but close to the line emitting regions concentrated towards the nucleus. The underlying continuum emission was subtracted in the uv -plane before making the line maps. We further analyzed these line cubes with MIRIAD (Sault et al. 1995). Figure D.1 and D.2 show the integrated intensity maps of HCN($1 - 0$) and $\text{HCO}^+(1 - 0)$ (we used the MIRIAD task MOMENT to make this map without any clipping), and the LSB spectrum extracted at the nucleus. The moment-0 values at the nucleus are $1.34 \pm 0.03 \text{ Jy beam}^{-1} \text{ km s}^{-1}$

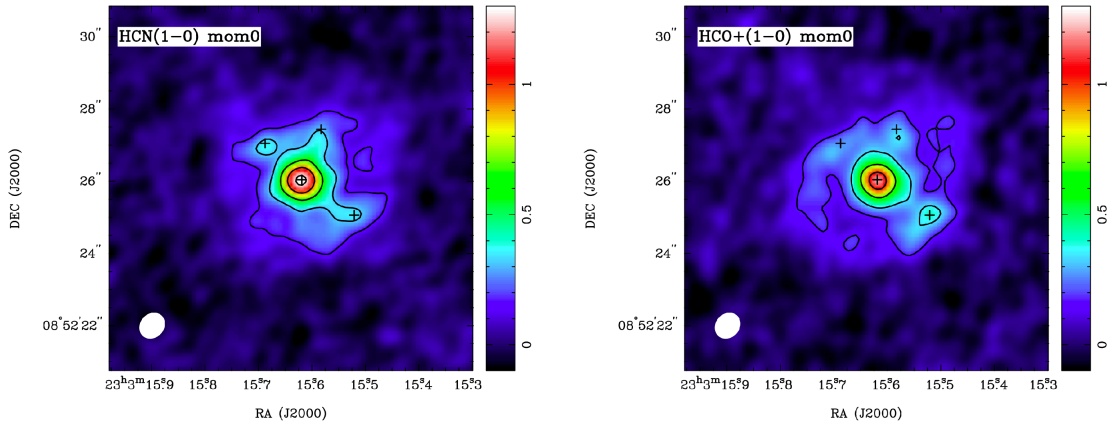


Figure D.1: (*left*) Spatial distribution of HCN(1–0) line emission in the central ~ 3 kpc region of NGC 7469 ($\text{Jy beam}^{-1} \text{ km s}^{-1}$ unit, Izumi et al. in prep.). $1'' = 330$ pc in this galaxy. The central CND is surrounded by the kpc scale circumnuclear SB ring. The bottom-left white ellipse indicates the synthesized beam ($0''.77 \times 0''.66$, P.A. = -42.12°). (*right*) That of HCO⁺(1–0) line emission.

for HCN(1–0) and $1.20 \pm 0.03 \text{ Jy beam}^{-1} \text{ km s}^{-1}$ for HCO⁺(1–0), respectively. Hence, the line ratio of HCN(1–0)/HCO⁺(1–0) exceeds unity at the nucleus, which is different from the previously reported value (~ 0.6 ; Kohno 2005), but is consistent with our prediction (generic HCN-diagram in Section 2.4.6). This discrepancy can be reconciled by considering the coarse spatial resolution in previous works, which covered not only the CND of NGC 7469 but also the surrounding SB ring, as stated in Section 2.4.6.

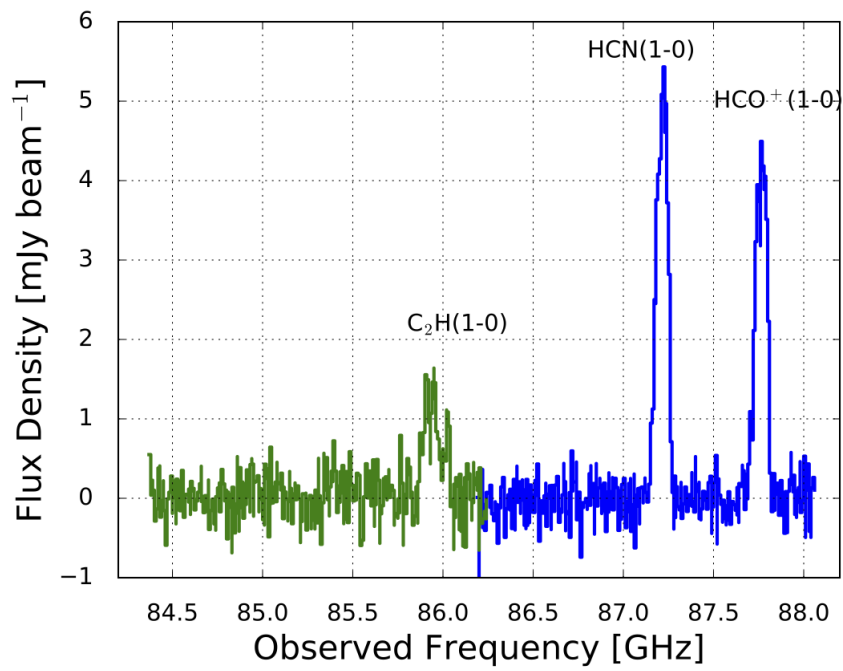


Figure D.2: ALMA Band 3 spectrum extracted at the CND of NGC 7469 with a single aperture ($0''.77 \times 0''.66$), which contains HCN(1-0) and HCO⁺(1-0) lines (Izumi et al. in prep.). One can clearly see that HCN(1-0)/HCO⁺(1-0) line ratio exceeds unity at this position.

Appendix E

Archival data of NGC 4579

NGC 4579 (luminosity distance = 21.7 Mpc) was observed with ALMA on 2014 April 25 with 37 antennas as a Cycle 1 early science program (ID = 2012.1.00456.S, PI = E. Murphy). Baseline lengths range from 16.4 m to 558.2 m. The observations were conducted in a single pointing with a $\sim 60''$ field of view, which fully covered the nuclear region of this galaxy. The phase tracking center was set to $(\alpha_{\text{J2000.0}}, \delta_{\text{J2000.0}}) = (12^{\text{h}}37^{\text{m}}43.6^{\text{s}}, +11^{\circ}49'02.0'')$. The HCN(1–0) emission line was covered in the lower side band (LSB), whereas the upper side band (USB) was used to improve the sensitivity to the underlying continuum emission. Both side bands in total covered ~ 7.5 GHz width. The velocity spacing was originally ~ 1.65 km s $^{-1}$ (488.281 kHz), but we binned 30 channels to achieve 50 km s $^{-1}$ resolution to improve the signal to noise ratio. The bandpass, phase, and absolute flux were calibrated with J1229+0203, J1239+0730, and Ceres, respectively. The total on-source time was ~ 0.2 hr and the typical system temperature was $\sim 50\text{--}75$ K.

The reduction and calibration of the data were conducted with CASA version 4.2 (McMullin et al. 2007; Petry & CASA Development Team 2012) in standard manners. The raw visibility data was extracted from the ALMA archive¹. The HCN(1–0) data cube was reconstructed with the CASA task CLEAN (gain = 0.1, threshold = 0.5 mJy, weighting = natural). The achieved synthesized beam was $1''.96 \times 1''.83$ (207 pc \times 193 pc) with P.A. = -37.75° . The rms noise in the channel map was ~ 0.70 mJy beam $^{-1}$ after the primary beam correction, which was measured at the areas free of line emission but close to the line emitting regions concentrated towards the nucleus. The underlying continuum emission ($\nu_{\text{rest}} = 95$ GHz; synthesized beam was $1''.89 \times 1''.68$, P.A. = -43.39°) was subtracted in the uv plane before making the line map. The rms noise in this continuum map was 0.20 mJy beam $^{-1}$. We further analyzed these line and continuum cubes with MIRIAD (Sault et al. 1995). Figure E.1 shows the integrated intensity map of HCN(1–0) (we used the MIRIAD task MOMENT to make this map without any clipping) and its spectrum extracted at the nucleus. The moment-0 value at the nucleus (0.437 ± 0.126 Jy beam $^{-1}$ km s $^{-1}$) is used to derive L'_{HCN} and M_{dense} in Chapter 4.

¹<https://almascience.nao.ac.jp/alma-data/archive>

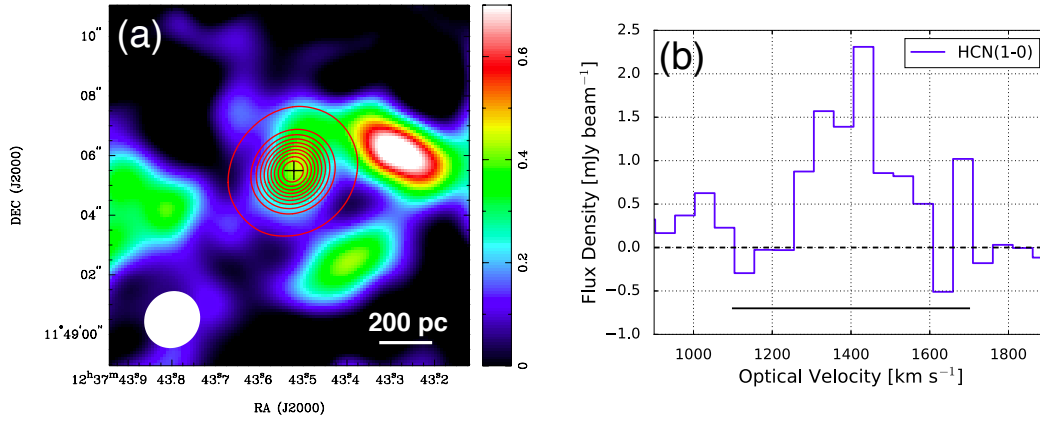


Figure E.1: (a) Spatial distributions of the HCN(1 – 0) emission (color) and the underlying 95 GHz continuum emission (contour) of the central 1.2 kpc region of NGC 4579. The central cross indicates the AGN position. The contours are, 10, 100, 150, 200, 250, 300, 350, 400, 450, and 500 σ , where $1\sigma = 0.196 \text{ mJy beam}^{-1}$ (maximum = $109 \text{ mJy beam}^{-1}$). The 1σ noise level in the HCN(1 – 0) integrated intensity map is $0.126 \text{ Jy beam}^{-1} \text{ km s}^{-1}$. The value at the AGN position is $0.437 \text{ Jy beam}^{-1} \text{ km s}^{-1}$ ($\sim 3.5\sigma$). The bottom-left white ellipse indicates the synthesized beam for the HCN(1 – 0) emission ($1''.96 \times 1''.83$, P.A. = -37.75°). (b) The HCN(1 – 0) spectrum extracted at the AGN position with a single synthesized beam with 1σ noise level of $0.70 \text{ mJy beam}^{-1}$. We integrated over the velocity range of $1100\text{--}1700 \text{ km s}^{-1}$ as indicated by the horizontal black, solid line, to make the moment-0 map shown in (a).

Bibliography

- Aalto, S., Polatidis, A. G., Hüttemeister, S., & Curran, S. J. 2002, *A&A*, 381, 783
- Aalto, S., Spaans, M., Wiedner, M. C., & Hüttemeister, S. 2007, *A&A*, 464, 193
- Aalto, S., Garcia-Burillo, S., Muller, S., et al. 2015a, *A&A*, 574, A85
- Aalto, S., Martín, S., Costagliola, F., et al. 2015b, *A&A*, 584, A42
- Abramowicz, M. A., & Fragile, P. C. 2013, *Living Reviews in Relativity*, 16, 1
- Aladro, R., Martín-Pintado, J., Martín, S., Mauersberger, R., & Bayet, E. 2011, *A&A*, 525, A89
- Aladro, R., Viti, S., Bayet, E., et al. 2013, *A&A*, 549, A39
- Alexander, D. M., Bauer, F. E., Chapman, S. C., et al. 2005, *ApJ*, 632, 736
- Alexander, D. M., & Hickox, R. C. 2012, *New A Rev.*, 56, 93
- Alexander, D. M., Young, S., & Hough, J. H. 1999, *MNRAS*, 304, L1
- Alonso-Herrero, A., Engelbracht, C. W., Rieke, M. J., Rieke, G. H., & Quillen, A. C. 2001, *ApJ*, 546, 952
- Alonso-Herrero, A., Pereira-Santaella, M., Rieke, G. H., et al. 2013, *ApJ*, 765, 78
- Alonso-Herrero, A., Pereira-Santaella, M., Rieke, G. H., & Rigopoulou, D. 2012a, *ApJ*, 744, 2
- Alonso-Herrero, A., Rieke, G. H., Rieke, M. J., & Scoville, N. Z. 2002, *AJ*, 124, 166
- Alonso-Herrero, A., Ward, M. J., & Kotilainen, J. K. 1997, *MNRAS*, 288, 977
- Alonso-Herrero, A., Sánchez-Portal, M., Ramos Almeida, C., et al. 2012b, *MNRAS*, 425, 311
- Alonso-Herrero, A., Ramos Almeida, C., Esquej, P., et al. 2014, *MNRAS*, 443, 2766
- Alonso-Herrero, A., Esquej, P., Roche, P. F., et al. 2016, *MNRAS*, 455, 563
- Antonucci, R. 1993, *ARA&A*, 31, 473
- Antonucci, R. R. J., & Miller, J. S. 1985, *ApJ*, 297, 621
- Armus, L., Heckman, T. M., & Miley, G. K. 1989, *ApJ*, 347, 727

-
- Baan, W. A., Henkel, C., Loenen, A. F., Baudry, A., & Wiklind, T. 2008, *A&A*, 477, 747
- Baldi, R. D., Behar, E., Laor, A., & Horesh, A. 2015, *MNRAS*, 454, 4277
- Ballantyne, D. R. 2008, *ApJ*, 685, 787
- Barbosa, F. K. B., Storchi-Bergmann, T., McGregor, P., Vale, T. B., & Rogemar Riffel, A. 2014, *MNRAS*, 445, 2353
- Barnes, J. E., & Hernquist, L. 1992, *ARA&A*, 30, 705
- Barth, A. J., Ho, L. C., Filippenko, A. V., & Sargent, W. L. 1995, *AJ*, 110, 1009
- Bayet, E., Davis, T. A., Bell, T. A., & Viti, S. 2012, *MNRAS*, 424, 2646
- Bayet, E., Viti, S., Williams, D. A., & Rawlings, J. M. C. 2008, *ApJ*, 676, 978
- Bayet, E., Viti, S., Williams, D. A., Rawlings, J. M. C., & Bell, T. 2009, *ApJ*, 696, 1466
- Bayet, E., Williams, D. A., Hartquist, T. W., & Viti, S. 2011, *MNRAS*, 414, 1583
- Beirão, P., Armus, L., Helou, G., et al. 2012, *ApJ*, 751, 144
- Bell, M. B., & Seaquist, E. R. 1978, *ApJ*, 223, 378
- Bentz, M. C., & Katz, S. 2015, *PASP*, 127, 67
- Blake, G. A., Sutton, E. C., Masson, C. R., & Phillips, T. G. 1987, *ApJ*, 315, 621
- Blustin, A. J., Kriss, G. A., Holczer, T., et al. 2007, *A&A*, 466, 107
- Bolatto, A. D., Jackson, J. M., Israel, F. P., Zhang, X., & Kim, S. 2000, *ApJ*, 545, 234
- Bolatto, A. D., Warren, S. R., Leroy, A. K., et al. 2013, *Nature*, 499, 450
- Bonatto, C. J., & Pastoriza, M. G. 1990, *ApJ*, 353, 445
- Bondi, H. 1952, *MNRAS*, 112, 195
- Brandl, B. R., Martín-Hernández, N. L., Schaerer, D., Rosenberg, M., & van der Werf, P. P. 2012, *A&A*, 543, A61
- Brandl, B. R., Bernard-Salas, J., Spoon, H. W. W., et al. 2006, *ApJ*, 653, 1129
- Bregman, J. N., Schulman, E., & Tomisaka, K. 1995, *ApJ*, 439, 155
- Brightman, M., & Nandra, K. 2011, *MNRAS*, 413, 1206
- Brooks, K. J., & Whiteoak, J. B. 1997, *MNRAS*, 291, 395
- Buchner, J., Georgakakis, A., Nandra, K., et al. 2015, *ApJ*, 802, 89
- Burlon, D., Ajello, M., Greiner, J., et al. 2011, *ApJ*, 728, 58

BIBLIOGRAPHY

- Cai, H.-B., Shu, X.-W., Zheng, Z.-Y., & Wang, J.-X. 2010, *Res. Astron. Astro-phys.*, 10, 427
- Carlson, L. R., Sewilo, M., Meixner, M., Romita, K. A., & Lawton, B. 2012, *A&A*, 542, A66
- Charnley, S. B. 1997, *ApJ*, 481, 396
- Charnley, S. B., & Rodgers, S. D. 2005, in *IAU Symposium*, Vol. 231, *Astrochemistry: Recent Successes and Current Challenges*, ed. D. C. Lis, G. A. Blake, & E. Herbst, 237–246
- Chen, C.-H. R., Indebetouw, R., Chu, Y.-H., et al. 2010, *ApJ*, 721, 1206
- Cheung, E., Trump, J. R., Athanassoula, E., et al. 2015, *MNRAS*, 447, 506
- Chou, R. C. Y., Peck, A. B., Lim, J., et al. 2007, *ApJ*, 670, 116
- Cid Fernandes, R., Gu, Q., Melnick, J., et al. 2004, *MNRAS*, 355, 273
- Ciotti, L., D’Ercole, A., Pellegrini, S., & Renzini, A. 1991, *ApJ*, 376, 380
- Cisternas, M., Sheth, K., Salvato, M., et al. 2015, *ApJ*, 802, 137
- Cisternas, M., Jahnke, K., Inskip, K. J., et al. 2011, *ApJ*, 726, 57
- Collier, S. J., Horne, K., Kaspi, S., et al. 1998, *ApJ*, 500, 162
- Collin, S., & Kawaguchi, T. 2004, *A&A*, 426, 797
- Combes, F., García-Burillo, S., Casasola, V., et al. 2014, *A&A*, 565, A97
- Condon, J. J., Condon, M. A., Gisler, G., & Puschell, J. J. 1982, *ApJ*, 252, 102
- Costagliola, F., Aalto, S., Rodriguez, M. I., et al. 2011, *A&A*, 528, A30
- Costagliola, F., Sakamoto, K., Muller, S., et al. 2015, *A&A*, 582, A91
- Cunningham, M. R., & Whiteoak, J. B. 2005, *MNRAS*, 364, 37
- Curran, S. J., Aalto, S., & Booth, R. S. 2000, *A&AS*, 141, 193
- Curran, S. J., Johansson, L. E. B., Bergman, P., Heikkilä, A., & Aalto, S. 2001, *A&A*, 367, 457
- Davies, R., Mark, D., & Sternberg, A. 2012, *A&A*, 537, A133
- Davies, R. I., Müller Sánchez, F., Genzel, R., et al. 2007, *ApJ*, 671, 1388
- Davies, R. I., Thomas, J., Genzel, R., et al. 2006, *ApJ*, 646, 754
- Davies, R. I., Burtscher, L., Rosario, D., et al. 2015, *ApJ*, 806, 127
- Davis, T. A., Bayet, E., Crocker, A., Topal, S., & Bureau, M. 2013, *MNRAS*, 433, 1659
- de Rosa, A., Panessa, F., Bassani, L., et al. 2012, *MNRAS*, 420, 2087

-
- Di Matteo, T., Springel, V., & Hernquist, L. 2005, *Nature*, 433, 604
- Diamond-Stanic, A. M., & Rieke, G. H. 2012, *ApJ*, 746, 168
- Diamond-Stanic, A. M., Rieke, G. H., & Rigby, J. R. 2009, *ApJ*, 698, 623
- Díaz-Santos, T., Alonso-Herrero, A., Colina, L., Ryder, S. D., & Knapen, J. H. 2007, *ApJ*, 661, 149
- Dickinson, D. F., Rodríguez Kuiper, E. N., Dinger, A. S. C., & Kuiper, T. B. H. 1980, *ApJ*, 237, L43
- Dietrich, M., Wagner, S. J., Courvoisier, T. J.-L., Bock, H., & North, P. 1999, *A&A*, 351, 31
- Draine, B. T. 2011, *Physics of the Interstellar and Intergalactic Medium* (Princeton Univ. Press, Princeton, NJ)
- Drouart, G., De Breuck, C., Vernet, J., et al. 2014, *A&A*, 566, A53
- Durret, F., & Bergeron, J. 1988, *A&AS*, 75, 273
- Elitzur, M. 1983, *ApJ*, 267, 174
- Elitzur, M., & Shlosman, I. 2006, *ApJ*, 648, L101
- Esplugues, G. B., Viti, S., Goicoechea, J. R., & Cernicharo, J. 2014, *A&A*, 567, A95
- Esquej, P., Alonso-Herrero, A., González-Martín, O., et al. 2014, *ApJ*, 780, 86
- Fathi, K., Lundgren, A. A., Kohno, K., et al. 2013, *ApJ*, 770, L27
- Fathi, K., Izumi, T., Romeo, A. B., et al. 2015, *ApJ*, 806, L34
- Ferland, G. J., Peterson, B. M., Horne, K., Welsh, W. F., & Nahar, S. N. 1992, *ApJ*, 387, 95
- Fernández-Ontiveros, J. A., Prieto, M. A., & Acosta-Pulido, J. A. 2009, *MNRAS*, 392, L16
- Ferrarese, L., & Merritt, D. 2000, *ApJ*, 539, L9
- Flower, D. R., & Pineau des Forêts, G. 2013, *MNRAS*, 436, 2143
- Forbes, D. A., Kotilainen, J. K., & Moorwood, A. F. M. 1994, *ApJ*, 433, L13
- Förster Schreiber, N. M., Genzel, R., Lutz, D., & Sternberg, A. 2003, *ApJ*, 599, 193
- Fukui, Y., Torii, K., Onishi, T., et al. 2015, *ApJ*, 798, 6
- Fukui, Y., Kawamura, A., Minamidani, T., et al. 2008, *ApJS*, 178, 56
- Gabor, J. M., Impey, C. D., Jahnke, K., et al. 2009, *ApJ*, 691, 705
- Galliano, E., Alloin, D., Granato, G. L., & Villar-Martín, M. 2003, *A&A*, 412, 615

BIBLIOGRAPHY

- Galliano, E., Alloin, D., Pantin, E., Lagage, P. O., & Marco, O. 2005, *A&A*, 438, 803
- Galliano, F., Dwek, E., & Chanial, P. 2008, *ApJ*, 672, 214
- Gallimore, J. F., Baum, S. A., & O’Dea, C. P. 2004, *ApJ*, 613, 794
- Gao, Y., & Solomon, P. M. 2004a, *ApJS*, 152, 63
- . 2004b, *ApJ*, 606, 271
- García-Burillo, S., Combes, F., Schinnerer, E., Boone, F., & Hunt, L. K. 2005, *A&A*, 441, 1011
- García-Burillo, S., Combes, F., Usero, A., & Graciá-Carpio, J. 2008, *Journal of Physics Conference Series*, 131, 012031
- García-Burillo, S., Combes, F., Hunt, L. K., et al. 2003, *A&A*, 407, 485
- García-Burillo, S., Usero, A., Fuente, A., et al. 2010, *A&A*, 519, A2
- García-Burillo, S., Combes, F., Usero, A., et al. 2014, *A&A*, 567, A125
- García-Burillo, S., Combes, F., Ramos Almeida, C., et al. 2016, *ApJ*, 823, L12
- García-Rissmann, A., Vega, L. R., Asari, N. V., et al. 2005, *MNRAS*, 359, 765
- Garrod, R. T., Weaver, S. L. W., & Herbst, E. 2008, *ApJ*, 682, 283
- Genzel, R., Eisenhauer, F., & Gillessen, S. 2010, *Reviews of Modern Physics*, 82, 3121
- Genzel, R., Weitzel, L., Tacconi-Garman, L. E., et al. 1995, *ApJ*, 444, 129
- González-Alfonso, E., Fischer, J., Graciá-Carpio, J., et al. 2012, *A&A*, 541, A4
- Goodrich, R. W., Veilleux, S., & Hill, G. J. 1994, *ApJ*, 422, 521
- Gordon, M. A., & Walmsley, C. M. 1990, *ApJ*, 365, 606
- Graciá-Carpio, J., García-Burillo, S., Planesas, P., & Colina, L. 2006, *ApJ*, 640, L135
- Greenhill, L. J., Gwinn, C. R., Antonucci, R., & Barvainis, R. 1996, *ApJ*, 472, L21
- Greenhill, L. J., Moran, J. M., & Herrnstein, J. R. 1997, *ApJ*, 481, L23
- Greenhill, L. J., Booth, R. S., Ellingsen, S. P., et al. 2003, *ApJ*, 590, 162
- Grier, C. J., Martini, P., Watson, L. C., et al. 2013, *ApJ*, 773, 90
- Guainazzi, M., Matt, G., Brandt, W. N., et al. 2000, *A&A*, 356, 463
- Gültekin, K., Richstone, D. O., Gebhardt, K., et al. 2009, *ApJ*, 698, 198
- Harada, N., Herbst, E., & Wakelam, V. 2010, *ApJ*, 721, 1570

-
- Harada, N., Thompson, T. A., & Herbst, E. 2013, *ApJ*, 765, 108
- Heckman, T., Krolik, J., Meurer, G., et al. 1995, *ApJ*, 452, 549
- Heyer, M. H., & Brunt, C. M. 2004, *ApJ*, 615, L45
- Hicks, E. K. S., Davies, R. I., Maciejewski, W., et al. 2013, *ApJ*, 768, 107
- Hicks, E. K. S., Davies, R. I., Malkan, M. A., et al. 2009, *ApJ*, 696, 448
- Ho, L. C. 2008, *ARA&A*, 46, 475
- Hobbs, A., Nayakshin, S., Power, C., & King, A. 2011, *MNRAS*, 413, 2633
- Hollenbach, D. J., & Tielens, A. G. G. M. 1997, *ARA&A*, 35, 179
- . 1999, *Reviews of Modern Physics*, 71, 173
- Hönig, S. F., Prieto, M. A., & Beckert, T. 2008, *A&A*, 485, 33
- Honma, M., Sofue, Y., & Arimoto, N. 1995, *A&A*, 304, 1
- Hopkins, P. F. 2012, *MNRAS*, 420, L8
- Hopkins, P. F., & Hernquist, L. 2006, *ApJS*, 166, 1
- . 2009, *ApJ*, 694, 599
- Hopkins, P. F., Hernquist, L., Cox, T. J., & Kereš, D. 2008, *ApJS*, 175, 356
- Hopkins, P. F., & Quataert, E. 2010, *MNRAS*, 407, 1529
- Hsieh, P.-Y., Ho, P. T. P., Kohno, K., Hwang, C.-Y., & Matsushita, S. 2012, *ApJ*, 747, 90
- Hsieh, P.-Y., Matsushita, S., Lim, J., Kohno, K., & Sawada-Satoh, S. 2008, *ApJ*, 683, 70
- Huchra, J. P., Vogeley, M. S., & Geller, M. J. 1999, *ApJS*, 121, 287
- Hunt, L. K., & Malkan, M. A. 2004, *ApJ*, 616, 707
- Hunter, I., Brott, I., Langer, N., et al. 2009, *A&A*, 496, 841
- Imanishi, M., Dudley, C. C., Maiolino, R., et al. 2007a, *ApJS*, 171, 72
- Imanishi, M., Dudley, C. C., & Maloney, P. R. 2006, *ApJ*, 637, 114
- Imanishi, M., Nakagawa, T., Shirahata, M., Ohyama, Y., & Onaka, T. 2010, *ApJ*, 721, 1233
- Imanishi, M., & Nakanishi, K. 2013a, *AJ*, 146, 91
- . 2013b, *AJ*, 146, 47
- . 2014, *AJ*, 148, 9

BIBLIOGRAPHY

- Imanishi, M., Nakanishi, K., & Izumi, T. 2016, ArXiv e-prints, arXiv:1605.00644
- Imanishi, M., Nakanishi, K., Kuno, N., & Kohno, K. 2004, *AJ*, 128, 2037
- Imanishi, M., Nakanishi, K., Tamura, Y., Oi, N., & Kohno, K. 2007b, *AJ*, 134, 2366
- Imanishi, M., & Wada, K. 2004, *ApJ*, 617, 214
- Izumi, T., Kohno, K., Martín, S., et al. 2013, *PASJ*, 65, 100
- Izumi, T., Kohno, K., Aalto, S., et al. 2015, *ApJ*, 811, 39
- Jackson, J. M., Paglione, T. A. D., Ishizuki, S., & Nguyen-Q-Rieu. 1993, *ApJ*, 418, L13
- Jenkins, L. P., Roberts, T. P., Ward, M. J., & Zezas, A. 2004, *MNRAS*, 352, 1335
- Jiang, X., Wang, J., & Gu, Q. 2011, *MNRAS*, 418, 1753
- Jogee, S. 2006, in *Lecture Notes in Physics*, Berlin Springer Verlag, Vol. 693, *Physics of Active Galactic Nuclei at all Scales*, ed. D. Alloin, 143
- Kamenetzky, J., Rangwala, N., Glenn, J., Maloney, P. R., & Conley, A. 2014, *ApJ*, 795, 174
- Kaviraj, S. 2014, *MNRAS*, 440, 2944
- Kawaguchi, T., Aoki, K., Ohta, K., & Collin, S. 2004, *A&A*, 420, L23
- Kawakatu, N., & Wada, K. 2008, *ApJ*, 681, 73
- . 2009, *ApJ*, 706, 676
- Kazandjian, M. V., Meijerink, R., Pelupessy, I., Israel, F. P., & Spaans, M. 2012, *A&A*, 542, A65
- . 2015, *A&A*, 574, A127
- Kelly, B. C. 2007, *ApJ*, 665, 1489
- Kennicutt, R. C., & Evans, N. J. 2012, *ARA&A*, 50, 531
- Kennicutt, Jr., R. C. 1998, *ApJ*, 498, 541
- Kim, D.-C., Veilleux, S., & Sanders, D. B. 2002, *ApJS*, 143, 277
- Klöckner, H.-R., & Baan, W. A. 2004, *A&A*, 419, 887
- Knudsen, K. K., Walter, F., Weiss, A., et al. 2007, *ApJ*, 666, 156
- Kohno, K. 2005, in *American Institute of Physics Conference Series*, Vol. 783, *The Evolution of Starbursts*, ed. S. Hüttmeister, E. Manthey, D. Bomans, & K. Weis, 203–208
- Kohno, K., Ishizuki, S., Matsushita, S., Vila-Vilaró, B., & Kawabe, R. 2003, *PASJ*, 55, L1

-
- Kohno, K., Kawabe, R., Tosaki, T., & Okumura, S. K. 1996, *ApJ*, 461, L29
- Kohno, K., Kawabe, R., & Vila-Vilaró, B. 1999, *ApJ*, 511, 157
- Kohno, K., Matsushita, S., Vila-Vilaró, B., et al. 2001, in *Astronomical Society of the Pacific Conference Series*, Vol. 249, *The Central Kiloparsec of Starbursts and AGN: The La Palma Connection*, ed. J. H. Knapen, J. E. Beckman, I. Shlosman, & T. J. Mahoney, 672
- Kohno, K., Nakanishi, K., Tosaki, T., et al. 2008, *Ap&SS*, 313, 279
- Koo, B.-C., & Moon, D.-S. 1997, *ApJ*, 485, 263
- Kormendy, J., & Ho, L. C. 2013, *ARA&A*, 51, 511
- Kormendy, J., & Kennicutt, Jr., R. C. 2004, *ARA&A*, 42, 603
- Koshida, S., Minezaki, T., Yoshii, Y., et al. 2014, *ApJ*, 788, 159
- Kotilainen, J. K., Moorwood, A. F. M., Ward, M. J., & Forbes, D. A. 1996, *A&A*, 305, 107
- Kraemer, S. B., Crenshaw, D. M., Dunn, J. P., et al. 2012, *ApJ*, 751, 84
- Krips, M., Neri, R., García-Burillo, S., et al. 2008, *ApJ*, 677, 262
- . 2007, *A&A*, 468, L63
- Krips, M., Martín, S., Eckart, A., et al. 2011, *ApJ*, 736, 37
- Krongold, Y., Nicastro, F., Elvis, M., et al. 2007, *ApJ*, 659, 1022
- Kuo, C. Y., Braatz, J. A., Condon, J. J., et al. 2011, *ApJ*, 727, 20
- Lang, K. R. 1980, *Astrophysical Formulae. A Compendium for the Physicist and Astrophysicist.* (Springer-Verlag, Berlin)
- Lansbury, G. B., Gandhi, P., Alexander, D. M., et al. 2015, *ApJ*, 809, 115
- Lepp, S., & Dalgarno, A. 1996, *A&A*, 306, L21
- Lin, M.-Y., Davies, R. I., Burtscher, L., et al. 2016, *MNRAS*, 458, 1375
- Lindblad, P. O. 1999, *A&ARv*, 9, 221
- Lípari, S., Díaz, R., Taniguchi, Y., et al. 2000, *AJ*, 120, 645
- Lira, P., Ward, M., Zezas, A., Alonso-Herrero, A., & Ueno, S. 2002, *MNRAS*, 330, 259
- Liu, J.-F., & Bregman, J. N. 2005, *ApJS*, 157, 59
- Liu, T., Wang, J.-X., Yang, H., Zhu, F.-F., & Zhou, Y.-Y. 2014, *ApJ*, 783, 106
- Lodato, G., & Bertin, G. 2003, *A&A*, 398, 517

BIBLIOGRAPHY

- Loenen, A. F., Spaans, M., Baan, W. A., & Meijerink, R. 2008, *A&A*, 488, L5
- Lonsdale, C. J., Lonsdale, C. J., Smith, H. E., & Diamond, P. J. 2003, *ApJ*, 592, 804
- Lutz, D., Maiolino, R., Moorwood, A. F. M., et al. 2002, *A&A*, 396, 439
- Lutz, D., Maiolino, R., Spoon, H. W. W., & Moorwood, A. F. M. 2004, *A&A*, 418, 465
- Lutz, D., Genzel, R., Sturm, E., et al. 2000, *ApJ*, 530, 733
- Lutz, D., Mainieri, V., Rafferty, D., et al. 2010, *ApJ*, 712, 1287
- Machida, M., & Matsumoto, R. 2003, *ApJ*, 585, 429
- Macri, L. M., Stanek, K. Z., Bersier, D., Greenhill, L. J., & Reid, M. J. 2006, *ApJ*, 652, 1133
- Magorrian, J., Tremaine, S., Richstone, D., et al. 1998, *AJ*, 115, 2285
- Maiolino, R., & Rieke, G. H. 1995, *ApJ*, 454, 95
- Maiolino, R., Ruiz, M., Rieke, G. H., & Papadopoulos, P. 1997, *ApJ*, 485, 552
- Maiolino, R., Comastri, A., Gilli, R., et al. 2003, *MNRAS*, 344, L59
- Makarov, D., Prugniel, P., Terekhova, N., Courtois, H., & Vauglin, I. 2014, *A&A*, 570, A13
- Maloney, P. R., Hollenbach, D. J., & Tielens, A. G. G. M. 1996, *ApJ*, 466, 561
- Marconi, A., & Hunt, L. K. 2003, *ApJ*, 589, L21
- Marconi, A., Oliva, E., van der Werf, P. P., et al. 2000, *A&A*, 357, 24
- Marconi, A., Risaliti, G., Gilli, R., et al. 2004, *MNRAS*, 351, 169
- Marinucci, A., Bianchi, S., Nicastro, F., Matt, G., & Goulding, A. D. 2012, *ApJ*, 748, 130
- Marinucci, A., Bianchi, S., Matt, G., et al. 2016, *MNRAS*, 456, L94
- Martín, S., Mauersberger, R., Martín-Pintado, J., Henkel, C., & García-Burillo, S. 2006, *ApJS*, 164, 450
- Martín, S., Kohno, K., Izumi, T., et al. 2015, *A&A*, 573, A116
- Martín, S., Aalto, S., Sakamoto, K., et al. 2016, *A&A*, 590, A25
- Martini, P., Regan, M. W., Mulchaey, J. S., & Pogge, R. W. 2003, *ApJ*, 589, 774
- Mason, R. E., Levenson, N. A., Packham, C., et al. 2007, *ApJ*, 659, 241
- Mason, R. E., Rodríguez-Ardila, A., Martins, L., et al. 2015, *ApJS*, 217, 13
- Matsushita, S., Kohno, K., Vila-Vilaro, B., Tosaki, T., & Kawabe, R. 1998, *ApJ*, 495, 267

-
- Matsushita, S., Trung, D.-V., Boone, F., et al. 2015, *ApJ*, 799, 26
- Matt, G., Fabian, A. C., Guainazzi, M., et al. 2000, *MNRAS*, 318, 173
- Mauersberger, R., Henkel, C., Weiß, A., Peck, A. B., & Hagiwara, Y. 2003, *A&A*, 403, 561
- McKee, C. F., & Ostriker, J. P. 1977, *ApJ*, 218, 148
- McMullin, J. P., Waters, B., Schiebel, D., Young, W., & Golap, K. 2007, in *Astronomical Society of the Pacific Conference Series*, Vol. 376, *Astronomical Data Analysis Software and Systems XVI*, ed. R. A. Shaw, F. Hill, & D. J. Bell, 127
- Meier, D. S., Walter, F., Bolatto, A. D., et al. 2015, *ApJ*, 801, 63
- Meijerink, R., & Spaans, M. 2005, *A&A*, 436, 397
- Meijerink, R., Spaans, M., & Israel, F. P. 2006, *ApJ*, 650, L103
- . 2007, *A&A*, 461, 793
- Meijerink, R., Spaans, M., Kamp, I., et al. 2013, *Journal of Physical Chemistry A*, 117, 9593
- Meijerink, R., Spaans, M., Loenen, A. F., & van der Werf, P. P. 2011, *A&A*, 525, A119
- Melo, V. P., Muñoz-Tuñón, C., Maíz-Apellániz, J., & Tenorio-Tagle, G. 2005, *ApJ*, 619, 270
- Mihos, J. C., & Hernquist, L. 1994, *ApJ*, 425, L13
- Minamidani, T., Mizuno, N., Mizuno, Y., et al. 2008, *ApJS*, 175, 485
- Minamidani, T., Tanaka, T., Mizuno, Y., et al. 2011, *AJ*, 141, 73
- Miyamoto, Y., Nakai, N., Seta, M., et al. 2015, *PASJ*, 67, 5
- Miyoshi, M., Moran, J., Herrnstein, J., et al. 1995, *Nature*, 373, 127
- Mizuno, Y., Kawamura, A., Onishi, T., et al. 2010, *PASJ*, 62, 51
- Momjian, E., Romney, J. D., Carilli, C. L., & Troland, T. H. 2003, *ApJ*, 597, 809
- Monje, R. R., Blain, A. W., & Phillips, T. G. 2011, *ApJS*, 195, 23
- Mortlock, D. J., Warren, S. J., Venemans, B. P., et al. 2011, *Nature*, 474, 616
- Mouri, H. 1994, *ApJ*, 427, 777
- Mulchaey, J. S., & Regan, M. W. 1997, *ApJ*, 482, L135
- Müller Sánchez, F., Davies, R. I., Genzel, R., et al. 2009, *ApJ*, 691, 749
- Müller-Sánchez, F., Prieto, M. A., Hicks, E. K. S., et al. 2011, *ApJ*, 739, 69
- Myers, P. C. 1978, *ApJ*, 225, 380

BIBLIOGRAPHY

- Nakajima, T., Takano, S., Kohno, K., & Inoue, H. 2011, *ApJ*, 728, L38
- Nakajima, T., Takano, S., Kohno, K., et al. 2015, *PASJ*, 67, 8
- Nandra, K., Le, T., George, I. M., et al. 2000, *ApJ*, 544, 734
- Narayan, R., & Yi, I. 1995, *ApJ*, 452, 710
- Nemmen, R., Storchi-Bergmann, T., & Eracleous, M. 2011, ArXiv e-prints, arXiv:1112.4640
- Netzer, H. 1990, in *Saas-Fee Advanced Course 20, Active Galactic Nuclei*, ed. R. D. Blandford, H. Netzer, L. Woltjer, T. J.-L. Courvoisier, & M. Mayor (Springer, Berlin), 57
- Neumayer, N. 2010, *PASA*, 27, 449
- Nomura, H., & Millar, T. J. 2004, *A&A*, 414, 409
- Norman, C., & Scoville, N. 1988, *ApJ*, 332, 124
- Norris, R. P., & Forbes, D. A. 1995, *ApJ*, 446, 594
- O’Connell, R. W., & Mangano, J. J. 1978, *ApJ*, 221, 62
- Ohyama, Y., Taniguchi, Y., Iye, M., et al. 2002, *PASJ*, 54, 891
- Okada, Y., Requena-Torres, M. A., Güsten, R., et al. 2015, *A&A*, 580, A54
- Oliveira, J. M., van Loon, J. T., Stanimirović, S., & Zijlstra, A. A. 2006, *MNRAS*, 372, 1509
- Olsson, E., Aalto, S., Thomasson, M., & Beswick, R. 2010, *A&A*, 513, A11
- Onishi, K., Iguchi, S., Sheth, K., & Kohno, K. 2015, *ApJ*, 806, 39
- Osterbrock, D. E., & Ferland, G. J. 2006, *Astrophysics of Gaseous Nebulae and Active Galactic Nuclei*, 2nd edn (University Science Books, Mill Valley, CA)
- Padovani, P., & Matteucci, F. 1993, *ApJ*, 416, 26
- Paglione, T. A. D., Tosaki, T., & Jackson, J. M. 1995, *ApJ*, 454, L117
- Pan, H.-A., Lim, J., Matsushita, S., Wong, T., & Ryder, S. 2013, *ApJ*, 768, 57
- Panessa, F., Bassani, L., Cappi, M., et al. 2006, *A&A*, 455, 173
- Papadopoulos, P. P. 2007, *ApJ*, 656, 792
- Papadopoulos, P. P., van der Werf, P., Xilouris, E., Isaak, K. G., & Gao, Y. 2012, *ApJ*, 751, 10
- Paron, S., Ortega, M. E., Cunningham, M., et al. 2014, *A&A*, 572, A56
- Paron, S., Ortega, M. E., Fariña, C., et al. 2016, *MNRAS*, 455, 518

-
- Peterson, B. M. 1997, *An Introduction to Active Galactic Nuclei* (Cambridge Univ. Press, Cambridge)
- Peterson, B. M., Grier, C. J., Horne, K., et al. 2014, *ApJ*, 795, 149
- Petry, D., & CASA Development Team. 2012, in *Astronomical Society of the Pacific Conference Series*, Vol. 461, *Astronomical Data Analysis Software and Systems XXI*, ed. P. Ballester, D. Egret, & N. P. F. Lorente, 849
- Pringle, J. E. 1981, *ARA&A*, 19, 137
- Privon, G. C., Herrero-Illana, R., Evans, A. S., et al. 2015, *ApJ*, 814, 39
- Puccetti, S., Comastri, A., Fiore, F., et al. 2014, *ApJ*, 793, 26
- Puxley, P. J., Brand, P. W. J. L., Moore, T. J. T., Mountain, C. M., & Nakai, N. 1991, *MNRAS*, 248, 585
- Rawlings, J. M. C., Redman, M. P., Keto, E., & Williams, D. A. 2004, *MNRAS*, 351, 1054
- Riechers, D. A., Walter, F., Carilli, C. L., et al. 2011, *ApJ*, 726, 50
- Rieke, G. H., Loken, K., Rieke, M. J., & Tamblyn, P. 1993, *ApJ*, 412, 99
- Riffel, R. A., Vale, T. B., Storchi-Bergmann, T., & McGregor, P. J. 2014, *MNRAS*, 442, 656
- Rigby, J. R., Diamond-Stanic, A. M., & Aniano, G. 2009, *ApJ*, 700, 1878
- Robson, I. 1996, *Active Galactic Nuclei* (Chichester, John Wiley & Sons, New York)
- Rocca-Volmerange, B., Drouart, G., & De Breuck, C. 2015, *ApJ*, 803, L8
- Rodgers, S. D., & Charnley, S. B. 2001, *ApJ*, 546, 324
- Rosenberg, M. J. F., Kazandjian, M. V., van der Werf, P. P., et al. 2014a, *A&A*, 564, A126
- Rosenberg, M. J. F., Meijerink, R., Israel, F. P., et al. 2014b, *A&A*, 568, A90
- Sakamoto, K., Aalto, S., Costagliola, F., et al. 2013, *ApJ*, 764, 42
- Sakamoto, K., Aalto, S., Evans, A. S., Wiedner, M. C., & Wilner, D. J. 2010, *ApJ*, 725, L228
- Sakamoto, K., Ho, P. T. P., Mao, R.-Q., Matsushita, S., & Peck, A. B. 2007, *ApJ*, 654, 782
- Sakamoto, K., Ho, P. T. P., & Peck, A. B. 2006a, *ApJ*, 644, 862
- Sakamoto, K., Mao, R.-Q., Matsushita, S., et al. 2011, *ApJ*, 735, 19
- Sakamoto, K., Okumura, S. K., Ishizuki, S., & Scoville, N. Z. 1999, *ApJ*, 525, 691
- Sakamoto, K., Ho, P. T. P., Iono, D., et al. 2006b, *ApJ*, 636, 685

BIBLIOGRAPHY

- Sandage, A., & Tammann, G. A. 1987, A revised Shapley-Ames Catalog of Bright Galaxies (2nd ed.; Washington, DC: Carnegie Institution of Washington Publication)
- Sanders, D. B., Mazzarella, J. M., Kim, D.-C., Surace, J. A., & Soifer, B. T. 2003, *AJ*, 126, 1607
- Sani, E., Davies, R. I., Sternberg, A., et al. 2012, *MNRAS*, 424, 1963
- Sault, R. J., Teuben, P. J., & Wright, M. C. H. 1995, in *Astronomical Society of the Pacific Conference Series*, Vol. 77, *Astronomical Data Analysis Software and Systems IV*, ed. R. A. Shaw, H. E. Payne, & J. J. E. Hayes, 433
- Schawinski, K., Virani, S., Simmons, B., et al. 2009, *ApJ*, 692, L19
- Schinnerer, E., Eckart, A., Quirrenbach, A., et al. 1997, *ApJ*, 488, 174
- Schinnerer, E., Eckart, A., Tacconi, L. J., Genzel, R., & Downes, D. 2000, *ApJ*, 533, 850
- Schleicher, D. R. G., Spaans, M., & Klessen, R. S. 2010, *A&A*, 513, A7
- Schmidt, M. 1959, *ApJ*, 129, 243
- Schöier, F. L., van der Tak, F. F. S., van Dishoeck, E. F., & Black, J. H. 2005, *A&A*, 432, 369
- Scott, J. E., Kriss, G. A., Lee, J. C., et al. 2005, *ApJ*, 634, 193
- Scoville, N., & Murchikova, L. 2013, *ApJ*, 779, 75
- Scoville, N., Sheth, K., Walter, F., et al. 2015, *ApJ*, 800, 70
- Scoville, N. Z., Soifer, B. T., Neugebauer, G., et al. 1985, *ApJ*, 289, 129
- Scoville, N. Z., & Solomon, P. M. 1974, *ApJ*, 187, L67
- Seale, J. P., Looney, L. W., Chu, Y.-H., et al. 2009, *ApJ*, 699, 150
- Seale, J. P., Looney, L. W., Wong, T., et al. 2012, *ApJ*, 751, 42
- Shakura, N. I., & Sunyaev, R. A. 1973, *A&A*, 24, 337
- Sheth, K., Vogel, S. N., Regan, M. W., Thornley, M. D., & Teuben, P. J. 2005, *ApJ*, 632, 217
- Shlosman, I., Begelman, M. C., & Frank, J. 1990, *Nature*, 345, 679
- Simões Lopes, R. D., Storchi-Bergmann, T., de Fátima Saraiva, M., & Martini, P. 2007, *ApJ*, 655, 718
- Snell, R. L., Narayanan, G., Yun, M. S., et al. 2011, *AJ*, 141, 38
- Soifer, B. T., Bock, J. J., Marsh, K., et al. 2003, *AJ*, 126, 143
- Solomon, P. M., Downes, D., & Radford, S. J. E. 1992a, *ApJ*, 387, L55

-
- . 1992b, *ApJ*, 398, L29
- Solomon, P. M., Radford, S. J. E., & Downes, D. 1990, *ApJ*, 348, L53
- Solomon, P. M., & Vanden Bout, P. A. 2005, *ARA&A*, 43, 677
- Spoon, H. W. W., & Holt, J. 2009, *ApJ*, 702, L42
- Spoon, H. W. W., Keane, J. V., Tielens, A. G. G. M., Lutz, D., & Moorwood, A. F. M. 2001, *A&A*, 365, L353
- Sternberg, A., Genzel, R., & Tacconi, L. 1994, *ApJ*, 436, L131
- Storchi-Bergmann, T. 1991, *MNRAS*, 249, 404
- Storchi-Bergmann, T., Eracleous, M., Teresa Ruiz, M., et al. 1997, *ApJ*, 489, 87
- Storchi-Bergmann, T., Nemmen, R. S., Spinelli, P. F., et al. 2005, *ApJ*, 624, L13
- Storey, P. J., & Hummer, D. G. 1995, *MNRAS*, 272, 41
- Strickland, D. K., Colbert, E. J. M., Heckman, T. M., et al. 2001, *ApJ*, 560, 707
- Strickland, D. K., Heckman, T. M., Colbert, E. J. M., Hoopes, C. G., & Weaver, K. A. 2004, *ApJ*, 606, 829
- Suganuma, M., Yoshii, Y., Kobayashi, Y., et al. 2006, *ApJ*, 639, 46
- Tacconi, L. J., Genzel, R., Blietz, M., et al. 1994, *ApJ*, 426, L77
- Takano, S., Takano, T., Nakai, N., Kawaguchi, K., & Schilke, P. 2013, *A&A*, 552, A34
- Takano, S., Nakajima, T., Kohno, K., et al. 2014, *PASJ*, 66, 75
- Taniguchi, Y. 1999, *ApJ*, 524, 65
- Telesco, C. M., & Decher, R. 1988, *ApJ*, 334, 573
- Telesco, C. M., & Harper, D. A. 1980, *ApJ*, 235, 392
- Thean, A., Pedlar, A., Kukula, M. J., Baum, S. A., & O’Dea, C. P. 2000, *MNRAS*, 314, 573
- Thompson, T. A., Quataert, E., & Murray, N. 2005, *ApJ*, 630, 167
- Toomre, A. 1964, *ApJ*, 139, 1217
- Treister, E., Schawinski, K., Urry, C. M., & Simmons, B. D. 2012, *ApJ*, 758, L39
- Tremaine, S., Gebhardt, K., Bender, R., et al. 2002, *ApJ*, 574, 740
- Tsai, A.-L., Matsushita, S., Kong, A. K. H., Matsumoto, H., & Kohno, K. 2012, *ApJ*, 752, 38
- Tully, R. B. 1988, *Nearby Galaxies Catalog* (Cambridge Univ. Press, Cambridge)

BIBLIOGRAPHY

- Ueda, Y., Akiyama, M., Hasinger, G., Miyaji, T., & Watson, M. G. 2014, *ApJ*, 786, 104
- Ueda, Y., Akiyama, M., Ohta, K., & Miyaji, T. 2003, *ApJ*, 598, 886
- Ulvestad, J. S., & Antonucci, R. R. J. 1997, *ApJ*, 488, 621
- Urry, C. M., & Padovani, P. 1995, *PASP*, 107, 803
- Usero, A., García-Burillo, S., Fuente, A., Martín-Pintado, J., & Rodríguez-Fernández, N. J. 2004, *A&A*, 419, 897
- van der Tak, F. F. S., Black, J. H., Schöier, F. L., Jansen, D. J., & van Dishoeck, E. F. 2007, *A&A*, 468, 627
- Veilleux, S., Kim, D.-C., & Sanders, D. B. 1999, *ApJ*, 522, 113
- Veilleux, S., Kim, D.-C., Sanders, D. B., Mazzarella, J. M., & Soifer, B. T. 1995, *ApJS*, 98, 171
- Veilleux, S., Sanders, D. B., & Kim, D.-C. 1997, *ApJ*, 484, 92
- Véron-Cetty, M.-P., & Véron, P. 2010, *A&A*, 518, A10
- Viti, S., García-Burillo, S., Fuente, A., et al. 2014, *A&A*, 570, A28
- Vollmer, B., Beckert, T., & Davies, R. I. 2008, *A&A*, 491, 441
- Wada, K., & Norman, C. A. 2002, *ApJ*, 566, L21
- Wada, K., Papadopoulos, P. P., & Spaans, M. 2009, *ApJ*, 702, 63
- Walton, D. J., Risaliti, G., Harrison, F. A., et al. 2014, *ApJ*, 788, 76
- Wang, M., Chin, Y.-N., Henkel, C., Whiteoak, J. B., & Cunningham, M. 2009, *ApJ*, 690, 580
- Wang, M., Henkel, C., Chin, Y.-N., et al. 2004, *A&A*, 422, 883
- Wang, R., Wagg, J., Carilli, C. L., et al. 2011, *ApJ*, 739, L34
- Weaver, K. A., Heckman, T. M., Strickland, D. K., & Dahlem, M. 2002, *ApJ*, 576, L19
- Weiß, A., Kovács, A., Güsten, R., et al. 2008, *A&A*, 490, 77
- Wild, V., Heckman, T., & Charlot, S. 2010, *MNRAS*, 405, 933
- Wild, W., & Eckart, A. 2000, *A&A*, 359, 483
- Willott, C. J., Omont, A., & Bergeron, J. 2013, *ApJ*, 770, 13
- Wu, J., Evans, II, N. J., Gao, Y., et al. 2005, *ApJ*, 635, L173
- Wu, Y., Charmandaris, V., Huang, J., Spinoglio, L., & Tommasin, S. 2009, *ApJ*, 701, 658
- Yamada, M., Wada, K., & Tomisaka, K. 2007, *ApJ*, 671, 73

Yamada, T. 1994, ApJ, 423, L27

Zepf, S. E., Ashman, K. M., English, J., Freeman, K. C., & Sharples, R. M. 1999, AJ, 118, 752

Zhang, Z.-Y., Gao, Y., Henkel, C., et al. 2014, ApJ, 784, L31

Zhao, J.-H., Anantharamaiah, K. R., Goss, W. M., & Viallefond, F. 1997, ApJ, 482, 186